Superconducting proximity effect in graphene and Bi nanowire based junctions

Chuan Li

UNIVERSITÉ PARIS SUD
Comprendre le monde, construire l'avenir®

LPS ORSAY

Université Paris-Sud

École Doctorale 564 Physique en Île de France
Laboratoire de Physique des Solides

Discipline : Physique des Solides

Thèse de doctorat

Soutenue le 26 novembre 2014 par

Chuan Li

Superconducting proximity effect in graphene and Bi nanowire based junctions

Directrice de thèse :	Mme. Sophie Guéron	Directrice de recherche (LPS, CNRS)
Composition du jury :		
Président du jury :	Pascal Simon	Professeur (LPS, Univ. Paris-sud)
Rapporteurs :	Christoph Strunk	Professeur (Rengensburg University)
	Claude Chapelier	Ingénieur (INAC CEA)
Examinateurs :	Alexander Brinkman	Professeur (University of Twente)
	Behnia Kamran	Directeur de recherche (ESPCI)
Invités :	Hélène Bouchiat	Professeur&Directrice de recherche (LPS, CNRS)

Superconducting proximity effect in Graphene and Bi nanowire junctions

A DISSERTATION PRESENTED
BY
CHUAN LI
TO
THE DEPARTMENT OF PHYSIC

IN PARTIAL FULFILLMENT OF THE REQUIREMENTS
FOR THE DEGREE OF
DOCTOR OF PHYSICS
IN THE SUBJECT OF
CONDENSED MATTER

UNIVERSITY OF PARIS SUD
ORSAY, FRANCE

NOVEMBER 2014

Contents

Remerciements

L'histoire entre moi et le LPS a commencé au même moment que mon arrivée en France, il y a plus de 6 ans. Il représente forcément une partie importante de ma vie en France et je voudrais remercier de nombreuses personnes du laboratoire.

Je tiens tout d'abord à remercier grandement l'ensemble du groupe MESO qui m'a accueilli avec beaucoup d'enthousiasme depuis 3 ans. Surtout Hélène et Sophie. Comme notre professeur de cours de Physique mésoscopique en M2, Hélène m'a amené au monde du « MESO ». Je suis complètement étonnée par sa passion de la physique et son humour incroyable de physicienne. Avec elle, on a non seulement fait les expériences mais on s'est vraiment amusé avec la physique. Sophie m'a appris les expériences pas à pas, m'a expliqué de façon claire et concise, m'a assuré à chaque étape et jusqu'à ce que je puisse manipuler comme une « grande ». J'ai bénéficié de toutes les discussions, les blagues, les bavardages qu'on a eu dans les bureaux, dans la salle de manips, pendant la pause-café, à la descente de la colline, ou même dans le train, dans la voiture... Ces innombrables moments changeaient petit à petit ma vie et ne disparaîtront jamais. Une preuve de ça est que je resterai « difficile » comme vous quand il s'agit de la physique.

Sandrine m'a beaucoup aidé (presque chaque fois) sur les cryostats et la dilu. Sans elle, il m'était apparu toujours long et difficile de trouver ce que je voulais. Je veux remercier Richard pour ses solutions efficaces et optimisées à tous genres de problèmes. Son attitude rigoureuse en recherche et le travail nous montre un modèle à suivre. C'est aussi un plaisir de discuter avec lui sur les points scientifiques et quotidiens. Alik est toujours un ami très encourageant. J'apprenais souvent de nouvelles choses quand je discute avec lui. Sa technique incomparable a renforcé nos expériences lors de tous les moments importants. I like the 'crazy ' experiments that we did.

Merci à Bastien pour l'accompagnement vivant pendant ces 3 ans (presque). Quand j'essayais de préparer l'album de photo pour ton départ du labo, je me suis rendue compte qu'on a passé vraiment pas mal de temps ensemble ! Pour te récompenser pour les petits cours de Français mélangés avec tes blagues dures, j'ai fait aussi des efforts pour te donner un nom chinois propre. Comment on arrivait à supporter l'autre ?

J'espère que j'ai laissé une impression quand même correcte à Raphaëlle et Anil, nos nouveaux et intelligents thésards du groupe, pendant la dernière année. J'apprécie beaucoup les soirées qu'on a passées aux restaurants ou à la maison. Ça ne vous fait pas trop peur la nourriture chinoise ? Je vous remercie pour m'avoir aidé à préparer ma soutenance. Surtout Raphaëlle a bien « occupé » mes parents ! Je vous souhaite une très bonne continuation.

I would like to thank Katsuyoshi and Shamashis, our post-docs each assisted the beginning and last year of my thesis. With you, I spent much pleasant time in both scientific discussions and casual chats. Also many thanks to Katsuyoshi for the beautiful pictures at every New Year!

Aussi merci à Meydi et Alexei pour m'aider quand j'ai eu besoin et pour m'encourager aux moments importants de loin et de près.

J'ai eu la chance d'être là pendant ces 3 ans pour « témoigner » de la naissance des trois bébés! Elisabeth de Sandrine et Gaëlle et Ewen de Richard. Ça devenait toujours très vivant quand la discussion des petits monstres se lançaient pendant les pauses.

En dehors du groupe, au labo j'ai une liste longue de personnes à remercier. Merci à Raphaël pour ses aides irremplaçables. Je l'ai beaucoup embêté avec des bagatelles. Je veux exprimer mes remerciements sincères à M. Claude Pasquier, qui m'accueilli sympathiquement la première fois au sein du groupe haute pression de ce labo quand je venais d'arriver en France. C'est un souvenir spécial pour moi. Il m'a toujours aidé quand j'en ai eu besoin, jusqu'à la veille de ma soutenance. Merci à M. Pierre-Antoine Albouy pour ses sourires encourageants pendant tous ces années au labo. Merci à M. Michel Héritier pour m'avoir aidé et encouragé pendant le M2. Merci à Mme. Hélène Raffy pour nous conseiller sur l'expérience et pour les communications en chinois aux occasions.

Je dois remercier mes amis doctorants du labo. Julien, en dehors de ses soirées sympathiques et ses BDs immanquables, il m'a aidé souvent sur les procédures administratives compliquées.

Beaucoup de remerciements à mes amis chinois à Paris. Merci à Lukui, pour m'avoir accueilli et supporté.

Je veux remercier mes amis du club de tennis de table à Fresnes. Merci pour vos accompagnements, encouragements, et soutiens.

En dernier, je remercie toujours du fond du cœur mes parents, même si ça ne suffira jamais. Je vous aime.

0 Résumé

Introduction

L'effet proximité de supraconductivité (EPS) est un probe sensible à la cohérence, propriété de spin, même le magnétisme des systèmes. Cet effet est profondément étudié depuis centaine années dans les systèmes variés (isolateur, métal normal, semi-conducteur, matériaux ferromagnétiques, etc..) et parfois combiné avec les autres effets (l'effet Hall quantique, couplage spin-orbite, interaction électron-électron, etc..).

Dans cette thèse, nous sommes intéressés par EPS dans deux systèmes particuliers : graphène et nanofil de Bismuth. Nous allons montrer que le EPS est un outil puissant à sonder et relever les physiques dans les systèmes différents. Parfois, la compréhension du EPS est améliorée par la combinaison avec ces effets.

Depuis la découverte du graphène en 2005, beaucoup d'effort est fait sur ce matériau 2D naturel. La relation dispersion linéaire à l'énergie basse ouvre la porte à la physique Dirac[1, 2]. La densité de charge modulable (même la signe de charge) nous permet de changer les paramètres physiques à un échelle beaucoup plus grand dans un seul système. En conséquence, au champ magnétique relativement bas, l'effet Hall quantique peut être observé[3, 4, 5, 6].

Non seulement la densité de charge, mais aussi les propriétés électroniques sont modulables dans graphène. En changeant une tension de grille, on peut tester l'effet proximité dans les jonctions S/G/S aux régimes différents. Nous avons examiné les jonctions diffusives courtes et longues et comparé le produit $eR_N I_c$ aux différentes échelles d'énergies (le gap supraconducteur, l'énergie de Thouless,...).

La réflexion Andreev ordinaire à l'interface S/N pour la conversion d'un pair de Cooper à un pair de quasi-particule d'électron-trou (ou vice versa) devient une réflexion spéculaire si le niveau de Fermi est ainsi proche au point Dirac[7]. En comparant le courant critique des jonctions S/G/S différentes, nous trouvons que la réflexion Andreev spéculaire est relevé indirectement[8] (Sec.3.3.2).

L'injection des pairs de Cooper aux canaux balistiques 1D

Après la première observation du contact normal atomique quantique (NQPC pour l'anglais normal quantum point contact), l'injection des pairs de Cooper à un canal balistique devient possible. Ce système est étudié théoriquement par Beenakker et van Houten[9] et un courant critique quantifié pour N modes occupées est donné :

$$\Delta I_c = \frac{\mathcal{T} e}{4\pi\tau}, \tag{1}$$

si la jonction est courte ($L/\xi_0 \to 0$). Il est observé pour la première fois par Takayanagi et al.[10].

Pour le case opposite d'une jonction longue ($L \gg \xi_0$) balistique S-QPC-S, le courant critique est quantifié à une valeur non-universelle

$$\Delta I_c = \frac{\mathcal{T} e}{4\pi\tau}, \tag{2}$$

où $\mathcal{T}$ est la probabilité de transmission normale par l'interface N/S selon la théorie BTK[11], et τ est le temps de voyage effectif, si une barrière finie à l'interface et un mismatch de la vitesse de Fermi sont rendu compte.

Pour le gaz d'électron 2D (2DEG en anglais pour 2D electron gas), dans un champ magnétique haut, les états de bord Hall quantique qui sont aussi les canaux balistiques 1D, sont établis. L'injection des pairs de Cooper est aussi considérée théoriquement[12] et tentée expérimentalement[13, 14]. Contrairement à la jonction S-QPC-S, la jonction S-QHS-S n'a pas montré un supercourant. Le

trace de l'effet supraconductivité est peut-être la réduction de la résistance autour des bords des plateaux Hall quantique[14]. Les difficultés expérimentales sont de faire des bons contacts avec les matériaux de haut H_c et d'avoir une meilleur configuration de mesure.

Dans le graphène, par contre, le regime d'Hall quantique peut être atteint au champ magnétique relativement bas ($\sim$4T). Comme les contacts ohmiques sont meilleurs sur graphène que sur le 2DEG [15, 16], la prospective d'injecter des pairs de Cooper au canaux des états de bords d'Hall quantique parait plus favorable. Il est un des buts de cette thèse, et sera discuté dans la chapitre 3.

L'intérêt du couplage spin-orbite

Le couplage spin-orbite (SOC pour l'anglais spin-orbit coupling) couple le degré de liberté du spin d'un électron à son mouvement orbital. Dans certains systèmes, le SOC peut être modulé par un champ électrique externe, ainsi offre une méthode pratique de contrôler le spin[17]. Un rôle important à cet effet peut être espéré pour le SOC dans le sprintronique. L'effet du SOC est aussi lié à la supraconductivité triplet. Par exemple, Gor'kov et al. a montré que le SOC Rashba peut conduire au mélange des appariements singlet et triplet dans le système supraconducteur 2D[18].

Beaucoup des études sont faits pour combiner la supraconductivité (induite) avec le SOC. Il conduit à une transition $0 - \pi$[19, 20] ou un splitting du spin du niveau Andreev dans certaines jonctions Josephson[21]. Même la formation des fermions Majorana est prédite[22, 23] et observée[24] dans les fils quantique avec un SOC fort.

Un autre effet spectaculaire dérivé du SOC est l'effet spin Hall quantique (QSHE pour l'anglai quantum spin Hall effect))[25]. Le QSHE engendre la conductance quantifiée en l'absence de champ magnétique, donc sans brise la symétrie reverse du temps. Les niveaux de Landau sont créés par le SOC. La différence entre le QSHE et le QHE est que la chiralité dépend de la direction du spin, i.e. les charges sont polarisés en spin quand ils propagent dans une direction et polarisés en direction du spin opposée quand ils propagent dans une autre direction.

Dans cette thèse, nous sommes intéressés à induire l'effet proximité de supraconductivité dans des systèmes différents avec un SOC (intrinsèque ou induit). Les concepts basiques sur le SOC sont décrites dans la section 2.4.

Induire le couplage spin-orbite dans graphène

Le petit SOC intrinsèque dans graphène empêche la formation d'un état isolant topologique dans le graphène. [26, 27]. Beaucoup de méthodes sont proposées à induire le SOC dans graphène pour les intérêts tous les deux dans spintronique (graphène a un temps de relaxation du spin très long) et les autre recherches fondamentales. La déposition des atomes sur graphène est théoriquement prédit à induire le SOC[28]. Une version similaire est la déposition des métallo-molécules

organique dans lesquels un atome métallique est encerclé par des molécules organiques cycliques. Plusieurs molécules sont prouvés d'apporter un moment magnétique quand ils sont ionisés[29, 30, 31, 32]. Nous utilisons les Pt-porphyrines dissous dans le solvant THF à fonctionnaliser graphène, espérant que les molécules se forment un arrangement ordonné sur graphène et induisent le SOC dans graphène par l'atome Pt.

Fort couplage spin-orbite dans Bismuth

Bismuth est un semi-métal avec fort couplage spin-orbite. Un grand nombre d'études sont effectués pour déterminer la structure de bande dans le bulk, surface (film mince) et nanofil[33, 34, 35]. Les mesures de photoémission à angle résolu (ARPES pour l'anglais Angle-resolved photoemission) [36, 37] et de STM (scanning tunneling microscope) [38] montrent que les états de surface se forment sur certaines facettes du cristalline de Bismuth (e.g. [111]). Les propriétés des états de surface sont complètement différentes que celles de bulk : densité de charge plus grande, longueur d'onde de Fermi plus petite et plus important, une splitting de spin dans la structure de bande due à la brise de la symétrie inversion. Dans les nanofils de Bismuth, le confinement quantique favorise la contribution des états de surface. L'état spin Hall quantique est aussi prédit théoriquement pour la facette [111] [39]. Les fils de Bismuth de bonne qualité sont mesurés pendant cette thèse. Ils fournissent un plate-forme pour le mesure de transport balistique.

Cette thèse

Cette thèse est en 5 chapitres : dans le premier chapitre, nous décriront les concepts théoriques importants. Il est principalement sur l'effet de proximité de supraconducteur, ainsi le graphène et Bismuth. Les chapitres 3 et 4 sont sur les jonctions de graphène et graphène fonctionnalisé. Ils sont fortement liés, en ce sens qu'ils partagent les mêmes échantillons mesurés avant et après la déposition des molécules. Dans le chapitre 5, nous montrons les résultats sur les jonctions de nanofils de Bi. Due au couplage spin-orbite très fort, l'effet de proximité de supraconducteur est beaucoup modifié. A partir de ces effets, nous déduiront les propriétés exotiques dans les nanofils de Bi.

1. Effet de proximité supraconducteur dans graphène

Le diagramme complet de eR_NI_c vs E_{Th} dans les jonctions S/G/S diffusives

Avant cette thèse, la supraconductivité induite dans graphène est réalisée par plusieurs groupes[40, 41, 42]. Par contre, les échantillons, malgré tout, sont plus tôt dans le régime de la jonction courte ($L \lesssim \xi_s$). Nous avons réussi à fabriquer les échantillons avec les contacts différents ainsi les longueurs

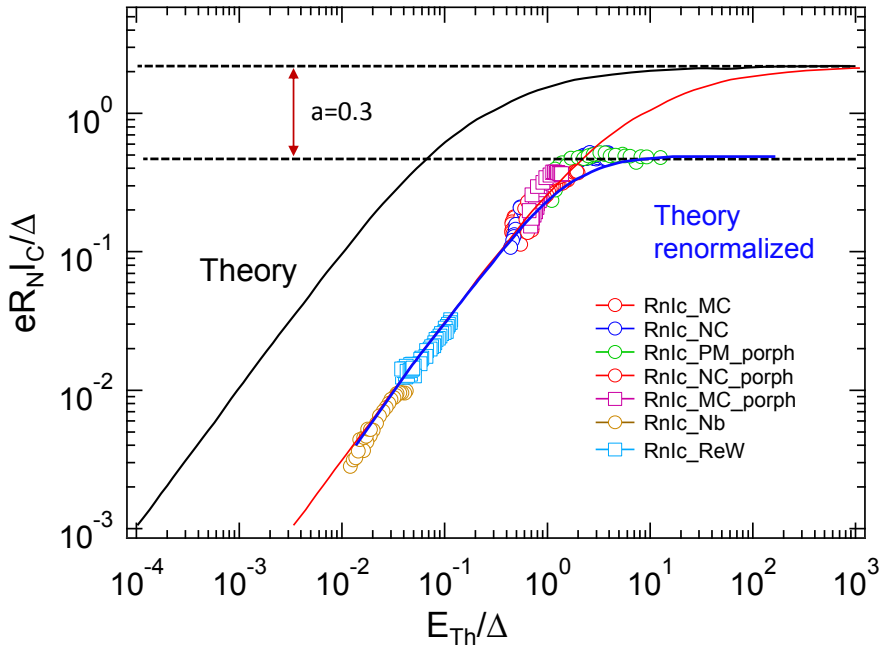

Figure 0.0.1: Relation normalisée de $R_N I_c - E_{Th}$ des jonctions S/G/S Les différentes couleurs correspondent aux échantillons différentes. Les données expérimentales sont 3 – 100 fois plus petites que la théorie. Quelques échantillons correspondent à $E_{Th}/\Delta \approx 1$ sont dans la limite intermédiaire. La jonction plus longue PM, qui correspond à une courbe plate dans la régime de la jonction courte. Les échantillons Nb et ReW sont proportionnels à E_{Th} dans la régime de la jonction longue.

pour que les échantillons se trouve dans un grand régime, puis compléter le diagramme de l'effet de proximité supraconducteur dans graphène. Quand on compare le courant critique experimental à la théorie pour une interface parfaite, une réduction existe toujours [40, 42, 41]. Selon notre diagramme d'effet de proximité (Fig.1.0.1), le facteur de réduction dépend la limite de jonction : il est près que constant dans la régime de la jonction courte, et décrois rapidement quand il entre dans le régime intermédiaire, et la régime de la jonction longue.

L'indication de la réflexion Adreev spéculaire (SAR pour l'anglais Specular Andreev Reflection)

Dans les jonctions longues, nous avons observé une suppression inattendue du supercurrent près du point Dirac, qui doit être robuste dans une jonction courte malgré la présence des puddles de charge. En excluant l'effet thermal et la transmission finie comme l'origine de cette suppression, nous pensons c'est une indication de la réflexion Andreev spéculaire (Fig.1.0.2).

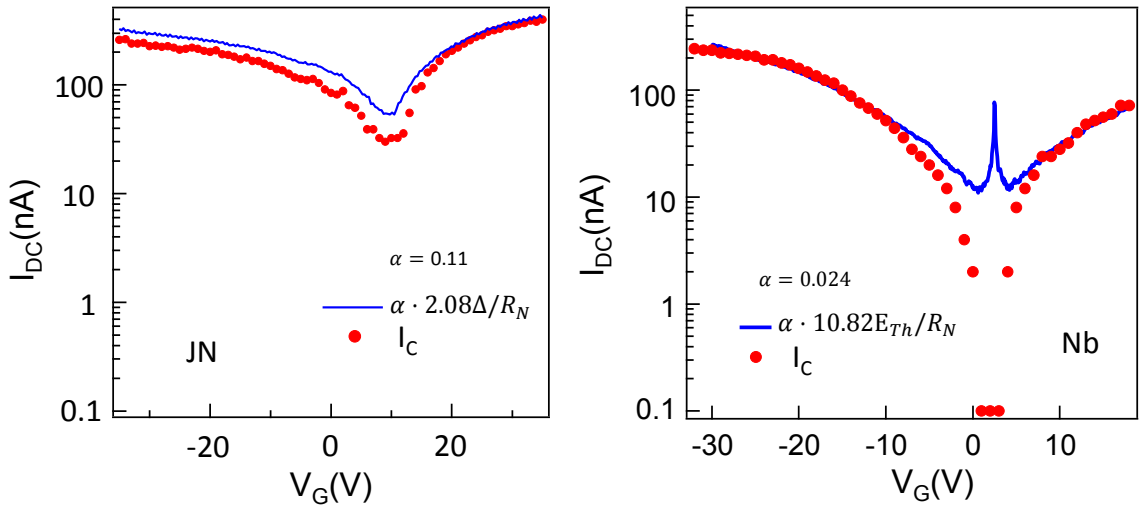

Figure 0.0.2: I_c théorique et mesuré des échantillons JN (Ti/Al) et Nb (Pd/Nb). (gauche) JN est dans la limite de la jonction courte, (droit) Nb est dans la limite de la jonction longue. Tous les deux a un courant critique plus petit que la théorie. Autour du point Dirac, I_c de Nb décroit beaucoup plus rapide que I_c de JN.

L'injection des pairs de Cooper dans le régime Hall quantique

L'interaction d'effet de proximité supraconducteur et l'effet Hall quantique est étudiée dans cette thèse. Un graphène feuille contacté par deux électrodes supraconducteurs haut H_c est une configuration possible à injecter les pairs de Cooper dans les canaux quantifiés Hall quantiques. L'effet Hall quantique est caractérisé by une conductance quantifiée avec un facteur de remplissage entier ν qui correspond aux niveaux de Landau. Dans le graphène, ce facteur est décalé par un demi-entier.

$$\begin{aligned}\sigma &= \frac{ge^2}{h}(n+\frac{1}{2}) \\ &= \frac{4e^2}{h}(n+\frac{1}{2})\end{aligned} \tag{3}$$

Nous avons réussi à connecter le graphène par les contacts de ReW qui a un champ critique $H_c \sim 8T$. Sur les plateaux, les courbes $dV/dI(I_{DC})$ ont toujours un peak à $I_{DC} = 0$ et en revanche, entre deux plateaux, parfois nous trouvions des creux à $I_{DC} = 0$ (Fig.1.0.4). C'est une indication de la présence de l'effet de proximité supraconducteur.

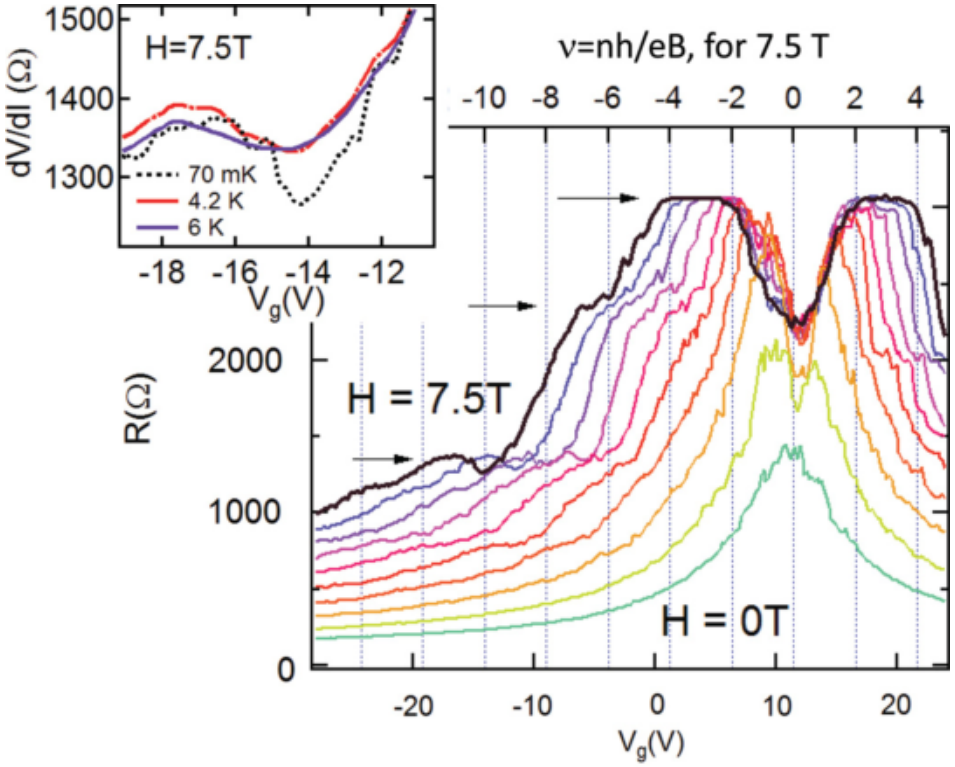

Figure 0.0.3: La résistance différentielle en fonction la grille d'échantillon ReW au champ magnétique de 0 à 7.5T. T=70mK. L'inséré montre comment le plateau Hall à 7.5T et $V_G = 14V$ évolue quand la température augmente.

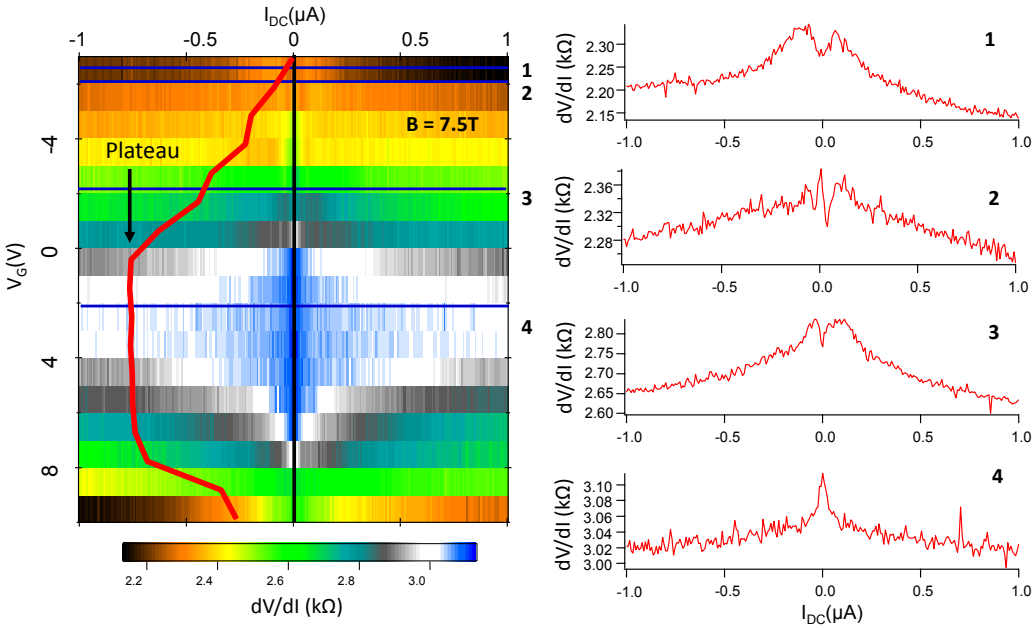

Figure 0.0.4: La résistance différentielle d'échantillon ReW à 7.5T pour les tensions de grille. Gauche : 2D-plot de $dV/dI(I_{DC}(nA))$ pour les tensions de grilles différentes (y axe). La courbe rouge est le profil de la résistance différentielle à $I_{DC} = 0$ Droit: les profils pour les $dV/dI(I_{DC})$ courbes à certaines tensions de grilles (lignes noires).

2. Effet de proximité supraconducteur dans le graphène greffé par les Pt-porphyrines

L'échange entre les métallo-porphyrines et graphène est associé à la formation d'un singlet mangétique délocalisé dans les molécules, indépendant à la nature de cet atome métallique. Nous étudions les modifications des propriétés de transport à basse température dans les jonctions de graphène avant et après la déposition des Pt-porphyrines.

Neutralisation de graphène : transfert de charge

Des dépostions similaires sont faites avant cette thèse [43, 44] et le spectroscope Raman d'une molécule sur graphène implique un dopage de charge dans graphène. Les molécules différentes sont sensée d'être soit un donneur soit un accepteur. Mais d'après notre mesure de transport, nous trouvons une neutralisation de graphène due à un transfert de charge(Fig.1.0.5).

Dépendance de la grille du magnétisme relevé par l'effet de proximité

Le modèle basique pour étudier la formation du moment magnétique dans un métal est le modèle d'impureté Anderson [45]. Basé sur ce modèle, Uchoa et al. montre que les impuretés dans

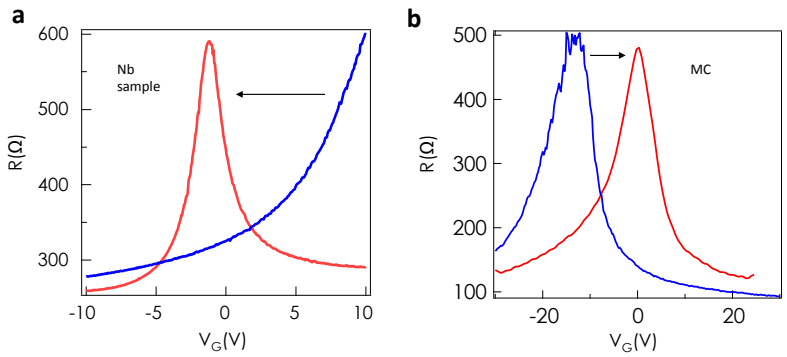

Figure 0.0.5: La dépendence de la grille de résistance avant et après la déposition des porphyrines sur deux échantillons : (a) Nb, (b) G92TiAl_MC . Sans porphyrines (bleu) les échantillons peuvent être dopé en trou (a) et en électron (b). Après la déposition, dans les deux cases, le point Dirac est ramené à zéro volte. Il implique un double sens transfert de charge.

graphène peuvent être changés de magnétique à non-magnétique en changeant le niveau de Fermi. Nous détectons ce modèle dans graphène par l'effet de proximité.

Pour les jonctions longues, nous observons que , après la dépostion de porphyrines, le supercourant devient asymétrique par rapport la grille : dans la région dopée en trou, I_c est plutôt inaffecté, au contraire dans la région dopé en électron, supercourant est supprimé. (Fig.1.0.9).

Nous expliquons ces résultats par une interaction RKKY de longue portée entre les molécules, via les porteurs de charge dans graphène, conduisant à un ordre magnétique collectif dans les porphyrines.

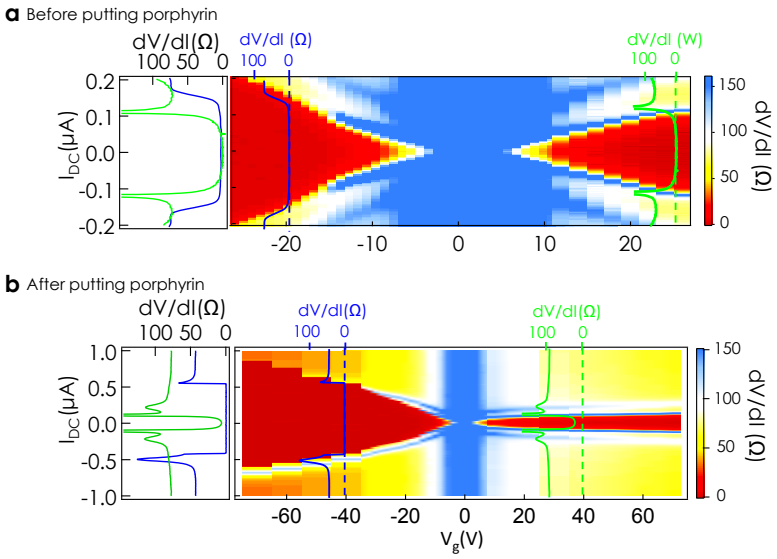

Figure 0.0.6: Da la supraconductivité induite bipolaire à unipolaire. Les régions rouges foncées correspondent à une résistance différentielle nulle. (a) avant de mettre les porphyrines, le supercourant est bipolaire, (b) après la déposition, le supercourant devient unipolaire.

3. Effet de proximité supraconducteur dans les nanofils de Bismuth

A basse température (100mK) et champ nul, nous arrivons à induire la supraconductivité dans les nanofils de Bi par les électrodes de tungstène. Les courant critique est entre 100nA et $1\mu A$.

Supercourant persistent à 11T

Les électrodes de tungstène ont un champ critique très élevé ($\sim 12T$). Nous trouvons l'état supraconducteur induit dans les fils de Bi jusqu'à 11T (Fig.1.0.10). C'est vraiment différent ce qu'on attend pour un fil d'or de la même taille.

Les oscillations du courant critique comme un SQUID modulées dans une grande échelle

Une oscillation comme un SQUID du courant critique de 0T à 9T et une modulation sur ces oscillations d'une échelle d'1T sont observées(Fig.1.0.11).. Elles correspondent respectivement une formation des états de bord 1D très confinés sur certaine surface du nanofil de Bismuth, et l'effet Zeeman.

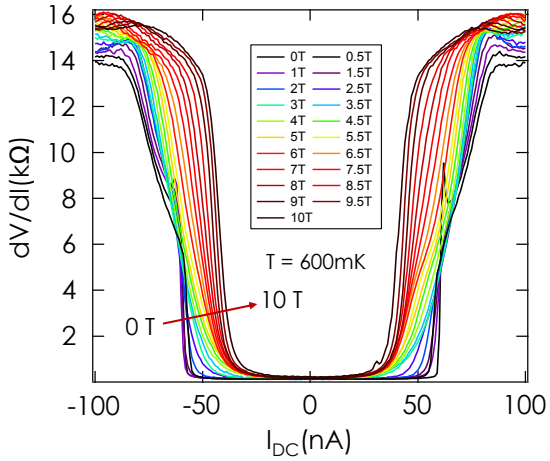

Figure 0.0.7: dV/dI coubes aux champs différents. Les courbes de la résistance différentielle en function du courant DC sont prises aux différents champs de 0 à 11T.

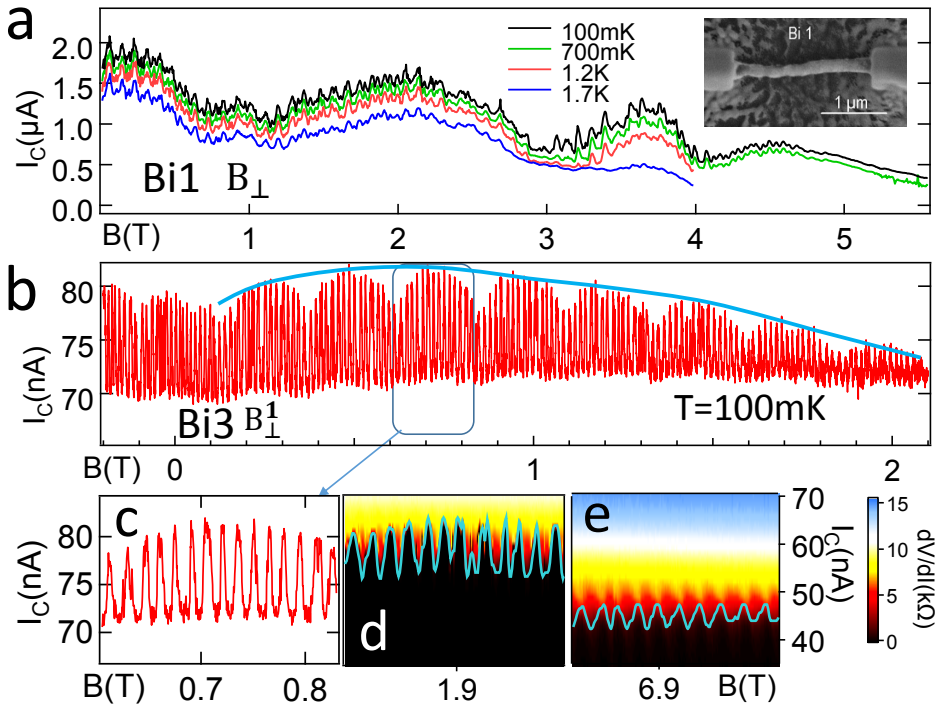

Figure 0.0.8: Oscillations comme un SQUID dans Bi1 et Bi3(a) and (b) montrent des oscillations du I_C en fonction du champ magnétique avec une période de 800 Gauss (a) et de 150 Gauss (b) pour l'autre;(c) est une figure zoomée sur une échelle de 2000 Gauss de (b); (d) et (e) sont les scans des courbes de dV/dI à different champs.

1 Introduction

The superconducting proximity effect (SPE) is a sensitive probe of the quantum coherence, spin properties, or even magnetism of systems in which superconducting correlations can be induced by coupling them to superconductors. This effect has been widely studied for almost 100 years in various systems (insulators, normal metals, semiconductors, ferromagnetic materials, etc...) and sometimes in combination with other effects (quantum Hall effect, spin-orbit coupling, electron-electron interaction, etc...).

In this thesis, we are interested in the SPE induced in two particular systems, graphene flakes and bismuth nanowires. We are going to show that the SPE is actually a powerful tool to probe and to reveal different physics in various systems. Sometimes, the understanding of the SPE can also be improved by combining it to other effects.

Since the discovery of graphene in 2005, a lot of attention has been paid to this natural 2D material. Graphene's special band structure leads to many interesting features. The linear dispersion relation at low energy opens the door to Dirac physics[1, 2]. The gate tunable carrier density (and even the sign of carriers) allows one to explore the physical parameters in a much larger range in both conduction and valence band in a single system. As a consequence, at a relatively low magnetic field, the quantum Hall effect can be observed in this natural 2D material[3, 4, 5, 6].

Not only the carrier density is tunable in graphene, but also the transport properties. By gating the sample, one can test the proximity effect in S/G/S junctions in different transport regimes: we have examined both diffusive short and long junctions system, and compared the proximity effect "figure of merit", the eR_NI_c product, to the theoretical predictions that involve different energy scales (superconducting gap, Thouless energy...).

The ordinary Andreev retro-reflection at the S/N interface for the conversion of a Cooper pair into an electron-hole quasi-particle pair (or vice versa) can become a specular reflection in S/Graphene interface when the Fermi level is close enough to the Neutrality point (or the Dirac point)[7]. By comparing the supercurrent in different S/G/S junctions, we find that the specular Andreev reflection is indirectly revealed [8] (Sec.3.3.2).

The injection of Cooper pairs into ballistic 1D channels

After the first observation of normal quantum point contact (NQPC), the injection of Cooper pairs into a ballistic channel became possible. This problem was theoretically addressed by Beenakker and van Houten[9] and a quantized critical current for N occupied modes is given by

$$I_c = N\frac{e\Delta_0}{\hbar} \tag{1.1}$$

if the junction is short ($L/\xi_0 \to 0$). This was observed for the first time by Takayanagi H. et al.[10].

For the opposite case of a long ($L \gg \xi_0$) ballistic S-QPC-S junction, the critical current is quantized at a non-universal value

$$\Delta I_c = \frac{\mathcal{T}e}{4\pi\tau}, \tag{1.2}$$

where $\mathcal{T}$ is the normal-transmission probability through the N/S interface according to BTK theory, and τ is the effective travel time, if a finite barrier at the interfaces and a Fermi velocity mismatch are considered.

For the 2DEG, in high magnetic field, the quantum Hall edge states are established, which are also 1D ballistic channels. The injection of Cooper pairs was also considered theoretically[12] and attempted experimentally[13, 14]. In contrast to S-QPC-S junction, the S-QHS-S junction didn't show a supercurrent and not even mention the critical current quantization. The trace of the su-

perconducting effect may be the reduction of the resistance around the edges of quantum Hall plateaus[14]. The experimental difficulties are in making the good high H_c contacts and the improvement of sample configuration. In graphene, however, the quantum Hall regime can be reached at relatively low field (4T). Since ohmic contacts are better on graphene than on usual heterostructure 2D electron gas[15, 16], the prospect of injecting Cooper pairs into quantum Hall edge states in graphene using high H_c superconductor electrodes seems more favorable. That's one of the goals of this thesis. We are going to discuss the results in Chapter 3.

The interests of spin-orbit coupling(SOC)

The spin-orbit coupling couples an electron's spin degree of freedom to its orbital motion. In certain systems the SOC can be modulated by an external electric field, thus providing a convenient method of spin control[17]. An important role can therefor be expected for the SOC in the sprintronics. The SO effect is also related to triplet superconductivity. For example, Gor'kov et al. showed that the Rashba SOC can lead to the mixing of singlet and triplet pairings in 2D superconducting system[18].

Much attention has been paid to combining the (induced) superconductivity with SOC. It leads to a possible $0-\pi$ junction transition[19, 20] or an Andreev level spin splitting in some Josephson junctions[21]. Even the formation of Majorana fermions[22, 23] is predicted and observed[24] in quantum wire with strong SOC.

Another spectacular effect derived from the SOC is the quantum spin Hall effect (QSHE)[25]. The QSHE gives rise to quantized conductance in the absence of magnetic field, thus without breaking the time reversal symmetry. The degenerate quantum Landau levels are created by the SOC. The QSHE differs from the quantum Hall effect in that the different chirality depends on the spin direction, i.e. the charges are spin polarized when they propagate in one direction and polarized in opposite spin direction when they propagate in the another direction.

In this thesis, we are also interested in inducing superconducting proximity effect in different systems with (intrinsic or induced) SOC. The basic concepts about SOC are described in Sec.2.3.

Inducing spin-orbit coupling in graphene

The intrinsic small SOC in graphene prevents the formation of a topological insulating state in graphene[26, 27]. Many ways are considered to induce the SOC into graphene sheet for the interest both in spintronics (graphene has a very long spin relaxation time) and other fundamental researches. Deposition of adatoms on graphene has been theoretically predicted to induce SOC in graphene[28]. This can be done with a similar vision by depositing organic metallo-molecules in which a metallic atom is encircled by cyclic organic molecules. Various molecules have been proved

to carry a magnetic moment when charge transfer occurs[29, 30, 31, 32]. In this thesis we use Pt-porphyrins in THF solvent to fictionalize graphene, the molecules are expected to constitute an ordered arrangement on graphene, with heavy Pt atoms inducing SOC in graphene.

Molecule deposition on graphene

Meanwhile, the molecule deposition on graphene is one of the approaches to controllably change the doping in graphene[46, 44] which holds great application interests and also interesting physic to be explored. The fact that certain molecules serve as donors[47] or acceptors[47, 44] of electrons can be understood by the simple HOMO-LUMO energy gap structure. However the bending of energy bands in molecules at the interface of molecules and metal, semi-metal, insulator is well studied in organic-semiconductor systems. Also a reduction in energy gap is observed when they interact with substrate, metal, or graphene for vast systems[48, 49]. In this thesis, we find a dual direction charge transfer between graphene and molecules. A auto-alignment mechanism[50, 51, 52] must be involved in this process. This may imply a more complex mechanism if the possible charge transfer in-between the molecules, like tunneling[53] or thermally activated hopping[54, 55] processes, are taken into count. The determination of the origin of this charge transfer is beyond the scope of this thesis, but it will be still carefully discussed in the Appendix B.

Strong SOC in Bismuth

If one talks about spin-orbit coupling, Bismuth has to be mentioned. Bismuth bulk is a semi-metal with strong SOC. A lot of work has been done to determine the band structures in bulk, surface (thin film), and nanowires[33, 34, 35]. Angle- resolved photoemission (ARPES) measurements[36, 37] and very recent STM and transport measurements[38] show that surface states form on certain facets of Bi crystals (e.g. [111]). These surface states have completely different properties than Bi bulk: higher carrier density, smaller Fermi wavelength λ_F, and in particular spin split bands due to inversion symmetry breaking. In Bi nanowires, quantum confinement favors the contribution of surface states compared to bulk states. The quantum spin Hall state is also predicted theoretically on the Bi [111] surface[39]. The high quality Bi crystal nanowires were measured during this thesis. They may provide the platform of the ballistic transport measurement.

Outline of this thesis

This thesis is written in 4 chapters: chapter 2 describes the important theoretical concepts and basic physics needed to understand this thesis. It is mainly about the proximity effect, with an introduction on graphene and Bismuth. Chapter 3 and chapter 4 are both on the S/Graphene/S junctions

and strongly related, in the sense that they share the similar physics of proximity effect and also that the experiments are carried out on the same samples before and after the deposition of porphyrins. In chapter 5 we show the results on S/Bi nanowire/S junctions. Due to the strong spin-orbit coupling in Bi nanowire, the results are quite different from those of graphene. Different systems (samples) are realized in this thesis, in Appendix A we address the sample fabrication procedures, as well as our measurement system.

1. Superconducting proximity effect in pristine graphene

The full eR_NI_c vs E_{Th} diagram in diffusive S/G/S junction

Before this thesis, inducing superconducting proximity effect in graphene was proved to be possible[40, 41, 42]. However experiments were all in the regime of near-short junction limit $L \lesssim \xi_s$). By making different length samples, we investigate the superconducting proximity effect through graphene from the short/intermediate junction limit to the long junction limit thus completing the diagram of the superconducting proximity effect in graphene.

When compared to theoretical prediction with perfect interface transmission, the experimentally detected critical current is always smaller[40, 42, 41]. We have established a full diagram from long junction to short junction of the behavior of our samples(Fig.1.0.1), and find that this discrepancy always exists and depends on the junction limit. The reduction factor in the long junction limit is 10 times higher than that in the short junction.

The indication of specular Andreev reflection (SAR)

Particularly in the long S/G/S junctions, we observed an unexpected suppression of supercurrent near the Dirac point of graphene. In many reported experiments (for short junctions), in this regime of gate voltage, the supercurrent was shown to be robust regardless of the presence of the charge puddles. Excluding the thermal effect and finite transmission, we attribute this suppression to the specular Andreev reflection (Fig.1.0.2). The field dependence of the critical current is also investigated for all samples.

Injection of Cooper pairs in Quantum Hall regime

The interplay of the superconducting proximity effect and quantum Hall effect was also investigated in this thesis. By using superconducting electrodes with high critical field (H_c) to contact a graphene sheet, the injection of Cooper (Andreev quasi-particle) pairs into graphene in quantum Hall regime becomes possible. This was considered as one of the ways to inject Cooper pairs into ballistic quantized channels. The quantum Hall effect is generally characterized by an quantized

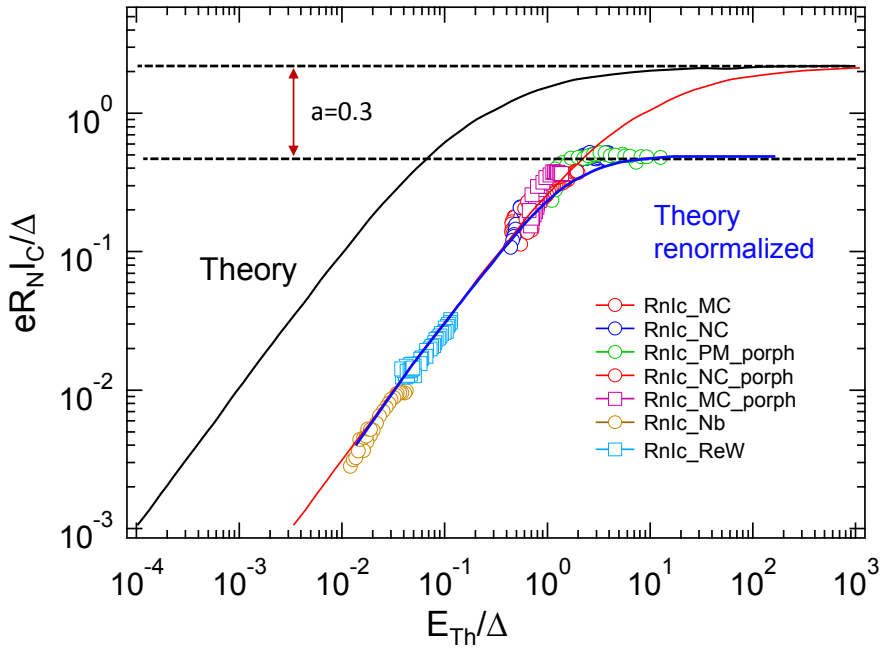

Figure 1.0.1: Normalized $R_N I_c - E_{Th}$ relation for SGS samples from short junction limit to long junction limit. Same color and shape dots correspond to a same sample. All of the $R_N I_c$ products are smaller than the theory curve (black) by a factor 3 to 100. Several samples correspond to $E_{Th}/\Delta \approx 1$: these samples are in the intermediate region and should behave like short junction. The shortest sample PM, which shows flat curve at doped region, is really in short junction limit. Nb and ReW samples depend linearly on E_{Th} with the same slope (the red curve is horizontal translation of the theory curve) in the long junction limit.

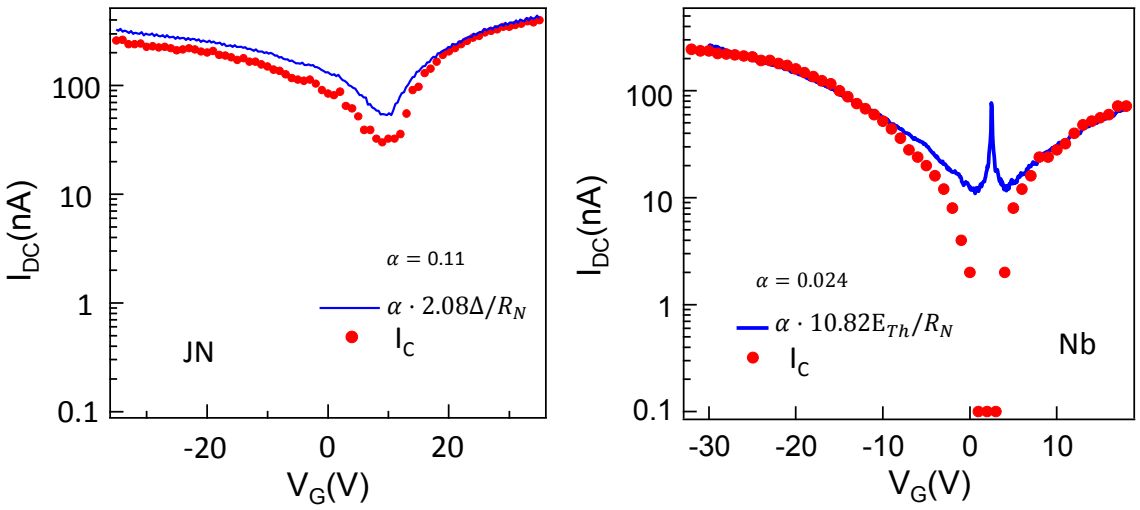

Figure 1.0.2: Theoretical and measured I_c of sample JN (Ti/Al) and sample Nb (Pd/Nb). (Left) JN sample is in the short/intermediate junction limit, (right) Nb sample is in the long junction limit. Both of them have a critical current smaller than expected. For JN, the prefactor $\alpha = 0.26$ implies that the critical current is 10 times smaller than expected for short junction. For Nb sample, the factor between theoretical and experimental results is about 40. The divergence of the theoretical curve is due to the dysfunction of the capacitance model:the presence of the charge puddles result in a finite conductance at the Dirac point instead of the theoretical vanishing of the density of states in graphene.

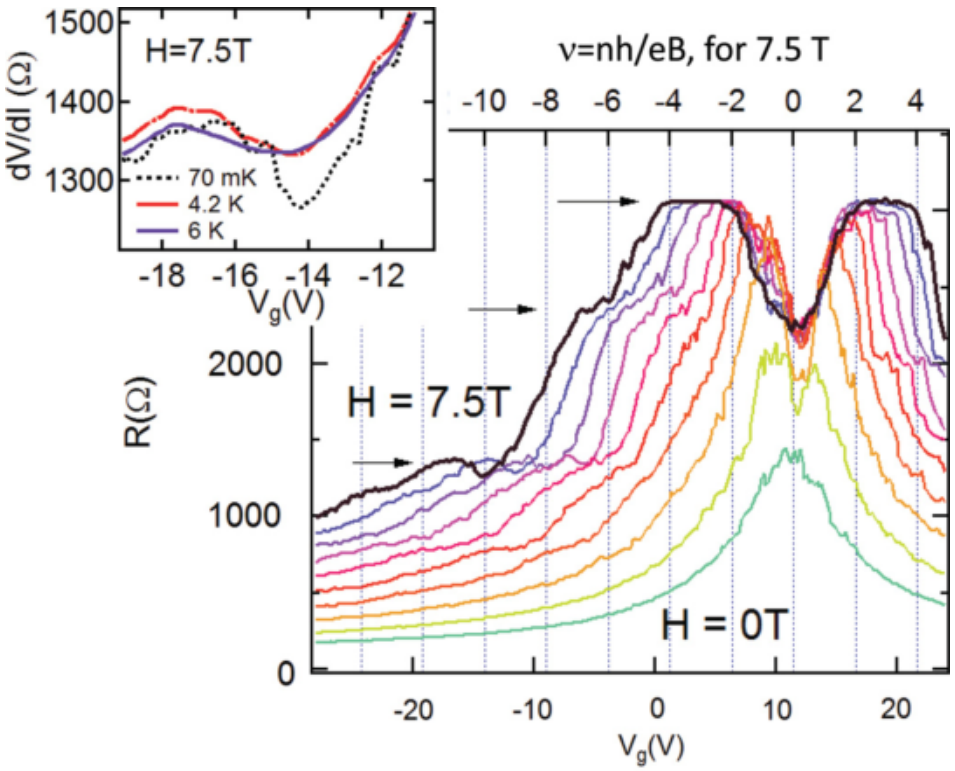

Figure 1.0.3: Two wire differential resistance as a function of gate voltage for the sample with ReW (H c > 7.5T), at magnetic fields from 0 to 7.5 T, every Tesla between 0 and 5 T, and every 0.5 T above 5 T. Temperature is 70 mK. The inset displays how the Hall plateau at 7.5 T and $V_G = 14V$ flattens out as temperature is increased.

conductance with an integer filling factor ν which corresponds to the Landau levels. In graphene, the quantum Hall effect is shifted by a half integer

$$\begin{aligned} \sigma &= \frac{ge^2}{h}(n+\frac{1}{2}) \\ &= \frac{4e^2}{h}(n+\frac{1}{2}) \end{aligned} \tag{1.3}$$

due to the electron-hole gapless band structure: the lowest Landau level is shared by the electron and the hole and there is no energy level at CNP[3, 4, 5, 6]. The quantum Hall effect (Fig.1.0.3)is observed in all our samples. One of the samples has ReW as contacts which has a high H_c up to 8T. We found a zero-bias conductance increase at the edge of the QHE plateaus and some dip features at zero bias of the dV/dI(I_{DC}) curves between two QHE plateaus in contrast to the seen peak for all curves taken on the plateaus (Fig.1.0.4). This is an indirect indication of the presence of the superconducting proximity effect.

Additionally, the third harmonic differential resistance was measured at different magnetic field, the sign of which indicates a peak or a dip feature in the dV/dI curves.

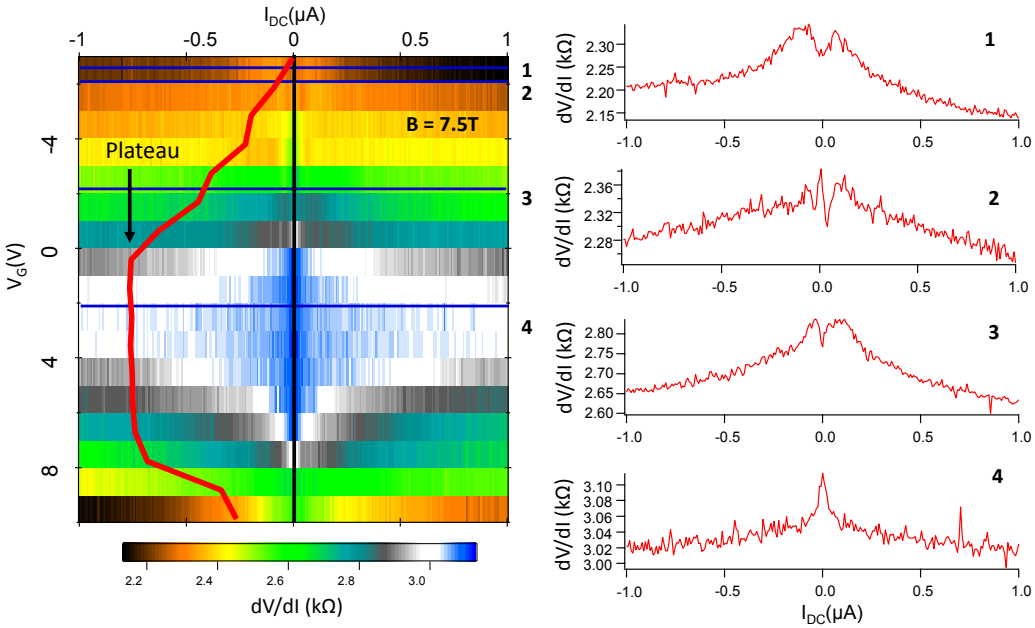

Figure 1.0.4: Differential resistance of ReW sample at 7.5T for different gate voltages. Left color-plot of $dV/dI(I_{DC}(nA))$ for different gate voltages (y axis). The red curve is the profile of the differential resistance at $I_{DC} = 0$ Right: the profiles for the $dV/dI(I_{DC})$ curves at certain gate voltages (black lines).

2. Superconducting proximity effect in Porphyrin-grafted graphene

Metallo-porphyrins molecules are known to interact with carbon based molecules with π orbitals, giving rise to electron or hole doping. This charge exchange between the porphyrin and graphitized carbon is associated to the formation of a magnetic singlet delocalized on the molecule independently of the nature of the metallic host atom, which can be not magnetic. We investigated the modification of low temperature transport properties of several graphene samples after deposition of Pt-porphyrins.

Neutralization of graphene: charge transfer

Similar molecule depositions were done before[43, 44], and Raman spectroscopy implies that a charge doping occurs in the graphene. Different kinds of molecules can be either donor or acceptor. Only one experiment with STM measurement shows a possible inversed charge transfer from a Nitrogen doping in graphene to H_2TPP molecule[48]. However, the transport measurement wasn't carried out systematically in these experiments. Our first results about the graphene grafted with molecules shows a surprising neutralization of graphene doping due to a charge transfer(Fig.1.0.5).

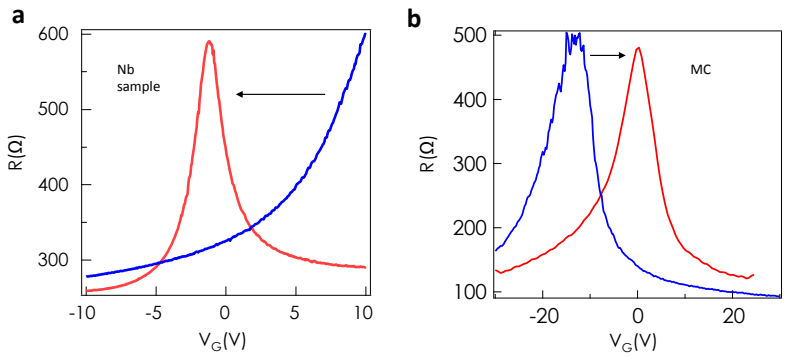

Figure 1.0.5: Gate dependence of resistance before and after the deposition of porphyrins for two samples, (a) Nb sample, (b) G92TiAl_MC. Without porphyrins (blue curves), the samples can be hole doped (a) and electron doped (b). After grafting porphyrins, in both case, the Dirac point of of graphene is brought to zero, graphene becomes neutral. This implies that charge transfer occurs between graphene and porphyrins and the molecules can be donors (a) as well as acceptors (b) of electrons.

The process can even be manipulated by an external gate.

Induced magnetism

As a consequence of the charge transfers, the molecules can be tuned to a special magnetic state. Based on this point of view, we investigated both normal contact samples and superconducting contacts samples. By measuring the magnetoresistance in both perpendicular field and parallel field, we found hysteresis in perpendicular field (Fig.1.0.6) and an asymmetric feature in parallel field (Fig.1.0.7).

Gate dependence of the magnetism revealed by proximity effect

The basic model for the study of magnetic moment formation in metals is the well-known Anderson impurity model[45]. Based on this model, Uchoa et al.[56] shows that the impurities in graphene can be tuned from magnetic to non-magnetic by just changing the Fermi level (thus the gate voltage), and vice versa. We can reveal this phenomenon thanks to the superconducting proximity effect that we induce in graphene.

In short junctions (with Ti/Al contacts), we find the magnetic field dependence of the critical current (Fraunhofer pattern) changes with the gate (Fig.1.0.8).

For the long junctions (sample connected to Pd/Nb superconducting electrodes), we observe that, after the porphyrin deposition, whereas the Josephson current is unaffected in the hole doped region, it is strongly quenched in the electron doped one (Fig.1.0.9). We relate this quenching of the Josephson current to the formation of magnetic moments on the ionized porphyrins. This magnetism is also revealed by a sizable hysteretic magnetoresistance in the electron doped region

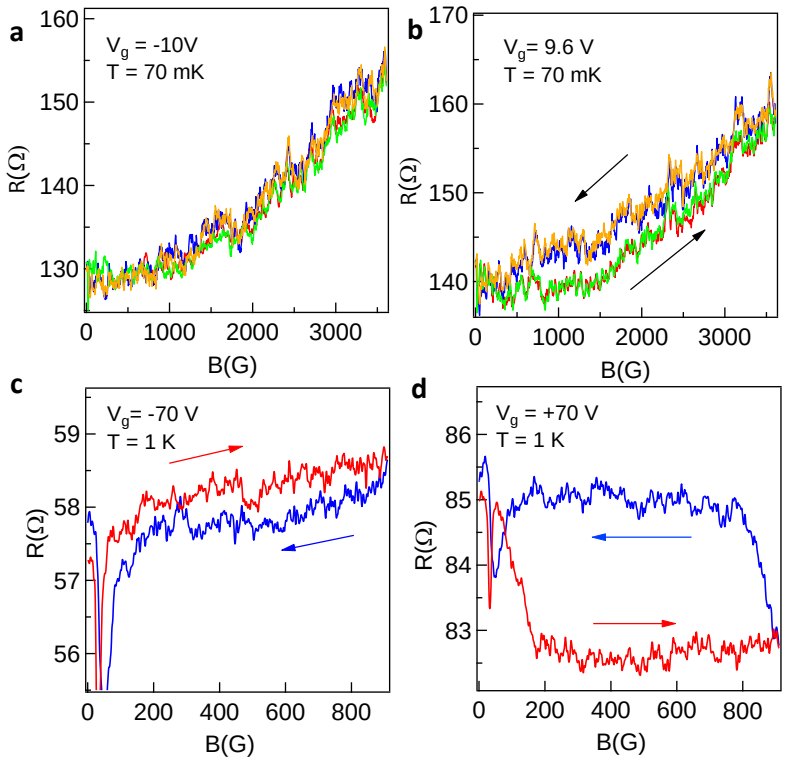

Figure 1.0.6: Unipolar hysteresis in the graphene's magnetoresistance after porphyrin deposition, at two temperatures, with a field direction perpendicular to the graphene plane. The hysteresis is quite large at positive gate voltage (electron doping, b and d) and negligible (at least an order of magnitude smaller) for hole doping (a and c),confirming the existence of a magnetic order that suppresses the supercurrent for electron doping. The anomalies at very low magnetic field correspond to the superconductivity of the contacts, and exist both in the electron and hole doped regions. The reproducible fluctuations at 100 mK are mesoscopic conductance fluctuations.

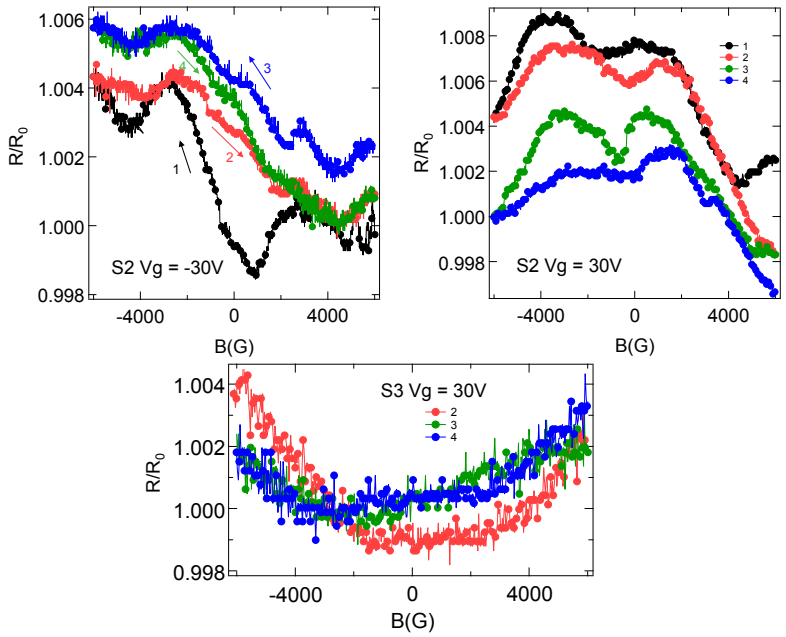

Figure 1.0.7: In plane field effect in sample G58. (a) Asymmetric magnetoresistance in parallel field for S2 (with porphyrins). The curves in different colors represent the sweeping order in magnetic field. (b) magnetoresistance in parallel field for S3 (without porphyrins).

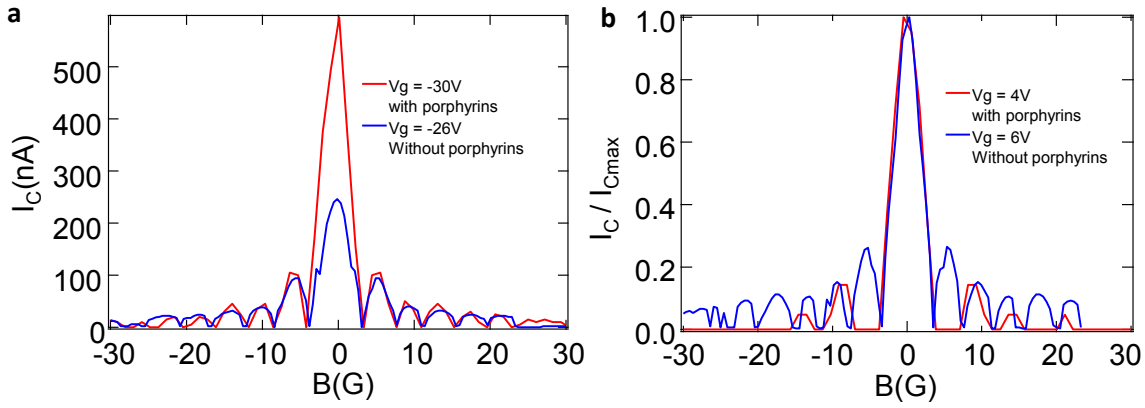

Figure 1.0.8: Fraunhofer pattern of sample MC before (blue) and after (red) grafting porphyrins at different gate voltages (a: negative values; b: positive values, normalized I_c/I_c^{max}). All the curves' minimum is shifted to zero.

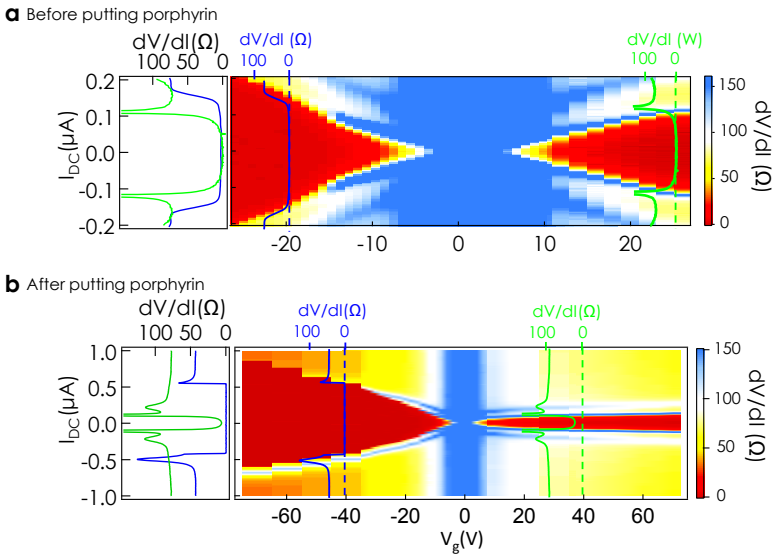

Figure 1.0.9: Change from bipolar to unipolar induced superconductivity upon deposition of Pt-porphyrin. Color-coded differential resistance as a function of dc current (y axis) and gate voltage (x axis), measured with a small ac current added to the dc current. The dark red regions correspond to that of zero differential resistance where a Josephson supercurrent runs through the S/graphene/S junction. Whereas the Josephson effect occurs symmetrically on both sides of the Dirac point on the pristine, uncoated sample (a, T=200 mK), it only occurs on the hole doped side (negative V_G) on the sample covered with porphyrins (b, T = 100 mK). The curves on and to the left of the color plots are the differential resistance curves as a function of dc current, measured at gate voltages symmetric with respect to the Dirac point.

(Fig.1.0.6). It is absent in the hole doped region. This spectacular effect of the critical current in long junction sample may be due to it's high sensitivity to magnetic field.

We explain these results by a long range RKKY interaction between the molecules, mediated by the charge carriers in graphene, leading to a collective magnetic order in porphyrins.

3. Superconducting proximity effect in Bi nanowires

At low temperature (100 mK) and zero field, we induced superconducting proximity effect in different Bi nanowire junctions by making tungsten contacts. The critical current is between 100nA and $1\mu A$ depending on the wire resistance and contact resistance.

Persistent supercurrent up to 11T

The tungsten wires have very high critical temperature $T_c \sim 4K$ and high critical field $H_c \sim 12T$. We find that the induced superconducting state in Bi nanowires persists up to 11T (Fig.1.0.10). That's is

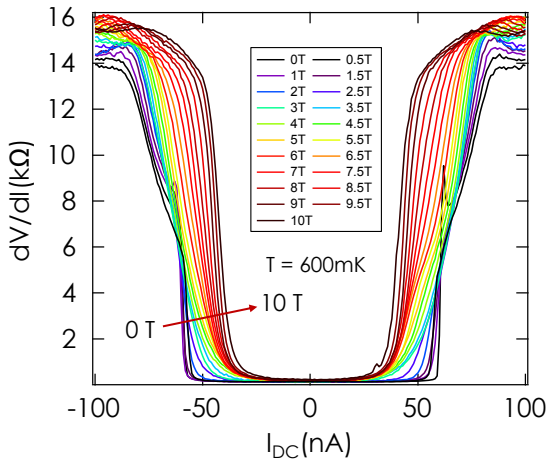

Figure 1.0.10: dV/dI curves at different field of Bi_3 The differential resistance as function of DC current curves are taken at different magnetic field from 0T to 11T at 600mK. The supercurrent is still very visible at 11T.

contrary to what is expected for the field dependence of the critical current in long nanowires which decreases on a scale of about a few hundred Gauss.

SQUID-like oscillations and large range modulation in critical current

The samples exhibit SQUID-like oscillations in critical current over a magnetic field range from 0 to 9T. In addition, the SQUID-like oscillations are modulated on a large field scale of the order of 1T (Fig.1.0.11). As predicted and measured, the strong SOC and confinement in Bi nanowires may result in the formation of particular edge states. We then attribute the SQUID-like oscillations to strong confined 1D edge states along certain facets of the nanowire, and the large scale modulation to the Zeeman effect.

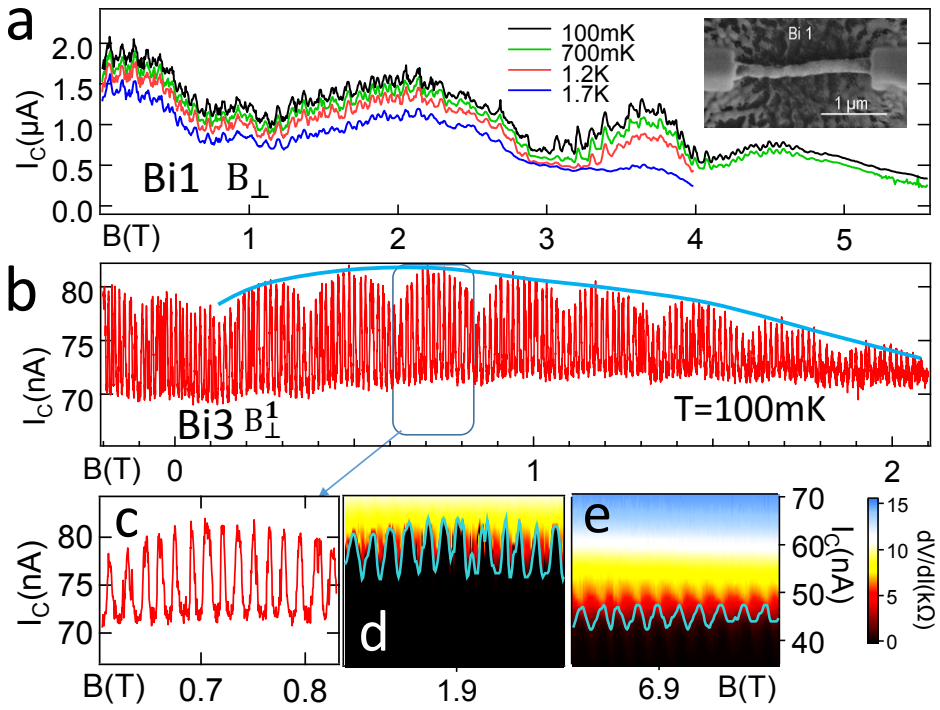

Figure 1.0.11: SQUID-like oscillations of Bi1 and Bi3(a) and (b) show direct I_C measurement as function of field for Bi1 and Bi3 with a period of about 800 Gauss(a) and 150 Gauss(b) respectively;(c) is the zoom figure of 2000 gauss rang of (b); (d) and (e) are scans of dV/dI curves at different range of magnetic field, show the persistent oscillations

2

Theoretical concepts

How does superconducting Proximity effect happen? Andreev bound states play the role of intermediate states between two superconducting electrodes linked by a normal metal or an insulator. How does it change when a magnetic field is applied?

2.1 Proximity effect

The proximity effect describes the phenomena that a occur when a superconductor (S) is placed in contact with a non-superconductor ("normal metal", N), and superconducting properties are induced in the N due to the propagation of correlated particles from the superconductor to the normal metal. This can lead to a zero resistance if the normal part is connected to two superconductors (SNS junction). This phenomenon was first described theoretically by Josephson, and is named the Josephson effect. This effect manifests itself in a non-dissipative dc current flowing through the Josephson junction at zero voltage. At weak coupling, e.g., in the S-I-S case where a thin insulator separates the two superconductors, the Josephson current can be expressed as $I_s = I_c \sin \delta$, where δ is the phase difference between the two superconducting condensates and the maximum supercurrent I_c is called the *critical current*.

We first describe the S-I-S junction, then show how the proximity effect is changed when a normal metal replaces the insulator as a coupling material. In particular, we discuss the Andreev bound states (ABS) that carry the supercurrent.

2.1.1 DC and AC Josephson effect[57]

The simplest way to understand the existence of a supercurrent is to include a coupling K between the two S wave function , each with their own phase θ_i. Suppose we have a SIS junction. We define Ψ_1 and Ψ_2 as the quantum mechanical wavefunction of the superconducting state in the left and the right superconductor, respectively. The dynamics of the two wavefunctions are then determinated by the following coupled Schrödinger equations:

$$\begin{aligned} i\hbar\frac{\partial\Psi_1}{\partial t} &= \mu_1\Psi_1 + K\Psi_2 \\ i\hbar\frac{\partial\Psi_2}{\partial t} &= \mu_2\Psi_2 + K\Psi_1 \end{aligned} \tag{2.1}$$

where K is a constant representing the coupling across the barrier and μ_1, μ_2 are the lowest energy states on either side.

In a simple way the wavefunctions can be written as

$$\begin{aligned} \Psi_1 &= \sqrt{n_1}e^{i\varphi_1} \\ \Psi_2 &= \sqrt{n_2}e^{i\varphi_2} \end{aligned} \tag{2.2}$$

where n_1, n_2 are the density of Cooper pairs and φ_1, φ_2 are the phases. Substituting equation (2.2)

in to (2.1) gives

$$\begin{aligned} \hbar\frac{\partial n_1}{\partial t} = -\hbar\frac{\partial n_2}{\partial t} = 2K\sqrt{n_1 n_2}\sin(\varphi_2 - \varphi_1) \\ -\hbar\frac{\partial}{\partial t}(\varphi_2 - \varphi_1) = \mu_2 - \mu_1 \end{aligned} \tag{2.3}$$

Let's check the transport properties in this structure. The time derivative of the density of the Cooper pairs describes a current and thus $I = \frac{\partial n_1}{\partial t}$. If a voltage V is applied between the junctions the energy levels will shift by $\mu_2 - \mu_1 = 2eV$. Then we get

$$I = I_0 \sin\varphi \qquad \text{DC} \tag{2.4}$$

$$\frac{\partial\varphi}{\partial t} = \frac{2eV}{\hbar} \qquad \text{AC} \tag{2.5}$$

By writing $I_0 = 2K\sqrt{n_1 n_2}/\hbar$ and $\varphi = \varphi_1 - \varphi_2$. Equations (2.4) and (2.5) represent the main results of the general theory of the Josephson junction. Eq. 2.4 shows that at zero bias, a non-dissipative (DC) supercurrent flows through junction modulated by the phase difference between two superconductor electrodes. Once one applies a voltage bias V at the two sides of the junction, the phase difference δ varies with a frequency $\frac{2eV}{h}$, induces a same frequency AC supercurrent in the junction. These are the so-called DC and AC Josephson effect. This strong non-linear current-voltage behavior is the origin for many different physical phenomena.

2.1.2 Andreev reflection

Because of the existence of an energy gap at the Fermi energy in the density of states of the superconductor, the transfer of single quasi-particle states with an energy ε below the gap Δ is forbidden for a direct transfer of charge. However, another type of transfer is possible when higher order processes are allowed. Andreev showed [58] that an incoming electron can be transferred into the superconductor if a second electron is also transferred through the interface thus forming a Cooper pair into the superconductor. In terms of single excitations, this process is equivalent to the reflection of a hole(Fig.2.1.3).

NS interface: retro-reflection

When an incident electron arrives at the NS interface, a hole will be reflected back with an opposite motion. This curious feature was noticed by Andreev. It was observed in particular by Benistant et al. [59] in an experiment with a pure silver single crystal. The Andreev reflection is a perfect retro-reflection only for electrons incident at the Fermi energy. When the energy is above the Fermi

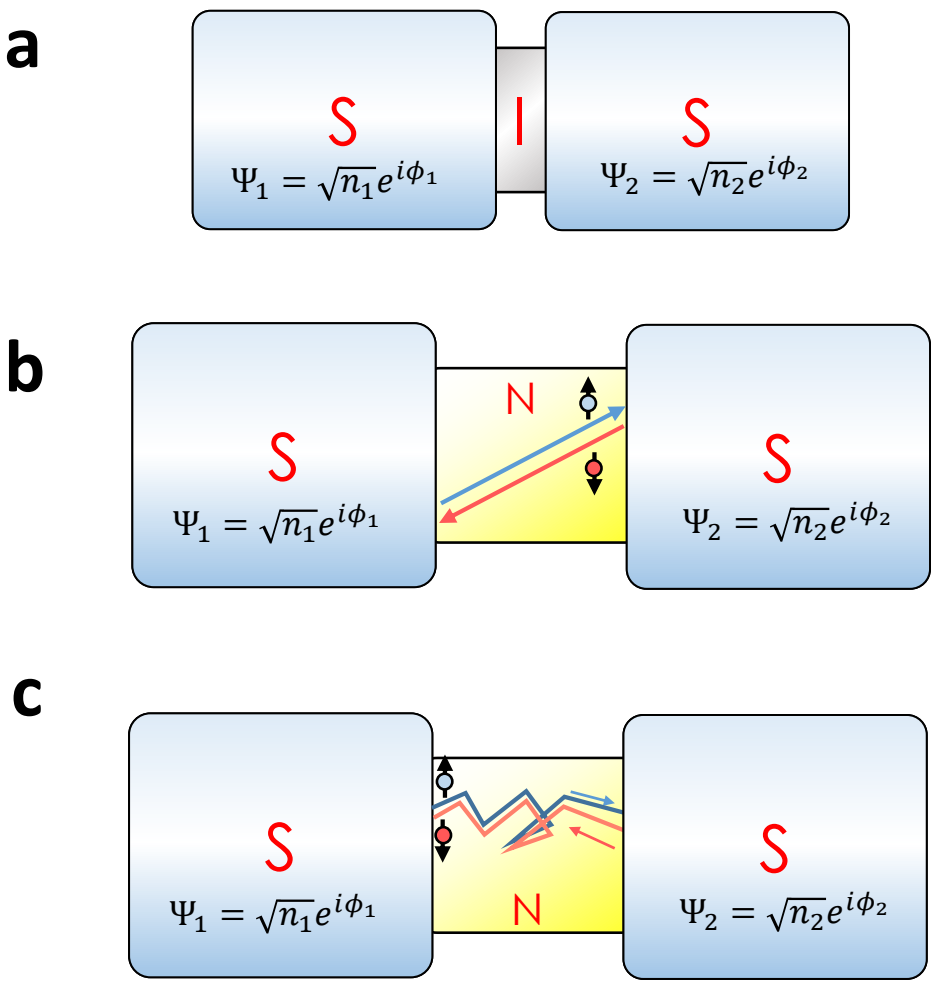

Figure 2.1.1: Josephson junctions. (a) Weak link Josephson junction (S-I-S), different phases in two electrodes. (b) Ballistic SNS junction. (c) Diffusive SNS junction. The coherent quasi-particles pair has same trajectories with time reversal symmetry.

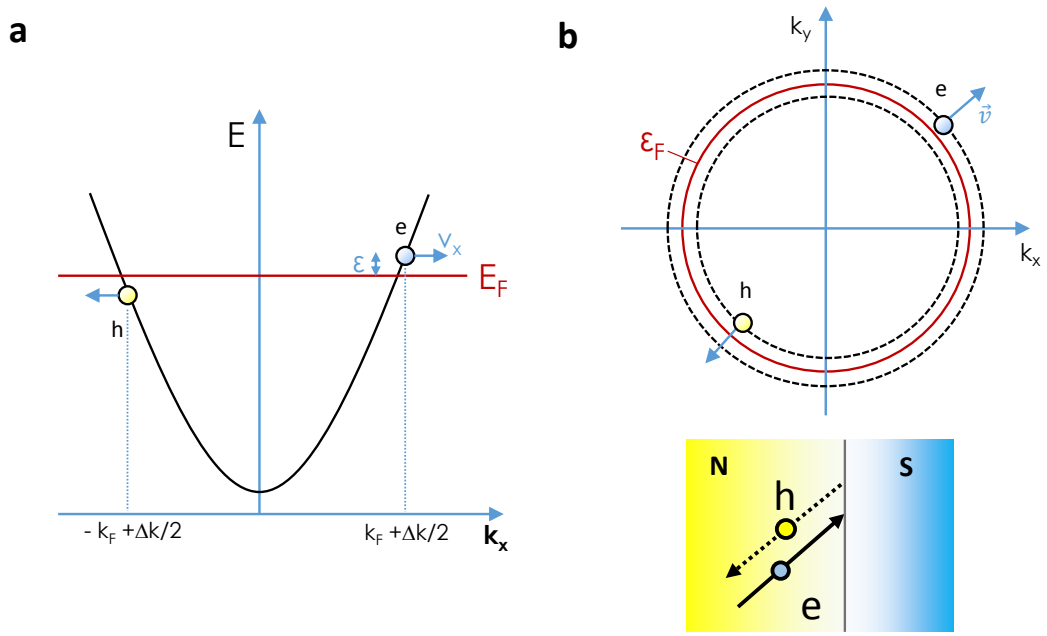

Figure 2.1.2: Retro-reflection at the N/S interface. An electron at $k_F + \delta k/2$with a excitation energy of ε above the Fermi energy ε_F will be reflected as a hole at $-k_F + \delta k/2$ with an energy of $\varepsilon_F - \varepsilon$. a) one dimensional case b) two dimensional case.

energy[60], the incident electron ($E_F + \varepsilon$,$k_F + \delta k/2$) and the reflected hole ($E_F - \varepsilon$, $-k_F + \delta k/2$) have different wavelengths in the normal metal. The wavevector mismatch is linear in energy : $\delta k = 2\varepsilon/\hbar v_F$(Fig. 2.1.2). The Cooper pair has energy $2E_F$, so that the energy is conserved. Incident and reflected quasiparticles have approximately equal wave vectors but opposite direction of motion (as follows from the opposite sign of the group velocity $\varepsilon/\hbar dk$ for the electrons and holes). Momentum is conserved up to the terms of order $\hbar\left|k^e - k^h\right| \lesssim \hbar/\xi_o$, with $\xi_o \equiv \hbar v_F/\pi\Delta_o$ the superconducting coherence length[61]. Once a hole is reflected, it can catch a phase at the interface: $\eta = \Phi + \arccos(\varepsilon/\Delta)$, where Φ is the phase of the superconductor.

This retro-reflection occurs in most cases, but as we will show further, another, so called specular, reflection can occur at S/graphene interface.

SNS JUNCTION - ANDREEV BOUND STATE (ABS)

In an SNS junction, the Andreev reflection occurs at the two NS interfaces. These reflections impose phase dependent boundary conditions on the eigenstates in the N region which are coherent superposition of electron and hole wave functions. In another word, standing waves will be formed in the normal part and lead to a quantization of excitation energy levels. We call these standing waves as "Andreev bound states (ABS)".

Let us consider the simplest case of a ballistic junction. As a first approximation, we assume in a

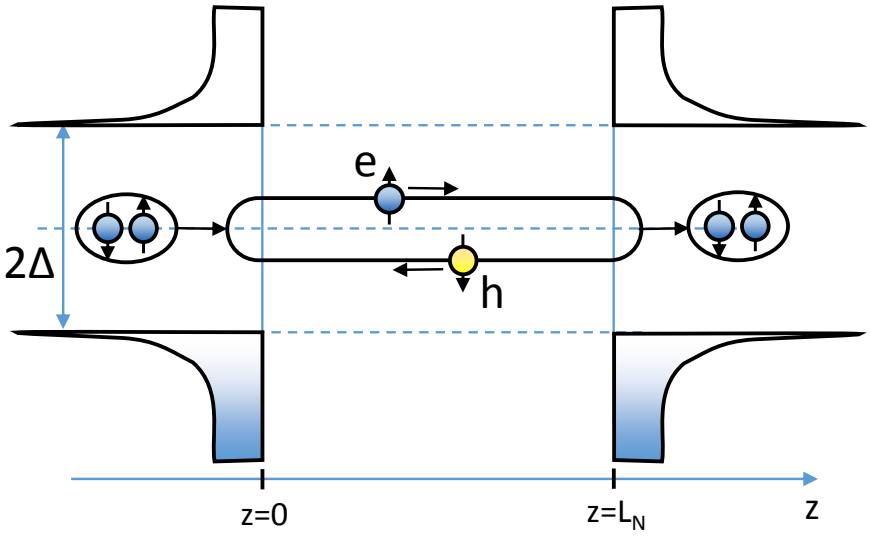

Figure 2.1.3: Andreev bound state. An Andreev pair formed with an electron and a hole is confined in between the energy of $\pm\Delta$. They require the constructive interference between the electron and the hole. Inspired from [63]

ballistic region of length L_N [61]:

$$\Delta(\boldsymbol{r}) = \begin{cases} \Delta_0 e^{i\varphi_1}, & \text{if} \quad z < 0 \\ 0, & \text{if} \quad 0 < z < L_N \\ \Delta_0 e^{i\varphi_2}, & \text{if} \quad z > L_N \end{cases} \tag{2.6}$$

The bound states for $\varepsilon < \Delta_0$ may be found by equating the phase shift acquired on a single round trip to an integer multiple of 2π. The resulting condition is [58, 62]

$$\frac{2\varepsilon L_N}{\hbar v_F \cos\theta} - 2\arccos\frac{\varepsilon}{\Delta_0} \pm \Delta\varphi = 2\pi m \qquad m = 1, 2, \ldots \tag{2.7}$$

where $\Delta\varphi \equiv \varphi_1 - \varphi_2 \in (-\pi, \pi)$ and θ is the angle with the normal to the N/S interface. The $\pm$ sign corresponds to the two directions of motion of the electron (or hole). For $\varepsilon \ll \Delta_0$ the spectrum depends linearly on $\delta\varphi$, according to $\varepsilon = [(2m+1)\pi \mp \Delta\varphi]\,\hbar v_F \cos\theta/(2L_N)$ (Fig.2.1.3). The first term is the phase cumulation during the propagation in the normal part, $2\Delta k \cdot L_N/\cos\theta$. The second term comes from the Andreev reflection at the interface.

Long junction limit: For $L_N \gg \xi_0$ the energy spectrum of the SNS junction depends sensi-

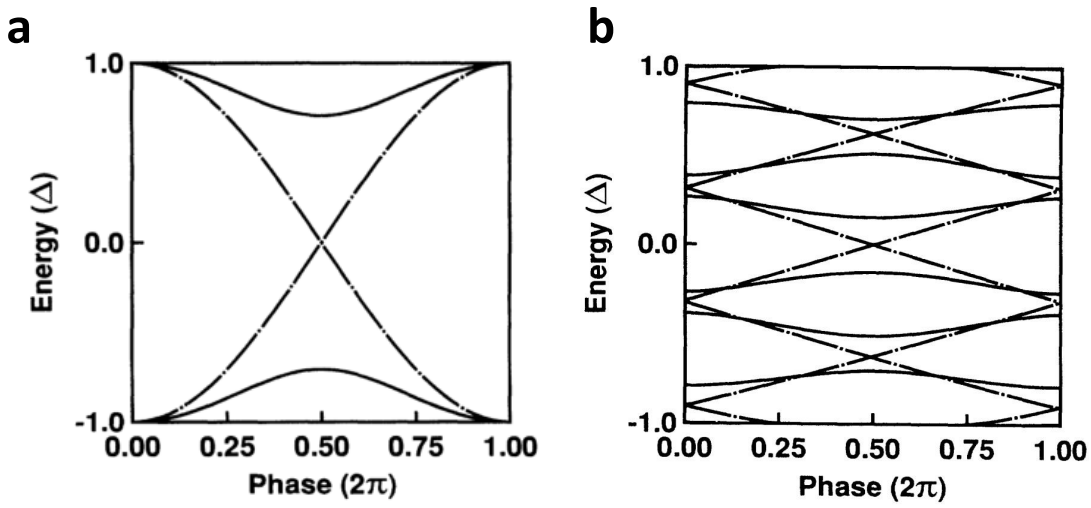

Figure 2.1.4: Spectrum of Andreev bound state. a) Short ballistic junction with (solid) and without (dotted) the presence of impurity (From Ref.[65]). b) Long ballistic junction. The discrete Andreev levels are shown with (solid) and without (dashed) the presence of an impurity. In both (a) and (b), an energy gap is opened in this quasi-particle spectrum. (From Ref.[65]).

tively on L_N. The Josephson current is a linear function of $\Delta\varphi$ with a critical current given by $I_c = aG\hbar v_F/eL_N$ where a is a numerical coefficient of order unity (dependent on the dimensionality of the system) and G is the normal state conductance of the SNS junction (Fig. 2.1.4b). The dependence of I_c on the junction geometry (through L_N) is characteristic of the case $L_N \gg \xi_o$, and persists if the SNS junction contains a constriction of the normal region.[64]

Short junction limit: In the opposite limit $L_N \ll \xi_o$, only a single bound state for each of the N transverse modes remains, at energy $\varepsilon = \Delta_o \cos(\Delta\varphi/2)$ independent of L_N (Fig. 2.1.4a). The supercurrent is given by the sum of the contribution of the energy levels. This result implies a zero-temperature Josephson current

$$\begin{aligned} I(\delta\varphi) &= \sum_n f_n i_n, \; i_n = -\frac{\partial \varepsilon_n}{\partial \varphi} \\ &= -N\frac{2e}{\hbar}\frac{d\varepsilon}{d\delta\varphi} \\ &= N\frac{e}{\hbar}\Delta_o \sin(\delta\varphi/2) \qquad -\pi < \delta\varphi < \pi \end{aligned} \tag{2.8}$$

and critical current

$$I_c = N\frac{e}{\hbar}\Delta_o \tag{2.9}$$

Both of which are independent of L_N.

Multiple Andreev Reflection (MAR)

If one applies a small voltage bias between the two superconducting electrodes, the junction is in the non-equilibrium state, and there is no more supercurrent. However, another consequence of the Andreev reflection can be observed. As shown in Fig. 2.1.5(c) and (d), multiple reflection of the quasi-particles can happen at all small bias voltage below the gap. Once the integer times of the bias energy neV is equal to the gap 2Δ, because of the high density of states near the gap, an enhanced conductance can be observed. This is so-called multiple Andreev reflection (MAR). With this effect we can determine the gap in our samples.

The consequences of Andreev reflection on the current voltage characteristics of a S-N junction were studied in detail in the so-called BTK theory[11]. The barrier strength was characterized by a simple parameter Z ranging from 0 for a perfect metallic contact to ∞ for a low transparency tunnel barrier. With this definition, the transparency reads $t = 1/(1 + Z^2)$. The Andreev process is significant when the transparency of the barrier is high. For a perfect contact (Z = 0) the sub-gap conductance was found to be twice the normal state conductance thus demonstrating the double charge transfer.

Diffusive SNS junction

Disorder changes strongly the ABS spectrum by lifting the degeneracies. The spectrum becomes quasi-continuous (see Fig. 2.1.6), with several striking features: a gap is induced in the spectrum which is modulated by the phase difference $\delta\varphi$. It closes at $\delta\varphi = \pi$. The amplitude of the induced gap depends on the junction length: in the short junction limit ($L \ll \xi_s$), it equals to the gap Δ; in the long junction limit ($L \gg \xi_s$), because another characteristic energy, so-called *Thouless energy* is involved to the system due to the disorders, there is an induced mini-gap ($3.5E_{Th} \ll \Delta$) inside the normal metal.

The transport properties in a diffusive metal can be described by a diffusion characteristic time $\tau_D = \dfrac{L^2}{D}$ in which electrons can travel through the metal and "feel" the edges (D is the diffusion constant of the metal). Then the characteristic energy, Thouless energy, is given by $E_{Th} = \dfrac{\hbar}{\tau_D} = \dfrac{\hbar D}{L^2}$. In different limits, the characteristic energies ($E_{Th}, \Delta, E_T = k_B T$) have different scales, and the properties of the a SNS junction are changed depending on these energies.

At sufficient low temperature, $E_T \ll E_{Th}, \Delta$, the thermal effect is very small. The superconducting coherence length in a diffusive junction is given by: $\xi_s = \sqrt{\dfrac{\hbar D}{\Delta}}$. By considering different energy scales, the SNS junction can be placed from short junction limit ($\Delta \ll E_{Th}$, $\xi_s \gg L$) to long junction limit ($\Delta \gg E_{Th}$, $\xi_s \ll L$). Ferrier et al. calculated the ABS spectrum (Fig. 2.1.6) of short and long junctions.

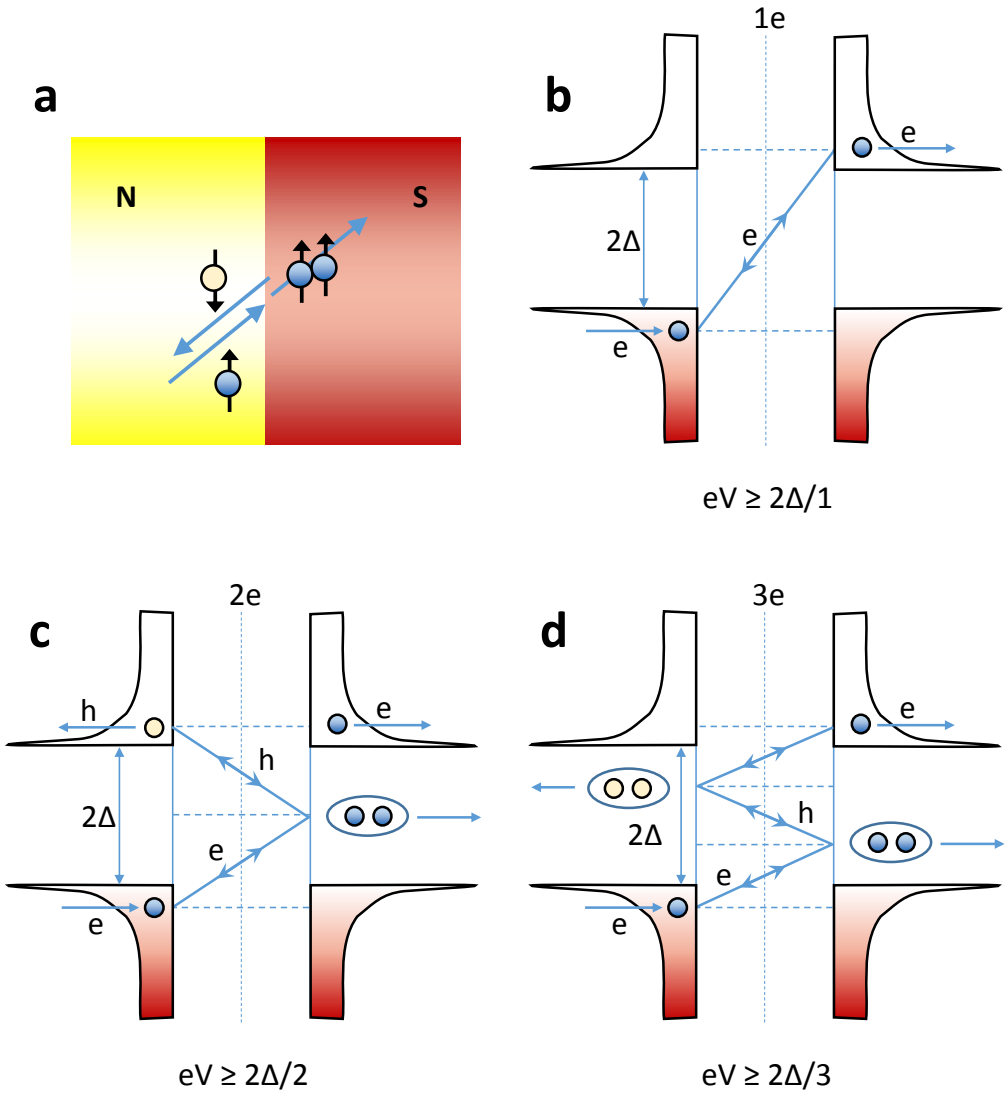

Figure 2.1.5: Andreev reflection, Multiple Andreev reflection(MAR) processes. (a) Retro-reflection process at the N-S interface. (b) charge transfer in the normal state. When the bias energy eV is higher the gap 2Δ, the transport is supported totally by the quasi-particles, thus there is no more superconducting state (supercurrent, zero resistance) inside the normal part. (c) and (d) multiple Andreev reflection with 2 and 3 times reflections in below the gap. Inspirited from Ref. [66]

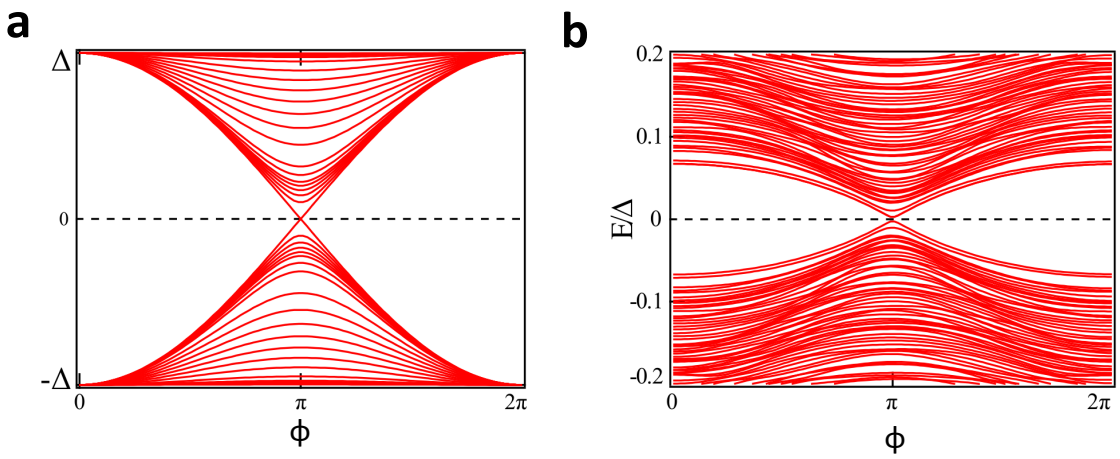

Figure 2.1.6: Numerical simulation of the Andreev bound states spectrum for diffusive SNS junction. The spectrum becomes continuum. a) In short junction limit. b) In long junction limit, Andreev bound states leads to the emergence of a phase-dependent minigap which is much smaller that the superconducting gap Δ. From Ref. [67]

To estimate the strength of the superconducting coherence in the SNS junction, we compare the product eR_NI_c and the characteristic energies. Fig.2.1.7 present the global feature of the relation between them from short junction limit to long junction limit.[68] In the long-junction limit, at zero temperature the product $eR_NI_c$is predicted to be proportional to E_{Th}:

$$eR_NI_c(T=0) = 10.82E_{Th} \tag{2.10}$$

In the short junction limit, the product is fixed to the gap with a constant factor:

$$eR_NI_c \approx 1.326\pi\Delta/2. \tag{2.11}$$

From the numerical results in Fig. 2.1.7, it confirms that it is the minimum of the gap Δ and the Thouless energy E_{Th} that limits the critical current in diffusive S-N-S junctions. At $E_{Th} \sim \Delta$, the critical current value remains close to the short-junction case. For usual normal metal SNS junction, one sample shows one point in this relation. However, in S/graphene/S junction, this relation can be tested in a finite range in one sample just by changing the gate voltage thanks to the tuneability of the Fermi level in graphene.

In real experiment, the critical current is often smaller than the prediction in ideal situation. The reasons are various: finite temperature can always suppress exponentially the critical current; inelastic disorders in the junction like magnetic impurity can decrease the coherence length l_φ inside the N, upon which the electrons can keep their correlation during the propagation[69]; particularly in

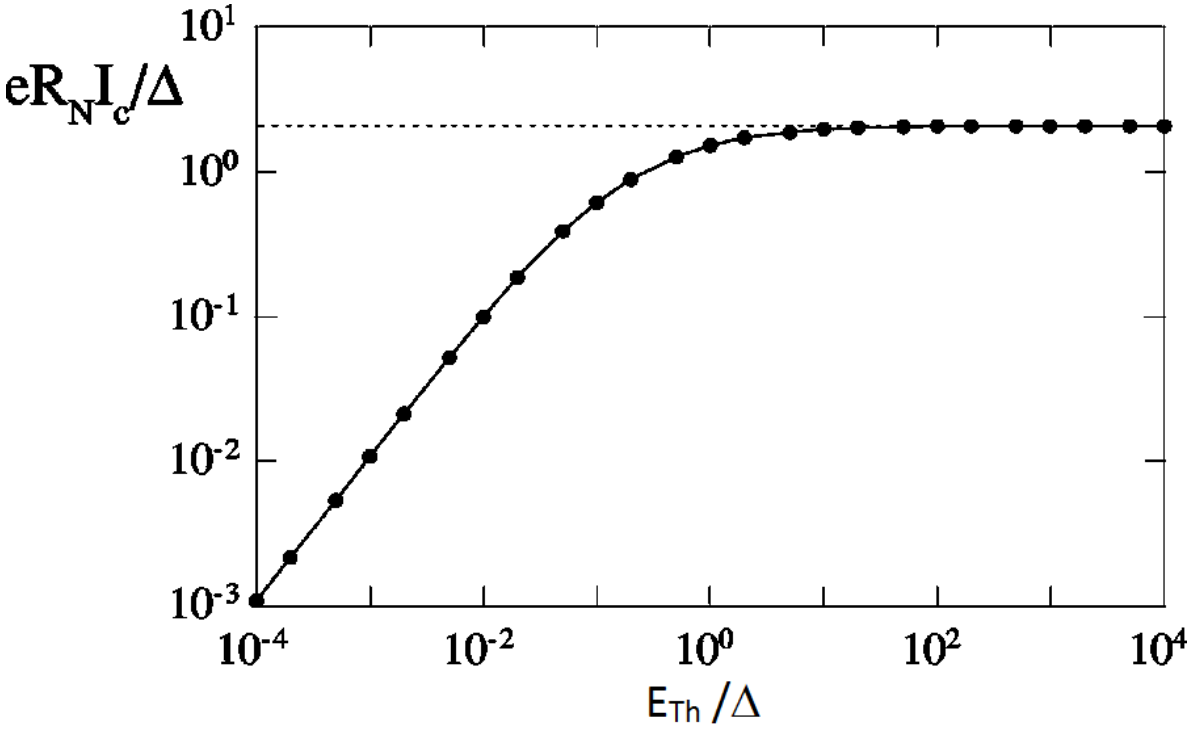

Figure 2.1.7: Calculated dependence of the zero-temperature $eR_N I_c$ product in units of D as a function of the ratio E_{Th}/Δ. I_c is the Josephson critical current, R_N the normal-state resistance, E_{Th} is the Thouless energy, and D is the superconducting gap of S. The long-junction regime is on the left part of the graph where $E_{Th} < \Delta$, the short-junction regime is on the right part where $E_{Th} > \Delta$. The dashed line corresponds to the limit of the $eR_N I_c$ product of short junction at $T = 0$. From Ref. [68].

graphene, near Dirac neutral point, the specular Andreev reflection can lead to strong suppression of critical current[8]; etc...

2.1.3 Effect of magnetic field in proximity effect

The magnetic field changes the Andreev pairs' phase in two ways, via both orbital and spin dephasing effect.

Just consider the interaction between the magnetic field and the spin, the Zeeman energy can be given as $E_z = g\mu_B \boldsymbol{H}\boldsymbol{\sigma}$, where μ_B is the Bohr magneton, σ is the spin and g is the Landé g-factor. The dephasing due to Zeeman effect is given by E_Z/τ. The Zeeman dephasing is usually small comparing to orbital effect, but in some special material with high g factor (like Bismuth), the Zeeman energy dephasing is comparable to orbital dephasing. The dephasing due to Zeeman energy can modulate the critical current, which is similar to the I_c oscillation in SFS junction.[70, 71, 72]

By controlling the magnetic field and different dephasing effect, the Josephson effect in magnetic field can be a beautiful tool to exhibit interference effects, manifestations of the phase coherence of the superconducting states in proximity effect. For example a single Josephson junction with a finite width exhibits an interference pattern reminiscent of the diffraction (Fraunhofer) pattern of a slit.[73]

A supercurrent flowing through a junction between two superconductors is given by the gauge invariant Josephson relation

$$I(\delta) = I_o \sin\left(\delta - \frac{2e}{\hbar}\int \boldsymbol{A}\cdot d\boldsymbol{l}\right) \tag{2.12}$$

where δ is the phase difference between the two superconductors by taking into count the effect of normal part (discussed in Sec.2.1.2 and Sec.2.1.2). More generally, the Josephson current resulting from all current paths has the form

$$I(\delta) = I_o \left\langle \sin\left(\delta(\mathcal{C}) - \frac{2e}{\hbar}\int_{\mathcal{C}} \boldsymbol{A}\cdot d\boldsymbol{l}\right)\right\rangle_{\mathcal{C}} \tag{2.13}$$

where $< \cdots >_{\mathcal{C}}$ denotes the average over all current paths through the junction. As choosing the same circulation above, the phase difference does not depend on x and is donated δ_o. Then the current can be rewritten as

$$I(\delta) = I_o \left\langle \sin\left(\delta_o - \frac{2e}{\hbar}\int_{\mathcal{C}} \boldsymbol{A}\cdot d\boldsymbol{l}\right)\right\rangle_{\mathcal{C}} \tag{2.14}$$

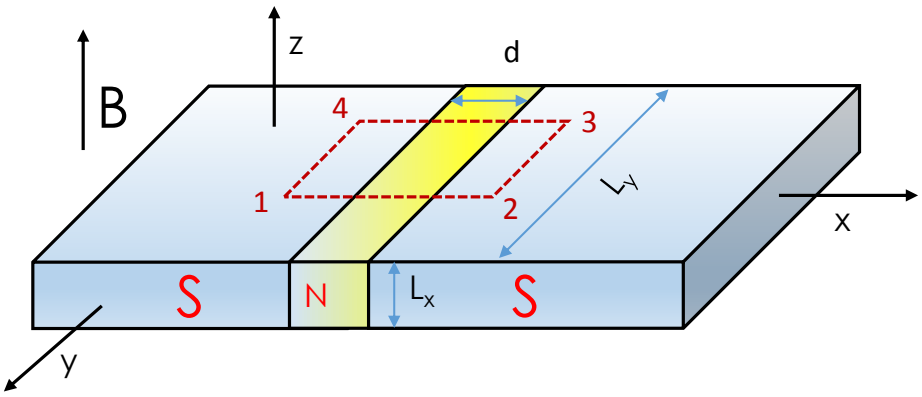

Figure 2.1.8: Schema of a Josephson junction in a perpendicular field.

assume the phase difference to be zero so that one can write the critical current $I_c = max[I(\delta)]$ as

$$I_c = I_o \left| \left\langle e^{-i\frac{2\pi}{\varphi_o}\int_C \mathbf{A}d\mathbf{l}} \right\rangle \right| \tag{2.15}$$

or, in a gauge independent form:

$$I_c = I_o \left| \left\langle e^{-i\frac{2\pi\varphi(C)}{\varphi_o}} \right\rangle \right| \tag{2.16}$$

Up till now, we assume a constant phase in the S, but it is not true if a magnetic field is present. Let's start with a simple case as a ballistic SNS short junction in a uniform perpendicular field. The magnetic field is along the axis $\hat{z}$ as $B(x)\hat{z}$ in the plan of the junction (see in Fig. 2.1.8). The potential vector in the Landau gauge is

$$\boldsymbol{A} = -B(x)y\hat{x} \tag{2.17}$$

In the junction, $B(x)$ varies slightly, we assume it makes no difference along x axis, and at every side B decreases as $\exp(x/\lambda)$. If we integrate $\int \boldsymbol{A}\cdot\boldsymbol{l}$ around a tour (red) $1 \to 4 \to 1$ as drown in Fig. 2.1.8. As we assumed before, the terms of $\int_2^3$ and $\int_4^1$ count for zero. And one can chose the gauge

to get term $\int_3^4$ to be zero. Then the phase difference that induced by the magnetic field is

$$\int_2^1 A_x dx = B_0 yl, \tag{2.18}$$

where $l = 2\lambda(T) + d$, $\lambda(T)$ is the London penetration length. The current has to be summed on the current paths

$$I_c = I_0 \left\langle e^{-\frac{2i\pi}{\varphi_0} Byl} \right\rangle = \frac{I_0}{w} \int_{-w/2}^{w/2} e^{-\frac{2i\pi}{\varphi_0} Byl} dy \tag{2.19}$$

leading to a total critical current:

$$I_c = I_0 \left| \frac{\sin \pi\varphi/\varphi_0}{\pi\varphi/\varphi_0} \right| \tag{2.20}$$

where $\varphi = BwL$. No matter how different the phase is, the current becomes zero each time the flux in the junction is an integer number of quantum flux. This form is known as Fraunhofer diffraction pattern by analogy with the spectrum of light passing through a narrow rectangular slit.

We can generalize this Fraunhofer pattern interference in ballistic junction: at a fixed magnetic field, the total critical current through the Josephson junction is a phase sensitive summation of supercurrent over the width of the junction. Along the y axis, the current obtains its own phase. This looks like optical trajectories induced phase cumulation in optical Fraunhofer pattern. Suppose we have a supercurrent density profile $J_S(x)$. Then its complex Fourier transform yields a complex critical current function $I_c(\beta)$[74]

$$J_c(\beta) = \int_{\infty}^{-\infty} dx J_S(y) e^{i\beta y} \tag{2.21}$$

where the normalized magnetic field unit $\beta = 2\pi(L + \lambda)B/\Phi_0$, $\lambda(T)$ is the London penetration length and the magnetic flux quantum $\Phi_0 = h/2e$. In the case above, it just takes a homogeneous current density distribution $J_s(y) = cst$.

A two channel edge states can cause strong interference pattern in large range magnetic field. See in Appendix for different cases calculation[75].

The critical current decays with the magnetic field despite the interference oscillations. The physic behind this decay can be described as a phase accumulation. The dephasing accumulated along diffusive trajectories is characterized by the average $\langle e^{-i\varphi_t} \rangle_{\mathcal{C}}$ along all diffusive paths $\mathcal{C}$ in the junction[73]. Since diffusion is a Gaussian process, the average over trajectories of a given length (a given diffusion time t) is

$$\left\langle e^{-i\varphi_t} \right\rangle_{\mathcal{C}} = e^{-\frac{1}{2}\left\langle \varphi_t^2 \right\rangle_{\mathcal{C}}} \tag{2.22}$$

where the average is given by $\langle \varphi_t^2 \rangle_C = \frac{4\pi}{\Phi_o^2}\overline{A^2}\langle x_t^2 \rangle_C$ for quasi-1D diffusive junction (A is an average taken from transverse direction $\overline{A^2} \propto B^2$). Immediately we can write $\langle e^{-i\varphi_t} \rangle_C = e^{t/\tau_B}$ as the phase factor averaged along all trajectories of time t, where $\frac{1}{\tau_B} = \frac{\pi^2 D\omega^2 B^2}{3\Phi_o^2}$. If we estimate the average travel time in a diffusive system is τ_D, we get

$$e^{t/\tau_B} \sim e^{a\Phi/\Phi_o} \tag{2.23}$$

where a is a prefactor related to the junction geometry, Φ is the flux included in normal metal part. In general, the critical current in a SNS junction decays in magnetic field when the flux included is the order of Φ_o.

The geometry effect in the field dependence

In general both the phase varies on the S electrodes (y direction) and along the N metal (x direction). They could both contribute and kill interference. Much more complicated than what we showed above, the total critical current can be affected by the current density distribution as well as the geometry of the junction. The geometry-related magnetic interference patterns were observed experimentally[76, 77] and discussed theoretically[78, 73].

We can show first two extreme limits:

Narrow-junction limit In the limit in which the width W is comparable or smaller than the magnetic length $\xi_H = \sqrt{\Phi_o/H}$ (in some cases, simply $L \gg W$). In both Ref. [78] and [73], they showed a monotonic Gaussian-like decay in field dependence of critical current($I_c(B)$). In Ref. [73], the exact expression was given:

$$I_c = I_c(0)\frac{\frac{\pi}{\sqrt{3}}\frac{\Phi}{\Phi_o}}{\sinh\left(\frac{\pi}{\sqrt{3}}\frac{\Phi}{\Phi_o}\right)} \tag{2.24}$$

Wide-junction limit For a sufficiently wide junction ($W \gg \xi_H, L$) one can re-find the magnetic field dependence of the supercurrent as follow

$$I(H,\varphi) = I_c(H=0)\int_{-1/2}^{1/2} d\tilde{y}\sin(\varphi - 2s\tilde{y})$$

where φ is the non-gauge invariant superconducting phase difference and $I_c(H=0)$ is the critical current at zero field. As a consequence, the critical current in the wide junction limit exhibits, as

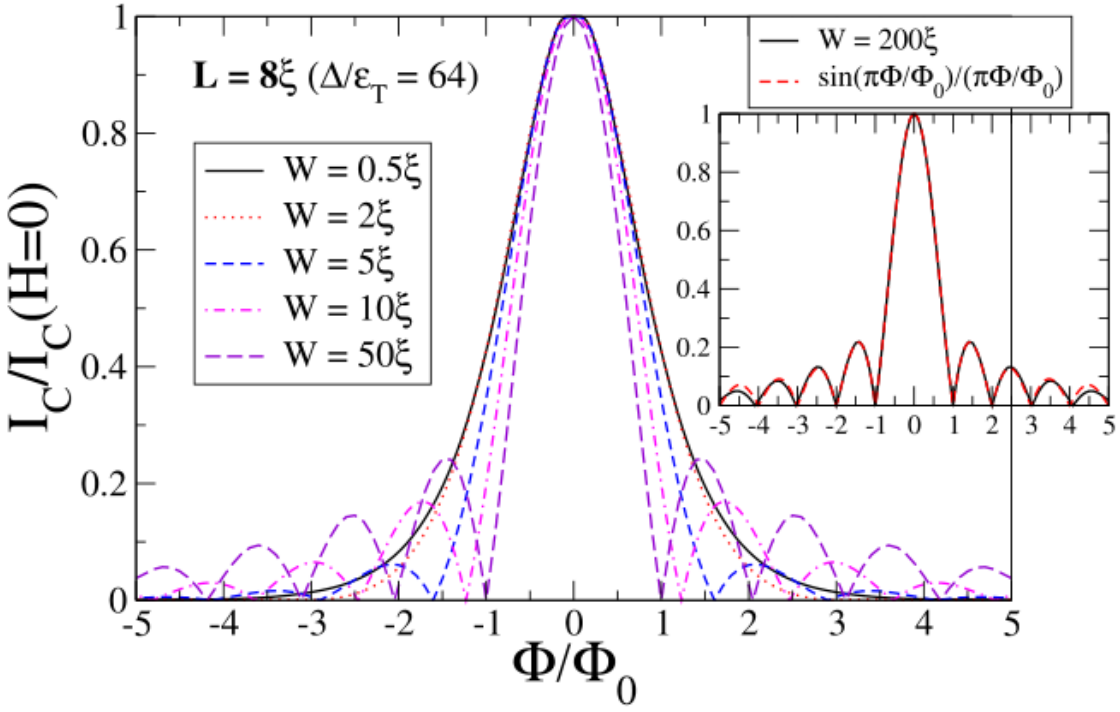

Figure 2.1.9: Critical current vs. magnetic flux in the weak proximity limit for a wire length $L = 8\xi$ and a temperature $k_B T = 0.01\Delta$. The different curves correspond to different values of the width of the wire, W. The inset shows a comparison between the critical current for a width $W = 200\xi$ and the Fraunhofer function (From Ref. [78])

expected, the well-known Fraunhofer pattern which is described by the expression

$$\frac{I_c(H)}{I_c(H=0)} = \frac{|\sin(\pi\Phi/\Phi_0)|}{\pi\Phi/\Phi_0} \tag{2.25}$$

Fig. 2.1.9 shows the field dependence of different aspects ratio junctions. The interference pattern is tunned from a Gaussian-like decay for narrow junction to a Fraunhofer pattern interference for wide junction. The transition seems to happen when the width of the normal part of the junction is comparable to the magnetic length ξ_H. This behavior is intimately attributed to the appearance of a linear array of vortices in the middle of the normal wire, the properties of which are very similar to those in the mixed state of a type II superconductor.

2.2 Graphene

Since the first graphene was isolated by Novoselov & Geim's group in 2005[79], the graphene is extensively studied . In this natural 2D material, which has a special band structure, electrostatic gating can tune the density of carriers and change the sign of their charge when the electron-hole symmetry point (Dirac point) is crossed. It can be described only by relativistic quantum physics. The electron transport is essentially governed by the Dirac's (relativistic) equation and the electrons in the graphene can be considered as massless 2D Dirac Fermions. Some special properties are revealed in transport measurement of the half-quantum Hall effect[3, 4, 5, 6], Klein tunneling[80, 81, 82, 83] etc.

2.2.1 Band structure[ref. cours M2]

The original properties of graphene are due to its special lattice structure. Graphene is made out of carbon atoms arranged in hexagonal structure, as shown in Fig. 2.2.1. hybridisation. The honeycomb lattice is not a Bravais lattice because two neighboring sites are not equivalent. The structure can be seen as a triangular lattice with a basis of two atoms per unit cell. The lattice vectors can be written as:

$$a_1 = \frac{a}{2}(\sqrt{3}, 3), a_2 = a(\sqrt{3}, 0) \tag{2.26}$$

where $a = 1.42\mathring{A}$ is the carbon-carbon distance. The reciprocal-lattice vectors are given by:

$$a_1^* = \frac{2\pi}{a}\frac{2}{3}(0, 1), a_2^* = \frac{2\pi}{a}\frac{2}{3}\left(\frac{\sqrt{3}}{2}, -\frac{1}{2}\right) \tag{2.27}$$

which forms also a honeycomb structure in reciprocal space. What is particularly important is that there are two points K and K' at the corners of the graphene Brillouin zone BZ. These are named Dirac points. Their positions in momentum space are given by

$$K = \left(\frac{2\pi}{3\sqrt{3}a}, \frac{2\pi}{3a}\right), K' = \left(-\frac{2\pi}{3\sqrt{3}a}, -\frac{2\pi}{3a}\right) = K \tag{2.28}$$

The three nearest-neighbor vectors in real space are given by

$$\delta_1 = \frac{a}{2}\left(\sqrt{3}, 1\right), \delta_2 = \frac{a}{2}\left(-\sqrt{3}, 1\right), \delta_3 = -a(0, 1) \tag{2.29}$$

If $V(rR)$ is the potential of an arbitrary atomic site, we can write the Hamiltonian of an electron in the graphene as :

$$\mathcal{H} = \frac{p^2}{2m} + V(r - R) + V(r - R - \delta) \tag{2.30}$$

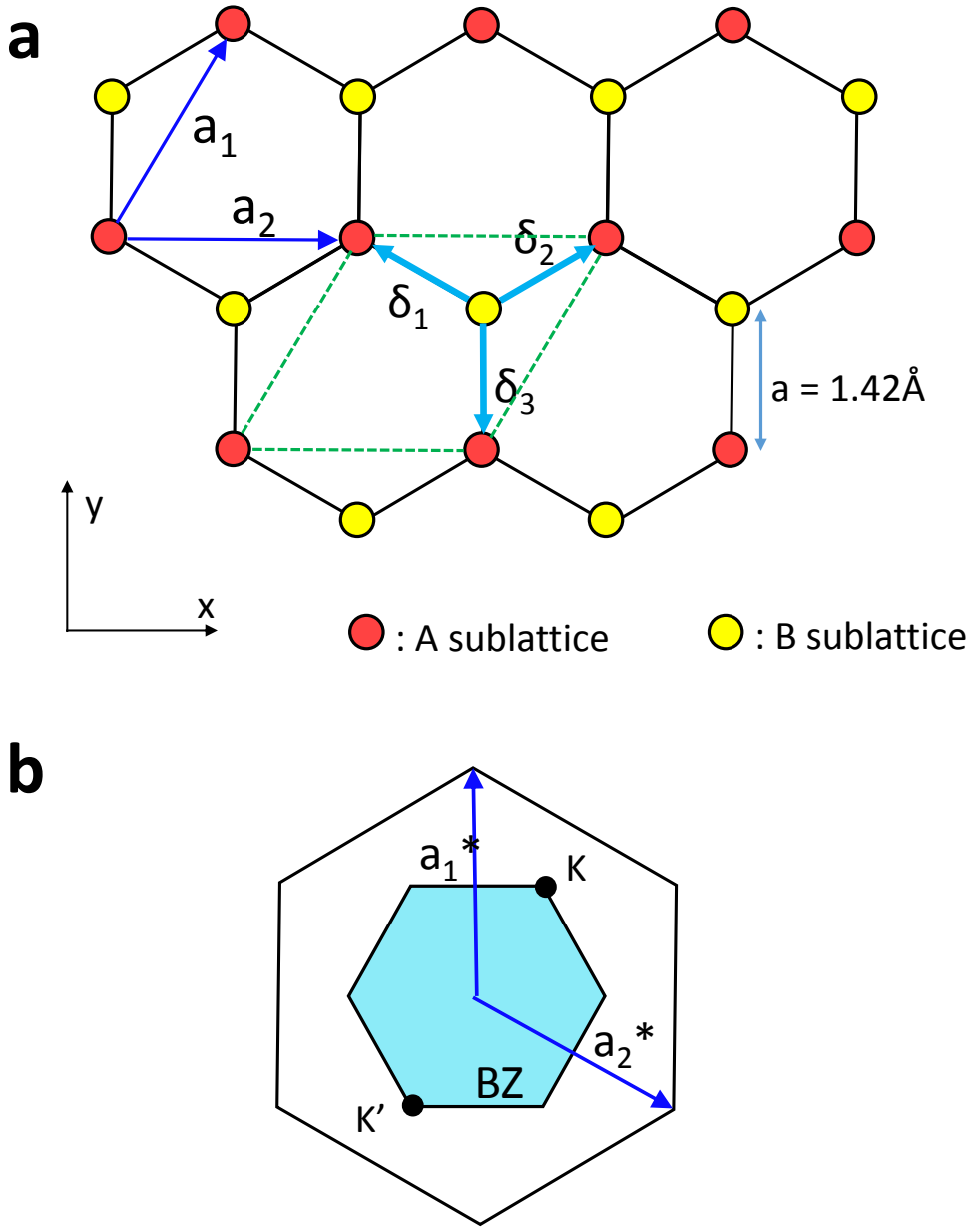

Figure 2.2.1: Honeycomb lattice and its Brillouin zone. **a**: lattice structure of graphene, made out of two inter-penetrating triangular lattices (a_1 and a_2 are the lattice unit vectors, and , δ_i= 1,2,3 are the nearest-neighbor vectors). The cell is indicated by green dashed line. **b**: corresponding Brillouin zone. The Dirac cones are located at the K and K' points.

δ can be any one of the nearest-neighbor vectors. For the following calculation, we choose $\delta = \delta_2$. $V(rR) + V(rR\delta)$ presents the potential of the two sublattices in graphene.

These are two atoms in a cell of graphene, each of them can be presented as a wavefunction $\left|\phi_k^{A/B}(\boldsymbol{R})\right\rangle$. According to the Bloch's theorem, the wavefunction of graphene can be written as a linear combination of the two wavefunctions :

$$|\Psi_k >= \frac{1}{\sqrt{N}} \sum_R e^{i\boldsymbol{k}\cdot\boldsymbol{R}} \left(a_k \left|\varphi_k^A(\boldsymbol{R})\right\rangle + b_k \left|\varphi_k^B(\boldsymbol{R})\right\rangle\right) \tag{2.31}$$

and we multiply a $\langle\Psi_k|$ |at left with the Schrödinger equation $\mathcal{H}|\Psi_k >= E|\Psi_k >$, we can get:

$$E_k \langle\Psi_k|\Psi_k\rangle = \langle\Psi_k| \mathcal{H} |\Psi_k\rangle \tag{2.32}$$

After diagonalizing the equation, one can get

$$E_k(a_k^* a_k + b_k^* b_k) = t_{aa} a_k^* a_k + t_{ab} a_k^* b_k + t - bab_k^* a_k + t_{bb} b_k^* b_k \tag{2.33}$$

t_{ij} is the factor for the diagonalization. Then we calculate respectively the partial derivations of $\frac{\partial}{\partial a_k}$ and $\frac{\partial}{\partial b_k}$ the equation:

$$\begin{aligned} E_k a_k^* &= t_{aa} a_k^* + t_{ba} b_k^* \\ E_k b_k^* &= t_{ab} a_k^* + t_{bb} b_k^* \end{aligned} \tag{2.34}$$

we present it in a matrix:

$$\begin{vmatrix} t_{aa} - E_k & t_{ba} \\ t_{ab} & t_{bb} - E_k \end{vmatrix} = 0 \tag{2.35}$$

The solution to it is

$$E_k = \frac{t_{aa} + t_{bb} \pm \sqrt{(t_{aa} + t_{bb})^2 + 4t_{ab}t_{ba}}}{2} \tag{2.36}$$

Considering that $t_{ab} = t_{ba}^*$ and $t_{aa} = t_{bb}$, $E_k = \frac{2t_{aa} \pm \sqrt{4t_{ab}t_{ab}^*}}{2} = t_{aa} \pm |t_{ab}|$. We rewrite the Hamiltonian as

$$\mathcal{H} = \mathcal{H}_0 + \Delta\mathcal{H} \tag{2.37}$$

Then by applying tight-band approximation and defining

$$\begin{aligned} t_0 &= \left\langle \phi_k^{A/B}(R) \right| \Delta\mathcal{H} \left|\varphi_k^{A/B}(R)\right\rangle && \text{on the same atom} \\ t &= N^{-1} \left\langle \phi_k^B(R') \right| \Delta\mathcal{H} \left|\varphi_k^A(R)\right\rangle && \text{Jump to a nearest-neighbor} \end{aligned} \tag{2.38}$$

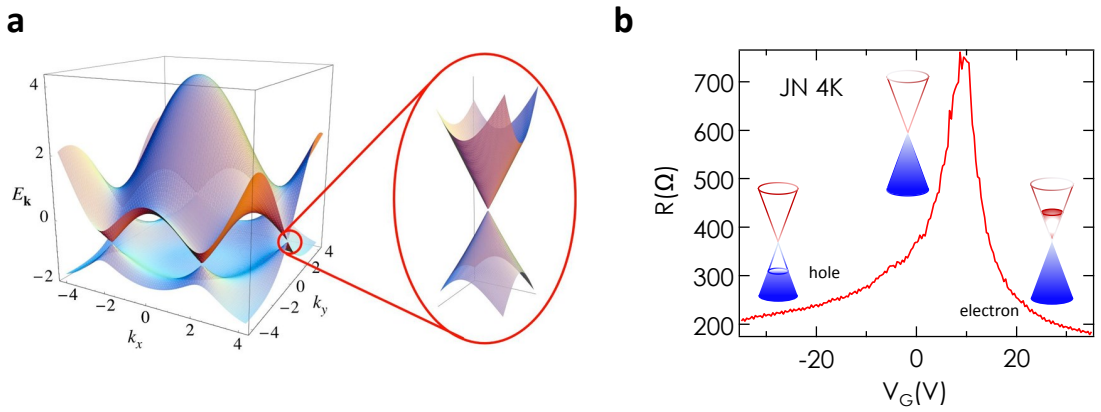

Figure 2.2.2: Electronic dispersion in the honeycomb lattice. a) Left: energy spectrum in units of t for finite values of t, with t = 2.7eV . Right: zoom in of the energy bands close to one of the Dirac points; b) Sample JN gate dependence of resistance. Different region for different doping in charge carriers. The Dirac point is at +10V.

only if the R and R' are nearest-neighbors. Then we can get

$$\begin{aligned} t_{aa} &= N^{-1}\sum_{RR'}\exp(i\boldsymbol{k}(\boldsymbol{R}-\boldsymbol{R'}))\left[E_o\delta_{R'R}+t_o\delta_{R'R}\right] \\ &= E_o + t_o \end{aligned} \tag{2.39}$$

in the same way, we get $t_{ab} = \sum_{RR'}\exp(i\boldsymbol{k}(\boldsymbol{R}-\boldsymbol{R'}))t$, if $R'(A)$ and R(B) are nearest-neighbors.

$$t_{ab} = t\left[1+e^{-i\boldsymbol{k}\cdot\boldsymbol{a_1}}+e^{-i\boldsymbol{k}(\boldsymbol{a_2}-\boldsymbol{a_1})}\right] \tag{2.40}$$

The energy eigenvalue is $E_k^{\pm} = E_o + t_o + |t_{ab}|$. We give the dispersion relation in Fig. 2.2.2.a We can find that there are 6 points at which the conduction band touches the valence band. If we develop the dispersion relation around any of the 6 points, we can find that

$$E_k^{\pm} = \frac{3}{2}ta\sqrt{(\Delta x)^2+(\Delta y)^2} = \pm\frac{3}{2}taq = \hbar v_F q \tag{2.41}$$

according to the experimental measurement,$t \approx 2.7eV$, Fermi velocity $v_F = \frac{3}{2}\hbar ta \approx 1\times 10^6 m/s$.

Due to this special band structure, one can tune the charge density by applying a gate voltage, which actually changes the Fermi energy E_F.

2.2.2 Specular Andreev reflection in graphene[7]

The electron and the hole should be taken at opposite corners of ±K of the Brillouin zone of graphene, in order to have a zero total momentum. Andreev reflection in graphene therefore switches the valleys.

If $\varepsilon < E_F$, both electron and hole are in the conduction band, so that there is an **intraband** reflection. For the $\varepsilon > E_F$, the reflected hole has to be in the valence band, leading to an **interband** reflection. Particularly in an undoped graphene(Fig. 2.2.3a), $E_F = 0$, Andreev reflection is interband at all energies scale of ε. In usual metals the interband Andreev reflection does not exist, because the Fermi level is far from the valence and conduction transition energy.

The intraband reflection in graphene is similar to the retro-reflection that we discussed in Sec.**??**. Let us discuss the interband reflection case. The linear dispersion relation in graphene may be written in terms of the excitation energy $\varepsilon = |E - E_F|$,

$$\varepsilon = \left| E_F \pm \hbar v (\delta k_x^2 + \delta k_y^2)^{1/2} \right| \tag{2.42}$$

The $\pm$ sign distinguishes excitations in the conduction and in the valence band. The electron comes from the positive x (Fig. 2.2.3b).

The reflection imposed conditions:

$$\begin{aligned} &\delta k_y^e + \delta k_y^h = 0, \varepsilon^e + \varepsilon^h = 0 \\ &v_x^e = -v_x^h \end{aligned} \tag{2.43}$$

The derivative $\hbar^{-1}\dfrac{d\varepsilon}{d\delta k_x}$ is the value v_x of the velocity in the x-direction, and keeping in mind that the slope has opposite sign when the hole is reflected in a valence band. Considering all the conditions, there is an only solution for the reflected hole which is shown in Fig.2.2.3b).

So we can say that, in graphene, the intraband Andreev reflection leads to retro-reflection, while interband Andreev reflection leads to specular reflection.

2.2.3 QHE in graphene

In two dimensions, when electrons are subjected to a magnetic field they follow circular cyclotron orbits. If the magnetic field is strong enough and the mobility of the electrons is high, the electrons can complete a circle. Due the quantum periodic condition, the circular cyclotron orbits have to be quantized, thus the energy of the orbits is also quantized as[84]:

$$E_n = \hbar\omega_c(n + 1/2) \tag{2.44}$$

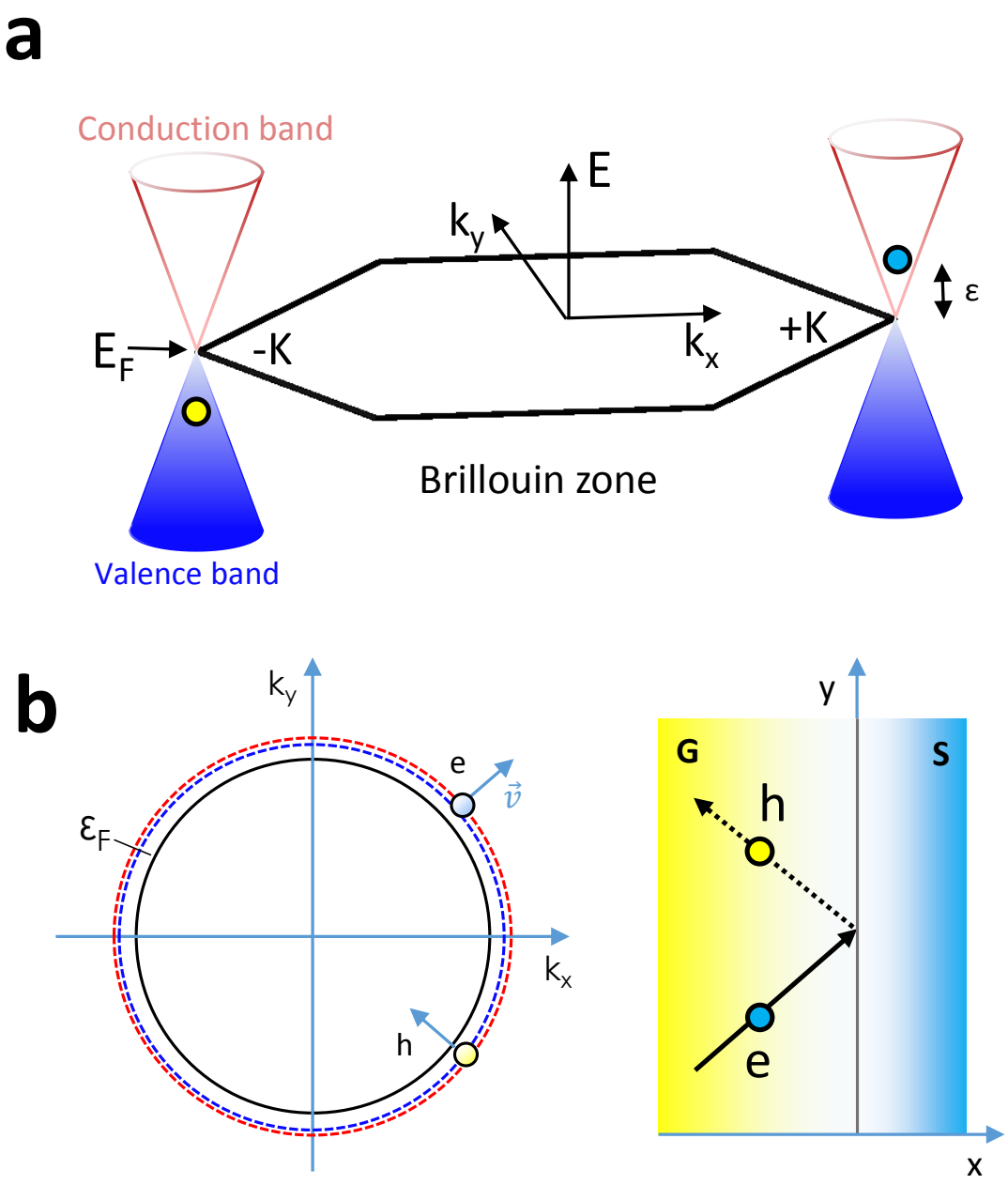

Figure 2.2.3: Interband reflection. a) Interband reflection in case of undoped graphene. Electron and hole excitations in the conical band structure of graphene filled and empty circles at energies $E_F \pm \varepsilon$), converted into each other by Andreev reflection at a superconductor. In this case, $E_F = 0$, the electron in the conduction band is converted into a hole in the valence band with same energy. Inspired from Ref.[7]. **b)** specular Andreev reflection 2D at the interface between undoped graphene and a superconductor. Left: in k space, an electron (blue particle) with an excitation energy ε on the conduction band (dotted red circle) is reflected as an hole (yellow particle) on the valence band (dotted blue circle. Right: in real space, an incident electron is reflected as an hole at the interface of undoped graphene and superconductor, exhibits a specular Andreev reflection.

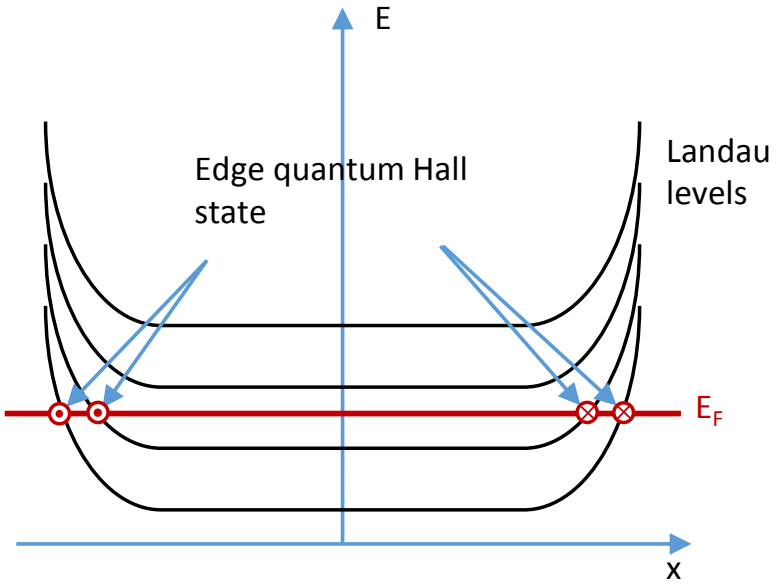

Figure 2.2.4: Landau levels of quantum Hall effect. The degenerate Landau levels are bended at the edge and the conducting edge channels are formed at the Fermi level (red line) with opposite motions.

ω_c is the cyclotron frequency. The quantized energy levels are known as the *Landau levels*. In strong magnetic field, the quantized Landau levels are highly degenerate. The degeneracy of each level is given by the filling factor $\nu = \Phi_0/\Phi_e$, where $\Phi_0 = h/e$ is the flux quantum, $\Phi_e = B/n_0$ is the flux per electron. Because of the quantum confinement, these Landau levels are bended at the edge of the 2D sample (Fig.2.2.4). So the conducting Landau levels are localized at the edge of the sample. In the conventional QHE system, the conductance can take the quantized values

$$\begin{aligned} \sigma &= \nu \frac{e^2}{h} \\ \nu &= 1, 2, 3, \ldots \end{aligned} \tag{2.45}$$

This is the conventional integer quantum Hall effect. The prefactor ν is known as the "filling factor".

In graphene, the linear dispersion relation and "relativistic" electron dynamics give the Landau level energy a different expression from usual 2D electron gas[85, 86]:

$$E_n = \mathrm{sgn}(n)\sqrt{2e\hbar v_F^2|n|B} \tag{2.46}$$

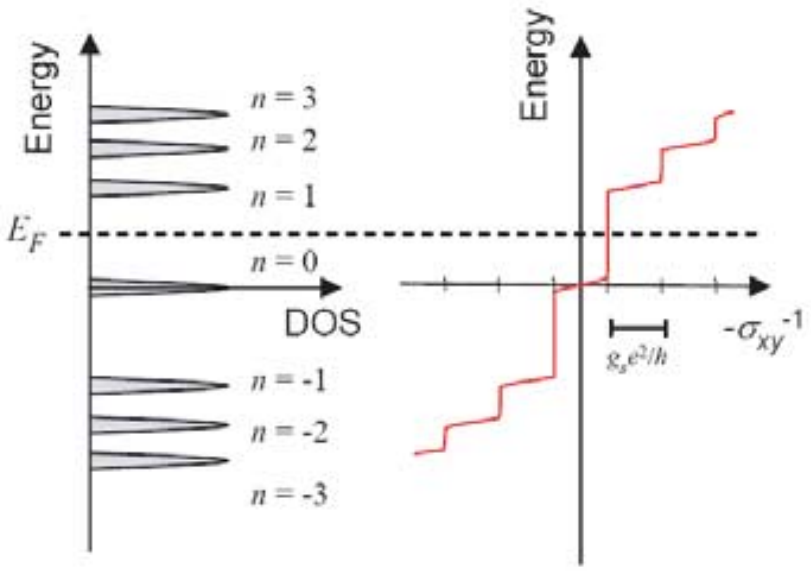

Figure 2.2.5: A schematic diagram of the Landau level density of states (DOS) and corresponding quantum Hall conductance (σ_{xy}) as a function of energy. The LL index n is shown next to the DOS peak. From Ref.[6].

the integer n represents an electron-like(n>0) or a hole-like (n<0) LL index. This causes a special half-integer quantum Hall effect in graphene[6, 87]:

$$\begin{aligned}\sigma &= \frac{ge^2}{h}(n+\frac{1}{2}) \\ &= \frac{4e^2}{h}(n+\frac{1}{2})\end{aligned} \tag{2.47}$$

Each LL has a degeneracy g = 4, since there are two spin degeneracy and two sublattice degeneracy (pseudo-spin). when a Landau level(LL) is crossed, the conductivity changes by $\frac{4e^2}{h}$. But we can note that, the lowest hole (N= -1, $\nu = -2$) and the lowest electron (N=0,$\nu = +2$) LLs don't have a $\frac{4e^2}{h}$ increase but a half (the origin of the name: Half-QHE): $\frac{2e^2}{h}$ (Fig.2.2.5).

Time-reversal invariance guarantees electron-hole symmetry; σ_{xy} is therefor an anti-symmetric function when the Fermi energy crosses the Dirac point[6, 85]. In graphene, the n=0 LL is universal ($E_0 = 0$ for all magnetic field)[85]. Thus the electron and hole share the first LL and the conductance plateau is situated at $\pm ge^2/2h$.

2.2.4 Sample characterization: Electric field effect

In our experiments, the graphene samples are at the same ground as gate voltage. There is capacitance is formed between the graphene and doped Si substrate. When there is a voltage difference imposed between the two layers, therefore, the charges can accumulate at both the surfaces of graphene

and Si. By changing V_G we can shift continuously the Fermi energy, thus the charge density. This leads to a change in the conduction properties of graphene, a so-called electric field effect.

From the gate dependence of resistance, we can deduce the variation of mean free path l_e, diffusion coefficient D and the Thouless energy $E_{Th} = \hbar D/L^2$. Using the capacitance model, the number of carriers induced by a gate voltage is given by

$$N_C = \frac{C\,|V_G - V_D|}{e} = \frac{\varepsilon_r \varepsilon_0 A}{ed}|V_G - V_D| \approx 7.1 \times 10^{14} A|V_G - V_D| \tag{2.48}$$

A is the area of the sample, V_D is the voltage corresponding Dirac point in the sample, usually $\varepsilon_r = 3.7$ for the SiO_2 $\varepsilon_0 = 8.85 \times 10^{-12} F \cdot m^{-1}$ is the dielectric permittivity, d = 285nm or 300nm in our cases. This relation shows a very important fact that the number of the carrier is tunable with the gate voltage.

On the other hand, the number of carriers can be also expressed by

$$N_C = g\sum_{k\leq k_F} \approx gA\int_{k\leq k_F} \frac{d^2k}{(2\pi)^2} = \frac{gA}{4\pi^2}\,2\pi\int_0^{k_F} dk\cdot k = \frac{gA}{4\pi}\,k_F^2 \tag{2.49}$$

in the case of graphene, the degeneracy g = 4 (2 for the spin, 2 for the degeneracy of valley or pseudo-spin), and we can deduce that $k_F = \sqrt{\pi n_C}$ (n_C is the carrier density per unit area). Thus we have $k_F = 4.75 \times 10^7 \times \sqrt{V_G - V_D} m^{-1}$ for d = 285 nm. The density of state $\nu(E_F) = \dfrac{\partial N}{\partial E} = \dfrac{2k_F}{\hbar v_F \pi} \approx 2.87 \times 10^{35}\sqrt{V_G - V_D}$.

We know the resistance $R = \rho\dfrac{L}{W}$, and $\rho^{-1} = \nu(E_F)e^2 D$, $D = \frac{1}{2}v_F l_e$, then we get

$$G = \frac{2e^2}{h}\frac{W}{L}k_F l_e \tag{2.50}$$

In ours samples, the l_e can vary from 50 nm to 90 nm for different gate voltage(charge density) and different contacts but they are all much shorter than the sample dimensions which places our samples in the diffusive regime.

2.2.5 Determination of the contact resistance

Since the mean-free path of the graphene in our samples is short (<100nm), our samples are all in diffusive regime which restrict the contacts to be very close in order to induce supercurrent through the samples. This makes us no choice but to have 2 terminal contacts on graphene as geometry. Additional contact resistance and normal wires connected in the circuit are included in the total resistance which is measured in 2 wires configuration. Then the geometry of the graphene flake in between the electrodes plays a important role in the transport measurement and one can deduce

the contact resistance from the magneto-resistance in certain limit.

How does the geometry of sample affect the conductance ?

The state of charge carriers transport can be significantly affected by the geometry of the sample. Here we will discuss three important cases. When the sample is subjected to a high magnetic field and a voltage difference is maintained across the sample, one can measure the Hall conductance. The components of current density is:

$$\begin{aligned} j_x &= \sigma_{xx}E_x + \sigma_{xy}E_y \\ j_y &= \sigma_{yx}E_x + \sigma_{yy}E_y \end{aligned} \tag{2.51}$$

and $\sigma_{xy} = -\sigma_{yx}$. We can also calculate the conductivity due to the Drude model in magnetic field, then get the conductivity components[88]:

$$\begin{aligned} \sigma_{xx} &= \frac{\sigma_0}{1 + (\omega_c\tau_{tr})^2} \\ \sigma_{xy} &= -\frac{\omega_c\tau\sigma_0}{1 + (\omega_c\tau_{tr})^2} \end{aligned} \tag{2.52}$$

$\omega_c = \dfrac{eB}{m^*}$, m^* is the cyclotron mass. For mono-layer graphene, $m^* = \dfrac{\hbar k_F}{v_F}$.

(a) Very long junction ($L \gg W$)In the limit, we can have $j_y = 0$. So that $E_y = \dfrac{\sigma_{xy}}{\sigma_{xx}}E_x$, and $j_x = \left(\sigma_{xx} + \dfrac{\sigma_{xy}^2}{\sigma_{xx}}\right)$. Using Eq. (2.52), $G_{xx} = \sigma_0$.

(b) Very wide junction ($L \ll W$) There is a certain relation between conductance of very large and that of very long sample:

$$G(L, W, \sigma) = \frac{\sigma_{xx}^2 + \sigma_{xy}^2}{G(W, L, \sigma)} \tag{2.53}$$

As we demonstrated above, $G(W, L, \sigma) = G_{long} = \sigma_0\frac{L}{W}$ and thus $G(L, W, \sigma) = G_{large} = \dfrac{\sigma_0}{1 + (\omega\tau)^2}\dfrac{W}{L}$. So that the resistance

$$R_{large} = \rho_0\left(1 + (\omega_c\tau)^2\right)\frac{L}{W} \tag{2.54}$$

(c) square junction ($L \approx W$) If the junction is square, the two wires measurement measures the longitudinal resistance and Hall resistivity at same time: $\rho = \sqrt{\rho_{xx}^2 + \rho_{xy}^2} = \rho_0\sqrt{1 + (\omega_c\tau_{tr})^2}$. The resistance $R = \rho\frac{L}{W}$, so $\rho = \rho_0\sqrt{1 + (\omega_c\tau_{tr})^2}$.

$$R_\square \approx \rho\left(1 + \frac{1}{2}(\omega_c\tau_{tr})^2\right) \tag{2.55}$$

Depending on the dimensions of the samples, we can classify them into different kind of junction. Then depending on the different type of junction, we use the equations shown before to estimate

the contact resistance. For most the cases, our samples are in the limit of very wide or square junction. Rewriting the Eq. 2.54 and Eq. 2.55 as follow,

$$R_{exp}(0) = R_{exp}(0) + \rho\left(\omega_c^2\tau_{tr}^2\right)\frac{L}{W} \qquad \text{large junction} \tag{2.56}$$

$$R_{exp}(B) = R_{exp}(B) + \rho\frac{\omega_c^2\tau_{tr}^2}{2} \qquad \text{square junction} \tag{2.57}$$

$R_{exp}(B) = R_c + R_i(B)$, R_c is the contact resistance which doesn't depend on the magnetic field, R_i is the intrinsic resistance which is equal to $\rho_0\frac{L}{W}$.

2.3 Spin-orbit coupling

Spin-orbit interaction is a well-known phenomenon that manifests itself in lifting the degeneracy of one-electron energy levels in atoms, molecules, and solids. In solid-state physics, the nonrelativistic Schrödinger equation is frequently used as a first approximation, e.g. in electron band-structure calculations. Without relativistic corrections, it leads to doubly-degenerated bands, spin-up and spin-down, which can be split by a spin-dependent term in the Hamiltonian. In this approach, spin-orbit interaction can be included as a relativistic correction to the Schrödinger equation.

If the electron is moving with velocity $\boldsymbol{v}$ in an electric field $-e\boldsymbol{E} = -\boldsymbol{\nabla} V$, taking into account relativistic effects, the electron sees in its rest frame a magnetic field, $\boldsymbol{B} = -v \times \boldsymbol{E}/c$. The interaction of the magnetic moment $\boldsymbol{\mu}_s$ with this magnetic field produces a term of potential energy:

$$V_{s-o} = -\boldsymbol{\mu}_s \cdot \boldsymbol{B} = \boldsymbol{\mu}_s \cdot \frac{v}{c} \times \boldsymbol{E} = \frac{1}{ec} \boldsymbol{\mu}_s \cdot \boldsymbol{v} \times \boldsymbol{\nabla} V \tag{2.58}$$

In an atom, the potential leads to a central electric field, $V = V(r)$, then,

$$V_{s-o} = \frac{1}{ecr} \frac{dV}{dr} \boldsymbol{\mu}_s \cdot \boldsymbol{v} \times \boldsymbol{r} = -\frac{1}{emcr} \boldsymbol{\mu}_s \cdot \boldsymbol{L}, \tag{2.59}$$

with $\boldsymbol{L} = \boldsymbol{r} \times \boldsymbol{p}$ the orbital angular momentum and m the electron mass.

Then the interaction of the magnetic moment with electric field can be alternatively seen as a spin-orbit coupling

$$V_s = \frac{\hbar}{2m^2c^2} \frac{1}{r} \frac{dV}{dr} \boldsymbol{\sigma} \cdot \boldsymbol{L}. \tag{2.60}$$

In a noncentral potential, this coupling is

$$V_s = \frac{\hbar}{2m^2c^2} \boldsymbol{\sigma} \cdot \boldsymbol{p} \times \boldsymbol{\nabla} V. \tag{2.61}$$

Finally, the full spin-orbit coupling term is

$$V_{s-o} = \frac{\hbar}{4m^2c^2} \boldsymbol{\sigma} \cdot \boldsymbol{p} \times \boldsymbol{\nabla} V. \tag{2.62}$$

by taking into count the *Thomas precession* which gives a contribution of the same form as (2.61), but opposite sign and half of the amplitude[89].

2.3.1 Rashba Spin-orbit coupling effect

The atomic spin-orbit coupling (SOC) can lead to a momentum-dependent splitting of spin bands in a solid state system if an asymmetric potential is present[90]. The asymmetric potential can be

introduced in different ways[91]:

- impurities: extrinsic effect arises only from the Mott scattering from impurity atoms[92]. This is usually weak in high quality system (ex. single crystal).
- Dresselhaus SOC: lack of crystal inversion symmetry[93]. In most III-V semiconductors, the lattice has zinc-blende structure and doesn't have inversion symmetry. Then the Krammer degeneracy is lifted.
- Rashba effect: lack of structural inversion symmetry of the confinement potential of electrons in a quantum well or surface state[94, 95]. In the case of 2D electron gas or a surface state, the Rashba effect is much larger than the other two effects.

If the electron is confined to a thin layer by an asymmetric potential, the Hamiltonian of the spin-orbit coupling of an electron is[94]

$$\hat{H}_R = a(\boldsymbol{p} \times \boldsymbol{\sigma}) \cdot \hat{\boldsymbol{z}} \tag{2.63}$$

where $\overrightarrow{\sigma}$ are the Pauli matrices. The unit vector $\hat{z}$ is directed along the normal of the plane. The operator $\hat{H}_R$ lifts the two fold spin degeneracy at $\boldsymbol{k} \neq 0$. a is the prefactor of Rashba effect.

The total Hamiltonian of electrons is given by $\hat{H} = \hat{H}_0 + \hat{H}_R$:

$$\begin{aligned} \hat{H} &= \frac{\boldsymbol{p}^2}{2m} + a(\boldsymbol{p} \times \hat{\boldsymbol{\sigma}}) \cdot \hat{z} \\ &= \frac{p_x^2 + p_y^2}{2m} + a(\hat{\sigma}_x p_y - \hat{\sigma}_y p_x) \end{aligned} \qquad E(\boldsymbol{k}) = \frac{\hbar^2 \boldsymbol{k}^2}{2m} \pm a\,|\boldsymbol{k}| \tag{2.64}$$

where the plus and minus sign correspond to the two possible spin directions($\uparrow, \downarrow$). The spin splitting energy is $\Delta = 2a\,|\boldsymbol{k}|$. The effect of a SOC term and a Zeeman term on a 1D dispersion relation is shown in Fig.2.3.1. The difference is that the Zeeman coupling leads to a spin polarization (different population in spin up and spin down) due to the time reversal symmetry breaking and not for SOC.

2.4 Bismuth and SOC

2.4.1 Bi bulk crystal structure

Bismuth crystallizes with rhombohedral symmetry in a structure which is typical for the group V semimetals. Since each atom has 3 nearest-neighbor atoms and 3 next-nearest neighbor atoms, in Bismuth bulk, bonded bilayers of atoms are formed perpendicular to the rhombohedral direction

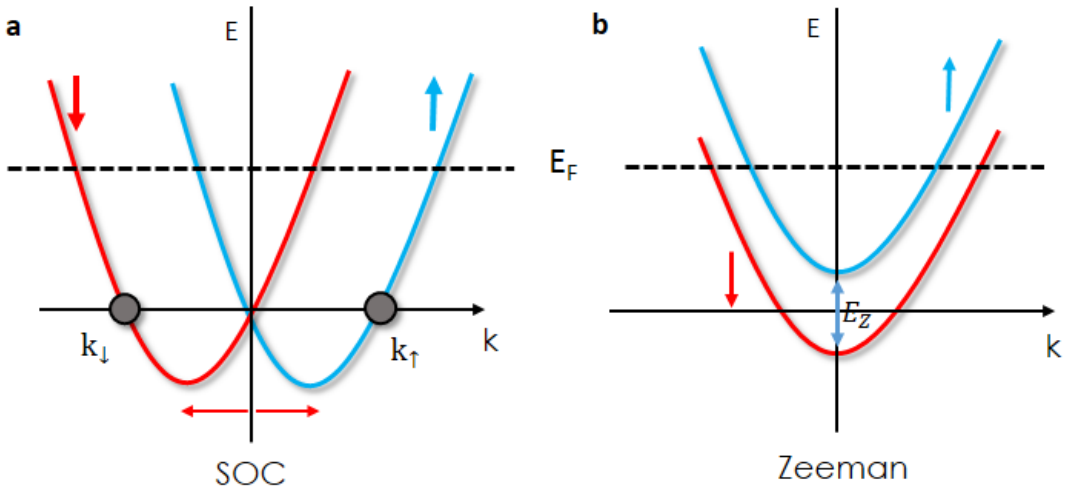

Figure 2.3.1: The 1D dispersion relation of a 2D system with the presence of SOC(a) and Zeeman coupling (b). The spin ↑ and spin ↓ bands are split in both systems.

[111]. Each atom covalently bonded to its three nearest-neighbors within each bilayer. The atom's next-nearest neighbors are in the adjacent bilayer. Actually the bonding within each bilayer is much stronger than the inter-layer bonding. This makes the (111) plane the natural cleaving plane. Among the studies, the Bismuth crystalline is also described as hexagonal with six atoms per unit cell or as a pseudocubic structure with one atom per unit cell.

we here focus on the rhombohedral symmetry description. The relation between these different unit cells is shown in Fig.2.4.1. The rhombohedral unit cell is indicated by green lines and the two different atoms in the unit cell are shown in blue and red. The length ratio d_1/d_2 is 0.88 (instead of 1) and therefore the red atom is closer to the three blue atoms below it than to the three atoms above it, forming the above-mentioned bilayers. The trigonal (C_3)) axis of the rhombohedral structure is the c axis of the hexagonal structure.

The simplest description of the Bi structure is obtained when using a rhombohedral Bravais lattice with two atoms per unit cell. The lattice is generated by three vectors $\overrightarrow{a_1}$, $\overrightarrow{a_2}$, $\overrightarrow{a_3}$ of equal magnitudea_rh[88]. These vectors are shown in Fig. 2.4.1 as solid green lines. The angle between any pair of the primitive vectors is α. The two basis atoms are chosen to be at the origin of the coordinate system and at $(\overrightarrow{a_1} + \overrightarrow{a_2} + \overrightarrow{a_3})d_1/(d_1 + d_2)$ (see Fig. 2.4.1). Thus the crystal structure is completely described by a_rh , d_1/d_2 , α. For Bi these values are $a_rh = 4.7236\mathring{A}$, $d_1/d_2 = 0.88$ and α = 57.35° at 4.2 K [96, 97]. For a more convenient comparison with the hexagonal lattice system, we write the rhombohedral lattice vectors using the characteristic parameters for the hexagonal system $a = 4.5332\mathring{A}$ and c = 11.7967 $\mathring{A}$. We use Cartesian coordinates such that the binary (C_2) axis is x, the bisectrix (C_1) axis is y the trigonal (C_3) axis is z. The vectors spanning the rhombohedral unit cell

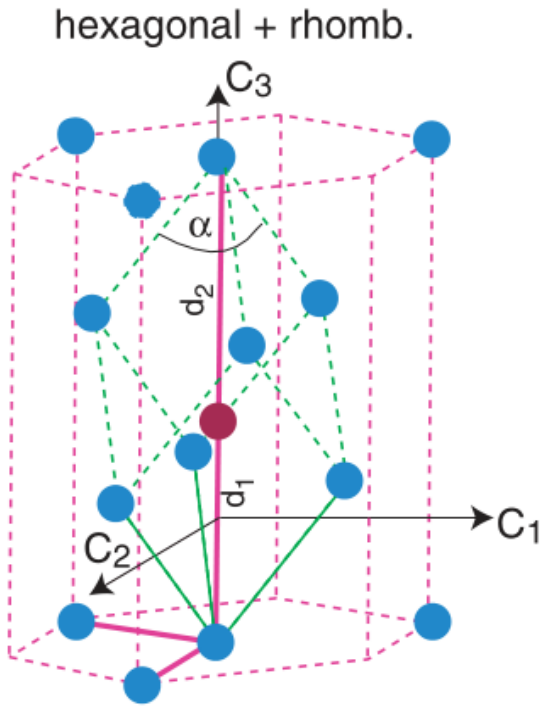

Figure 2.4.1: Bulk structure of Bi. Rhombohedral unit cell (dashed green lines) together with the hexagonal unit cell (dashed pink lines). Not all the atoms are shown. Blue and red mark the two atoms in the rhombohedral unit cell. The solid green and pink lines are the vectors spanning the rhombohedral and hexagonal lattice, respectively. The three cartesian axes are: bisectrix (C1 ,y), binary (C2 ,x) and trigonal (C3 ,z).

are then

$$\begin{aligned}
\overrightarrow{a_1} &= \left(-\frac{1}{2}a, -\frac{\sqrt{3}}{6}a, \frac{1}{3}c\right), \\
\overrightarrow{a_2} &= \left(\frac{1}{2}a, -\frac{\sqrt{3}}{6}a, \frac{1}{3}c\right), \\
\overrightarrow{a_3} &= \left(0, \frac{\sqrt{3}}{3}a, \frac{1}{3}c\right).
\end{aligned} \tag{2.65}$$

These vectors are shown as solid green lines in the left part of Fig. 2.4.1. The reciprocal lattice is given by

$$\begin{aligned}
\overrightarrow{a_1} &= 2\pi\left(-\frac{1}{a}, -\frac{\sqrt{3}}{3a}, \frac{1}{c}\right), \\
\overrightarrow{a_2} &= \left(\frac{1}{a}, -\frac{\sqrt{3}}{3a}, \frac{1}{c}\right), \\
\overrightarrow{a_3} &= \left(0, \frac{2\sqrt{3}}{3a}, \frac{1}{c}\right).
\end{aligned} \tag{2.66}$$

As usual, the (mno) surface in the rhombohedral notation is the surface plane which is perpendicular to the reciprocal lattice vector $m\overrightarrow{b_1} + n\overrightarrow{b_2} + o\overrightarrow{b_3}$ [88].

2.4.2 ELECTRONIC STRUCTURE OF Bi BULK[33]

Bi (bulk) is classified as semi-metal, and there are quite lot unique properties are related to its special electronic structure. There are in general two methods of calculations have been carried out succeed. One of these is the tight-band calculation for the detailed description around Fermi level first published by Liu and Allan in 1995[97] for Bi. Another one is done by Gonze et al.[98] using first-Principe calculation. The result of the calculation is shown in Fig. 2.4.2, the bulk Brillouin zone is shown in Fig. 2.4.3.

The band structure can be described by 2 filled s bands and 3 filled p bands separated by a gap about several eV. These five bands can contain the 10 valence electrons per unit cell, five from each Bi atom. However, if one look closely to the T and L points the p bands cross the Fermi level, creating hole pocket at T point and electron pocket at L point. These pockets are shallow: the Fermi energy is 27.2 meV for the electrons and 10.8 meV for the holes which leads to a very low carrier density about $3 \times 10^{-7} cm^{-3}$ and small effective mass of carrier, for example, for electrons along the trigonal axis $m^* \approx 0.003 m_e$.

One should note that when the bulk structure is calculated, inclusion of spin–orbit coupling has

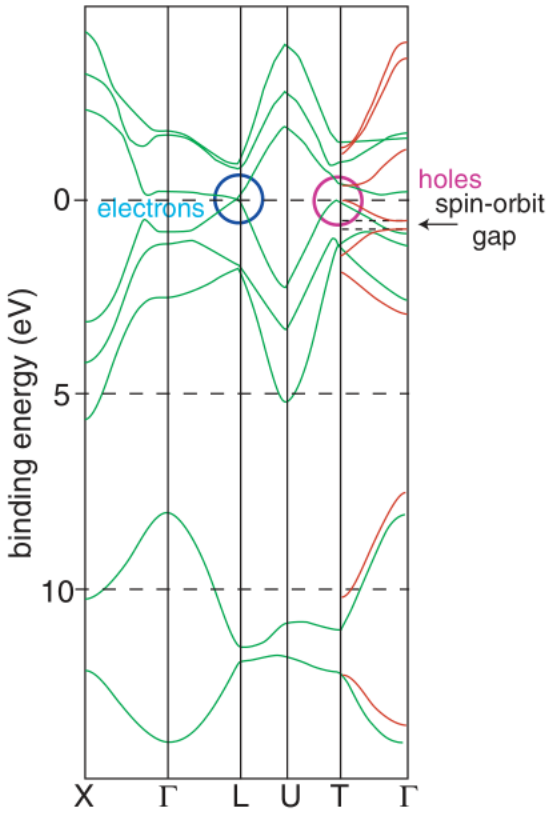

Figure 2.4.2: Bulk band structure of Bi from the tight-binding calculation of Liu and Allan (Ref. [97], green lines); first-principles calculation by Gonze et al. (Ref. [98], red lines), only in the $\Gamma - T$ direction.

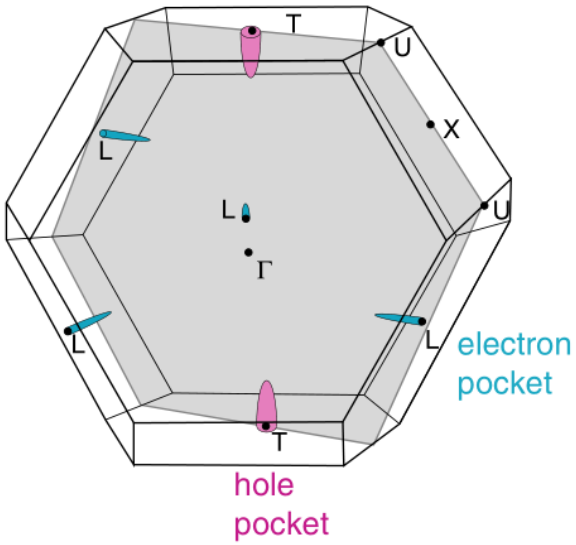

Figure 2.4.3: Bulk Brillouin zone of Bi and a schematic sketch of the Fermi surface (not to scale). The $\Gamma - T$ line corresponds to the C3 axis and the [111] direction in real space.(Figure taken from ref.[33])

only a small effect on the two lowest bands. The bands close to the Fermi level, however, are strongly affected: the strong spin–orbit interaction essentially accounts for the existence of the hole Fermi surface at the *T* point. We can tell from the Fig. 2.4.2, the red curve shows the result considering the effect of spin-orbit coupling and a gap is opened at the T point. Most importantly from a surface point of view, the spin–orbit coupling does not lead to any lifting of the spin degeneracy, i.e. there are still two possible spin states at the k point. This is caused by the *bulk inversion symmetry* in Bi. recently, the angle dependent magnetoresistance measurements in Bi bulk have been done by Zhu et al.[99] which show a low temperature field dependent transition to a valley polarization state in Bi bulk and the three electron pockets become inequivalent.

2.4.3 Bi thin film and surface properties

There are two aspects that can affect much of the properties of Bi when the size decreases: First, the electronic structure is intimately related to the symmetries of the rhombohedral phase in Bismuth and at the surface or in thin films, some of the symmetries are broken. Second, when the thickness (of the thin film) or the size (for the nanowires or nanostructures) attain to certain limits, the quantum-size effect can play an important role.

Ogrin et al., who started the research on quantum size effects in thin films, argued that the Bi thin film is ideal to observe such effect for several reasons: 1. the low Fermi energy and the small effective mass of the carriers lead to a long de Broglie wavelength of around 120 ; 2. long mean-free-path($\sim$ 1*mm*) in Bi ensure the interference inside of the nano-size object phenomenon. Up to date, these are thickness dependent transport oscillations are observed but not critical thickness for a sudden change. The reason for this experiment and theory discrepancy is still under debate.

(111) Bi surface structure

There are three surfaces in the rhombohedral description: [111], [110], [100]. For Bi(111) and Bi(110) both experimental and calculated structural results are discussed, for Bi(100) only calculated structural parameters are available. Here we will focus rather on (111) surface which is most studied and also important for practical application. It is the natural cleavage plane of Bi crystals and it also turns out to be the preferred direction of epitaxial growth. The truncated bulk crystal structure of Bi(111) is shown in Fig. 2.4.4. For the figure, it is assumed that the crystal is terminated with a Bi bilayer.

(111) Bi surface electronic structure

Bi(111) is the only surface of Bi for which angle-resolved photoemission spectroscopy (ARPES) studies have been performed by many authors. This is the only direction for which photoemission data

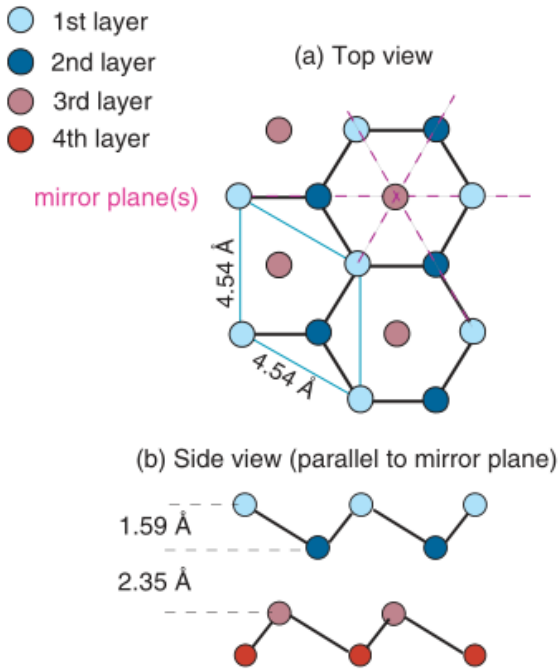

Figure 2.4.4: Truncated-bulk structure of Bi(111). The dark solid lines indicate covalent bonds between the atoms within the bilayers. (a) Top view of the first three atomic layers. Each layer consists of a two-dimensional trigonal lattice and the lattice constants are given. The mirror planes of the structure are shown as dashed lines. (b) Side view of the first four layers along a mirror plane. The alternating short and long interlayer spacings are evident. After Ref.[100].

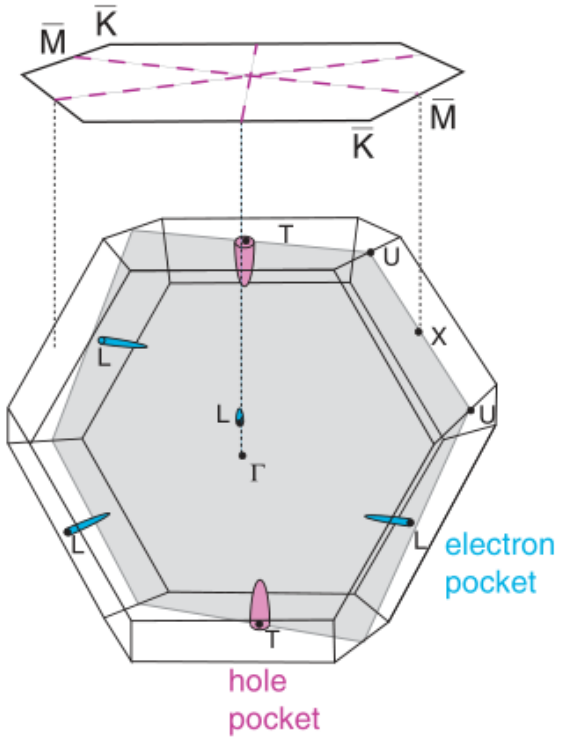

Figure 2.4.5: Bulk Brillouin zone of Bi and projection on the (111) surface. The elements of the bulk Fermi surface are indicated but not to scale. The surface Brillouin zone has a threefold rotational axis and three mirror lines, shown as pink dashed lines. After Ref.[33]

for the determination of the bulk electronic structure have been taken so far [101, 102, 103, 104, 105].The bulk Brillouin zone (BZ) of Bi and the projection on the (111) surface are shown in Fig. 2.4.5. A state supported by the surface in the spin-orbit gap was observed and also debated. Finally, it was clarified by Ast and Höchst, using synchrotron radiation[106] an energy resolution of 25 meV and a very high momentum resolution of 23 m$\mathring{A}$. The dispersion of the states close to $\overline{\Gamma}$ is shown in Fig. 2.4.6. The most important conclusion from these results is that the number of surface charge carriers is much higher than the corresponding number of (projected) bulk carriers. An inner ring(hexagon actually) and six narrow lobes in the $\overline{\Gamma} - \overline{M}$ directions. The theoretical results are also obtained with first principle calculation by Koroteev et al. [36] with and without the inclusion of the spin-orbit coupling(Fig.2.4.7). We can find that, when the SOC is included, a spin-splitting of the surface state in all directions appears and the energy levels degenerate only at $\overline{\Gamma}$ and T. And the ultimate proof of the strong spin-orbit splitting lies in the comparison with the experimental findings. Koroteev et al. also showed experiment results realized by high resolution ARPES measurement fitted with the calculation(Fig. 2.4.8).

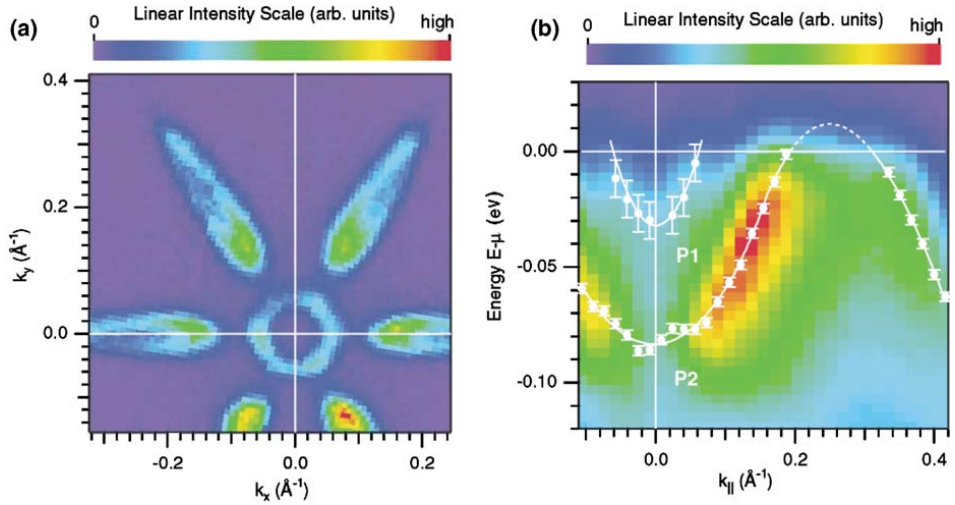

Figure 2.4.6: (a) Photoemission intensity at the Fermi level of Bi(111). k x and k y are the parallel components of the electron momentum along the C–M and C–K direction, respectively. (b) Band structure along the C–M direction. From Ref.[106]

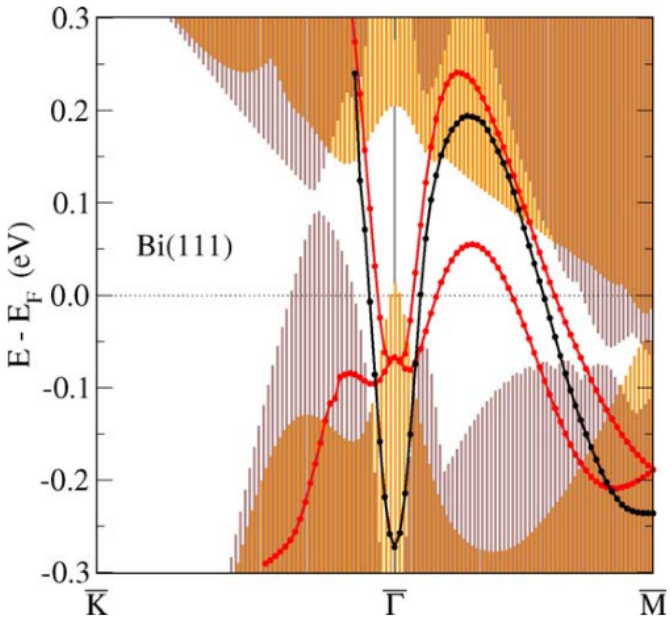

Figure 2.4.7: Surface states of Bi(111) calculated without (black) and with (red) spin–orbit splitting included. The shaded areas show the projection of the bulk bands obtained without (violet) and with (yellow) SOC and their superposition (brown). After Ref.[36]

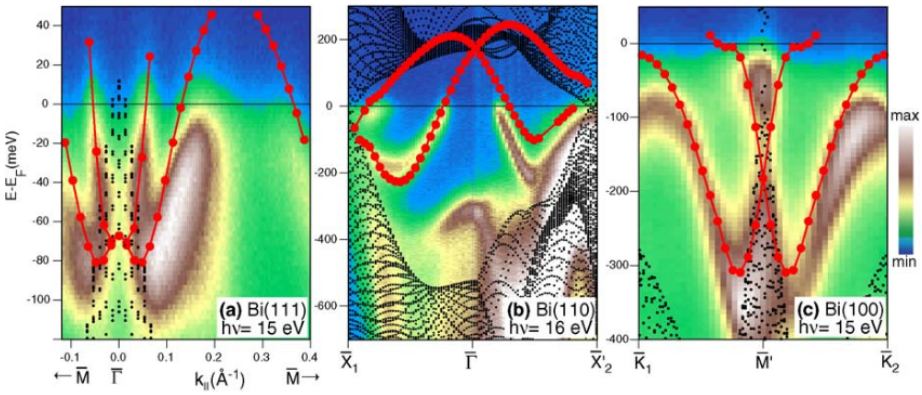

Figure 2.4.8: Calculated and measured electronic structure in the vicinity of two high symmetry points on three surfaces of Bi. (a) C on Bi(111), (b) C on Bi(110), and (c) M 1 on Bi(100). The small black dots are the projected bulk band structure calculated using the tight-binding model of Liu and Allen. The red filled circles are the calculated surface state energies, thin red line is a guide to the eye. After Ref.[36]

	carrier density	λ_F	v_F
Bulk	$3 \times 10^{17} cm^{-3}$	large $\sim 50nm$	small
Surface	$3 \times 10^{13} cm^{-2}$	small	large

Transport measurement on surface states

Recently, Ning W. et al.[38] measured the angular-dependent magnetoresistance (AMR) measurements on single-crystal bismuth nanoribbons(with a preferential $[110]_{hex}$ growth direction) of different thicknesses, and in magnetic fields up to 31 T(Fig.2.4.9). In thin nanoribbons of about 40 nm thick, a two-fold rational symmetry of the low field AMR spectra and two sets of 1/2-shifted (i.e.,$\gamma = 1/2$) Shubnikov de Haas (SdH) quantum oscillations with exact two-dimensional (2D) character were obtained. However, when the thickness of the ribbon increases, a 3D bulk-like SdH oscillations with $\gamma = 0$ and a four-fold rotational symmetry of the AMR spectra appear. There results provide a transport evidence of the topological 2D metallic surface states in thinner nanoribbons with an insulating bulk.

2.4.4 Bi nanowires

A similar situation has also been found in Bi nanowires research. Lin et al. predicted a critical diameter about 55 nm of Bi nanowire for a semimetal-semiconductor transition [107]. Experimentally, Bi nanowires are found to have SdH quantum oscillations[108, 109, 110], which were attributed to the formation of surface state on Bi nanowires. We will see that our experiments on Bi nanowires signal the existence of 1D edge states, expected at the edges of specific topological surfaces of Bi.

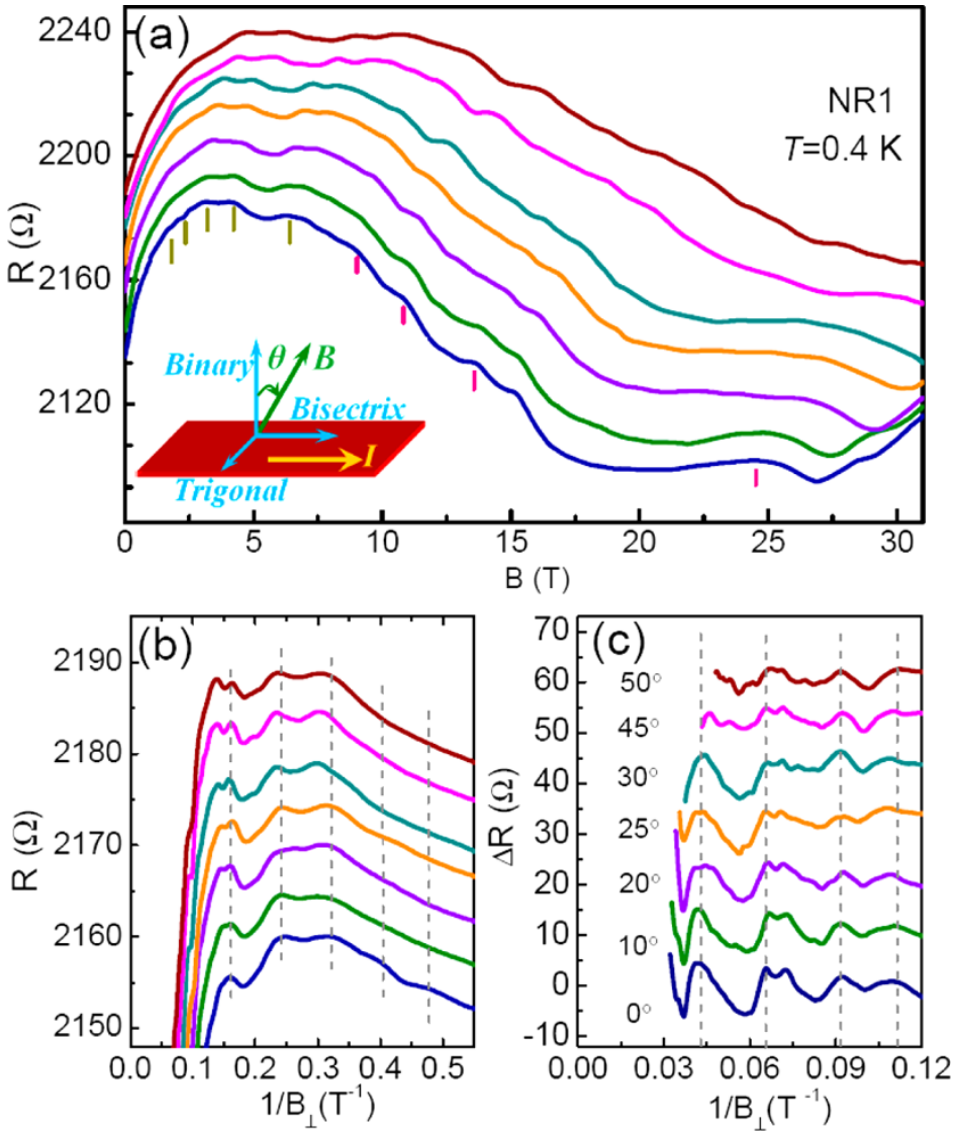

Figure 2.4.9: 2D SdH oscillations of conduction in 40 nm Bi nanoribbon. (a) Resistance of sample NR1 (40 nm) as a function of magnetic field at different tilted angle,θ,at 0.4K(B rotates within binary and bisectrix plane).The inset is the schematic of B orientation in different planes of nanoribbon.(b)Enlarged MR in low B-regime of B<9 Tesla function of $1/B_{\perp}$. (c) Amplitude of the resistance oscillations, ΔR, in high B-regime (B $>$ 9 T) versus $1/B_{\perp}$. Both oscillation spectra show periodic behavior with $1/B\cos\theta$, indicating a typical 2D character of electronic structure.After Ref.[38]

3

Superconducting proximity effect in S/G/S junction

This chapter presents the experimental results in superconducting proximity effect in graphene with different superconducting electrodes at zero and low field. We emphasize the differences between the proximity effect in short junction limit (samples with Ti/Al electrodes) and in the long junction limit (with Pd/Nb and Pd/ReW electrodes).We also compare various $R_N I_c$ products of the junctions in different limits. There is a huge disparity in $R_N I_c$ product for the long junction samples comparing to the theoretical prediction. This may be a sign of the presence of specular Andreev reflection.

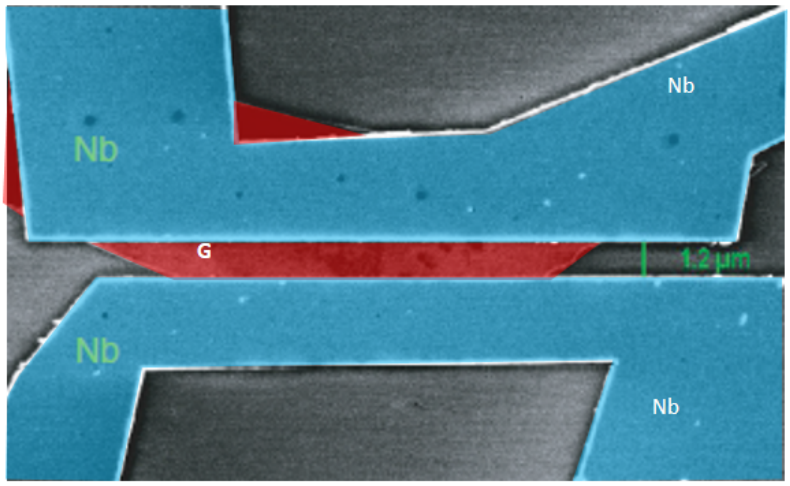

Figure 3.1.1: SEM image of Nb sample (fake colors). In-between the Nb electrodes (blue), a large graphene sheet (red) is connected.

3.1 Sample description and characterization

We measured 7 samples that exhibit supercurrent at low temperature. They have different materials as contacts, and different dimensions.

Five of them are connected to Ti/Al electrodes, one is connected to Pd/Nb/Pd electrodes, one is connected to Pd/ReW/Pd electrodes. All samples were mechanically exfoliated with blue scotch tape and deposited on a doped silicon substrate (Append.A for more details). The Ti/Al samples are in the short junction limit ($L \lesssim \xi_s$), and the Nb and ReW samples are in the long junction region ($L \gg \xi_s$). All the graphene sheets are wide ($L \ll W$).

For the Ti/Al(6nm/70nm) samples, the electrodes are deposited by electron-gun evaporation. For the Pd/Nb/Pd(8nm/70nm/6nm) sample, the electrodes are made by Ar plasma sputtering.

The SEM image of the Nb sample is shown in (Figure 3.1.1)

Using electric field effect method described in the introduction, we first characterize all these samples. The mean-free path, the diffusion constant, the coherence length etc. can be deduced from the gate dependence of the resistance. We show in Fig.3.1.2 and Tab. 3.1.1 some typical physical quantities at different gate voltage values.

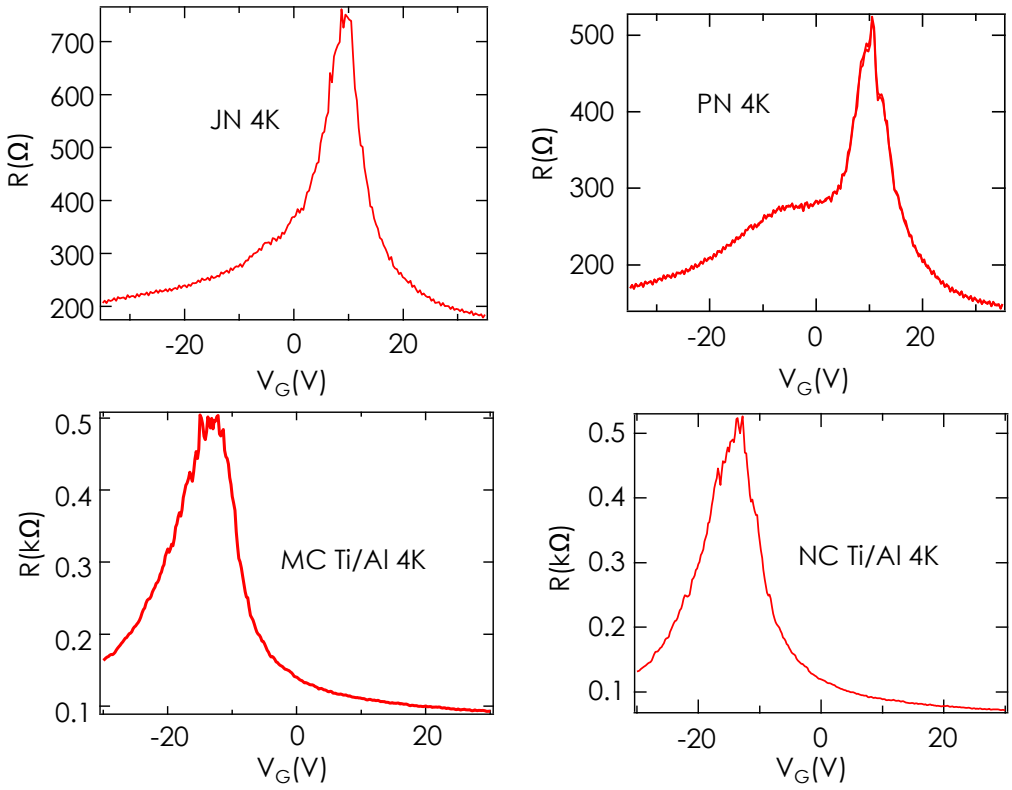

Figure 3.1.2: Gate dependence of resistance for samples JN,PN,MC,NC. JN and PN are on the same graphene flake, and same for MC and NC. All of these samples are connected to Ti/Al electrodes.

Table 3.1.1: Sample characterization.
The samples are classified into short junctions and long junctions with different contact materials.

	Short / intermediate junction					Long junction	
	Ti/Al (6nm/70nm)					Pd/Nb (8nm/70nm)	Pd/ReW (8nm/70nm)
notation	JN	PN	PM (+porphyrins)	MC	NC	Nb	ReW
L (nm)	500	400	350	450	500	1200	700
W (μm)	3.4	4	4	4	4	12	5
$\overline{l_e}\ (nm)$	120 ± 40	140± 60	150	120	170	60± 30	70± 30
$\overline{\xi_s}\ (nm)$	400	500	430	420	520	120	120
E_{th} (Δ)	0.8 - 10						

From Tab.3.1.1, we can tell that the lengths of our samples are longer than the mean-free path in graphene ($L > l_e$), so that the S/G/S junction is diffusive.

3.2 Sample in short junction limit

We measured 5 samples in short junction limit (Ti/Al as contacts). The superconducting gap (Δ) of Al is about 150 μeV (estimated by MAR, see Fig.3.2.2), $T_C \simeq 1K$. The $L/\xi_s = 1\,1.8$ for $\pm 30V$ gate voltage regime. We measure first the gate dependence at 4K (see Figure 3.1.2)and then it reaches the superconducting state at low temperature(100mK) by applying a small magnetic field to compensate the residual magnetic field in the coil.

3.2.1 Gate tunable supercurrent

Once we optimize the field (to compensate the earth field and possible residual magnetic field in the coil) for superconducting proximity effect, we measure the DC current dependence of the differential resistance(Figure 3.2.1.a). The sharp jump(peak) indicates the transition from superconducting state to normal state. We define the DC current at that point as the critical current I_c.

Figure3.2.1.c shows that the critical current of sample JN is modulated by the gate voltage: from the Dirac point to electron(hole) doped regime, I_C is changed from 20nA to 400nA(300nA).

Multiple Andreev reflection (MAR) These 5 samples all show multiple-Andreev reflection. In figure.3.2.2, we show the dV/dI curve as function of DC voltage. We see clearly the superconducting gap of Al and the sequent dips in differential resistance, each of which is corresponding to a quasi-particles reflection below of the gap. The presence of MAR implies an imperfect interface between metal contact and graphene[11]. The gap (2Δ) is estimated to be $300\mu V$.

3.2.2 Low field dependence: Fraunhofer pattern

Similar to optic experiment, the supercurrent can be analogue to a light beam and show interfering intensity pattern. For short junction, this pattern is expected to be close to theoretical prediction of an SIS junction (The Fraunhofer pattern). In figure.3.2.3, we show the Fraunhofer pattern of JN at $V_G = 30V$. They have a center lobe width about 20 Gauss.

3.3 Samples in long junction limit

The Nb sample and the ReW sample are in long junction limit, they both show complete proximity effect with a supercurrent flowing through at low temperature(200 mK for Nb sample, 55 mK for

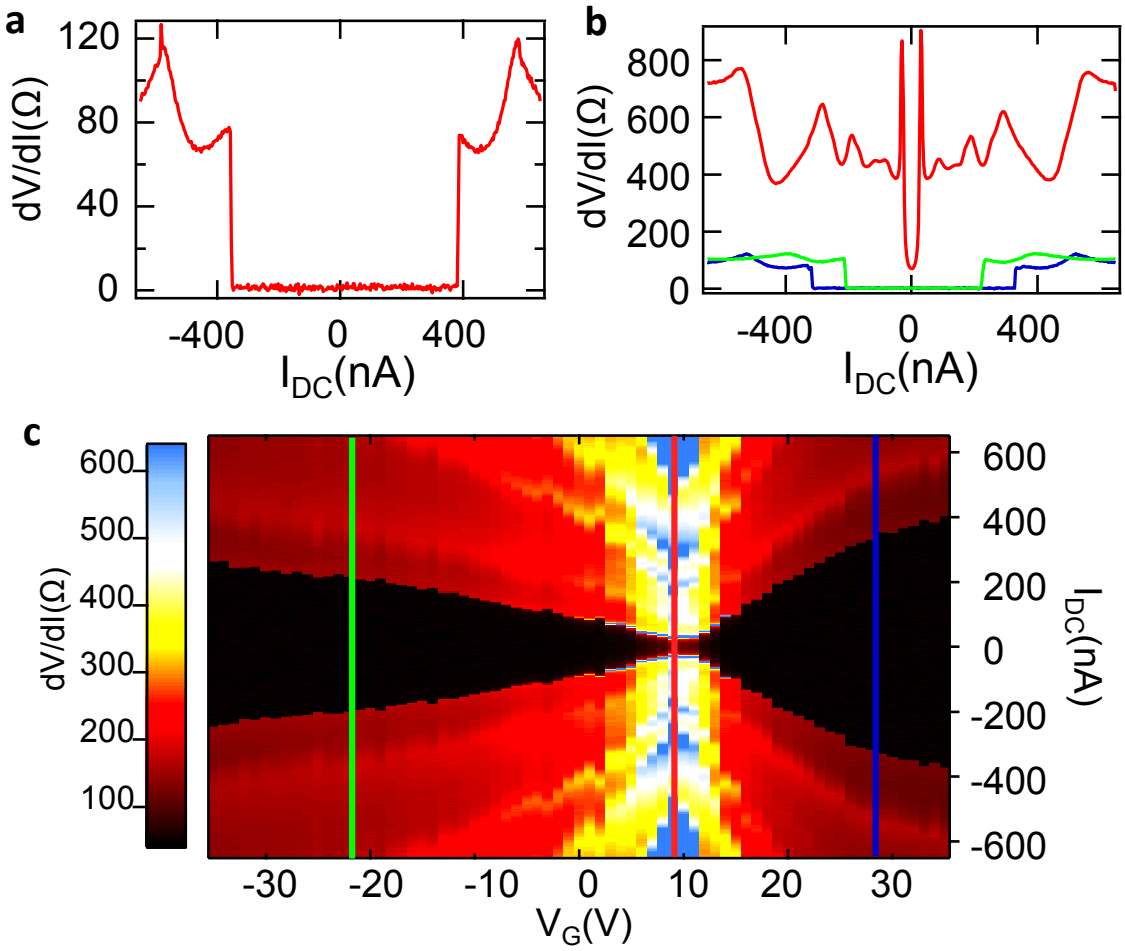

Figure 3.2.1: Proximity effect in sample JN which is identified as a short junction. (a) shows a typical dV/dI vs DC current curve. Two sharp jumps(peaks) indicate the edges of superconducting gap in graphene; (b) dV/dI curves at different gate voltages, different colors correspond to different positions indicated in (c) 2D color plot. (c) two-dimensional color plot of full gate voltage range dV/dI curves. The black regime corresponds to zero resistance(superconducting) state

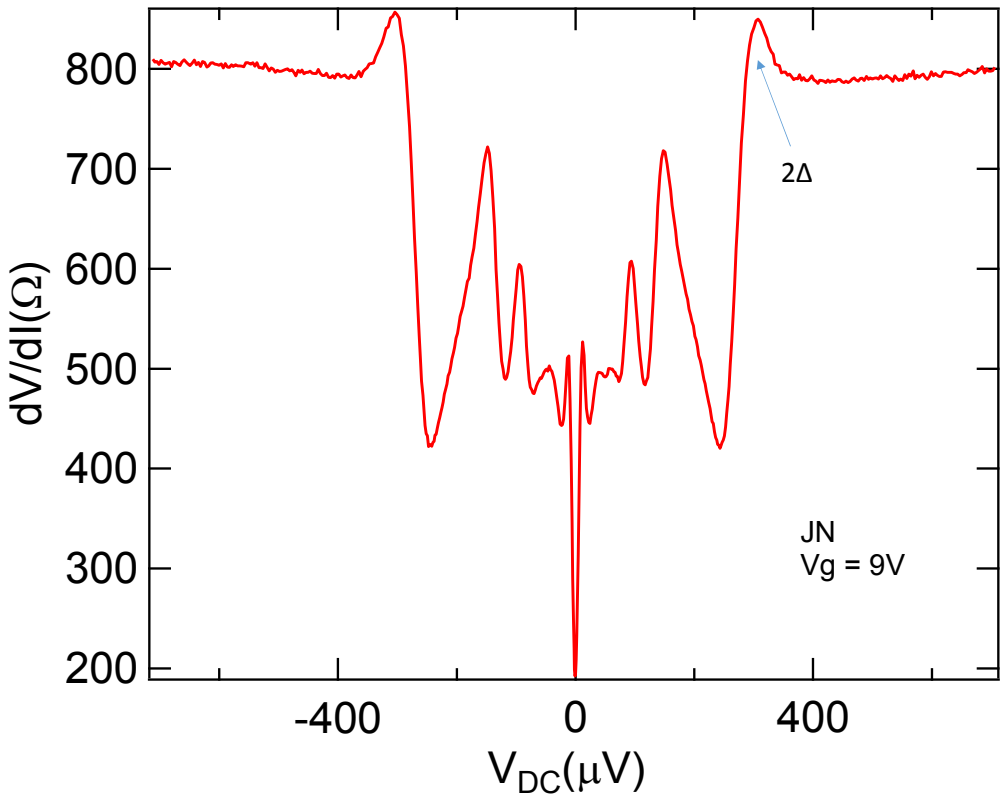

Figure 3.2.2: Multi-Andreev reflection. (a) shows a dV/dI curve at Vg=9V, inside of the superconducting gap of Al, one can see several dips of the differential resistance. Each dip corresponds to a reflection inside of the gap. The 2Δ, Δ,$2\Delta/3$ are indicated in the figure. we estimate the gap $2\Delta = 350\mu V$

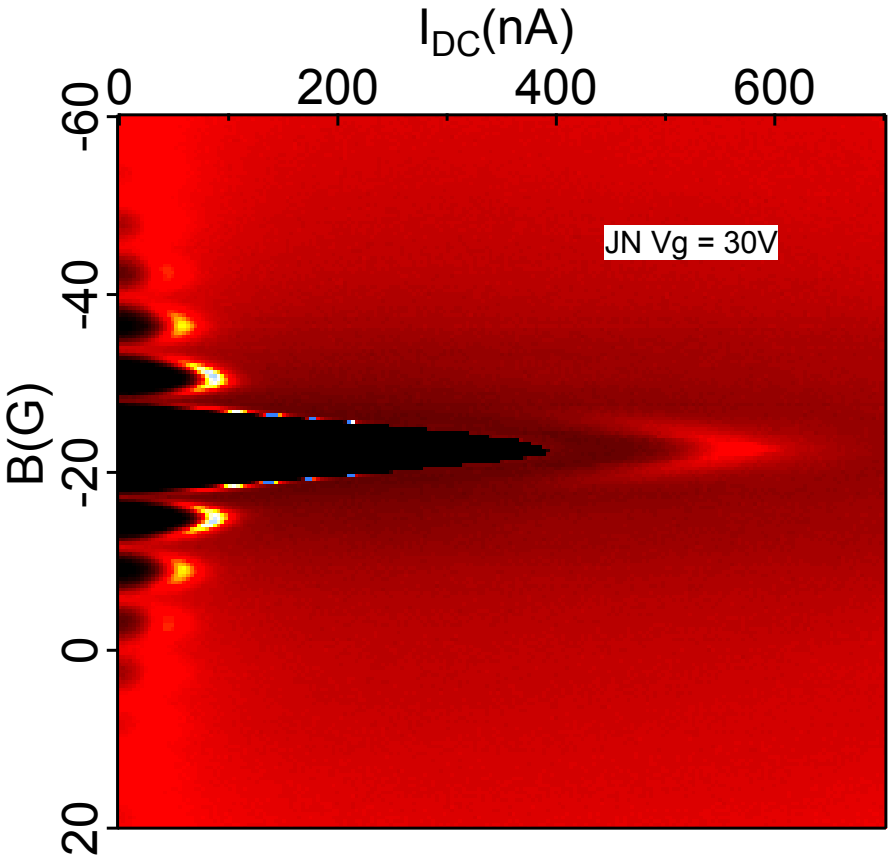

Figure 3.2.3: The Fraunhofer pattern of sample JN.

ReW sample). They display similar dV/dI curves and gate dependences as shown in Figure 3.3.1 and Figure 3.3.2 for the two samples respectively.

3.3.1 Gate tunable supercurrent

Similar to samples in the short junction limit, Nb and ReW samples display a gate tunable supercurrent from hole to electron doped regions. The critical current is smaller than that in short junctions.

3.3.2 suppression of supercurrent near Dirac neutral point

As is clearly seen in the two figures (Fig.3.3.1 and Fig.3.3.2) (especially the bottom-left 2D color plot sub-figure), the supercurrent is completely suppressed near the Dirac point which is robust as the doped regime in our short junction samples, and also reported by others groups[40, 41, 42]. We attribute this unexpected suppression of supercurrent to the specular Andreev reflection at the electron-hole puddles interfaces. To understand this suppression, we compare the measured critical current to theoretical result[68].

In the theory of the proximity effect in the diffusive[68], long junction limit, the critical current has a maximum zero-temperature value given by the Thouless energy E_{Th} divided by the normal resistance state R_N, multiplied by a numerical factor a that depends on the junction length L: $I_C = aE_{Th}/eR_N$, where $E_{Th} = \hbar D/L^2$, with D = $v_F l_e/2$ the diffusion constant in two dimensions,v_F the Fermi velocity and l_e the mean free path.

To probe this relation, we compare the $I_c(V_G)$ to the theoretically predicted $I_c = aE_{Th}/eR_N$ (see Fig.3.3.3). When the gate voltage approaches the Dirac point, the measured I_c decreases much faster than the theory calculation and even vanishes near the Dirac point. This is a non-trivial phenomena, even though one could have the first impression that all this can be explained by a bad interface (we show further that this is not the case).

For these two samples, we find a L/ξ_s ratio (depending on gate voltage),where $\xi_s = \sqrt{\frac{\hbar D}{\Delta}}$ is the coherence length, L is the length of the sample, between 4.4 and 6.2 for the ReW sample, and between 9.3 and 10.7 for the Nb one, which places these junctions in the long (but not infinitely long) junction limit.

In the limit of infinite Δ/E_{Th}, the $R_B I_C$ product is simplified to

$$eR_N I_C = \frac{32}{3+2\sqrt{2}} E_{Th} \left[\frac{L}{L_T}\right]^3 e^{-L/L_T} \tag{3.1}$$

We plot the temperature dependence for different ratios Δ/E_{Th} in figure.3.3.4. From it, one finds that a factor 10 suppression of the I_c requires an effective temperature of 5 to 10 E_{Th}, in our case 3K, much higher than the experiment temperature of 200 mK or 55 mK. we can tell that at low

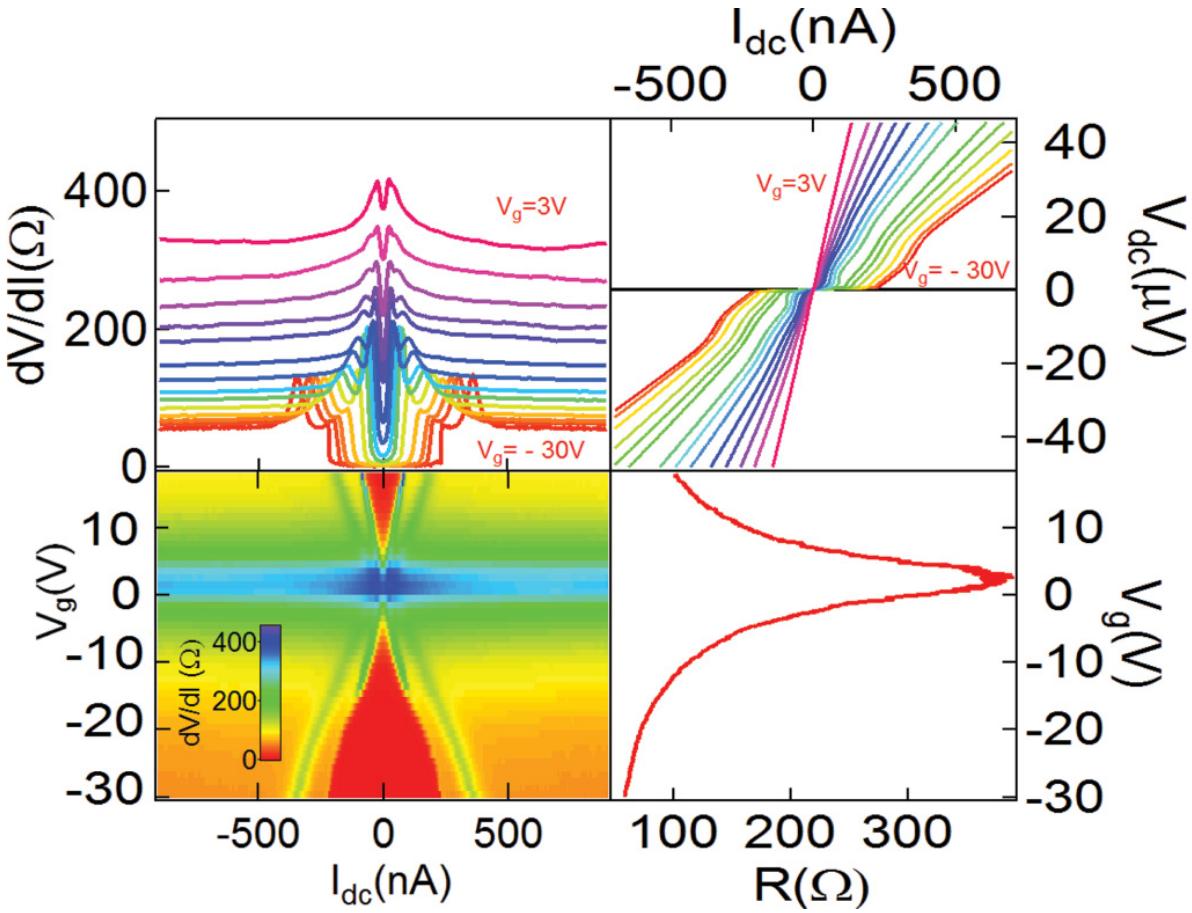

Figure 3.3.1: Proximity effect in graphene connected to Nb electrodes at 200 mK. Upper left panel: dV/dI vs Idc for different gate voltages, and, bottom left panel, its two-dimensional color plot. The suppression of critical current in a gate voltage region of $\pm$10V around the charge neutrality point is noticeable. Upper right panel: I(V) curves for different gate voltages, showing how the proximity effect varies between a full proximity effect with zero resistance at high doping, and quasi-normal behavior with a linear I (V) around the charge neutrality point. (Lower right panel) Zero-bias differential resistance as a function of gate voltage in the normal state from which the R_N is determined. A small magnetic field was applied to destroy the constructive interference leading to the supercurrent.

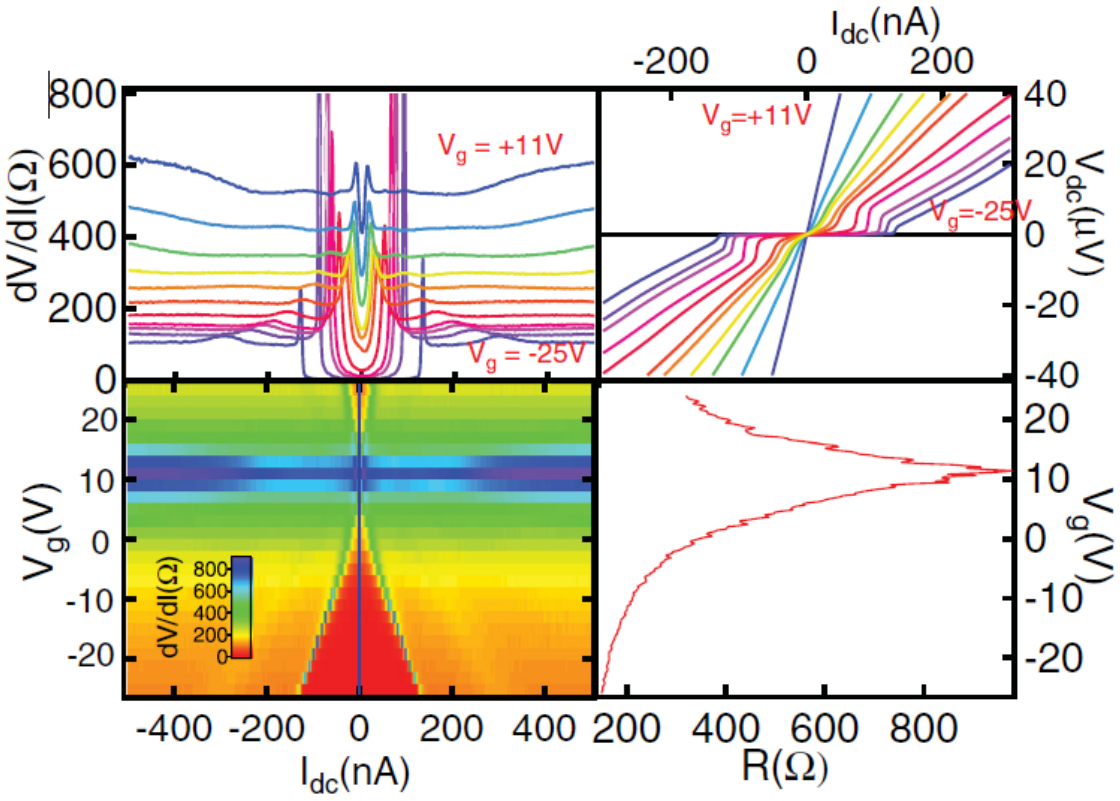

Figure 3.3.2: Proximity effect in graphene connected to ReW electrodes at 55 mK. (Top left) dV/dI vs I_{dc}. The peaks in differential resistance reflect the voltage jumps as the SGS junction switches from a zero-resistance state to a finite resistance state. (Top right) I(V) curve for different gate voltages. (Bottom left) Two-dimensional color plot emphasizing the suppression of the supercurrent around the charge neutrality point. (Bottom right) Resistance as a function of gate voltage in a small magnetic field that suppresses the constructive interference leading to supercurrent.

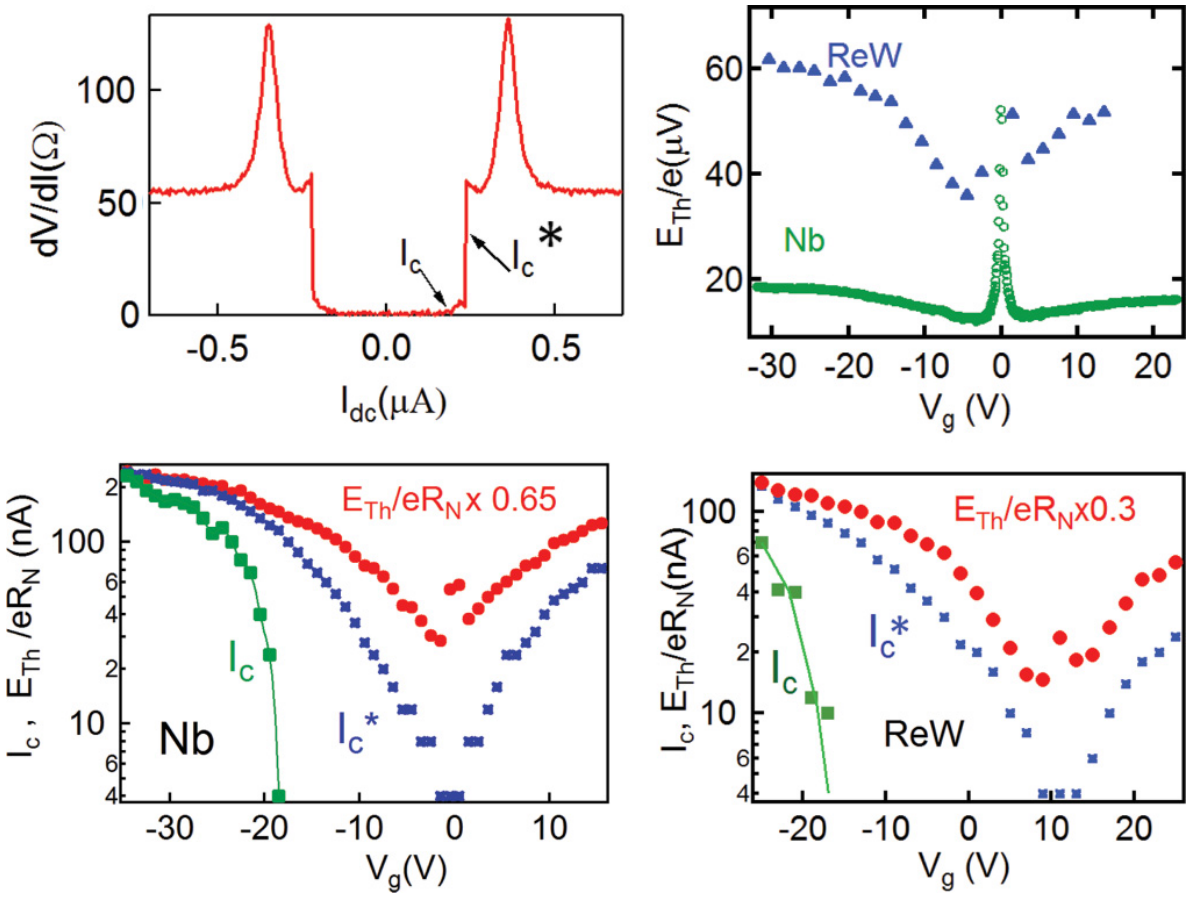

Figure 3.3.3: Comparison of switching current with Thouless energy. (Upper left) Two ways of defining the switching current: I_C, the largest current for which the differential resistance dV/dI is zero, and I_C^*, the inflection point of the jump in dV/dI towards large resistance. As the Dirac region is approached, the switching current Ic reaches zero but a steep resistance increase still occurs at I_C^*. (Upper right) Variations of the Thouless energy with gate voltage, deduced from the sample resistance in the normal state, for both samples. The resistance of the Nb sample was measured at 1 K. The resistance of the ReW sample was measured at 55 mK at a current bias above the critical current of the proximity effect. The factor 3 difference in Thouless energies is due to the different lengths of the two samples, 0.7 and 1.2 micrometers, which have similar diffusion constants. (Bottom) Comparison of Ic and I_C^* with E_{Th}/eR_N for the sample with Nb electrodes at 200 mK, and with ReW electrodes at 55 mK. Continuous lines are guides to show the fast decrease of I_C.

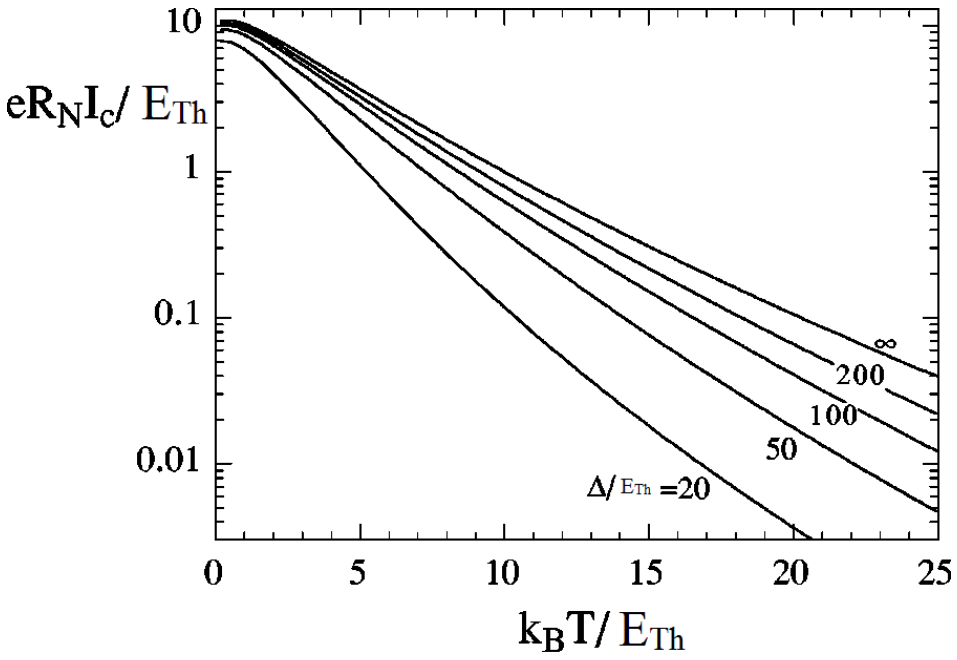

Figure 3.3.4: Simulation of temperature dependence of $R_N I_C$. For our samples, the ratio Δ/E_{Th} =100 and 25 in average. From Ref.[68]

.

temperature region (200mK is the max in our experiment), it is impossible to find a decay of factor 10 by just increasing the temperature.

In Figure.3.3.3, we plot together the theoretical value and measured value of I_C. The factor 0.26(for Nb sample) and 0.3(for ReW sample) which allows us to fit the curves in high doped regime, are more than 20 times smaller than expected. This reduced critical current is a feature noted in practically all experiments on S/graphene/S junction, and is attributed to partial transmission at the S/graphene interface. Also, we compare the critical current of short and long junctions in Fig.3.3.5.

To confirm and estimate the effect of interface, we measured the temperature dependence of the critical current(Fig.3.3.6.a), and the critical current decay with temperature is faster than expected for a perfect interface[111].

Generally, the critical current is always smaller than expected. However an additional feature is noticed in Fig.3.3.5: the critical current is suppressed near the DP in long junctions and not in short junctions. We attribute this suppression of supercurrent close to the CNP to specular reflection of an Andreev pair at the charge puddle contours, as sketched in Fig.3.3.7. In fact, near the DP there is a coexistence of electron-doped regime and hole-doped regime (n and p type doping regime). These regimes form a network of so-called puddles.[112] when the doping changes from electron to hole, at the boundaries, it is necessary to cross the 'zero doping' which is very close to the DP. When a counter-propagating electron-hole quasi-particles pair comes to the boundary which is Fermi en-

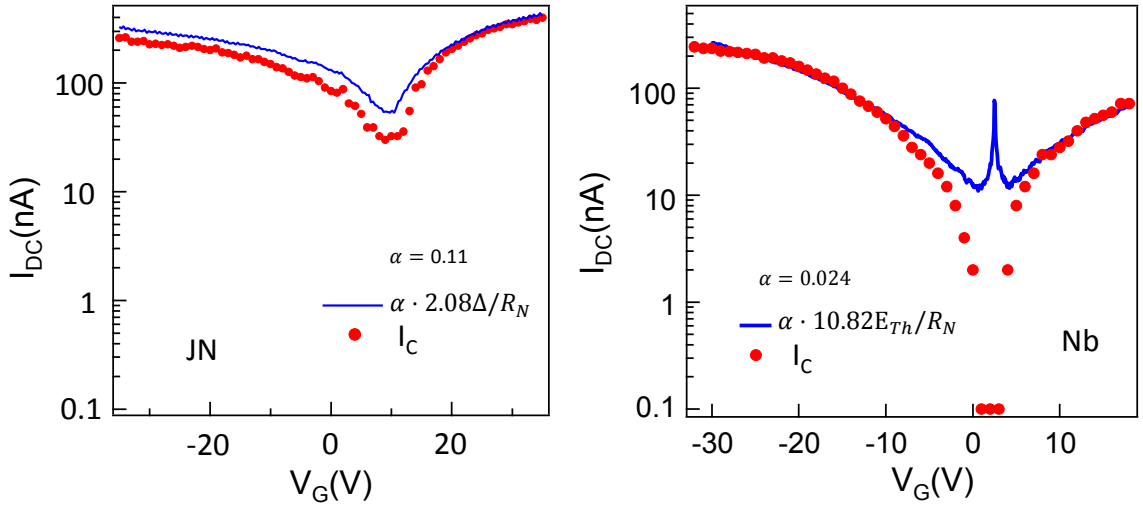

Figure 3.3.5: Theoretical and measured I_c of sample JN (Ti/Al) and sample Nb (Pd/Nb). (Left) JN sample is in the short/intermediate junction limit, (right) Nb sample is in the long junction limit. Both of them have a critical current smaller than expected. Nb sample has even an order smaller prefactor suggesting a stronger suppression of the critical current in long junction sample.

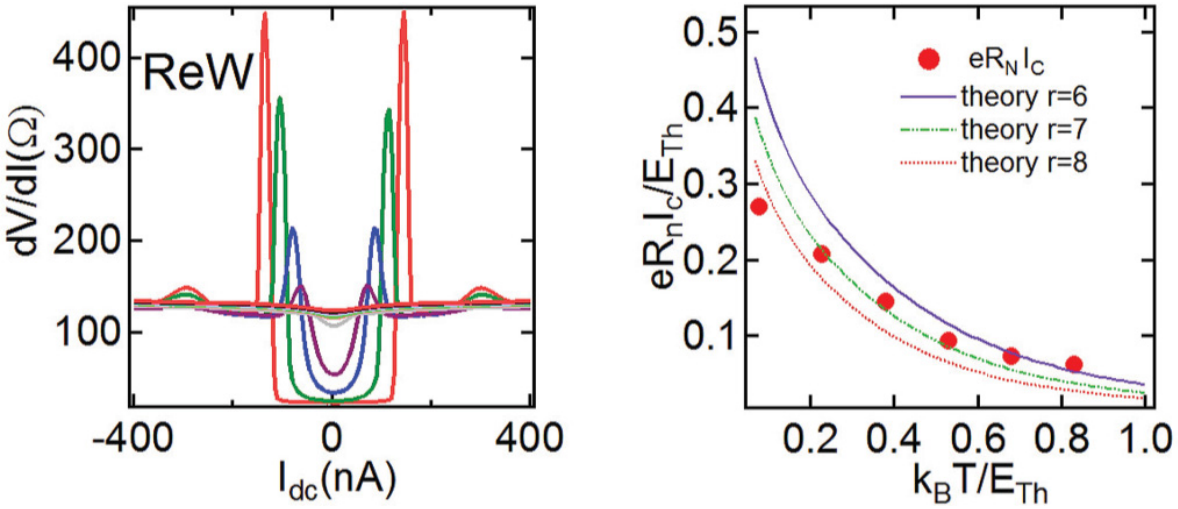

Figure 3.3.6: Temperature dependence of the proximity effect through the ReW sample. (Left) Differential resistance curves at temperatures ranging from 100 to 800 mK. (Right) Comparison of the extracted critical currents with the theoretically expected decay with temperature, for different ratios r of the contact resistance to the graphene sheet resistance. Both the overall suppression of the critical current with respect to the Thouless energy at low temperature, and the decay with temperature, are accounted for assuming a ratio r of roughly 7.

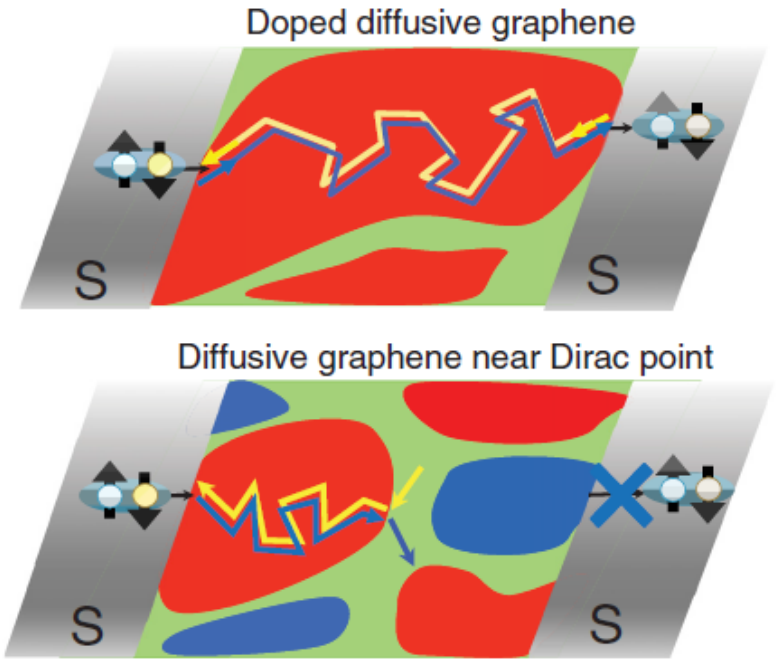

Figure 3.3.7: Sketch of the superconducting proximity effect through diffusive graphene, at high and low doping. (Top) Highly doped regime. The usual Andreev retroreflection at the S/G interface leads to diffusive counterpropagation with zero total phase accumulation. (Bottom) Low-doping regime.Specular Andreev reflection of propagating Andreev pairs can occur at an n/0 or p/0 junction, leading to loss of counterpropagation and thus large phase accumulation within an Andreev pair. Supercurrent, which results from all Andreev trajectories, is destroyed. The red region is electron doped, the blue one is hole doped, and the green region in between has zero doping ($E_F < E_{Th}$).

ergy is very close to the DP, the reflected (time reversal symmetrical) hole has to be converted into another band, and to change the velocity. This change in relative velocity between the electron-hole quasi-particles can destroy the counter propagation of the pair. It can make the two quasi-particles have different trajectories and increase the phase accumulation between these two quasi-particles in such way the destructive interference occurs. This supplementary phase accumulation can suppress easily the supercurrent through the sample. If we consider the size of the puddles, they are in general larger than the coherence length of pairs. This makes the supercurrent very sensitive to this effect.

3.3.3 Suppression of supercurrent by small magnetic field

These two samples have relatively large surface, but we still observed Fraunhofer pattern at low field. But the supercurrent is suppressed immediately after applying few Gauss. Fig.3.3.8 displays the differential resistance as a function of current for different magnetic fields, and shows that the supercurrent is suppressed in an oscillatory manner, as expected for wide proximity junctions[76].

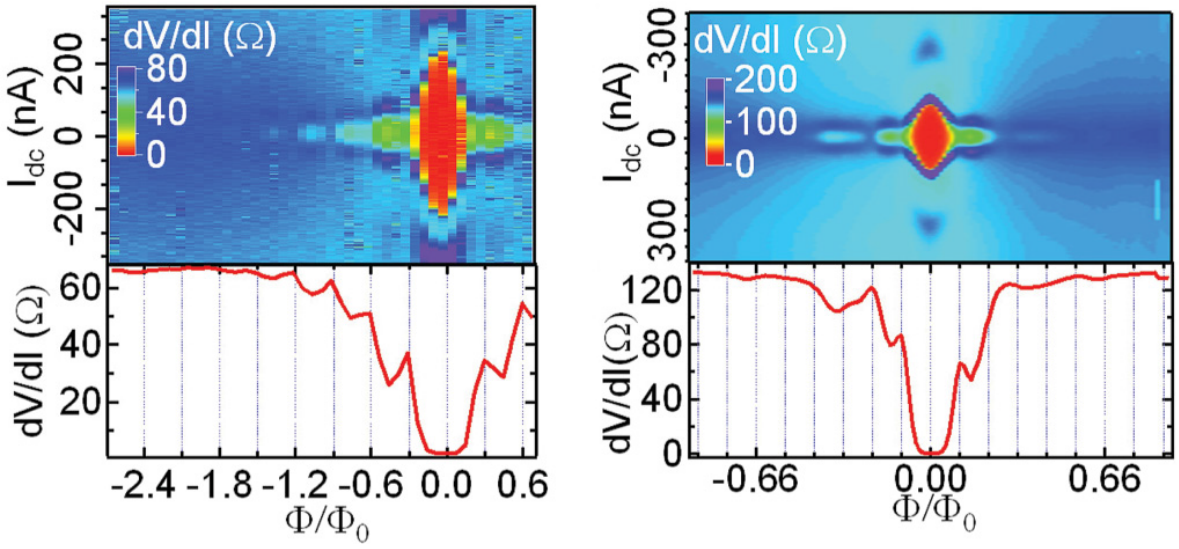

Figure 3.3.8: Low-field dependence of $dV/dI(I_{DC})$ for the sample with Nb (left) and ReW (right) electrodes, at T = 200 mK for Nb and 55 mK for ReW, and at high doping. (Bottom) Line traces of dV/dI at zero current bias as a function of magnetic flux through the graphene. We attribute the small period of the flux dependence to strong focusing of the magnetic field by the large superconducting electrodes.

However, the supercurrent is not recovered periodically,but rather the resistance oscillates away from zero in a periodic manner. We attribute the absence of full supercurrent recovery to the asymmetric (trapezoid-like) shape of the graphene samples, and to probable irregularities in the transmission between electrodes and graphene, which lead to inhomogeneous supercurrent densities[75]. The fact that the oscillation period is smaller than one flux quantum φ_o through the sample is attributed to the focusing effect of the field by the superconducting electrodes. Although the interference patterns look similar for both samples, one can notice an asymmetry in the field dependence of the sample with ReW electrodes, which we attribute to trapped flux in these high H_{c2} but low H_{c1} electrodes.

3.3.4 Junction under radio frequency irradiation

As also reported by others, the junctions display Shapiro steps, i.e., replica of the zero-resistance state, which appear at finite dc voltage,when submitted to radio frequency irradiation (via an antenna placed near the sample). This is shown in the top panel of Fig.3.3.9 for the sample with ReW electrodes at high doping that displays a full proximity effect with a critical current of 130 nA. What is more original is the observation of sequential nonlinearities in the I-V curves of the junctions at gate voltages such that a full proximity effect with a zero resistance state does not develop, demonstrating that nonlinearities in the I-V curve are sufficient to induce phase locking and replica of nonlinear features (bottom).

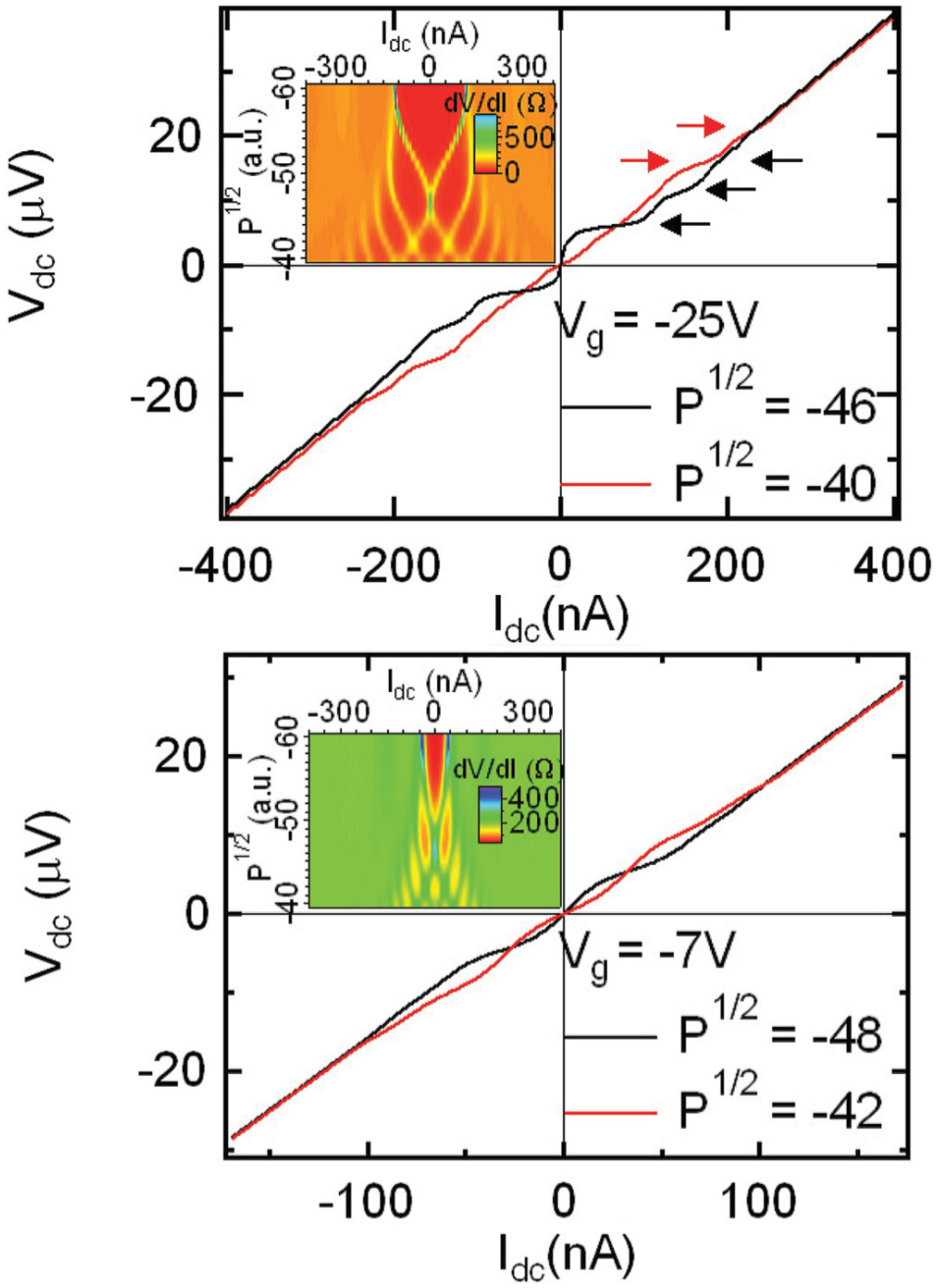

Figure 3.3.9: Effect of radio frequency irradiation on the junction with ReW electrodes. (Top) Junction under irradiation of 2.4 GHz, at a gate voltage of V g $= -25$V. (Bottom) Junction under irradiation of 2.4 GHz, at a gate voltage of $V_G = 7V$ for which no full proximity effect (supercurrent) is observed, but only a lower low-bias differential resistance.Nonetheless Shapiro-like features develop under irradiation. The insets display the rf power dependence of the proximity effect. The arrows point to the dc voltage plateaus, distant by $\Delta = 5.3\mu V$, close to the expected interval $\Delta V = \hbar\omega/2e = 4.9\mu V$.

3.4 Diffusive SGS junction from short junction to long junction limit

Our short junction and long junction samples show always a gate tunable supercurrent, consequently, with one sample, one can probe the relation between $R_N I_c$ product and E_{Th} in a tunable range of carrier density (instead of a point in usual metal).But since the capacitance model of gating is only correct away from the DP, we restrict the data to the doped region. In Fig.3.4.1, we show the global feature of all these samples in a normalized energy scale. Qualitatively, samples show a nice agreement with the theory: several samples with Ti/Al contacts have a Thouless energy of the same order as the superconducting gap ($E_{Th}/\Delta \approx 1$), one (sample PM) is in the short junction region. Their $R_N I_c$ products are mostly dominated by the gap. In the long junction region, Nb and ReW samples depend linearly on the Thouless energy with the rate close to the theory calculation (a =10.82). However, quantitatively, there seems to be a huge discrepancy with the theory: a factor 3-5 between the theory and experimental data for short junctions, and a factor 100 for long junctions.

To understand the unexpected reduction of $R_N I_c$ in long junctions, we address the imperfect transmission and thermal effect. As shown in Fig.3.3.6, the temperature dependence of critical current in the ReW samples give us a smaller effective Thouless energy E^*_{Th}: instead of $e^{-k_B T/4E_{Th}}$ exponential decrease, we have about 10 times fast decrease as $e^{-k_B T/0.4E_{Th}}$, and our effective Thouless energy E^*_{Th} was about 10 time less than E_{Th}. This is attributed to the non-perfect transmission at the G/contact interface. The effect is to both decrease the critical current I_c directly and the reduction in the mini-gap eventually to an effective Thouless energy E^*_{Th}. In this case, we can represent the theory curve by rescaling both in x and y axis (Fig.3.4.1 blue line).

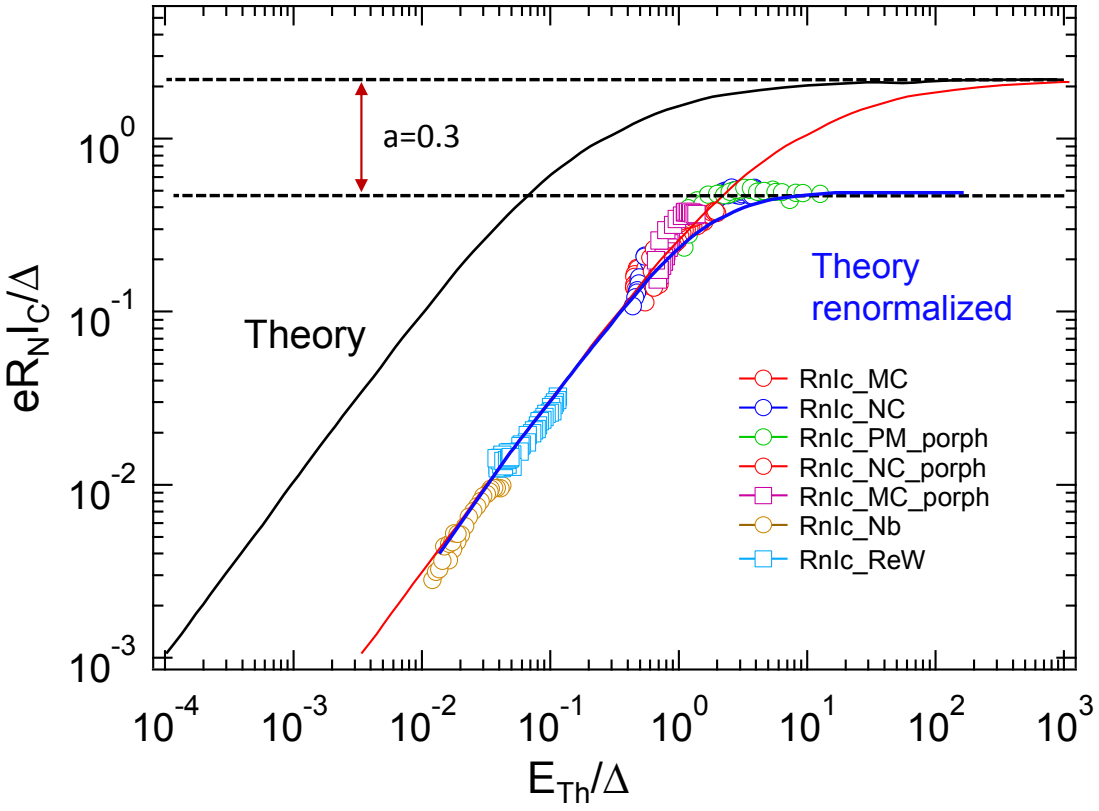

Figure 3.4.1: Normalized $R_N I_c - E_{Th}$ relation for SGS samples from short junction limit to long junction limit. Same color and shape dots correspond to a same sample. All of the $R_N I_c$ products are smaller than the theory curve (black) from a factor 3 to 100. Several samples present around $E_{Th}/\Delta \approxeq 1$, it implies that these samples are in the intermediate region and should behave like short junction. The shortest sample PM, which shows flat curve at doped region, is really in short junction limit. Nb and ReW samples depend linearly on E_{Th} with the same slope (the red curve is horizontal translation of the theory curve) in the long junction limit.

3.5 Proximity effect in the integer quantum Hall regime

The injection of Cooper pairs into quantum edge states is an issue addressing a lot attention, especially in topological systems. Quantum Hall effect provides the edge states in a 2 dimensional system, like graphene. Such a supercurrent would have to be carried by edge states, so that the time reversed electrons injected from the superconductor would be injected into the edge states at the opposite edges of the sample. One of the goals for this thesis is to probe the properties of superconducting proximity effect in Quantum Hall regime. It requires high critical field superconductors as the contacting materials. The best materials for electrodes to investigate the electronic properties in graphene are those that have both high T_C and high H_C , also good contact. The observation of supercurrent through graphene contacted to the high H_c superconductor ReW suggests the exciting possibility of observing a supercurrent through a conductor in the quantum Hall regime. Only few authors have considered this scenario theoretically[12, 113]. They have shown that in principle such a proximity effect is possible in the integer quantum Hall regime, with a maximal critical current given by the ballistic limit of ev_d/L, where L is the perimeter of the sample and v_d the drift velocity. In the following, we show that we achieve the quantum Hall regime in graphene with superconducting electrodes, and present elements that suggest the existence of coherent interference within the sample, modulated by magnetic field or gate voltage, hinting to a tunable proximity effect through graphene in the quantum Hall regime.

3.5.1 Half-integer quantum Hall effect in graphene

Fig. 3.5.1 shows the zero current differential resistance of the SGS junction as a function of gate voltage, for fields between 0 and 7.5 T, at low temperature (70 mK). The quantum Hall effect is visible, in form of plateaus, at fields above 5 T. Indeed, it has been shown that the quantum Hall regime is detectable in a two-wire measurement, in the form of regions in which the conductance is quantized at the Hall conductance value[114]. The exact shape of the conductance versus filling factor curve (i.e., whether peaks or dips separate the plateau regions) depends on the sample aspect ratio since the two wire resistance is a weighed combination of the sample's ρ_{xx} and ρ_{xy} Fig. 3.5.2 shows that the filling factors corresponding to the plateaus are those expected for graphene [$\nu = nh/(eB) = \pm 2, \pm 6, ...$], but that the values of the conductance plateaus are larger than those expected for graphene. We attribute this discrepancy to scattering, which broadens the Landau levels, and to sample inhomogeneities typical of wide graphene sheets, which change the plateaus conductance values, as has been observed by others[115]. The factor of roughly 2 in conductance enhancement could also be interpreted as due to two effective samples in parallel.

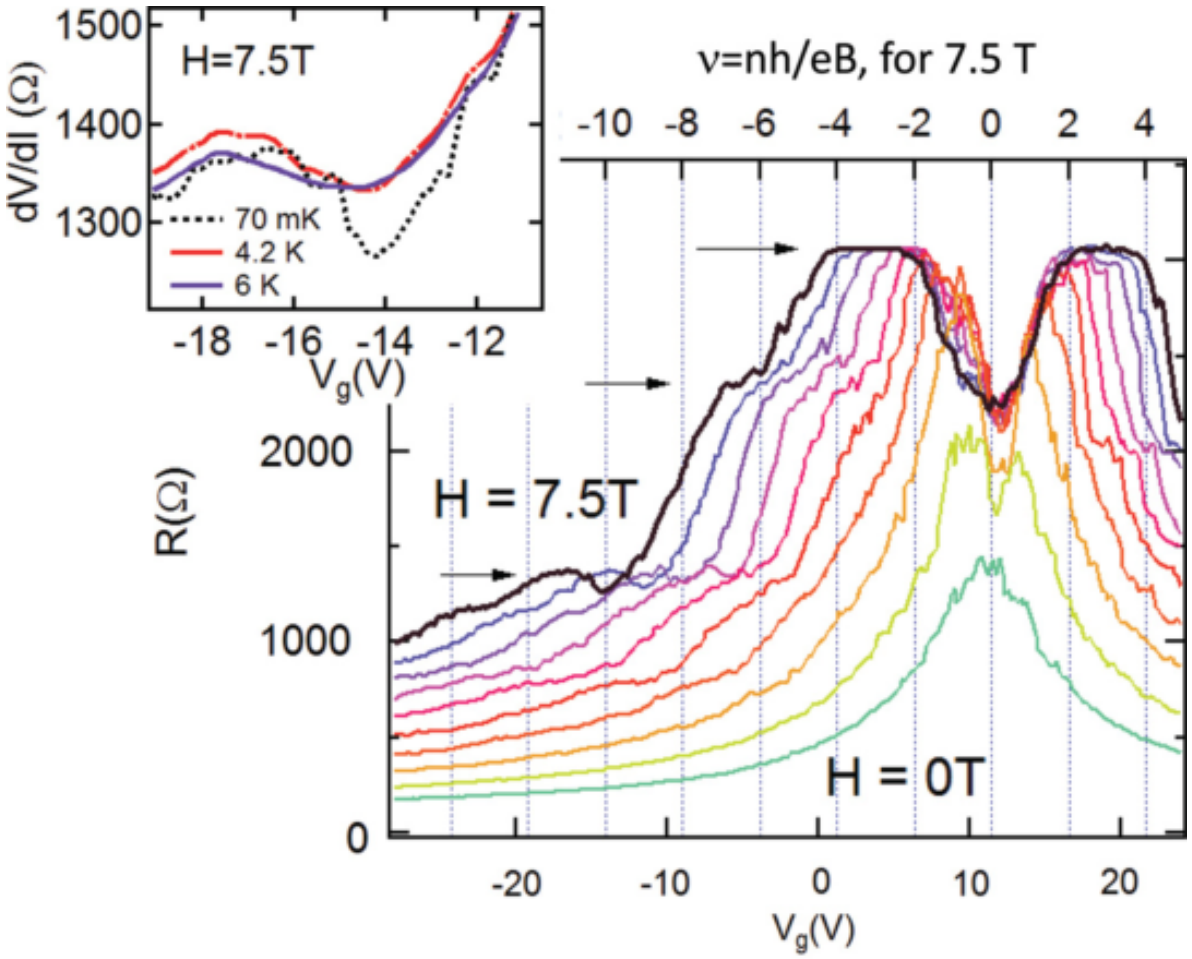

Figure 3.5.1: Two wire differential resistance as a function of gate voltage for the sample with ReW (H c $>$ 7.5T), at magnetic fields from 0 to 7.5 T, every Tesla between 0 and 5 T, and every 0.5 T above 5 T. Temperature is 70 mK. The inset displays how the Hall plateau at 7.5 T and $V_G = 14V$ flattens out as temperature is increased.

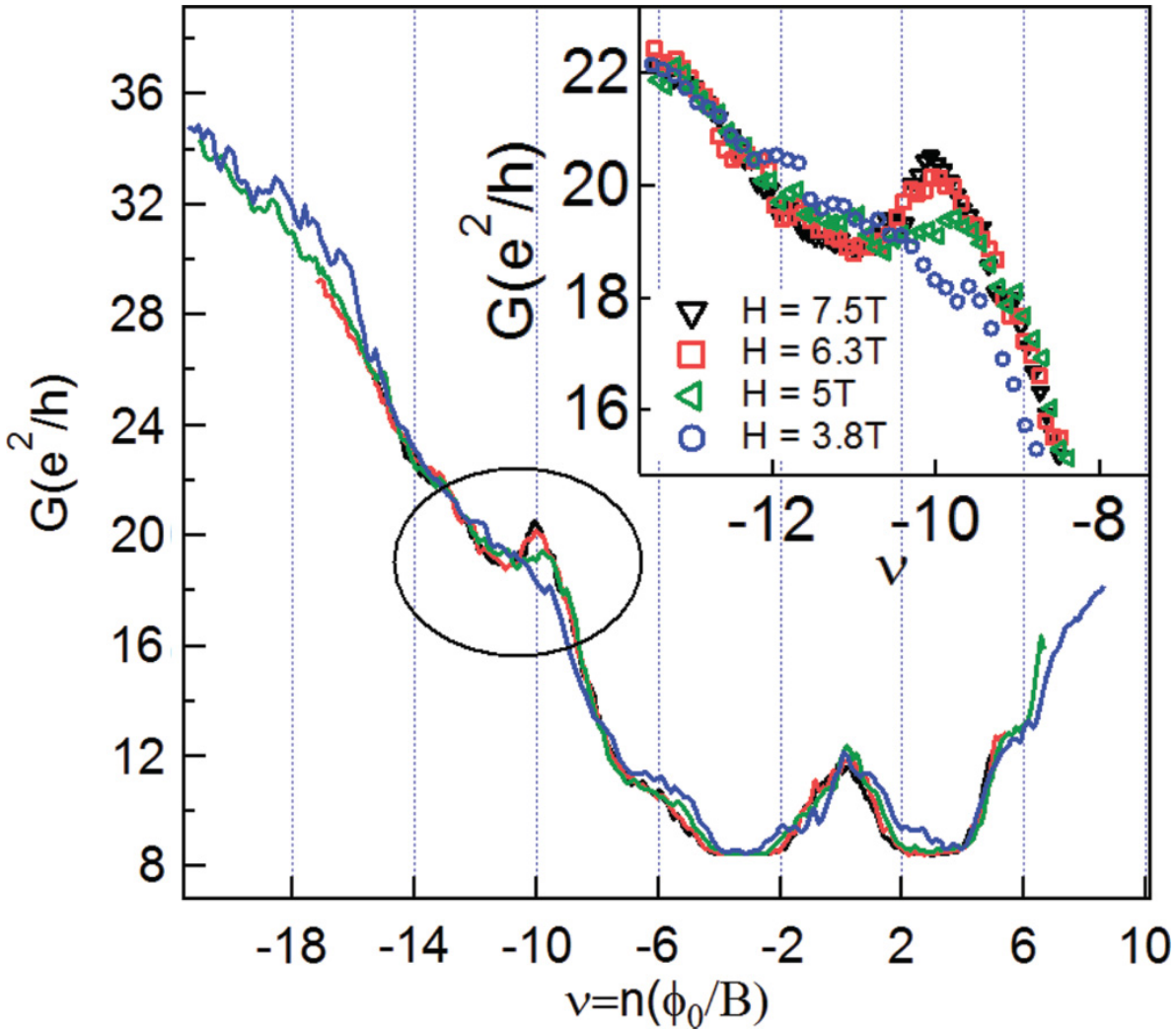

Figure 3.5.2: Quantum Hall effect of graphene sample with ReW electrodes, plotted as a function of filling factor $\nu = en/Bh$. Two-wire differential conductance as a function of filling factor in the quantum Hall regime. Inset: Zoom of the $\nu = -10$ region, which displays oscillations in conductance of up to 10% at the edge of the plateau

3.5.2 Proximity effect in the quantum Hall regime

We have seen in previous sections that the supercurrent is killed in a diffusive sample, with a field scale of one φ_0 in the sample area. So using a high H_c superconducting electrode seems vain. So even the high H_c ReW electrodes are superconducting up to more than 7.5 T (we found a critical current of 3.5μA at 7.5 T and low temperature, measured through slightly wider ReW leads, see Appendix), we couldn't expect a supercurrent in Quantum hall region.

What will be the signature? Especially measured in a two-wire configuration.

Some hints of the superconducting proximity effect can be found. We show below that we find signatures of the proximity effect both in the incoherent regime, where the S/graphene/S junction can be viewed as two uncorrelated S/graphene junctions in series, and in the coherent regime, where signatures of the coherent propagation of pairs through the graphene via quantum Hall edge states are visible.

The incoherent proximity effect is visible in the shape of the plateaus themselves. As shown in the inset of Fig. 3.5.1 for the $\nu = 10$ plateau, and also reported in AlGaAs/GaAs heterostructure connected to high H_{c2} NbN electrodes[14], the plateaus are far less flat at low temperature than at high temperature. The resistance at the transition between two Hall plateaus exhibits a non-monotonous variation with filling factor, with a decrease of resistance of up to ten percent. This amplitude variation of the resistance was interpreted in Ref.[14] as the effect of a change in conductance at an NS interface with respect to an NN interface as the edge channel transmission coefficient changes with filling factor. Analytical and numerical computations of the NS conductance in the specific case of the quantum Hall regime were considered in Refs. [116, 117]. They predict that the N/S conductance is not twice the NN conductance, in contrast to what one might naively expect for two electrons being transmitted via perfectly conducting edge channels at the quantum Hall plateau. This is because the two electrons of a pair must travel along different edges, much as in the normal case. However, interference effects at the N/S interfaces lead to a predicted oscillatory behavior around the quantized Hall conductance in Ref.[116]. When disorder at the interface is included, [117] the two-wire conductance is at most the quantized Hall value, in contrast to our experimental results and those of Ref. [14].

Signatures of a coherent proximity effect (i.e., a coherent propagation of pairs and a supercurrent) in the quantum Hall regime are visible when one exploits the nonlinearity of the reproducible fluctuations in the conductance (or resistance) as a function of magnetic field or gate voltage.These fluctuations, which stem from quantum interference between different diffusive trajectories, are known to be amplified in the case of superconducting contacts[118]. But in some instances, in this sample we find that the interference leads to a decrease of differential resistance around zero current, in contrast to the peaked differential resistance at zero current that is commonly observed in disordered samples at low temperature (due to electron-electron interactions or to the effect of the

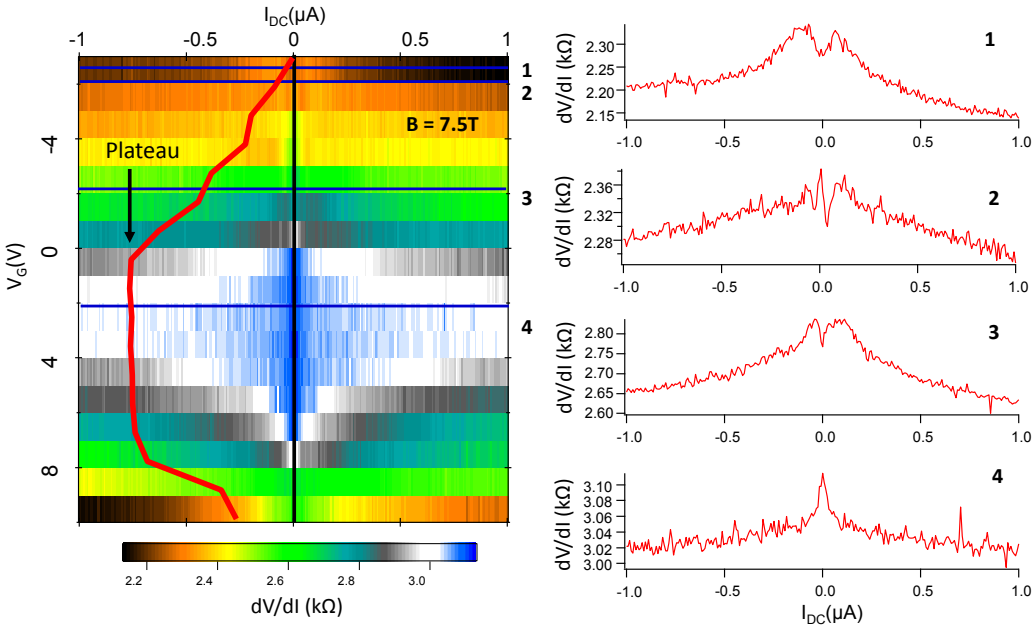

Figure 3.5.3: Differential resistance of ReW sample at 7.5T for different gate voltages. Left color-plot of $dV/dI(I_{DC}(nA))$ for different gate voltages (y axis). The red curve is the profile of the differential resistance at $I_{DC} = 0$. It shows the plateau of $\nu = 8$. Right: the profiles for the $dV/dI(I_{DC})$ curves at certain gate voltages (black lines).

electromagnetic environment)[119, 120]. Since in our two-wire geometry the quantized Hall resistivity adds to the zero longitudinal resistance of a supercurrent, we do not expect a zero two-wire resistance. But the signature of the supercurrent should be the differential resistance dip at zero bias. In addition, it was predicted in Ref.[12] that the supercurrent intensity should be modulated by the Fermi energy or the magnetic field, in an Aharonov-Bohm-like way, and, interestingly, we do observe alternating constructive and destructive interference, as a function of changing gate voltage or magnetic field, are demonstrated in Figs.3.5.3-. Similar features have been reported in 2D electron gases made in heterostructure in Ref. [13] with varying magnetic fields, but not gate voltages, and in samples in which no supercurrent was demonstrated at low field, in contrast to what we have achieved. In fact, we find that the dips in the differential resistance have an amplitude of up to 50Ω, and a current range of about 100nA, comparable to the critical current measured in zero field.

To be noticed that on the plateau(white region in the color plot of Fig.3.5.3), where the quantum Hall edge states are established, the dV/dI curves show robustly a peak at zero-bias. But when it is at the edge of plateau, where the Fermi level is almost aligned to one of the Landau levels, we can find some dips appear at zero-bias. This may be understood as a low possibility of the injection of Cooper pairs to a edge states in which the time reversal symmetry is broken for hole and electron, and the possible electron and hole channels for one Andreev pair are spatially separated. In contrast, more trajectories will be allowed if the Fermi level is exactly on one of the Landau levels.

3.6 Conclusion

We investigate the proximity effect in different S/G/S junctions from the short junction limit to the long junction limit. We show that the proximity effect can be even induced in a graphene junction up to 1.2 micrometers long. The relation between the eR_NI_c products and Thouless energy E_{Th} is in a large range. We find a strong suppression of the supercurrent near the charge neutrality point, and attribute it to the specular Andreev reflection specific to monolayer graphene, at the boundaries between p and n puddles. This effect is all the stronger that the superconducting coherence length is short and that the junction is long, since Andreev pairs cannot avoid these junction regions.

In the quantum Hall regime,a two-wire measurement cannot reveal directly a supercurrent carried by edge states. But we argue that the dip in differential resistance at zero current is a signature of the coherence due to the proximity effect. This interference is modulated by gate voltage and magnetic field, as expected theoretically. The question that needs to be addressed in the future is how to demonstrate that the coherent particles are circulating in the structure in the quantum Hall regime. Since a two-wire transport measurement necessarily displays nonzero resistance, one must find a different experimental configuration. In addition, it will be necessary to devise a method of distinguishing the dissipationless supercurrent from the dissipationless edge state transport. The detection of an orbital magnetic moment with a signature of pairs (via its field periodicity)[121] may be a route towards this fascinating goal.

4

Superconducting proximity effect in molecule grafted graphene

Graphene grafted with molecules

This section is devoted to the electronic properties of graphene grafted with Pt porphyrins. The initial motivation was to induce spin orbit interactions in graphene by the coupling of graphene's charge carriers with the heavy Pt atom in each of these molecules. These molecules are known to constitute ordered arrays on crystalline surfaces of metals such as Au, Cu as well as graphite and graphene. We first show (section 1) that the deposition of molecules does not create disorder in graphene in contrast with what happens with deposition of metallic atoms by Joule evaporation or sputtering. More surprisingly, when graphene is initially electron or hole doped, with a position of the Dirac point at finite gate voltage, we observe that after deposition of the molecules the Dirac point shifts to zero V_g. This means that porphyrins tend to neutralize graphene by exchanging charge carriers (either electron or holes) with graphene. This also increases the mobility of the functionalized samples. At room temperature we observe hysteresis and long time relaxation in the gate dependent resistance of graphene due to the small but finite conduction of the molecules. These effects completely disappear at low temperature.

Whereas clear signatures of the desired enhanced spin-orbit interactions where not yet detected

we found another interesting effect which is a strong gate dependent low temperature magnetism induced by the molecules. The porphyrin molecules when neutral are not magnetic but acquire, when ionized, a magnetic moment due to the existence of an unpaired electron delocalised through the molecule. We present low temperature magneto-transport measurement of several graphene samples showing evidence of an induced collective magnetism which depends on the gate voltage. We first discuss (section 2)samples with normal electrodes that exhibit at 1K an asymmetric magnetoresistance in perpendicular magnetic fields (not detected in uncoated samples). This asymmetry disappears at low temperature where on the other hand it shows up on the magneto-resistance measured in parallel field.

In section 3 we present data on samples with superconducting electrodes. The strong sensitivity of the Josephson effect to induced magnetism in graphene, provides a tool to detect signatures of gate dependent magnetism. The amplitude of the effects found, strongly depend on the length of the junction as well as the degree of initial ionization of graphene since it determines the spatial concentration of ionized thus magnetic porphyrins on graphene.

This gate dependent magnetism is attributed to a long range interaction between ionized molecules via the charge carriers in graphene.

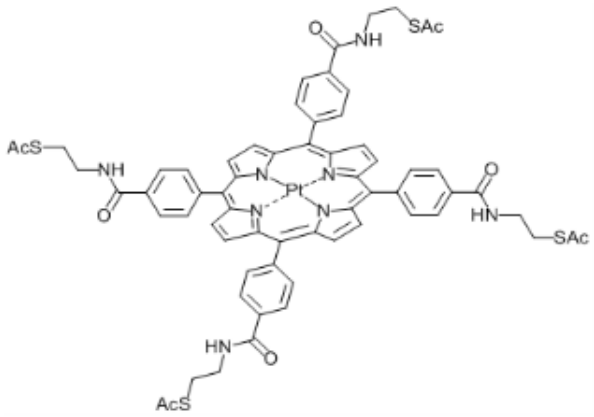

Figure 4.1.1: (left)Molecule of Pt-porphyrin. A Pt atom planted in the middle. (right) Solution of Pt-porphyrin in THF at room temperature.

4.1 Sample preparation

The graphene samples are prepared as explained in previous sections with several kinds of contacts, Ti/Au, Ti/Al and Pd/Nb. All samples were measured at room temperature before deposition of the molecules. Most of the samples with superconducting electrodes were also characterized at low temperature before deposition of the porphyrins.

The Pt-porphyrin (see figure 4.1.1) contains a Pt atom in the middle of the characteristic organic cage of porphyrins constituted by four pyrrole subunits interconnected via methine bridges (=CH−). They were prepared as follows by our colleagues Arianna FILORAMO and Stéphane Campidelli in Saclay (method described in Appendix A). The electronic structure of the porphyrins were determined from optical absorption measurements and Scanning Tunneling Spectroscopy. It is characterized by a HOMO (Highest occupied molecular Orbital) -LUMO (Lowest unoccupied molecular orbital)gap of the order of 2 eV.

We deposited Pt porphyrins on the already connected graphene samples at room temperature according to the following protocol. We dissolve a few milligrams of powder in a dry solution of tetrahydrofuran (THF). The solution is orange, depending on the concentration, it can vary from light to relatively dark. We have checked that deposition of the sole THF solvent tetrahydrofuran (THF) does not modify the gate voltage dependence of the sample's conductance. We then deposited a 10 µl drop of a 0.1 to 1 mM solution of Pt porphyrins in THF. This corresponds to a few hundred layers of porphyrins covering the graphene layer after evaporation of the THF solvent.

(See Fig.4.1.1)

A single drop of solution typically spreads on $2mm^2$ and completely covers the graphene which is already contacted by electrodes.

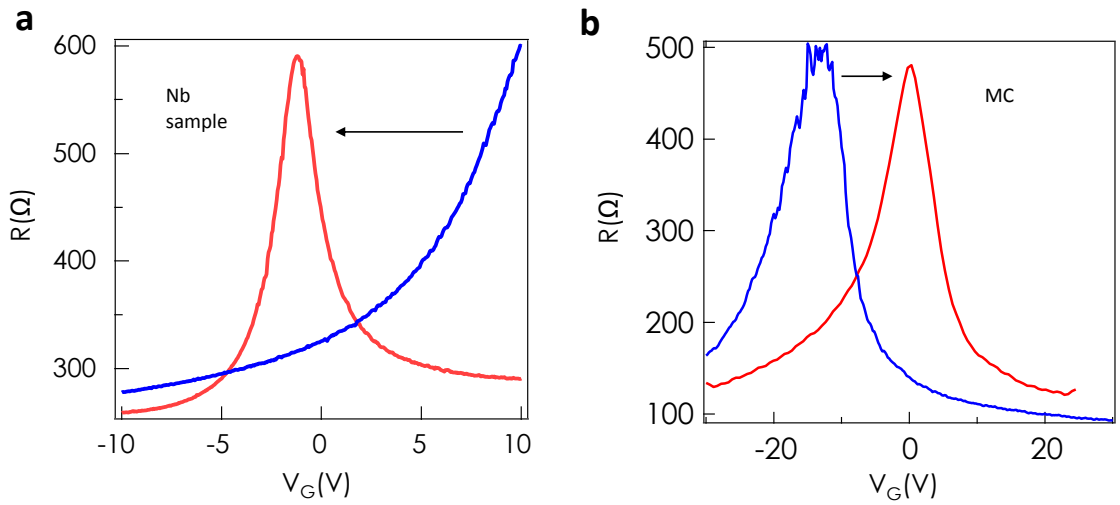

Figure 4.2.1: Gate dependence of resistance before and after the deposition of porphyrins for two samples, (a) Nb sample, (b) G92TiAl_MC. Without porphyrins (blue curves), the samples can be hole doped (a) and electron doped (b). After grafting porphyrins, in both case, the Dirac point of of graphene is brought to zero, graphene becomes neutral. This implies that charge transfer occurs between graphene and porphyrins and the molecules can be donors (a) as well as acceptors (b) of electrons.

4.2 Charge transfer between graphene and porphyrins: Neutralization of graphene by porphyrins

At room temperature, we systematically measure the gate voltage dependence of the resistance of the investigated graphene samples before and after deposition of porphyrins. A surprising neutralization effect is observed.

4.2.1 Charge transfer between graphene and porphyrins

The position of the Dirac point of all the samples is shifted to nearly zero (within 1V). Interestingly, no matter whether the sample is initially hole doped (a) or electron doped (b), porphyrins always bring them to a neutral state (see Fig.4.2.1). This means that charges are transferred between porphyrins and graphene. Porphyrins can, either, be donors or acceptors. Such effect has been reported for porphyrin-grafted carbon nanotubes[122, 123], and, more recently, for Zn-porphyrins grafted graphene[124]. STM experiments (in progress) will be useful to understand these charge transfers between the porphyrins and graphene.

At room temperature the gate dependence of the resistance is hysteretic, with slow exponential relaxation of the sample's resistance in response to a fast gate voltage change (Fig.4.2.2.a). We relate the RT hysteresis and slow relaxation to hopping processes through neighboring molecules[125, 53],

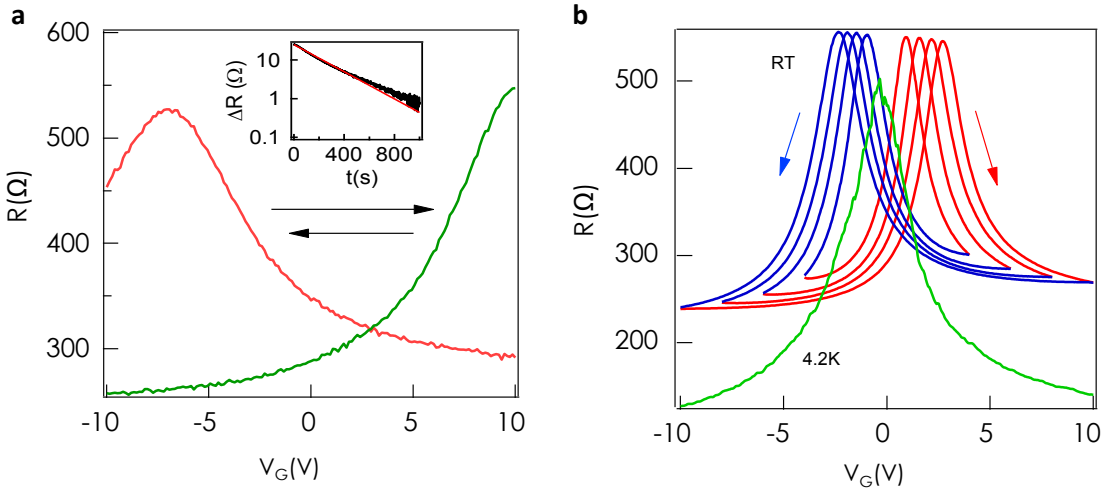

Figure 4.2.2: Hysteresis in gate dependence at room temperature (a) Modification of the Dirac point position after keeping the sample for one hour at $V_G = \pm 10V$. Inset: Time evolution of the sample resistance at fixed gate voltage after a rapid gate shift from -10 to +10 V . The slow relaxation can be fitted by $\Delta R = R_o e^{-t/t_o}$ with $R_o = 165\Omega$ and $t_o = 187$ s. (b)top curves, room temperature gate variations of the two-wire resistance for different gate voltage ramps with grafted porphyrins: the hysteresis increases with gate bias amplitude. Lower curve, gate voltage variation of two-wire resistance at 4.2 K. The hysteresis disappears at low temperature. The resistance decreases by 110 Ω at low temperature is due to the transition to the superconducting state of the Pd/Nb electrodes.

leading to a slow (hundred second time scale) charge transfer through neighboring porphyrin layers above the graphene. In contrast, we believe that a much faster charge transfer occurs between the graphene and the porphyrin molecules directly in contact with graphene. 4.2.2 (middle) illustrates how the Dirac point is shifted to $-V_o$ with a broadened gate dependence of resistance by keeping sample at a non-zero gate voltage V_o leads at room temperature. This phenomena can be seen as an indication of artificial doping of graphene temporarily by transferring and stoking the charges in the molecules.

We also find that cooling the sample at an applied zero gate voltage leads to a non zero-voltage Dirac peak at low temperature. But cooling the sample under zero gate voltage, the Dirac point stays unchanged at near zero gate voltage. At low temperature (4.2K) the hysteresis has disappeared (Fig. 4.2.2(b)), and there is no more charge transfer between porphyrins and graphene.

Another important property to be noted is that the gate dependence of resistance is much sharper after porphyrin deposition, with a higher resistance at the charge neutrality point (Dirac point) (see in Fig.4.2.3a the comparison at 4.2 K), implying that coating with Pt-porphyrins results in a higher sample quality: higher mobility, better homogeneity. The same consequences of Porphyrin deposition were measured on the samples with normal metal contacts, at room temperature and 4.2 K.

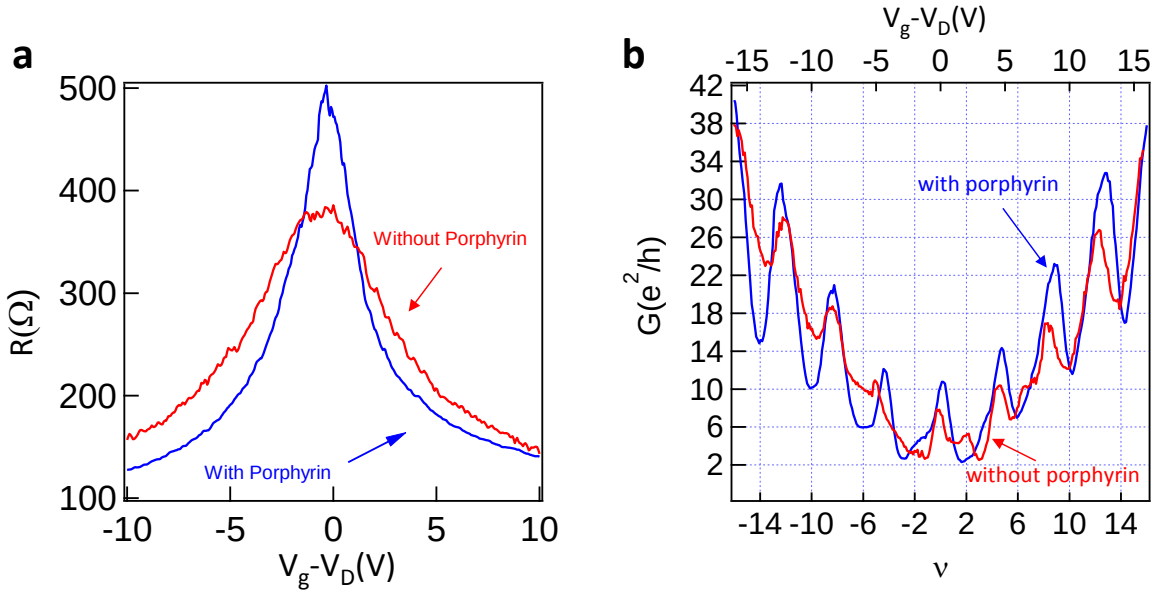

Figure 4.2.3: Improvement of the sample quality after porphyrin grafting. a: Zero magnetic field gate voltage sweep of two wire resistance at 4.2 K, before (red) and after (blue) deposition of the Pt-porphyrins. The origin is taken at the Dirac point V_D for both curves. The sharper curve with a higher Dirac peaks demonstrates that the sample quality has improved thanks to porphyrin coating, with a mobility increase of 20%. b: Quantum Hall regime at 100 mK and in a perpendicular magnetic field of B = 5 T (for which the Nb electrodes are non superconducting),before (red curve) and after (blue curve) grafting. The gate voltage is expressed in terms of the filling factor $\nu = n_c\varphi_o/B$, with the charge density n c computed assuming that only the backgate charges the graphene. The Hall plateaus are better defined, confirming the higher sample quality. The gate voltage position of the plateaus is unchanged, demonstrating that the charge transfer between porphyrins and graphene is gate independent, and fixed at low temperature.

These observations suggest that the deposited porphyrins tend to **neutralize** the charged scattering centers on the graphene surface, leading to a reduced scattering potential and an increased mobility (from $\mu = 8000$ to $10000 cm^2 V^{-1} s^1$ near the Dirac point, at $n_c = 1.6 \times 10^{15} m^2$, corresponding to $V_G = -2.5$ V , see Fig. 4.2.3.a. At high magnetic field the observation of the quantum Hall effect confirms the absence of gate dependent charge transfer between the molecules and graphene at low temperature. If one calculates the carrier density(n_c) with the same parameters as in the absence of porphyrins on the graphene sample (same capacitance,etc.), one can find the same value of filling factor as before.

4.3 Low temperature magneto-transport of functionalized samples with normal electrodes: asymmetry of the magnetoresistance

At low temperature and moderate magnetic field samples show curious responses to magnetic field. In both perpendicular or parallel field, depending on temperature, we find an hysterestic and asymmetric field dependence of resistance.

4.3.1 Perpendicular field $B_\perp$

We have investigated 3 independent graphene flakes with Ti/Au contacts (chip G58). Two (S1, S2) of them are grafted with porphyrins and another (S3) not. They were measured at same time, and we can compare the differences between them.

We observe that at 100 mK, the magnetoresistance in perpendicular field for all samples exhibit reproducible magneto-conductance fluctuations due to interferences between all the coherent trajectories across the samples. All the curves are even symmetric functions of magnetic field as expected for 2 probes measurements on a mesoscopic sample in the presence of time reversal symmetry (see Fig.4.3.1).

On the other hand, when we heat the samples to 1K, there is a clear difference between the samples with and without porphyrins(Fig. 4.3.2): an asymmetry in magnetoresistance appears for samples with porphyrins and not for the pristine graphene sample. We relate his asymmetry to the presence of a magnetic moment perpendicular to the plane of the sample as will be further discussed later on.

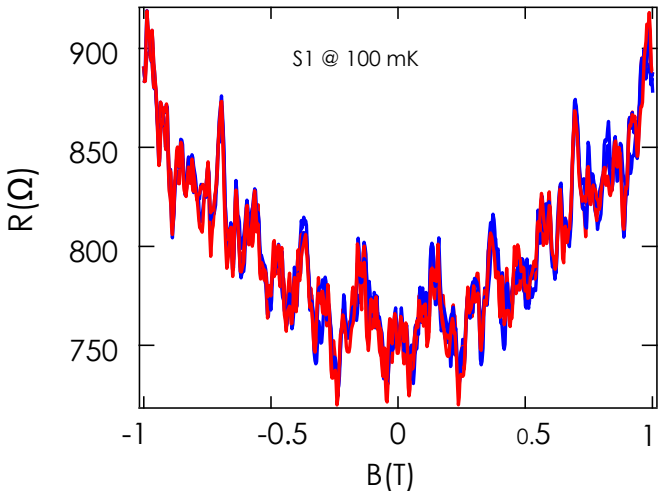

Figure 4.3.1: Symmetric magnetoresistance of S1 in perpendicular field. At low temperature(100 mK), the magnetoresistance to the perpendicular field is always symmetric around zero field. The up(red) and down(blue) curves are quite reproducible.

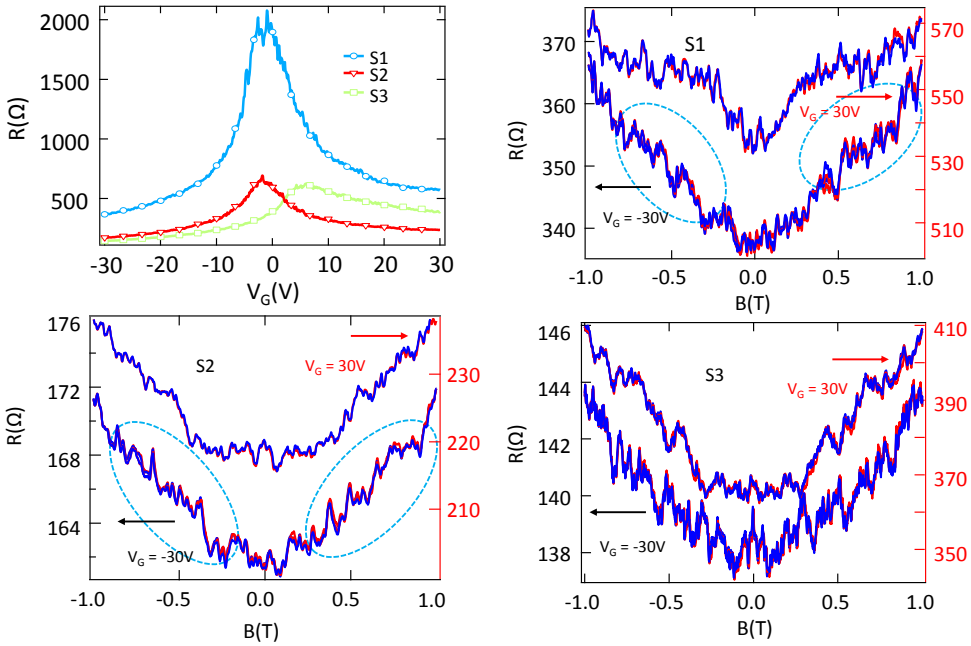

Figure 4.3.2: Asymmetric magnetoresistance in perpendicular field at 1K. (a) Field dependence of 3 graphene flakes of G58. (b) and (c): samples with porphyrins (S1, S2) show asymmetry in B⊥ at 1K.(d) In S3 the B⊥ is maintained. Dashed blue circles help to identify the asymmetries of the magnetoresistance in porphyrins grafted samples.

4.3.2 In plane field $B_{||}$

We have also studied the effect of a parallel field effect in these samples. (see Fig. 4.3.3). In samples with porphyrins (Fig. 4.3.3(a)), a gate dependent magnetoresistance in parallel field is found. This signal is an asymmetric function of magnetic field with a strong odd component which indicates the presence of a magnetic moment in the graphene plane in zero magnetic field. Interestingly, this magnetic moment is found to be strongly gate voltage dependent. Several up and down sweeping curves were taken to examine the reproducibility and possible hysteresis of the data. However, these curves are not so reproducible as in perpendicular field which makes it difficult to reveal a well defined hysteresis. Compared to these findings, in the sample without porphyrins (Fig. 4.3.3 (b)), the magnetoresistance is much smaller. This asymmetric magnetoresistance, cannot be detected any more at 1K where the grafted samples become very noisy. On the other hand, as shown above, the data measured in perpendicular magnetic field suggest that the initially in plane magnetic moment at 100mK can be rotated out of plane at 1K .

4.4 Samples with superconducting contacts

We now discuss the data obtained on samples with superconducting electrodes. The idea is to take advantage of the extreme sensitivity of the Josephson current to magnetism. Whereas only small effects are found in short junction we will see that more spectacular signatures for induced magnetism are found in long junctions.

4.4.1 Short junctions

We have investigated the Josephson effect in several samples connected to Ti/Al contacts before (see section proximity effect in pristine graphene)and after deposition of porphyrins. Our results are summarized in Fig.4.4.1 to Fig.4.4.4. We find that in spite of the important shift of the Dirac point (up to 15V) induced by the deposition of the porphyrins (Fig.4.2.1), the $R_N I_c$ product was only slightly modified as well as its gate voltage dependence as function of $V_g - V_D$ (Fig.4.4.1).

We also observed important gate voltage dependences on the Fraunhofer pattern with the presence of porphyrins (Fig.4.4.2). For a value of gate voltage equal to 4V (Fig.4.4.2.b) we observed that for the range of magnetic field corresponding to the first secondary lobe, the critical current is completely suppressed.

The determination of a full Fraunhofer pattern like in Fig.4.4.2 implies the measurement of the whole dV/dI characteristics for various values of magnetic field. The investigation of the detailed gate voltage dependence of such a Fraunhofer pattern is very much time consuming.This is why we focused on the resistance at zero dc current as shown in Fig.4.4.3. The field regions where this

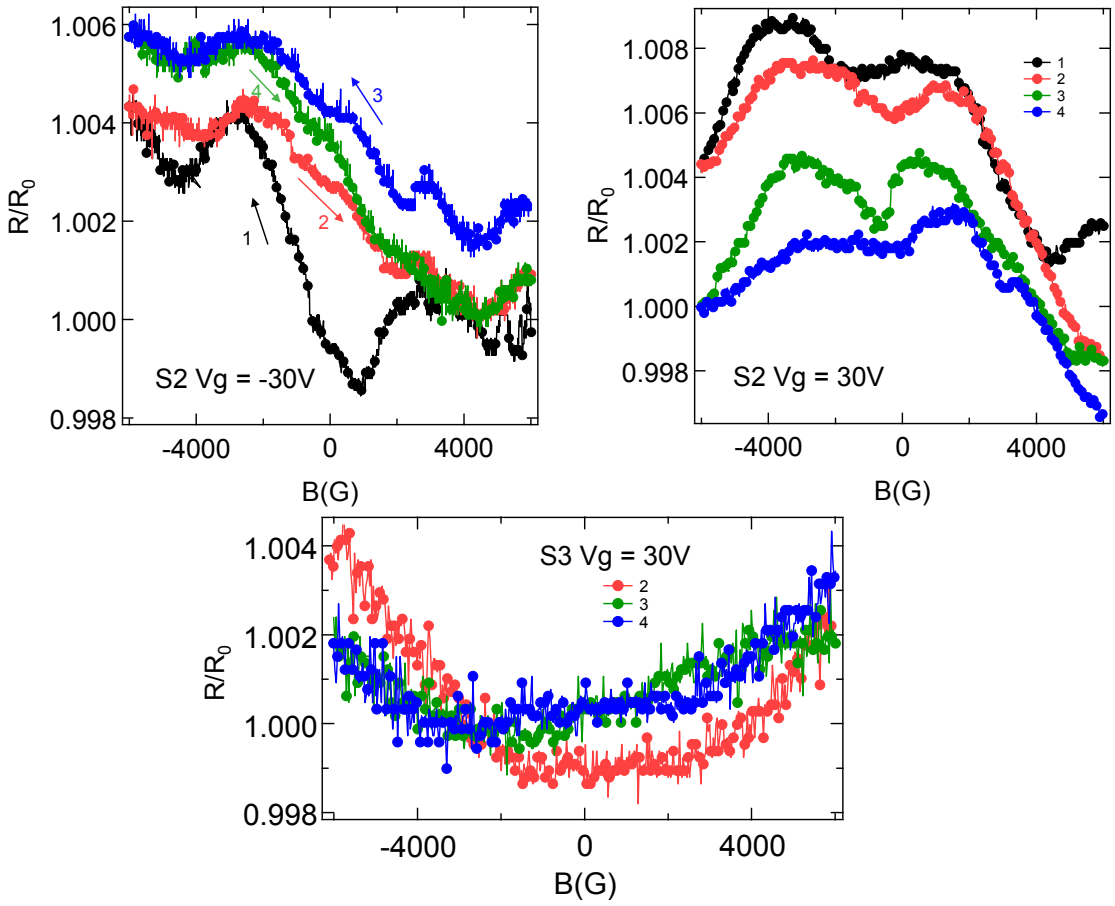

Figure 4.3.3: In plane field effect in sample G58. (a) Asymmetric magnetoresistance in parallel field for S2 (with porphyrins). The curves in different colors represent the sweeping order in magnetic field. (b) magnetoresistance in parallel field for S3 (without porphyrins).

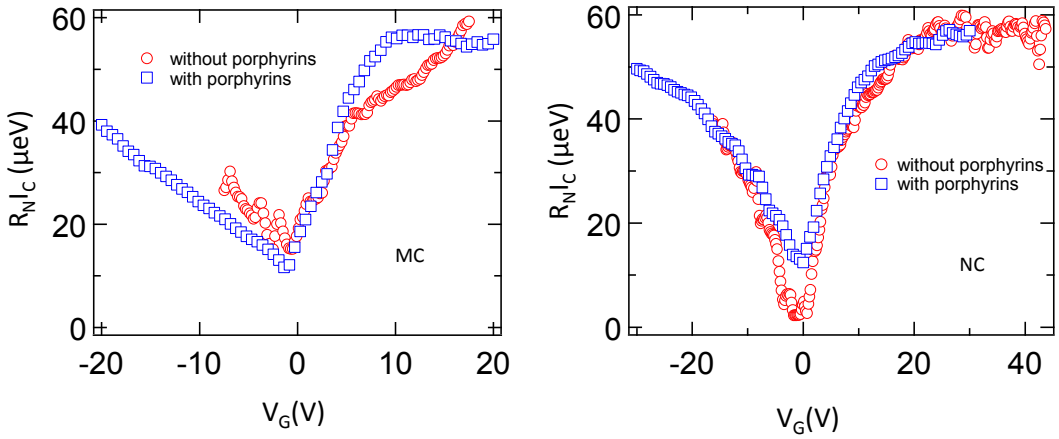

Figure 4.4.1: $R_N I_c$ product as function of V_G of sample MC (a) and NC (b) before (blue squares) and after (red circles) putting porphyrins. All the results are shifted to neutral point for comparison.

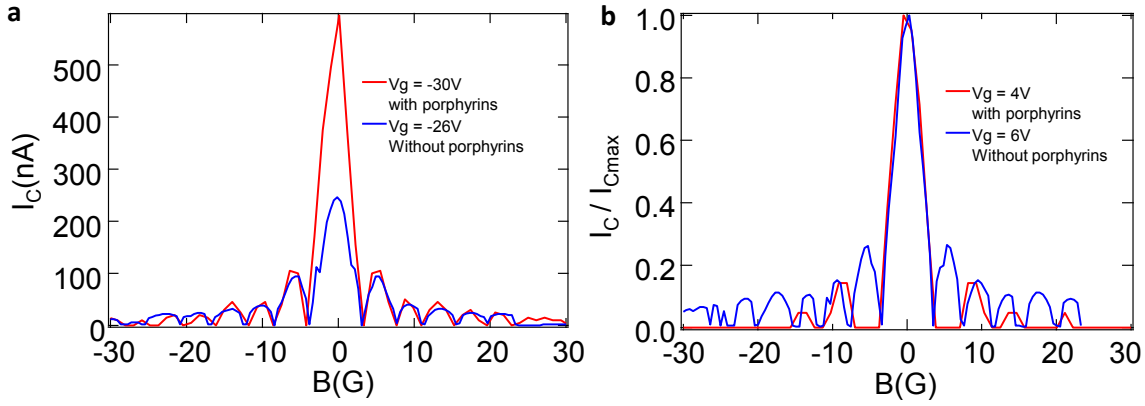

Figure 4.4.2: Fraunhofer pattern of sample MC before (blue) and after (red) grafting porphyrins at different gate voltages (a: negative values; b: positive values, normalized I_c/I_c^{max}). All the curves' minimum is shifted to zero.

resistance is zero corresponds to the lobes of the Fraunhofer pattern. We find that the width of the principal lobe depends on gate voltage and is wider in the hole doped region ($V_g < 0$) compared to the electron doped region ($V_g > 0$). This is illustrated by a strong asymmetry of the gate dependence of the differential resistance measured at 33.6 Gauss (Fig.4.4.3.c). From the color plot in Fig.4.4.3.a, we can also clearly identify a range of gate voltage between 3 and 10 V for which the resistance is finite in the domain of magnetic field corresponding to the first secondary lobe of the Fraunhofer pattern. This is consistent with the observation made at $V_g = 4V$ on the field dependence of the critical current. Since the Fraunhofer pattern is simply related to the Fourier transform of the supercurrent density through the sample [75], these results show that the deposition of porphyrins has induced gate voltage and field dependent supercurrent spatial inhomogeneities along the axis perpendicular to the current. The main effect could be attributed to the existence of inhomogeneous gate dependent magnetic regions in the sample but we cannot exclude a signature of spin orbit interactions. Even more, we measured the gate dependent critical current in different magnetic field. We show that the asymmetry of critical current in gate can be modulated by the field (Fig.4.4.4).

4.4.2 Investigation of a long junction sample

We have also deposited porphyrins on the sample described in previous section with Pd/Nb contacts. In contrast with previous samples in the short junction limit with a relatively large lobe in the Fraunhofer pattern in magnetic field scale and only slightly sensitive to the presence of magnetic moment in porphyrins, we find a much more spectacular effect in this much longer sample.

Unipolar supercurrent

Fig.4.4.5 compares the differential resistance (supercurrent) with gate voltage, around 100 mK, before and after deposition of the porphyrins. Before the deposition, the graphene junction has zero differential resistance at low dc current, in highly doped regions (away from the Dirac point), both for hole and electron doping (Fig.4.4.5.a): this is the signature of a Josephson effect. This we have discussed in previous chapter about the proximity effect in pristine graphene and we attribute the suppression of supercurrent near Dirac point to the specular Andreev reflexion on the charge puddles. Interestingly, after the deposition(Fig.4.4.5.b), in the hole doped region(negative gate voltage) the supercurrent is enhanced. But in the electron doped region(positive gate voltage), the supercurrent is strongly suppressed. Only a dip in the differential resistance is visible at low current bias and high positive gate voltage, but no strictly zero resistance. Fig.4.4.5 c, which displays the critical current amplitude as a function of gate voltage, shows how porphyrin deposition turns the behavior from bipolar to unipolar.

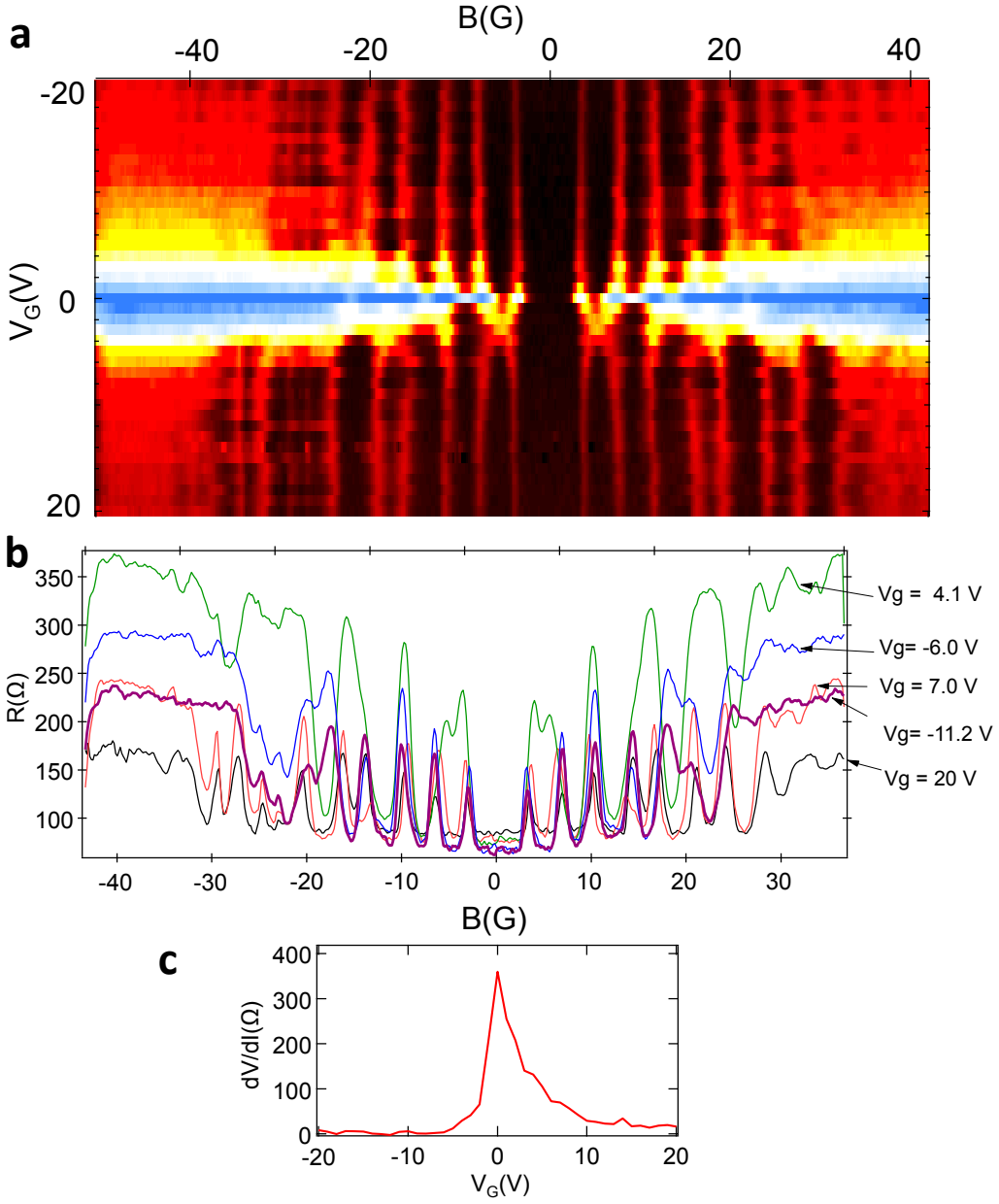

Figure 4.4.3: Gate dependent Fraunhofer pattern profile on sample MC with porphyrins.(a)dV/dI curve at each gate voltage between +20 V and -20 V. The color represents the value of the differential resistance. The dark regions correspond to zero resistance and finite supercurrent through the sample. (b) extraction of dV/dI curves at certain gate voltages. (c) A dV/dI(V_G) profile at 33.6 Gauss shows the asymmetry in gate dependent Fraunhofer pattern.

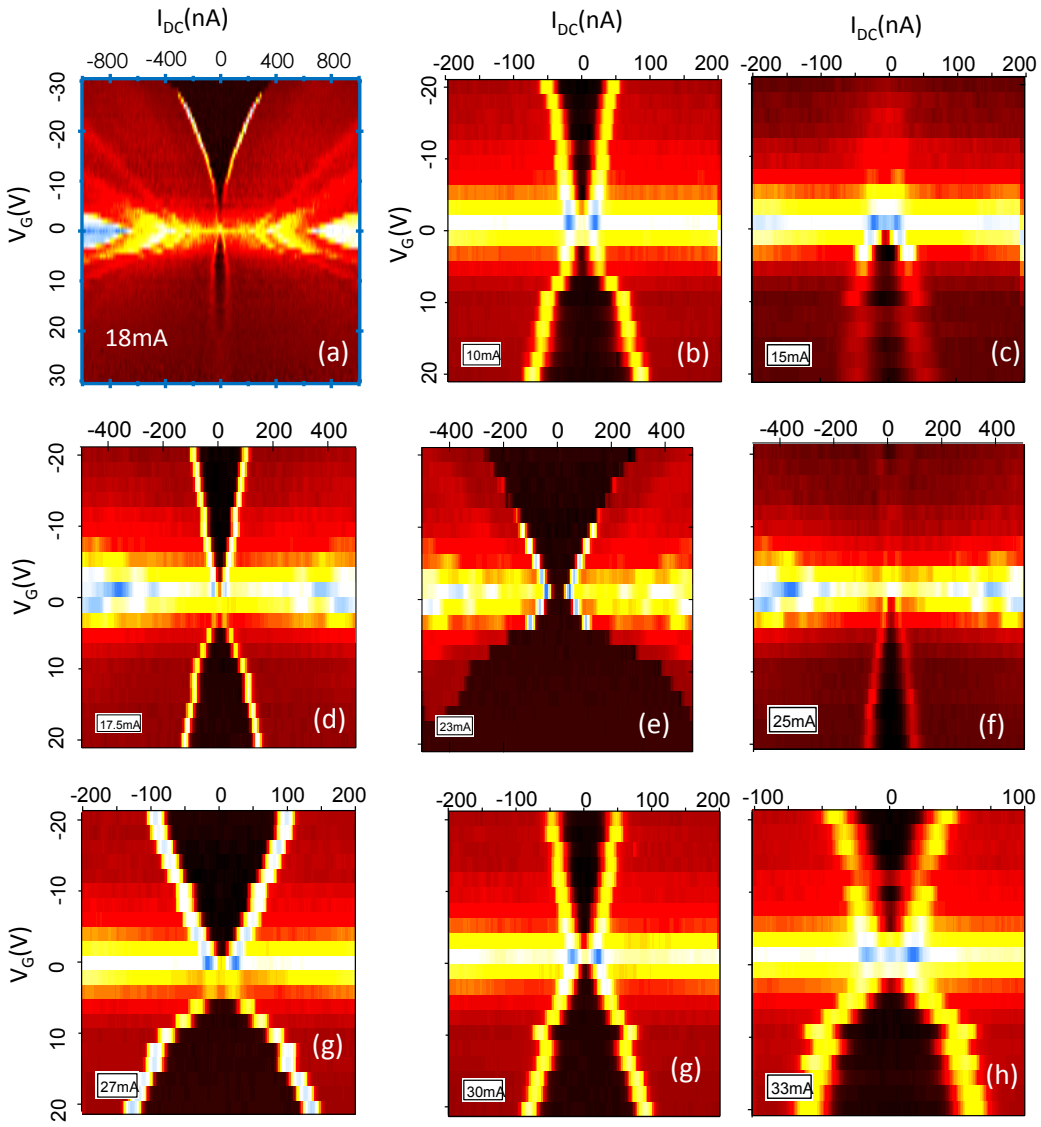

Figure 4.4.4: Gate dependent critical current of sample MC with porphyrins in different magnetic field(a) measured before increasing the field to 100G. A strong asymmetry in gate dependent critical current. (b-h) $I_c(V_G)$ for different field.

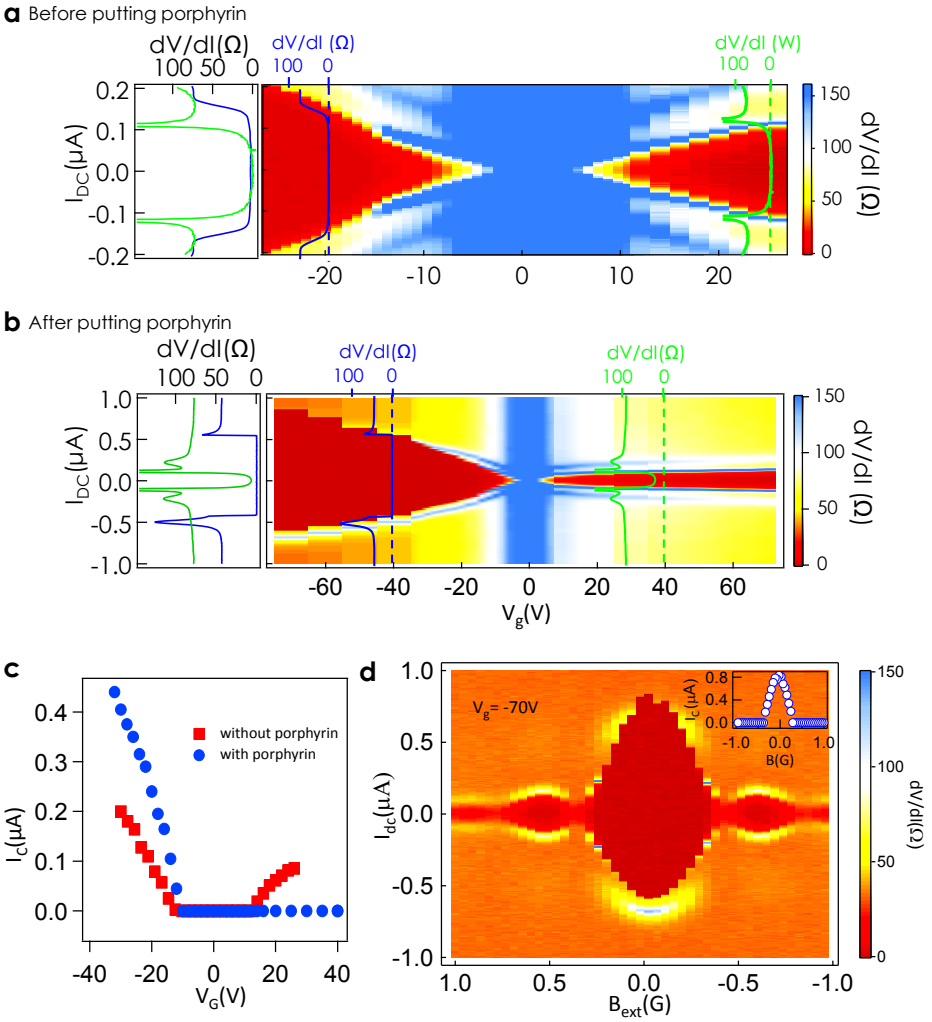

Figure 4.4.5: Change from bipolar to unipolar induced superconductivity upon deposition of Pt-porphyrin. Color-coded differential resistance as a function of dc current (x axis) and gate voltage (y axis), measured with a small ac current added to the dc current. The dark red regions correspond to regions of zero differential resistance where a Josephson supercurrent runs through the S/graphene/S junction. Whereas the Josephson effect occurs symmetrically on both sides of the Dirac point on the pristine, uncoated sample (**a**, T=200 mK), it only occurs on the hole doped side (negative V_G) on the sample covered with porphyrins (**b**, T = 100 mK). The curves on and to the left of the color plots are the differential resistance curves as a function of dc current, measured at gate voltages symmetric with respect the Dirac point. **c**: The change form bipolarity to unipolarity revealed by the variations with gate voltage of the critical current, i.e. highest dc current for which the differential resistance is zero, extracted from panels **a** and **b**. Before (red squares, bipolar) and after (blue circles, unipolar) porphyrin deposition. **d**: Differential resistance as a function of dc current and external magnetic field (applied perpendicular to the graphene sheet), for the graphene with porphyrin molecules, at $V_G = -70$ V. It is clear that a field as small as a fraction of a Gauss can suppress the induced supercurrent through graphene, because of destructive interference between Andreev pairs diffusing across the graphene. This explains how the porphyrin's magnetic spins, if they lead to magnetic domains at positive gate voltage, can create an inhomogeneous magnetic flux sufficient to destroy the proximity effect, thereby leading to a unipolar supercurrent

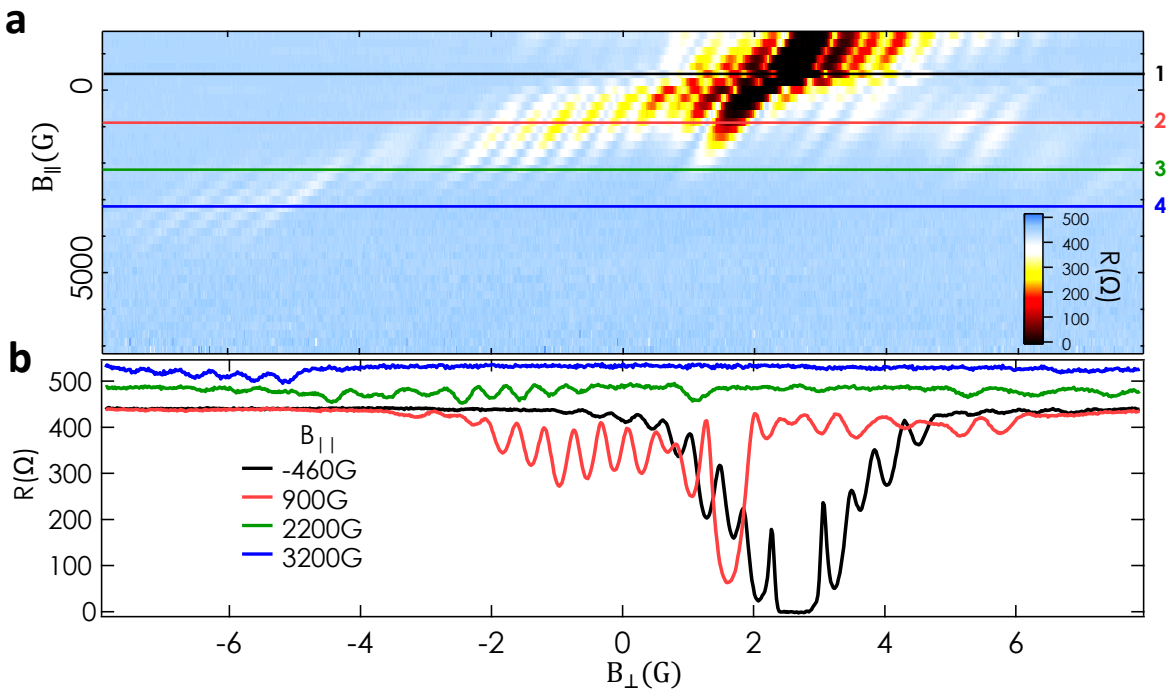

Figure 4.4.6: Full Fraunhofer pattern parallel field. (a): the color plot figure as function of perpendicular field(x axis) and parallel field(y axis). The whole feature is tilted due to the misalignment of parallel field which gives a perpendicular component. (b): the profiles magnetoresistance at low $B_\perp$ at different parallel fields. Different profiles are indicated in color plot figure with different colors. At high parallel field, an abnormal interference pattern arise at high perpendicular field rather than low field region.The blue and green curves are vertically shifted for clarity.

We also investigated the effect of a parallel field effect in the superconducting state. It yielded surprising results and puzzles.

In this sample with Nb electrodes, we measured the Fraunhofer pattern as a function of the perpendicular field $B_\perp$ for different values of parallel fields (See Fig. 4.4.6). The black region represents the interference pattern of supercurrent which is tilted due to the slight misalignment of parallel field coil. At $B_{||} \simeq 0$, the dependences of resistance with $B_\perp$ are symmetric with respect to B = 0 and we see clearly identify the central lobe region of supercurrent due to the Fraunhofer-like interference (Fig.4.4.6.b, black curve). However, when the $B_{||}$ is increased, some different features arise. At high parallel field (Fig.4.4.6.b, blue curve), in contrast with low $B_{||}$, the center lobe disappears, and high order interferences(in high $B_\perp$) appear yielding to SQUID like periodic fringes.

These features are very surprising and they strongly suggest that the in plane field enhances the higher order interferences. This may be related to the spin-orbit coupling.

Magnetoresistance in the normal state

In this sample we also find an electron-hole asymmetry in the magnetoresistance (with magnetic field perpendicular to the graphene plane), presented in Fig.4.4.7. As seen in Fig.4.4.7(b) and (d), the low temperature magnetoresistance is hysteretic at positive gate voltage (electron doping). This hysteresis decreases with increasing temperature and disappears above 6 K. In contrast, Fig.4.4.7.a and 4.4.7.c show that the hysteresis is at least an order of magnitude smaller at negative gate voltage (hole doping). All these experiments were done after cooling the sample through the superconducting transition in zero field, to avoid any contribution from the superconducting contacts. Such a contribution would anyhow be symmetric in gate voltage.

4.4.3 Highly doped samples

We now discuss the data obtained on initially strongly electron doped samples (chip G92) on Ti/Al contacts for which the Dirac point could not be detected down to $V_g = -40V$. This strong doping was the result of oxygen plasma cleaning of the oxidized Si substrate before deposition of graphene. (inset of Fig.4.4.8). Once we put the porphyrins, the position of the Dirac point of graphene was shifted to near zero despite the strong doping. These spectacular observations attest the huge capacity of charge transfer and neutralization of porphyrins. In this case, the porphyrins play a role of acceptor of electrons in order to neutralize these graphene samples initially doped with electrons. We expect a much concentration of ionized porphyrins in these samples compared to the ones discussed above where the Dirac point shift did not exceed 15 volts in gate voltage. The resistance at the Dirac point is quite large 40 $k\Omega$ which indicates a mobility at least 10 times smaller than for samples discussed above. As a result we estimate a Thouless energy of the order of $4\mu eV$ smaller than the gap o the contacts. The sample is in the long junction limit. We do not observe a critical current but only at most a 75% drop of differential resistance at zero bias at large electron or hole doping. The low field magnetoresistance was measured for different gate voltages. Whereas at large doping,the magnetoresistance curves exhibit a dip at zero field followed by oscillations characteristic of a Fraunhofer interference pattern, the magnetoresistance is clearly negative close to the Dirac point and exhibits jumps at well defined values of magnetic field. A large hysteresis is observed at all doping which indicates that the origin of this magnetoresistance is due to the formation of magnetic domains on the graphene sample. The magnetic response of these domains is more important when it is close to the Dirac point. It seems to indicate that it is favored by the presence of electron and hole puddles.

In Fig. 4.4.8 hysterestic magnetoresistance of one of these samples is shown. A significant hysteresis suggests a magnetic order is formed inside the samples probably induced by porphyrins since similar effect was not observed before putting the molecules.

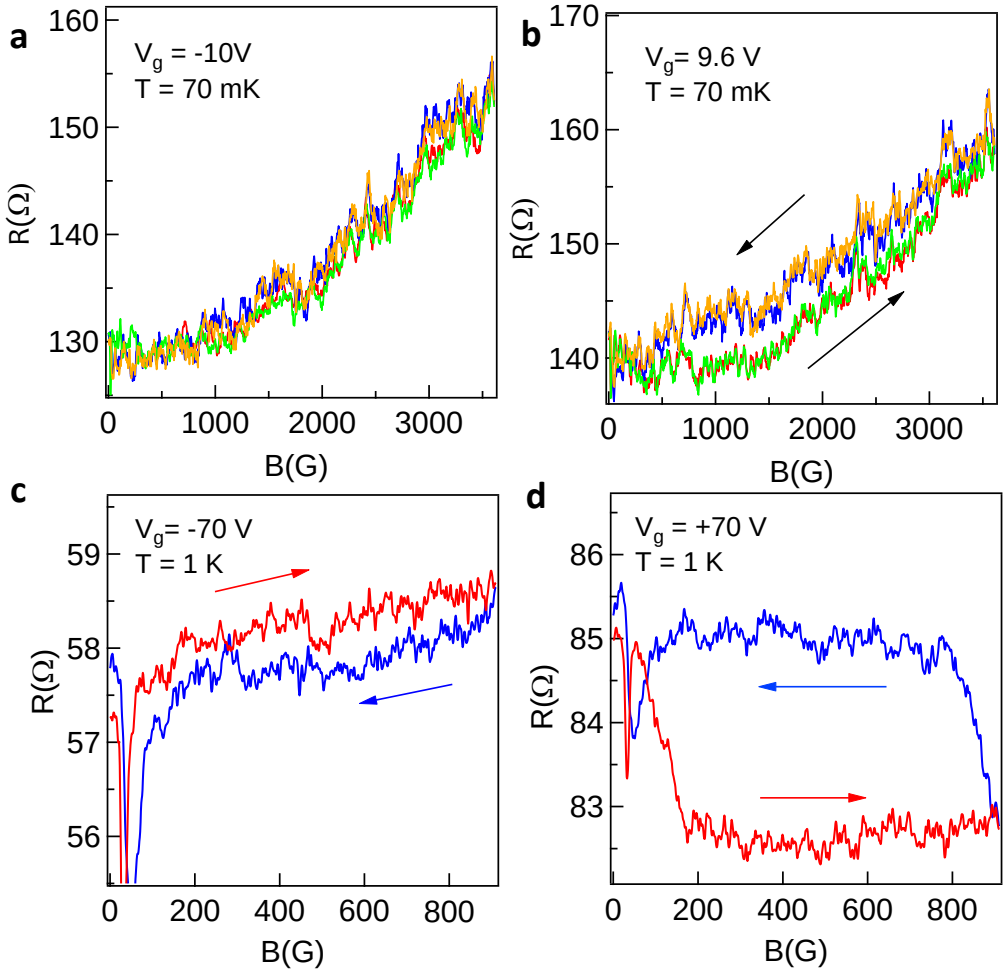

Figure 4.4.7: Unipolar hysteresis in the graphene's magnetoresistance after porphyrin deposition, at two temperatures, with a field direction perpendicular to the graphene plane. The hysteresis is quite large at positive gate voltage (electron doping, b and d) and negligible (at least an order of magnitude smaller) for hole doping (a and c),confirming the existence of a magnetic order that suppresses the supercurrent for electron doping. The anomalies at very low magnetic field correspond to the superconductivity of the contacts, and exist both in the electron and hole doped regions. The reproducible fluctuations at 100 mK are mesoscopic conductance fluctuations. Interestingly, the amplitude of these fluctuations does not depend on carrier type, implying that the magnetic spins do not suppress the superconducting proximity effect via a drastic decrease of phase coherence but rather because of the magnetic flux they induce.

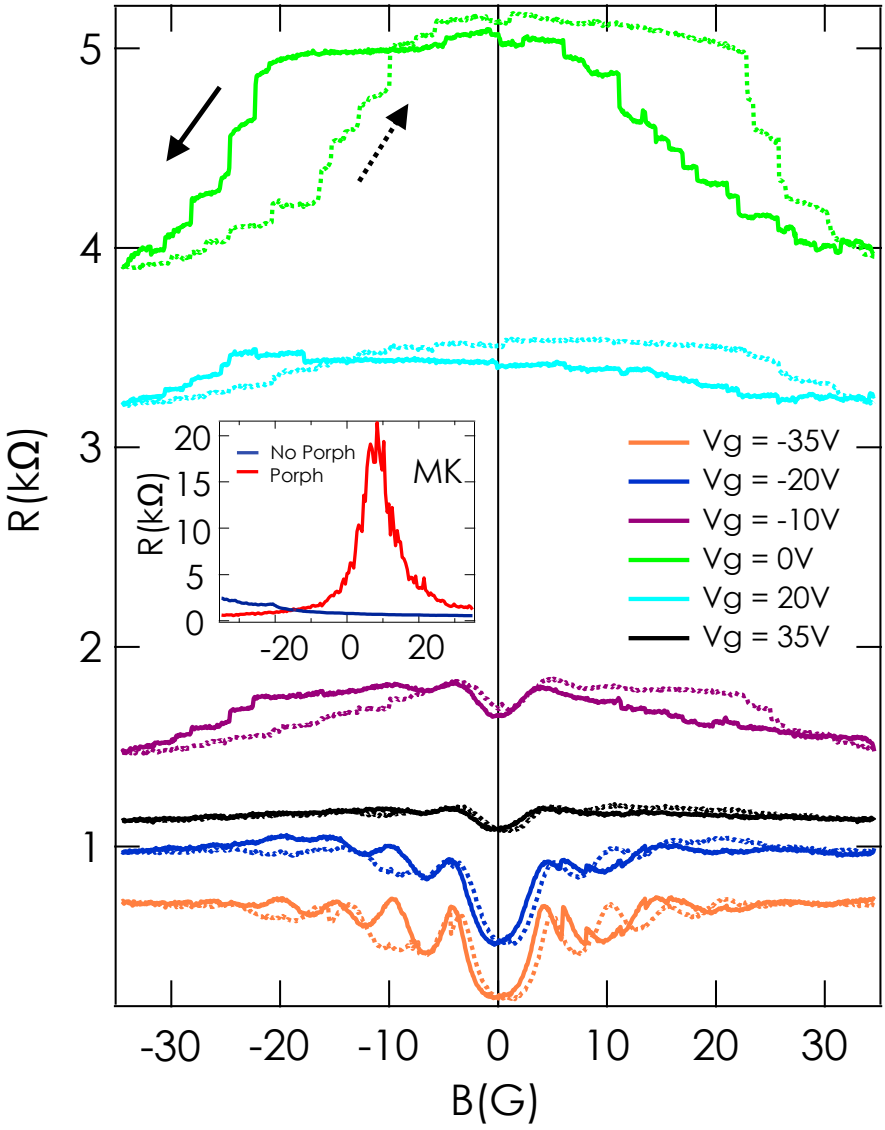

Figure 4.4.8: Hysterestic magnetoresistance of sample MK. The magnetoresistance is plotted with different colors for different gate voltages. Opposite order of magnetic field sweepings are distinguished by solid lines(down) and dashed lines (up) indicated by arrows. Inset: gate dependence before(blue) and after(red) putting porphyrins. The hysteresis is accompanied by plenty of jumps corresponding to the domains.

This enhanced magnetic effect is also observed by other group in iron-porphyrin[126] on pristine graphene with defects. Their studies show that the magnetic ordering between the molecular spins has been realized either by exchange coupling with the magnetic substrates(in their case Ni is used as substrate) or by externally applied magnetic field. And also the porphyrins has the tendency to localize on these defects.

4.5 Discussion

Magnetism of ionized porphyrin molecules

We attribute the doping-dependent hysteresis in magnetic field and the doping-dependent suppression of Josephson current, to the magnetism of the ionized porphyrin molecules. The absence of magnetic hysteresis and the large Josephson current in the hole doped region indicate either a quenched magnetic moment for the porphyrins or a reduced exchange interaction between porphyrin's localized spins and the graphene holes, compared to electrons. Moreover the magnetic hysteresis in the hole doped region points to the formation of a magnetic order of the molecular spins, with partially oriented magnetic domains, generating a non uniform magnetic field that is revealed by the magnetoresistance of graphene, and explains the suppressed Josephson current for this doping (see schematic feature in Fig.4.5.1). Indeed, as is shown in Fig.4.4.7d, the induced proximity effect is extremely sensitive to magnetic flux. A fraction of a flux quantum through the graphene sheet suppresses the supercurrent, by destructive interference amongst Andreev pairs [76]. Since the average distance between ionized porphyrins is a few nanometers, our findings suggest a relatively long ranged magnetic interaction mediated by graphene's conduction electrons or holes.

Gate dependent magnetism – RKKY interaction

The physics of magnetic impurities on graphene has led to a variety of interesting theoretical predictions specific to the band structure of graphene. Unlike metals, the exchange coupling in graphene is expected to be controlled by gating [36]. This effect has two important consequences. First, the amplitude of the magnetic moment of an individual impurity should strongly depend on gate voltage, causing a tunable Kondo effect. Depending on the relative energy of the impurity level with respect to the Dirac point, this Kondo effect could be strongly asymmetric with gate voltage [56]. Second, the long range magnetic Rudderman, Kittel, Kasuya,Yosida (RKKY) interactions mediated by the carriers should also be gate voltage dependent. Such interactions have been investigated theoretically and numerically by several groups[127, 128]. Characteristic coupling energies in the Kelvin range are predicted between spins 1/2 a few nanometers apart. The magnetic hysteresis we observe could then be explained by a spin glass type of order taking place at low temperature. It is how-

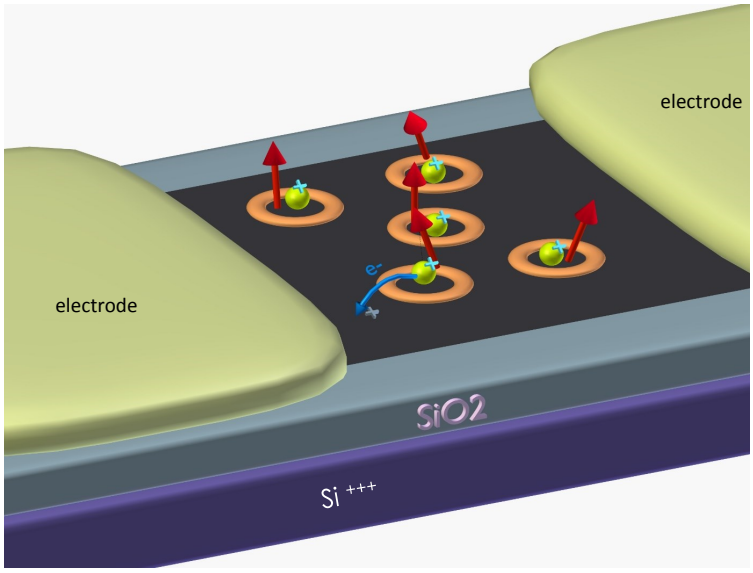

Figure 4.5.1: Schematic model for magnetism in ionized porphyrins.

ever not straight forward to extrapolate the theoretical RKKY coupling between localized spins on graphene to the situation of Pt-porphyrins, where each spin is delocalized over the entire nanometer sized molecule. This eventual spin glass order of magnetic porphyrins mediated by conduction electrons is of great potential interest and motivates further investigations of different porphyrin species, including metal free porphyrins or ones carrying a magnetic atom.

Electron–electron interaction: gate dependent magnetism in graphene

Adatom on graphene can form a local magnetic moment[56, 127]. The well-know Anderson impurity model describes an hybridization of an ion (with energy ε_0) with a conduction sea of electrons via a hopping term (energy V). The conductions have essentially constant density of states (DOS), thus the impurity ion is strongly interacting. If the $\varepsilon_0 + U$ (U is the Coulomb energy, which is the required energy of double occupancy of an energy level in the ion) is larger than Fermi energy (μ), a magnetic state is possible if U is sufficiently large and/or V is small.

Uchoa et al. calculated for the case of graphene with an adatom[56]. In Fig.4.5.2, it shows the boundary between magnetic and non-magnetic impurity states as a function of the parameters $x = D\Delta/U$ and $y = (\mu - \varepsilon_0)/U$ scaling both with the Coulomb energy U. $\Delta = \pi V^2/D^2$ is the dimensionless hybridization parameter and D is the band width of graphene, which is not important if $\mu \ll D$[129].

Clearly, when the chemical potential in graphene is tuned, the local impurities can be changed into magnetic or nonmagnetic states by the application of a gate voltage. The low density of states around the localized level also makes the formation of local moments in graphene much easier than

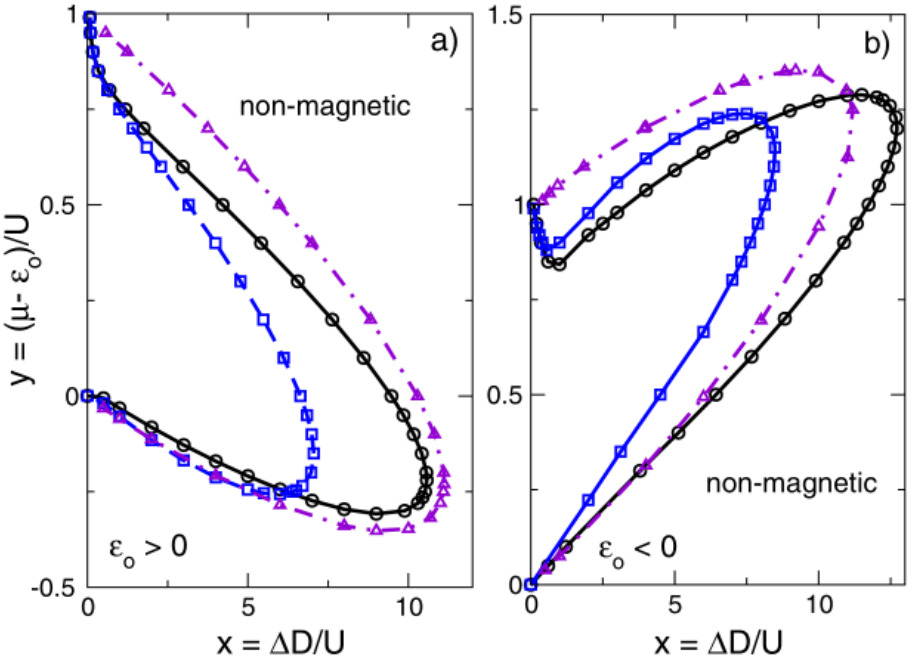

Figure 4.5.2: Boundary between magnetic and non magnetic impurity states in the scaling variables x and y for $\varepsilon_o > 0$ (a) and $\varepsilon_o < 0$ (b). Circles: $|\varepsilon_o|/D = 0.029$, $V/D = 0.14$; squares: $|\varepsilon_o|/D = 0.43$ and $V/D = 0.14$; triangles:$|\varepsilon_o|/D = 0.029$, $V/D = 0.03$. The upturn close to y = 1 and $x \to 0$ on panel (b) is not visible in this scale when V is very small (triangles). From Ref. [56]

in usual metallic hosts. As a result, the adatoms can achieve high magnetic moments at relatively small U[56].

4.6 Conclusion

We have shown that grafting Pt-porphyrins onto a mesoscopic graphene sheet leads to signatures of charge transfer, and that the deposited porphyrins tend to neutralize the charged scattering centers on the graphene surface. In addition, we have found that the Josephson current induced via Nb superconducting electrodes in a long junction is suppressed in the electron-doped region, but unaffected in the hole doped region. We attribute this suppression of the Josephson current to the formation of magnetic moments on the ionized porphyrins. This magnetism is also revealed by a sizable hysteretic magnetoresistance in the electron doped region, that is absent in the hole doped region. Both findings suggest a doping dependent exchange coupling between the localized magnetic moments of the porphyrins and the charge carriers in graphene, that can therefore be changed by gate voltage.

Also the in plane field in the graphene/porphyrins system has unexpected effect. For normal electrodes, a strong asymmetric and non reproducible magnetoresistance of parallel field suggests a complex molecules/graphene interaction system. The surprising high order interferences of quasiparticles in both high $B_\perp$ and $B_{||}$ may be the signature of the spin-orbit coupling induced by porphyrins.

5

Superconducting proximity effect in Bismuth nanowire

Proximity effect induced in strong spin-orbit coupling system is predicted to have much new physical phenomenas like the formation of Majorana Fermions, or triplet superconducting system. Many work has been done to determine the band structure in both bulk, surface state or even edge state. In this chapter, we will present the results of proximity effect in Bismuth nanowires which suggest that a SQUID structure is formed in S/Bi/S junction.

We investigate proximity induced superconductivity in micrometer-long bismuth nanowires connected to superconducting electrodes with a high critical field. At low temperature we measure a supercurrent that persists in magnetic fields as high as the critical field of the electrodes (above 11T). The critical current is also strongly modulated by the magnetic field. In certain samples we find regular, rapid SQUID-like periodic oscillations occurring up to high fields. Other samples exhibit less periodic but full modulations of the critical current on Tesla field scales, with field-caused extinctions of the supercurrent. These findings indicate the existence of low dimensionally, phase coherent, interfering conducting regions through the samples, with a subtle interplay between orbital and spin contributions. We relate these surprising results to the electronic properties of the surface states of bismuth, strong Rashba spin-orbit coupling, large effective g factors, and their ef-

fect on the induced superconducting correlations.

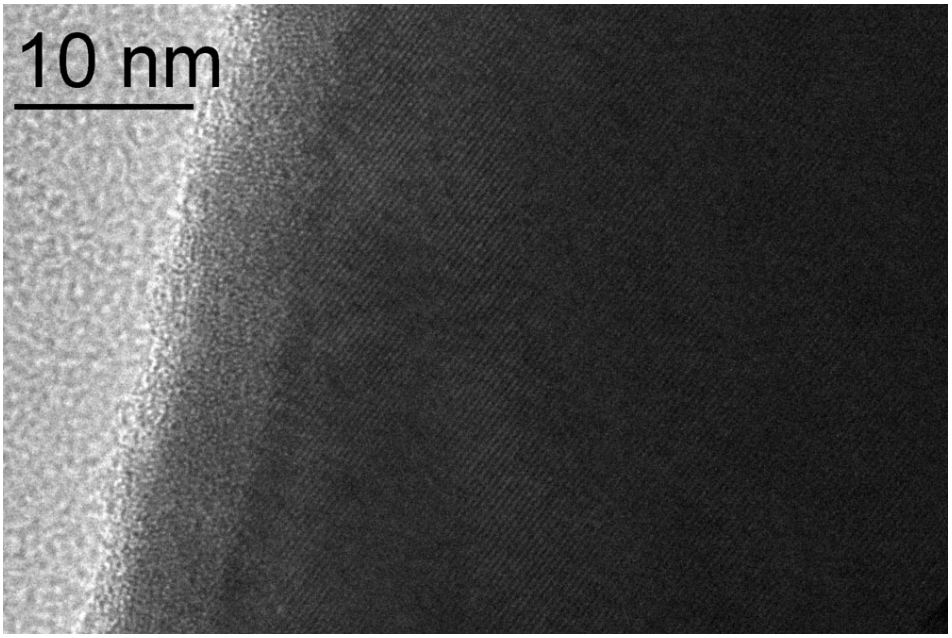

Figure 5.0.1: High resolution TEM image of a cavity-free region of Bi nanowire.

Samples description

Bi wires were grown from a solution prepared by dissolving 4.8 g $Bi(NO_3)_3{}^*5H_2O$ in 100 ml of water : ethylene glycol mixture (3:7 vol) (See the Append.A for more details). The high resolution TEM images (Fig.5.0.1) and diffraction patterns show that the nanowires are good quality single crystalline (See Append.A for more details).

Proximity induced superconductivity gives rise to a resistance decrease below the T c of the W electrodes in five samples out of ten. A supercurrent, corresponding to a zero resistant state, is detectable in three samples. Two other samples display only an incomplete proximity effect: the resistance drop is small (3% - 10%), and turns into a resistance increase (of about 10%) as the temperature is lowered further.

We will focus on the 3 samples with a detectable supercurrent, which are named as Bi_1, Bi_2,Bi_3. Also, later, the Bi_3 was cooled down to low temperature 3 times more for different orientations relative to the field. We change its name to Bi_3^* because its room temperature resistance had increased to $27k\Omega$, may due to the a worsening of the contact to the W electrodes.

5.1 Proximity effect in Bismuth nanowire at zero field

At low temperature(100mK in our experiments), the resistance is dominated by the two probes resistance of the Bi nanowires. This two wire resistance of wires of similar length and width ranges

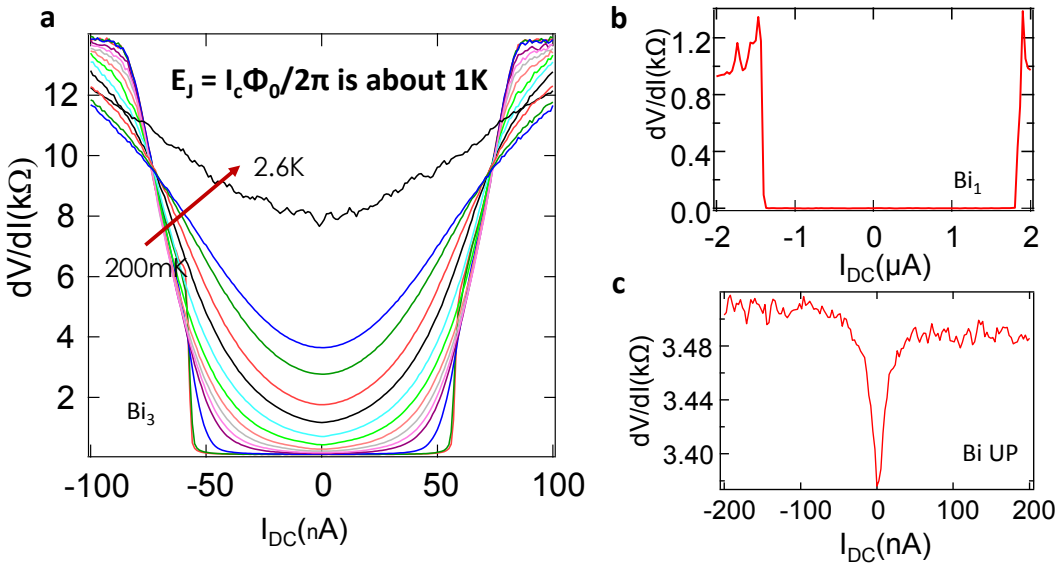

Figure 5.1.1: dV/dI vs DC current at Low temperature zero field (a) and (b) both show a supercurrent at low current (zero differential resistance) of Bi_3 and Bi_1. (c) incomplete superconducting proximity effect in sample UP. Instead of decreasing to zero, the differential resistance shows a small dip at zero energy.

Table 5.1.1: summary of the $R_N I_c$ products values and the length of samples.

	Bi_1	Bi_2	Bi_3
R_N	0.9kΩ	10kΩ	15kΩ
I_C	1.7μA	140 nA	70nA
eR_NI_C	1.53meV	1.4 meV	1.05meV
length	1.9μm	2μm	1.6μm

from 1 to 30 $k\Omega$, indicating that the resistance of the wire/contact interface dominates. This is compatible with an intrinsic resistance of the Bi wires of only a few hundred Ohms, estimated by extrapolating reports on much longer wires of similar diameters[34].

5.1.1 SUPERCURRENT AT ZERO FIELD

The supercurrent in three samples is detected at low temperature(Fig.5.1.1). It varies between 100nA and few μA depending on the normal resistance and the contact.

In Tab.5.1.1 we compare the normal resistance and critical current of different samples.

The $R_N I_c$ product ranges from 1meV to 1.56meV the same magnitude as the superconducting gap of the W wires. This is consistent with what is expected for short Josephson SNS junctions with an induced gap of the order of the gap of the electrode.

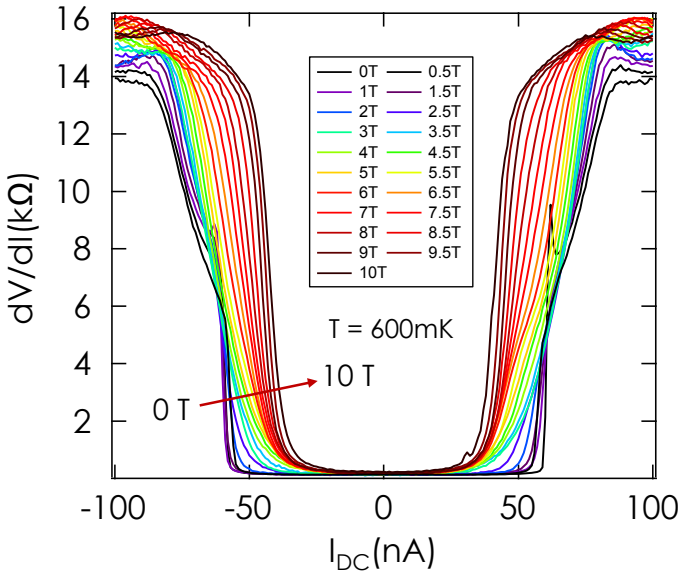

Figure 5.2.1: dV/dI curves at different field of Bi_3 The differential resistance as function of DC current curves are taken at different magnetic field from 0T to 11T at 600mK. The supercurrent is still very visible at 11T.

5.2 Field dependence of critical current

The samples have a very unusual field dependence of their critical current. Completely different behaviors compared to W-Au-W junction with same dimensions Au wire[76].

5.2.1 Persistent supercurrent up to high magnetic field

First, We find that for all these samples, the supercurrent persists up to very high magnetic field: higher than 6T for Bi_1 and Bi_2; higher than 11T for Bi_3. In all case those values are merely limited by the highest field achievable with the superconducting magnet used in the experiment. In Fig.5.2.1 we show the dV/dI curves taken at different magnetic field. At the very high field, the switching jump is rounded, but the supercurrent is still clear. This is a surprising finding compared to any other SNS system

5.2.2 SQUID-like oscillations in critical current

The critical current of all these samples are strongly modulated by the magnetic field. Bi_1 and Bi_3 both show SQUID-like oscillations of critical current in magnetic field. Fig.5.2.2 shows these oscillations at different rang of magnetic field. Surprisingly the SQUID-like oscillations persist up to several Teslas for 2 samples(6T for Bi_1 and 11T for Bi_3). The period is about 800G for Bi_1 and 150G for Bi_3. The amplitude of the modulations is about 10% of the critical current for two samples at

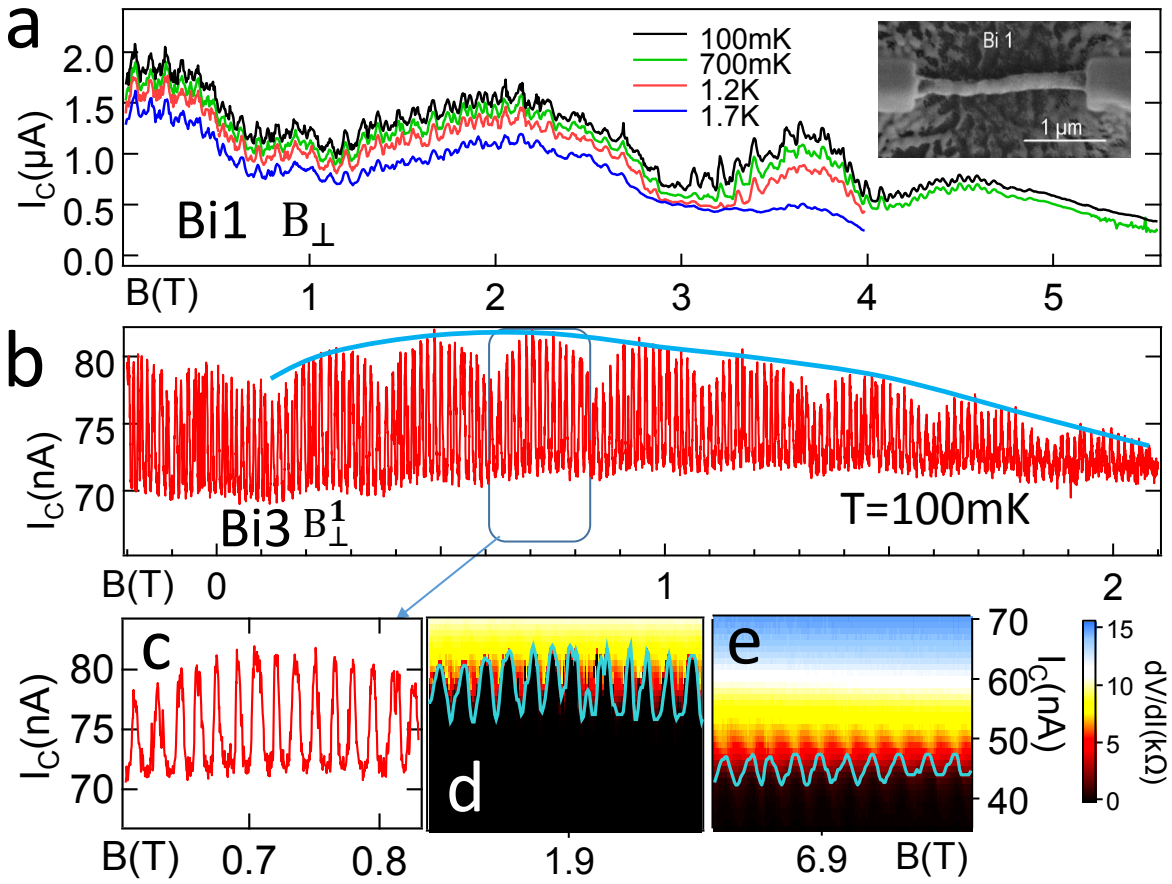

Figure 5.2.2: SQUID-like oscillations of Bi_1 and Bi_3(a) and (b) show direct I_C measurement as function of field;(c) is the zoom figure of 2000 gauss rang of (b), the blue line indicates the envelope of the whole critical current modulation; (d) and (e) are scans of dV/dI curves at different range of magnetic field, show the persistent oscillations

low field. At higher field, the amplitude is decreased.

5.2.3 Large range modulation

The critical current of Bi_3 is also modulated with a second period of 0.3 T. And for Bi_1, Bi_2 and Bi_3^* the supercurrent is also modulated aperiodically on the Tesla scale(Fig.5.2.2,Fig.5.2.3). In samples without SQUID-like rapid modulations, the large field modulation causes a full extinction of the supercurrent in Bi_2 and Bi_3^*, with entire magnetic field intervals having zero supercurrent and finite resistance.

5.2.4 Different orientations on Bi*3

We also explored the effect of field orientation on sample Bi_3^*, by measuring it in 3 perpendicular field orientations, including one along the wire axis (Fig.5.2.4). The field modulation patterns of

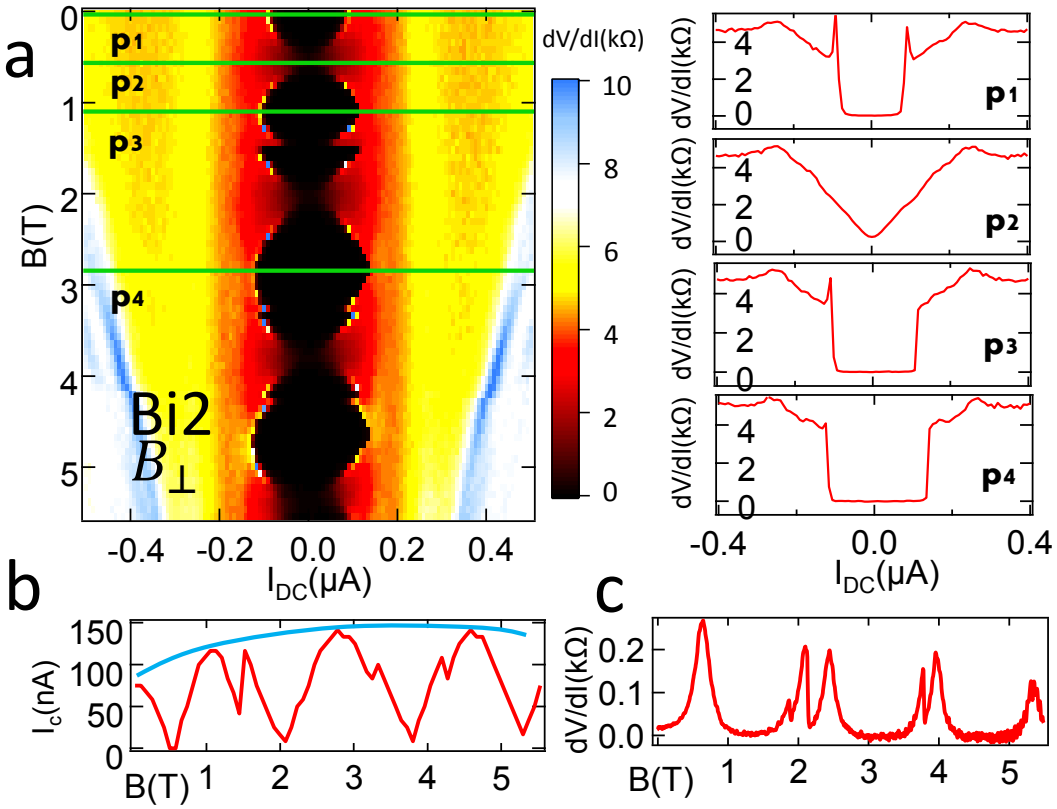

Figure 5.2.3: (a) Left panel: Color plot of the field dependence of the differential resistance of Bi 2 , with some characteristic differential resistance curves (right panel). (b) and (c) Field dependence of the critical current and zero bias differential resistance extracted from the color plot (a). Note the oscillatory behavior on the 1 Tesla field scale, and also how the maximal critical current increases with field. The blue line in (b) indicates the envelope of the critical current, increasing as the field increases.

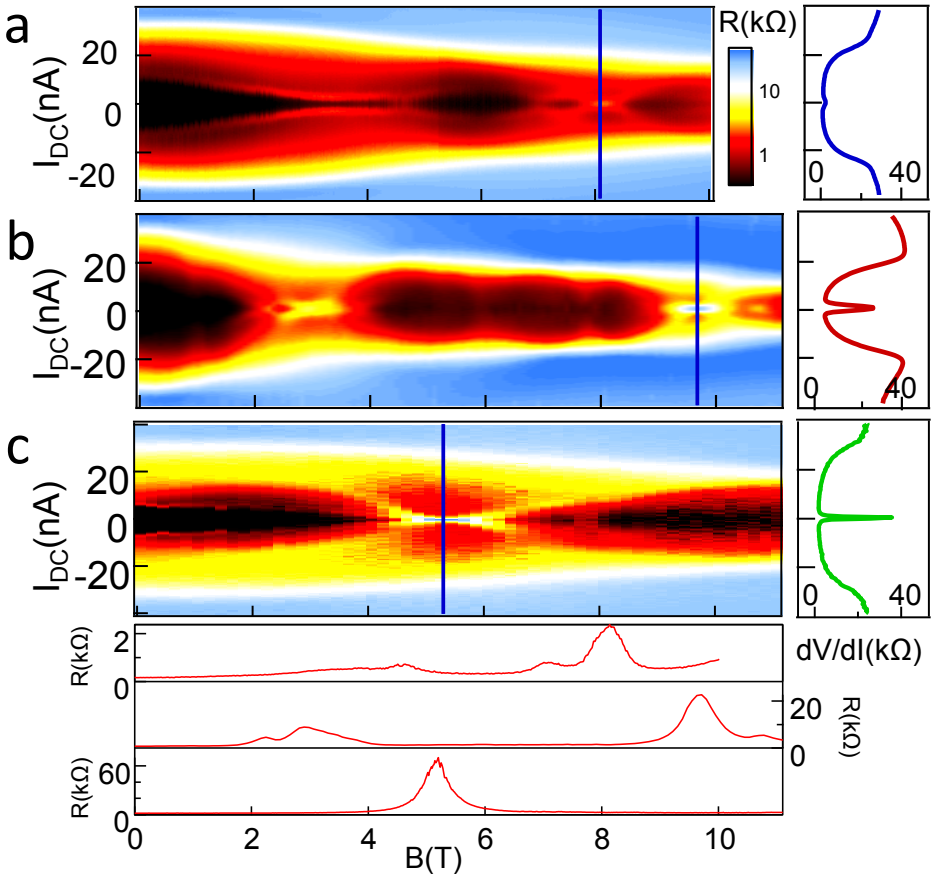

Figure 5.2.4: Orientation measurement in Bi3*Color plots showing the magnetic field dependent differential resistance and zero bias differential resistance for 3 different field orientations measured for Bi3* (which corresponds to Bi 3 after warming up at room temperature. (a) field along the nanowire axis, (b) and (c) field orientations perpendicular to the wire axis.

the critical current differ. High resistance peaks occur for different magnetic field values (8, 9 and 5 T, see dashed lines in Fig. 5.2.4 a, b and c) The small period, squid-like oscillations of the first cool-down are not detectable any more in these subsequent cool downs.

5.2.5 Shubnikov de Haas (SdH) oscillation @ 6K

We measure the SdH oscillations of the Bi nanowires above the critical temperature of tungsten (Fig.5.2.5). The field derivative differential resistance shows a clear oscillation with a period about 0.2 T^{-1}.

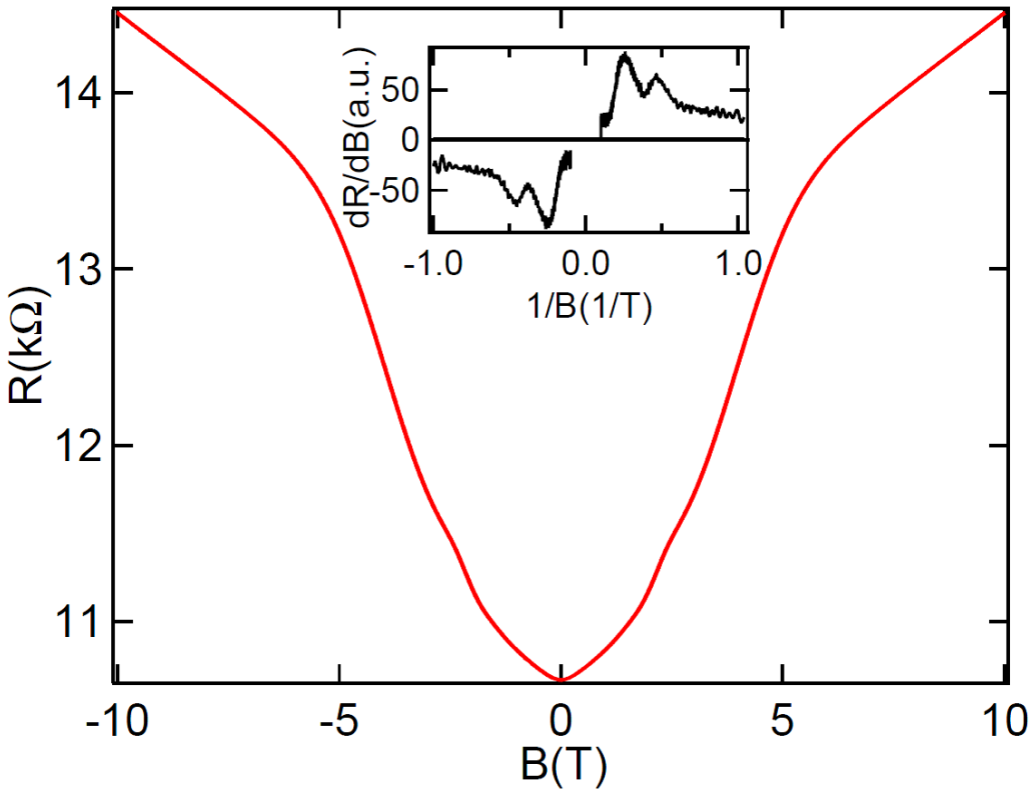

Figure 5.2.5: Magnetoresistance of a Bi nanowire similar to Bi3 measured at 6K, (i.e above the critical temperature of the W wires). Inset: the field derivative reveals Shubnikov de Haas oscillations periodic in $1/B$ whose period is of the order of 0.2 T^{-1} which complete analysis would require a full angular analysis

5.3 DISCUSSION

To understand these unusual features, we first compare them to the ordinary diffusive SNS junction with a large number of conduction channels. The supercurrent is strongly suppressed by magnetic field due to two mechanisms: orbital destructive interference between the quasi-particles going through the normal part and Zeeman effect in electron-hole pair phase cumulation. In the semi-classic limit(Fermi wavelength is much smaller than all sample dimensions), there is the Aharonov-Bohm phase difference between different Andreev pairs that follow different trajectories through the N part. This can cause orbital phase breaking. This orbital dephasing suppresses the supercurrent at fields corresponding to a flux quantum through the sample, as observed experimentally e.g. in Au wires[76].

SQUID STRUCTURE – EDGE STATES

All three Bi samples have an area perpendicular to the magnetic field of $2\mu m$ by 100 nm, so that one flux quantum corresponds to a magnetic field of 50 G, three orders of magnitude smaller than the supercurrent extinction field found in the experiment. The persistence of supercurrents to field as high as 10 T can only be understood if transport is confined to a very few, quasi ballistic, 1D channels whose width should not exceed the Fermi wavelength. we can get a possible configuration for the channels inside of the Bi nanowires: these 1D ballistic channels can form at the edges of particular facets parallel to the nanowire axis. In Fig. 5.3.1, we show a simple scheme for the edge states supported SQUID structure in W-Bi nanowire-W. Such edge states could be the topological edge states of the (111)[130] or (114)[131] surfaces, or of other possessing similar topological properties. Since the field periodicity of the oscillation corresponds to the enclosed flux between the interfering channels, the measured periods of 140G for Bi 3 and 800G for Bi_1 would correspond to 1D channels along the samples axis respectively distant by 70 and 12 nm.

The interpretations suggest meanwhile a distribution of density of current along certain edge(s). This can recall a recent observation of the periodic oscillations of the Josephson current carried by spin Hall edge states in a 2D topological insulator connected to superconducting electrodes[74]. We show in Fig. a simulation of the interference between two channels with different g factors. (produced by Buzdin A. et al.) and also the Fourier transform simulation in farther section.

ZEEMAN DEPHASING – LARGE SCALE MODULATION

In samples with a very small area perpendicular to the magnetic field, this orbital dephasing is weak, and the spin phase breaking caused by the Zeeman effect becomes noticeable. The Zeeman effect causes a phase difference between the electron and hole components of a given Andreev pair, given

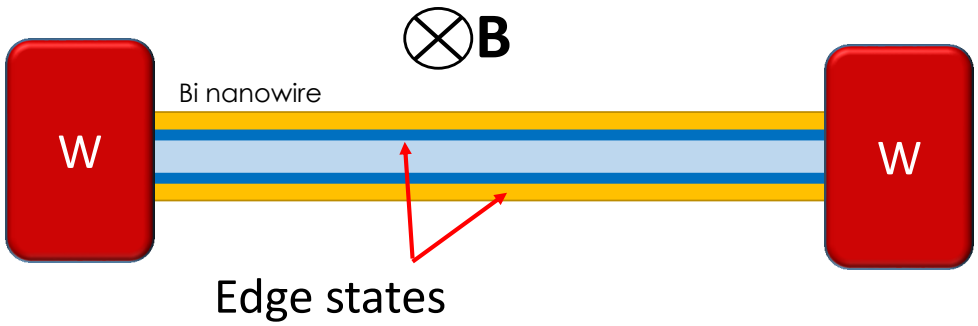

Figure 5.3.1: SQUID structure - edge states W - Bi nanowire - W with edge states(dark blue lines) on particular facet(light blue) of Bismuth nanowire(yellow represent other facets). The edge states formed on the particular facet have a enclosed surface smaller than the entire wire. The magnetic field is in the perpendicular direction.

by $E_Z\tau/\hbar$ on a trajectory of length L_t(E_Z is the Zeeman energy and $\tau = L_t/v_F$ is the time for the quasi-particles across the sample). This leads to a strong exponential supercurrent suppression with magnetic field after summing the contributions of all Andreev pairs trajectories when the number of channels is large. A similar suppression occurs when the normal sample is ferromagnetic, with E_Z replaced by the exchange energy. Note that this spin pair breaking mechanism does not exist for triplet pairing. Magnetic field induced Zeeman energy can shift the wavevectors of carriers of opposite spin at the Fermi level[132, 133]. Within linear approximation, the phase difference accumulated between the electron and hole components of opposite spin along a 1D ballistic trajectory of length L is

$$\begin{aligned}\delta\varphi(B) &= E_Z L/(\hbar \cdot v_F) \\ &= g_{eff} \cdot \mu_B \cdot B_{||}/(\hbar v_F/L)\end{aligned} \tag{5.1}$$

where L/v_F is the time of flight across the wire and $B_{||}$ is the component of the applied magnetic field along the spin orbit field. If we use typical Bi surface states parameters ($v_F \simeq 3 \times 10^5 m/s$ and $g_{eff} = 30$), we obtain a characteristic modulation period in the Tesla range (order of 1 T).

As well as for the three field orientations of Bi_3^*, this difference in interference pattern is expected.

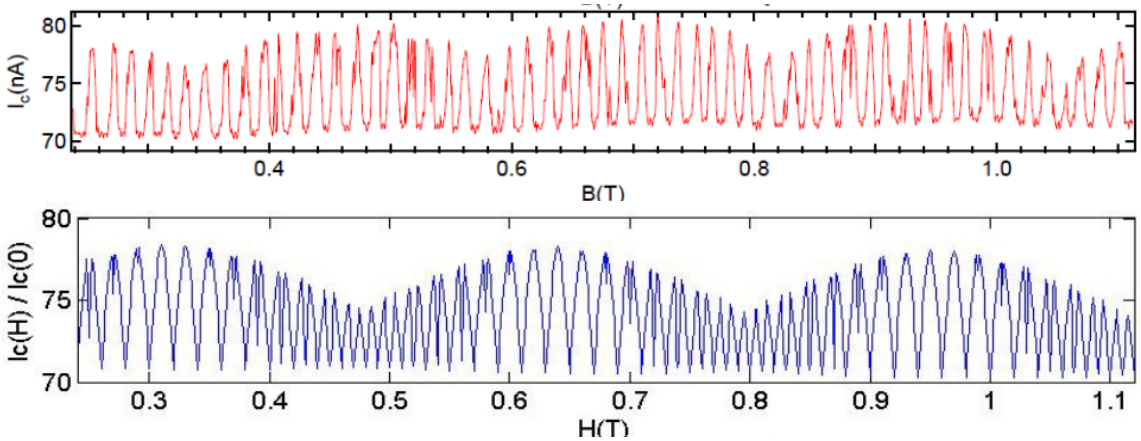

Figure 5.3.2: Simulation of two 1D channels interference (upper) Experimental results of Bi_3; (lower) theoretical simulation of two 1D ballistic channels interference in magnetic field by taken into count the Zeeman effect. The high frequency oscillations is due to the orbital interference between the 2 channels, and the low frequency oscillation is attributed to Zeeman effect.

Considering the anisotropy of the different facets of Bi and the corresponding different g_{eff} values, this range can vary by more than an order of magnitude. Fig.5.3.2 shows a comparison of theoretical calculation and our experimental results considering the interference between two 1D ballistic channels[134].

However, the simulation above is without the spin-orbit couping which should play an important role in this interference pattern. Considering the strong spin-orbit coupling, the energy band of the Bi could have spin splitting and the Zeeman effect can tune the phase difference between particles in different bands with $\uparrow$ and $\downarrow$ (See Fig. 5.3.3).

In this picture, the full extinction of the supercurrent at nearly periodic field values is attributed to the $(2n + 1)\pi$ phase differences (with n integer) between the electron and hole components of the supercurrent-carrying Andreev pairs. Such full extinction (complete destructive interference) is thus restricted to a single current-carrying channel. This seems to be the case in Bi_2 and Bi_3^*, since they do not display SQUID-like oscillations (that require two channels). The Bi_3^* behavior is especially dramatic around 5 T (see Fig. 5.2.4 c and c'), with a zero bias resistance that peaks at a value even greater than the normal state resistance.

The traces of the π junction or φ junction

Some of our results implies really exotic properties of Bi nanowires related to the strong spin-orbit coupling.

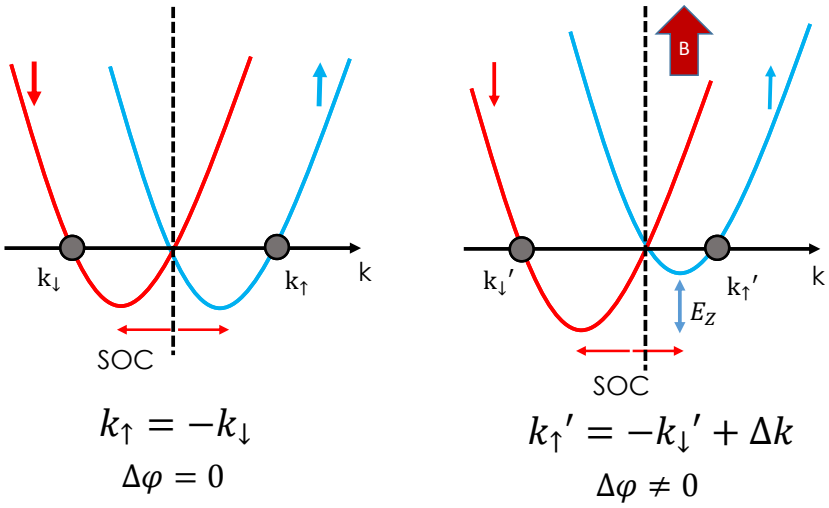

Figure 5.3.3: Zeeman effect in strong spin-orbit coupling system (left) Spin splitting due strong spin-orbit coupling, without Zeeman effect, the constructive interference is still conserved between the electrons in ↑ band and ↓ band; (right) Spin-orbit coupling + Zeeman effect can induce a phase accumulation between two electrons which is related to the shift in wavevectors.

Minimum of the I_c oscillations at zero magnetic field

As we presented, we observed a SQUID-like I_c oscillations in 2 samples with different periodicities. If one looks carefully at the zero field regime, one always finds a minimum of the oscillations (Fig.5.3.4). This simple results actually implies a very surprising physical phenomena: an intrinsic π phase shift in the S/Bi/S junction. The vortex seems not enough to explain a 400 Gauss shift in field (for Bi_1) and the reproducibility in two samples. However the full understanding of this π shift is missing here. One of the possible configurations is that one of the S/1D channel/S junctions holds a π phase, thus a π junction[135]. But theoretical support is strongly needed to understand the origin of this π phase shift.

Magnetic field enhanced supercurrent

Another important finding is the enhancement of the critical current by the magnetic field. The critical current of Bi_2 at 5 T is twice the one at zero field (see Fig. 5.2.3 (a)right or (b) left). A similar but smaller increase between 0 and 0.75 T is also seen in Bi_3 . This increase of supercurrent with magnetic field may be attributed to the strong spin-orbit interaction, as predicted in the context of φ junctions[136, 134].

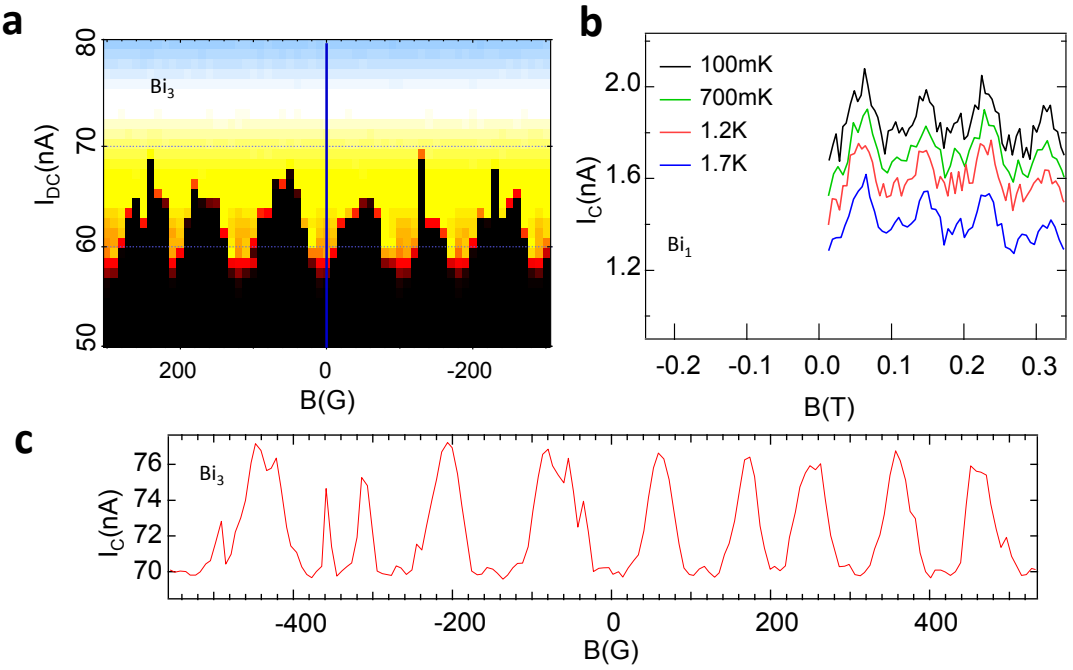

Figure 5.3.4: Minimum of the I_c oscillations at zero magnetic field (a) and (c) show the field dependence of the critical current of Bi_3 around zero field; (b) for Bi_1. (a) is taken by scanning the dV/dI(I_{DC}) curves at different field value. The blue line indicates the zero field.

Shapiro steps

When a radio frequency source is applied to the superconducting Bi nanowires, the Shappiro steps are observed (Fig.5.3.5 for Bi_3). The positions of the steps correspond to hf=2neV, in which the factor 2 is due to Cooper pairs in the ordinary superconducting state.

5.4 Conclusion

In this chapter, we have shown evidence of quantum interferences in Bi nanowires based Josephson junctions which persist up to very high magnetic fields. Sample dependent periodic oscillations of the critical current reveal complex interference patterns involving both orbital and spin degrees of freedom between a small number of strongly confined 1D channels possibly located at the edges between facets of different crystalline orientations along the wires. The physical origin of this confinement of induced superconductivity in such quasi one-dimensional channels is not yet well understood. In particular, we hope to be able in future studies on single crystals of known orientation, to disentangle the role played by the crystalline structure of the wires from the existence of a high spin orbit coupling. It is also possible that this confinement is favored in the S state by the high

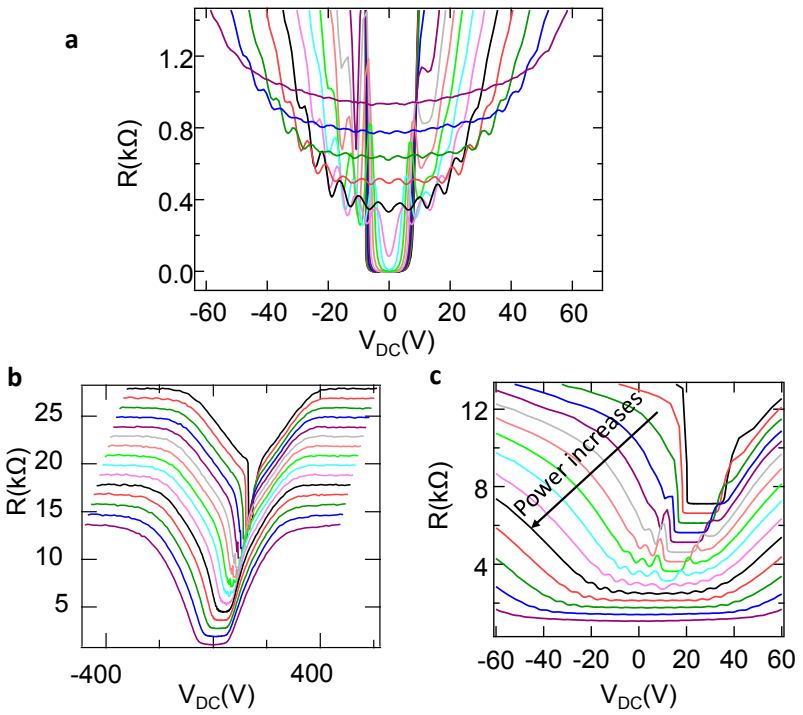

Figure 5.3.5: Shapiro steps in Bi_3. Evolution of the radio frequency induced Shapiro steps on the differential resistance of the Bi_3 sample for different power excitations at f=2.2 GHz at 100mK The position of the steps correspond to hf = 2neV where V is the voltage drop through the sample.

magnetic field which is known to induce inhomogeneous superconductivity in 2D superconductors with large Rashba spin orbit interactions [137].

6

Conclusion and outlook

In this thesis we investigated graphene and Bi nanowire systems by inducing superconducting proximity effect in them. Typically the samples are realized in the form of S/N/S junction. The special properties of these systems are revealed by observing some unusual proximity effect in them. The interplay of the superconducting proximity effect and other effects (spin-orbit coupling, Zeeman effect, quantum Hall effect, impurities, etc...) at the mesoscopic scale gives rise to new physics. Some of our main results are listed below.

Graphene

The full eR_NI_c vs E_{Th} diagram in diffusive S/G/S junction

We succeeded to induce superconducting proximity effect in the very long junction limit, thus completing the diagram of the superconducting proximity effect in graphene. Since by changing the gate voltage, one changes the carrier density in graphene and eventually the transport characteristic quantities (l_e, E_{Th} etc...). we could scan a whole range of Thouless energy. We present a diagram of eR_NI_c vs Thouless energy (E_{Th}) compared to theoretical prediction. In this diagram, we see clearly how the Thouless energy dependence of the eR_NI_c products varies from the long junction limit to the short junction limit.

The discrepancy (mainly due to the imperfect S/G interface) between theory and experiment is also limit dependent: in the short junction limit, the eR_NI_c products are smaller than the theoretical prediction (with a perfect interface) by a factor of about 3-4; in the long junction limit, however, the disagreement is increased to about 100. We show that the factor deduced from the junctions in different limits is length dependent. This can be explained by the effect of finite transmission at the S/G interface in both the critical current I_c and the induced mini-gap in the graphene.

The indication of specular Andreev reflection (SAR)

Particularly in the long S/G/S junctions, we observed an unexpected suppression of supercurrent near the Dirac point of graphene. In many reported experiments (for short junctions), in this regime of gate voltage, the supercurrent was shown to be robust regardless of the presence of the charge puddles. Excluding the thermal effect and finite transmission, we attribute this suppression of I_c near the Dirac point to the special specular Andreev reflection (SAR) in long graphene junction. The SAR actually separates the trajectories of the electron and the hole in one Andreev quasi-particle pair, finally destroys the constructive interference between the Andreev Bound states in an S/G/S junction.

Injection of Cooper pairs in the Quantum Hall regime

The interplay of the superconducting proximity effect and the quantum Hall effect was also investigated in this thesis. By using superconducting electrodes with high critical field (H_c) to contact a graphene sheet, the injection of Cooper (Andreev quasi-particle) pairs into graphene in quantum Hall regime becomes possible. We found a zero-bias conductance increase at the edge of the QHE plateaus and some dip features at zero bias of the dV/dI(I_{DC}) curves between two QHE plateaus which is always a peak for the curves taken on the plateaus. This is an indirect indication of the presence of the superconducting proximity effect. The difficulty of this experiment is the two-probes sample configuration in which one measures a combination of ρ_{xx} and ρ_{xy}. Certainly better configurations proposed in the outlook should be tested in future.

Graphene grafted with Pt-porphyrins

Positive and negative charge transfer

By grafting the Pt-porphyrin molecules on graphene, we first observed at room temperature a shifting of Dirac point of the graphene to zero gate voltage from/to either electron doping or hole doping thus a charge transfer between the graphene and the porphyrins in both directions. Actually, this is the first time that a dual direction charge transfer induced graphene doping is reported. This

may open a new possible application research approach to the controllable graphene doping. This wet grafting technique, different from the evaporation deposition of molecules, would allow the pretreatment on many different kinds of nano-devices. How the dual direction charge transfer happens is still not clear from the point of view of the LOMO-HUMO structure, since the gap of LOMO-HUMO band of Pt-porphyrin is 2eV, much higher than the gate tunable energy in graphene. But the universal energy level alignment at the organic-metal interface may be the answer to this puzzle.

Gate dependent magnetism and unipolar supercurrent

One of the important consequences of the charge transfer is that when the molecules are ionized , a collective magnetic order can be formed by the long range RKKY interaction: the magnetic moments interact via the carrier in graphene. This effect is detected by a hysteretic magnetoresistance of the graphene in a perpendicular field and the asymmetric magnetoresistance in parallel field. Even more striking, the observation of an unipolar supercurrent in S/G/S junction implies that this magnetism induced by porphyrins is gate dependent. The theoretical calculations by Uchoa et al. using the Anderson model indeed find that the gate voltage should tune the impurities in graphene between non-magnetic state and magnetic state[56].

Bi nanowire

1D ballistic edge channels on certain facets of Bi

The experimental results on Bi nanowires, especially the field dependence, are very interesting. The SQUID-like oscillations persist up to 10 T and thousands Gauss range modulation in I_c hint to a complex physic in the W-Bi nanowire-W junctions.

The results are consistent with a SQUID structure consisting of 2 edges channels which could have an I_c oscillation with period defined by the area between the two edges, typically the size of the nanowire. The origin of the edge states formation is attributed to the strong spin-orbit coupling in Bi[131], that leads to the quantum spin Hall state. This is very similar to the experiment in other QSH systems, like HgTe/(Hg,Cd)Te quantum wells[74].

The thousands Gauss range modulation is the consequence of the interplay between the Zeeman effect and the proximity effect. The phase accumulation in an Andreev quasiparticle pair is $\Delta\varphi = g_{eff} \cdot \mu_B \cdot B_{||}/(\hbar v_F/L)$ which is of the order of few thousands Gauss. In one particular sample (Bi_2), a full modulation of the critical current with about 1 T range is observed. This is similar to the proximity effect in S/F/S junctions which suggests a $0-\pi$ junction transition. In fact the proximity effect in Bi nanowire can be summarized as 3 effects:

Orbital dephasing due to the interference between the edge states: $\varphi_0/S \sim 10mT$. S is the area enclosed by the edge states.

Zeeman dephasing Zeeman field induced phase accumulation between electron-hole pair. $\Delta\varphi = g_{eff} \cdot \mu_B \cdot B_{||}/(\hbar v_F/L)$. If we take some typical values for the quantities, one gets a 1 T range modulation of critical current in field.

$0-\pi$ junction transition combined with a strong spin-orbit coupling, the S/Bi nanowire/S junction shows a possible $0-\pi$ junction transition.

Outlook

In this thesis, we use the superconducting proximity effect as a powerful tool to probe systems of interests. It turns out it can reveal more interesting properties of these system than usual normal metal contact transport measurement (of course, normal metal contact are still an important reference to compare the results). Sometimes, these results in different systems could also improve the understanding of the superconducting proximity effect itself. We made improvement experimentally to the understanding the physic in topological system with induced superconducting properties, even in high magnetic field. Beyond this thesis, certainly, many paths will be followed and extended.

For the graphene, some better configurations for measurement are proposed:

SSNN and graphene-SQUID configurations for SPE in QH regime

The combination of superconducting proximity effect and QHE is still very interesting and fundamental question. Since the Hall bar structure is hard to make in proximity effect experiment (the 2 electrodes have to be close enough to get a complete proximity effect), we need a reference measurement to calibrate transport properties in the ballistic QH edge states. So a simple configuration is proposed here by just making 2 superconducting electrodes and 2 normal metal electrodes on the same graphene flake (Fig.6.0.1). The shape of the graphene should be regular (rectangle would be better). Naively supposing that the transport properties (disorder, mobility..) on the same graphene flake should be very similar, then the difference between the results from the two superconducting electrodes and 2 normal metal electrodes may reveal the superconducting coherent properties induced by the electrodes. Graphene based SQUID is also a good configuration to probe the coherence in the QH regime. To do so, one needs also a good high H_c material.

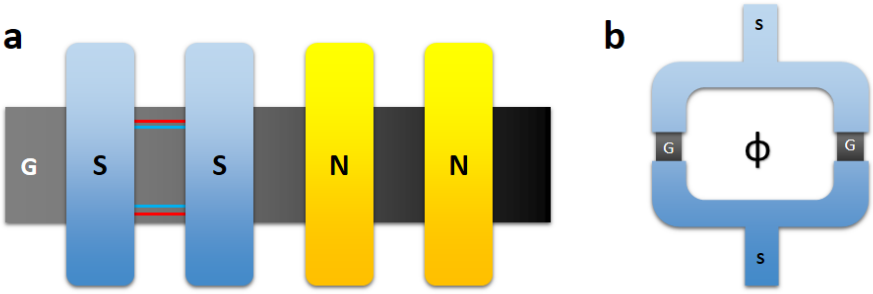

Figure 6.0.1: Proposed SSNN and graphene-SQUID configuration. a) 2 superconducting electrodes and 2 normal metal electrodes. b) Graphene-SQUID using high H_c superconducting material.

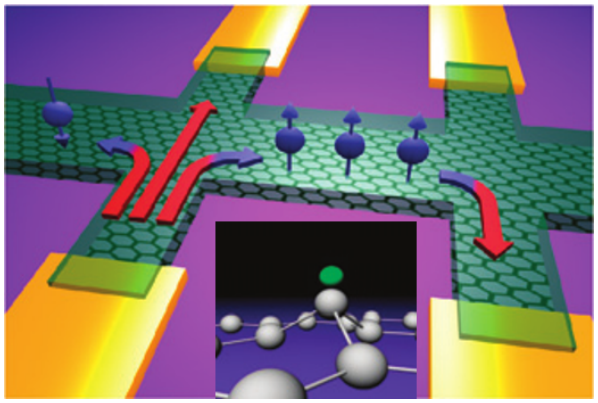

Figure 6.0.2: Measurement schematics for the non-local spin Hall measurement. Inset: schematics showing the deformation of the graphene hexagonal lattice due to hydrogenation. From Ref.[139]

Spin Hall effect measurement

As we stated at beginning of Sec.4, the motivation of the porphyrins on graphene experiment is to investigate the spin-orbit coupling induced by the Pt atoms. We could not conclude from the experiments that we have on this point because of the observation of an unexpected gate voltage dependent magnetism. We observed an unusual interference pattern in Nb long junction sample by applying both perpendicular and parallel field (Sec.4.4.2, Fig.4.4.6). Since the effect is not strong enough to be revealed only by 2 wires measurement, we should consider a Hall bar structure[138, 139]. Because the non local measurement on Hall bar structures should help us to distinguish the contributions of SOC from the induced magnetism.

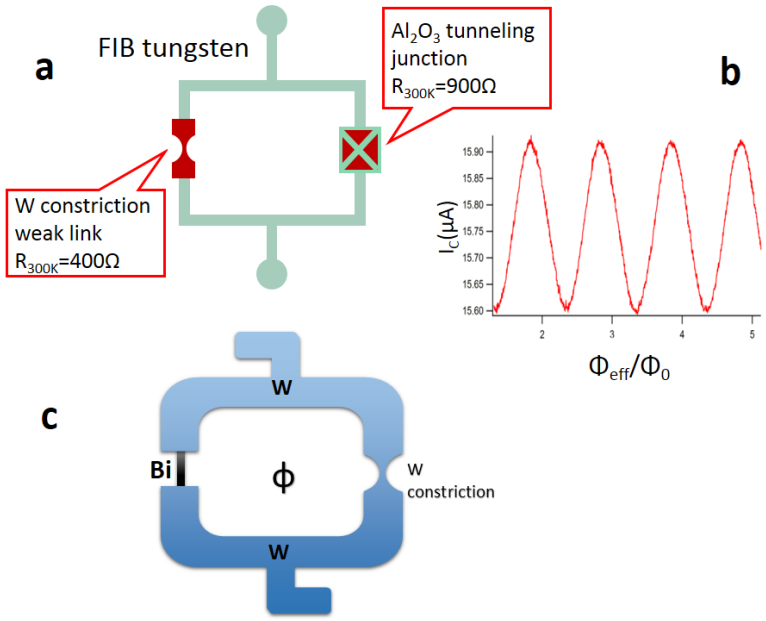

Figure 6.0.3: Bi nanowire based high magnetic field SQUID. a) Configuration of the critical current calibration with Al_2O_3 junction-W constriction based asymmetric SQUID. b) the critical current oscillation. about 10% modulation. (Done by A. Murani and R. Delagrange) c) Final configuration for the current-phase relation measurement in Bi nanowire.

Current-phase relation measurement in Bi nanowire

Many exciting experiments can be done with Bi nanowires. The possible $0-\pi$ junction transition is one of the most interesting physic to probe. Then a current-phase relation measurement should certainly be done in near future. The first step (done by A. Murami and R. Delagrange Fig.6.0.3.a and .b) was to make an asymmetric SQUID consisting of a W constriction weak link in parallel with a normal tunnel junction by FIB (Fig.6.0.3).

A

Sample fabrication and characterization

A.1 Graphene suspension

To improve the quality of graphene, many methods are suggested. The main stream is in two directions:

- graphene on high quality single crystal boron nitride (hBN), which decouples the graphene from the SiO_2 substrate and has (so far) a best lattice matching to graphene. So the graphene on hBN flakes is like a "free" sheet.
- Suspended graphene. Ideally the graphene is only fixed at two (or more) terminals without any coupling to the substrate. The mechanical vibration resonance in graphene is possible in this configuration.

We succeed to make suspended graphene samples with superconducting electrodes with different methods (Fig.A.1.1).

A.1.1 LOR resist technique

One method to realize the suspension of graphene is the "LOR substrate" method which is first introduced by Tombros et al.[140]. FigureA.1.2 shows the main procedures in the fabrication. LOR

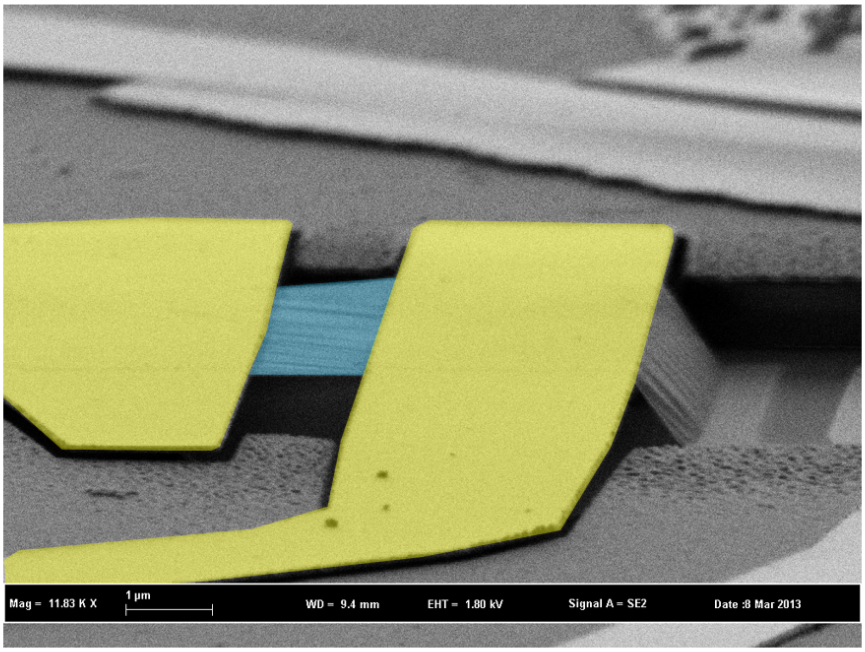

Figure A.1.1: SEM picture of sample G46LOR. Graphene is suspended with ReW electrodes.

resist is based on polydimethylglutarimide. The parameters and performances can be find at LOR resist.

Since the LOR resist has a different exposing dose and developer solution to PMMA or MMA polymer, one can proceed a standard lithography on top of LOR resist by using PMMA. The key point in this fabrication method is the exposal dose. For a single PMMA layer, 300$\mu C/cm^2$ is the typical dose for the first lithography. Then to remove the LOR resist underneath of graphene, 700 $\mu C/cm^2$ can be used.

One of the problem with this technique is that the graphene is always polluted by the resist and becomes very doped and disordered. One can barely see the gate effect at room temperature within a variation about 10V. That's why we also tried another technique with which the graphene is completely supported by metal electrodes without any resist underneath.

A.1.2 PMMA/MMA double layer technique

This double layer technique is first introduced by . We adapt it to superconducting contacts making.

The main steps for PMMA/MMA bilayer suspension technique is described in Fig.A.1.3. First we spin PMMA on the Silicon chip by choosing a suitable parameter for the thickness. Then the graphene is exfoliated on the PMMA layer. Once the graphene flakes are located, we coat the chip with another layer of MMA copolymer. Then a standard lithography step is carried out. After the lift-off, all the polymer layer will disappear and the graphene should be suspended completely by

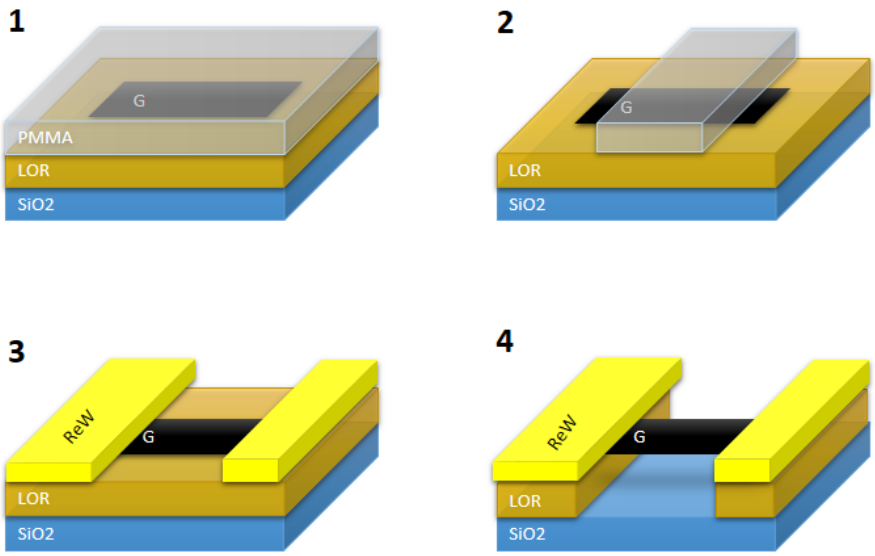

Figure A.1.2: Schematic procedures for graphene suspension on LOR substrate. 1. the graphene is directly exfoliated on the chip covered already by LOR resist. Then another layer of PMMA is spinned on it.2) a standard lithography procedure on top of LOR resist by using PMMA as the mask layer. 3) after deposition of the metal contacts, one proceed the lift-off of PMMA layer and finally the contacts remain on top of LOR resist layer. 4) another lithography step on the part between 2 electrodes and the LOR under the graphene is removed after the development (of LOR resist). Finally graphene is suspended between 2 electrodes.

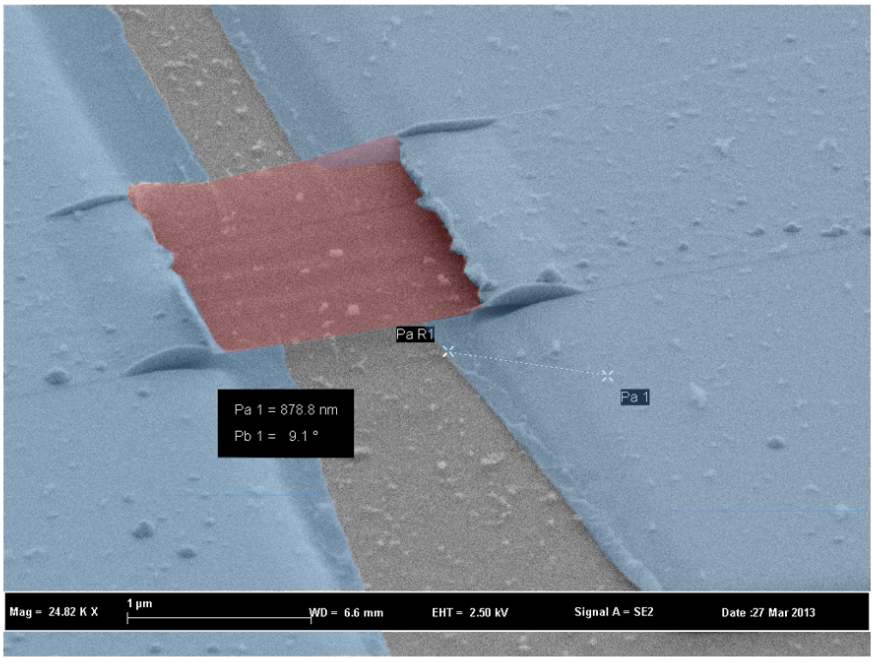

Figure A.1.3: SEM picture of sample G56MMA. Graphene is suspended with PMMA/MMA bilayer technique. Finally the graphene is suspended by only metallic electrodes.

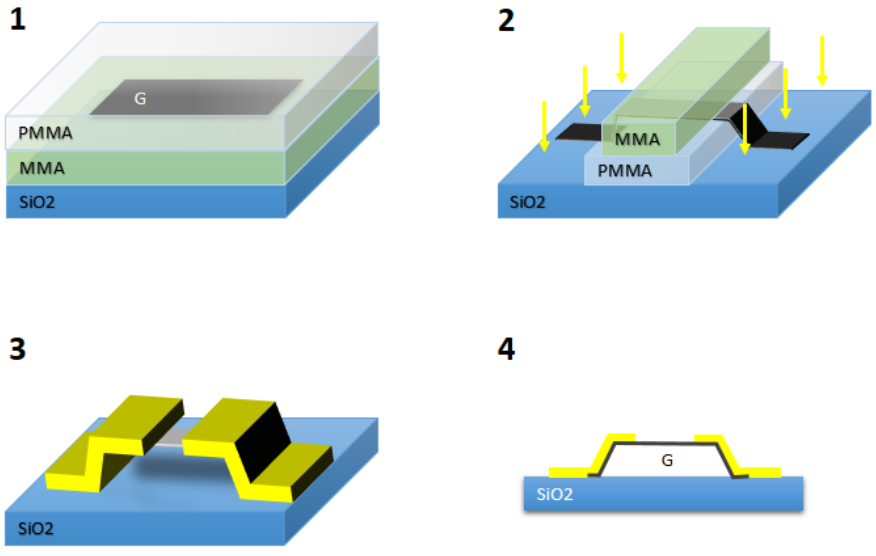

Figure A.1.4: Schematic procedures for graphene suspension with PMMA/MMA bilayer. 1). the graphene is directly exfoliated on the chip covered already by PMMA resist. Then another layer of MMA is spinned on it. 2) a standard lithography procedure on top of the bilayer resist. 3) after deposition of the metal contacts, one proceed the lift-off of PMMA and MMA bilayer and finally the contacts remain and support the graphene suspension 4) side-view of this structure.

the metal electrodes.

A.2 Pt–porphyrin molecules

PtII tetrakis (4-carboxyphenyl)-porphyrin[141](15 mg, 10.8 *µmol*) was dissolved in NMP (4 ml). S-acetylcysteamine hydrochloride (13.54 mg, 86 *µmol*), benzotriazol-1-yloxytripyrrolidinophosphonium hexafluorophosphate (Py-BOP) reagent (44.7 mg, 86 µmol) and dry DIEA (30µl, 172 µ mol) were sequentially added and the resulting reaction mixture was stirred at room temperature for 4 h. The reaction was checked for completion by TLC (CH_2Cl_2 /MeOH, 96:4, v/v). Thereafter, the crude was diluted with AcOEt (40 ml), washed by aq. 10% citric acid (40 ml), aq. sat. $NaHCO_3$ (40 ml) and brine (40 ml). The organic layer was dried over Na_2SO_4 , filtrated and evaporated to dryness. The resulting residue was purified by chromatography on a silica gel, eluent (CH_2Cl_2 /MeOH: 100/0 to 97/3) , yielding porphyrins as a brown-orange solid (9.9 mg, 7.1 *µmol*, yield = 66%).1 H NMR (300 MHz, CDCl 3): δ = 3.64 (s, 3H), 3.85 (t,J = 5.1 Hz, 2H), 4.16-4.19, (m, 2H), 8.09 (s, 8H), 8.15-8.23 (m, 12H), 8.70 (s, 4H). MS (MALDI-TOF) m/z = 1387.26 $[M]^+$, calculated for $C_64H_56N_8O_8S_4$ Pt: 1387.28 g/mol.

A.3 Bi nanowire

Nanowire fabrication

Bi wires were grown from a solution prepared by dissolving 4.8 g $Bi(NO_3)3 * 5H_2O$ in 100 ml of water : ethylene glycol mixture (3:7 vol). This electrolyte was used earlier in Ref.[142]. In contrast to other typical electrolytes for Bi deposition, it contains neither chlorides nor complex forming molecules. Metal growth was templated using polycarbonate track-etched membranes (09-300-51 Whatman, No. WHT110405) with a nominal pore diameter of 100 nm.

Before electro-deposition, a 100-200 nm thick gold contact was fabricated on one external surface of a membrane by either thermal evaporation or magnetron sputtering. The three-electrode cell used for electrochemical experiments contained the metalized membrane at the bottom, the Bi reference electrode on the cell axis, and a Pt wire ring as a counter electrode located in parallel to the surface of the working electrode, to provide homogeneous current distribution. Potentiostatic deposition (-0.2 V vs Bi in the same solution) was carried out at room temperature, with current and charge monitoring. Deposition was stopped when a sharp current growth started, which indicated that some wires were close to the upper external surface of the membrane. According to gravimetric analysis and scanning electron microscopy (SEM), the current efficiency was at least 95

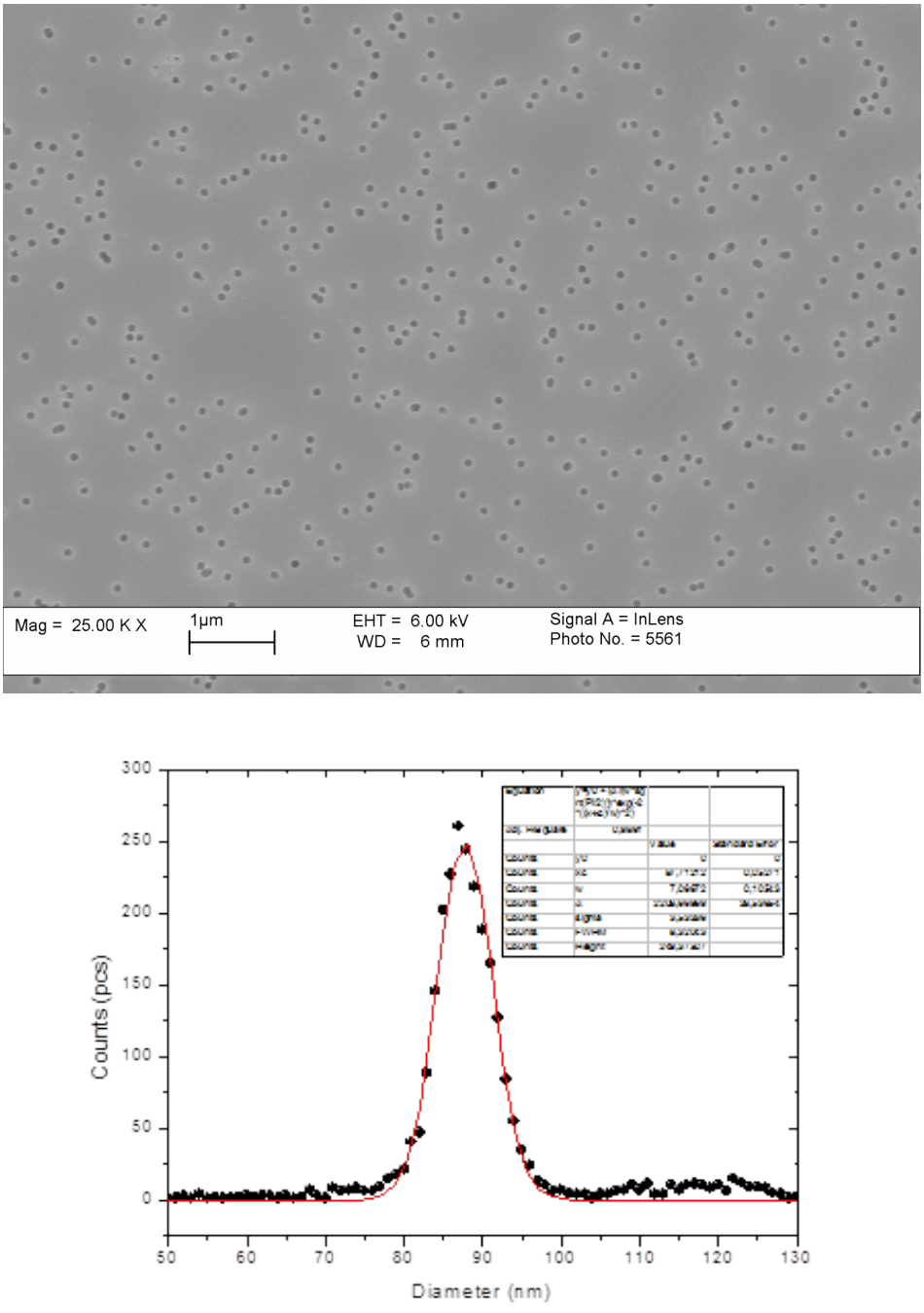

Figure A.3.1: SEM picture and pore size distribution of the Whatman membrane used for the growth of Bi nanowires.

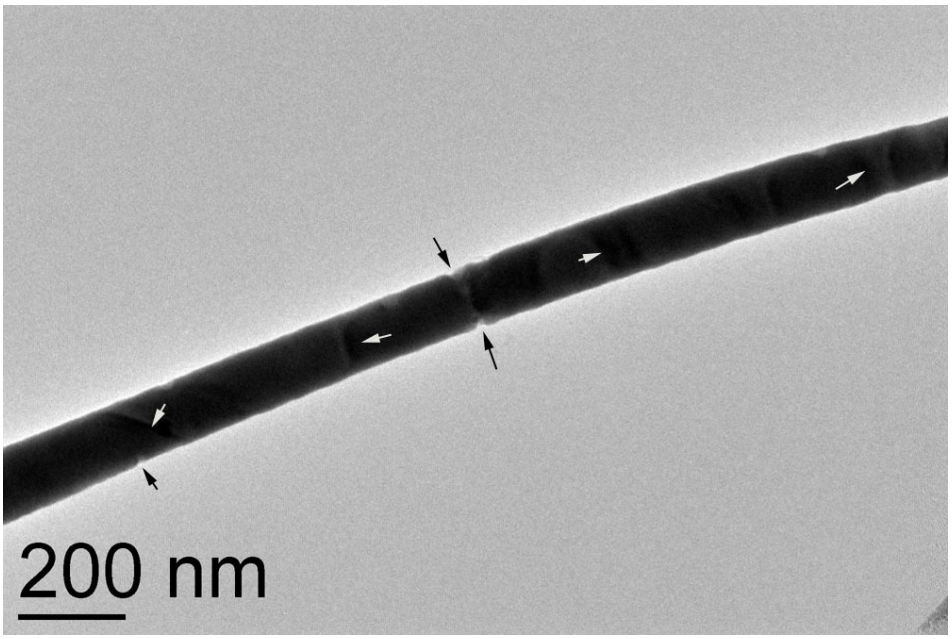

Figure A.3.2: TEM image of Bi wire demonstrating the typical variation of contrast (white arrows) and cavities (black arrows).

%, and the membrane filling with wires was typically ca. 50 %. After the electro-deposition process the samples were shortly washed by deionized water and were dried in air at ambient temperature.

X-Ray diffraction (XRD) of a membrane filled with wires confirmed that crystalline trigonal bismuth (JCPDS No. 44-1246) is deposited. XRD did not detect any byproducts. The polymer template was dissolved in dichloromethane, with several subsequent washing procedures. Finally, in order to obtain the suspension of Bi nanowires, the sample in H_2Cl_2 was treated by ultrasound during 3-5 seconds. The suspension containing a small amount of residual polymer was used for wires immobilization either on the grids (for TEM and electron diffraction (ED) characterization), or on silicon/silicon oxide wafers (for SEM and transport measurements).

Transmission electron microscopy characterization

The observed diameter of wires is in the 100 – 150 nm range. For any given wire, the diameter variation along the wire does not exceed 10 – 20 nm. The observed diameter of Bi nanowires is larger than the pore diameter of track-etched membranes which means that the wires are covered by an extra 10 to 20 nm thick layer as discussed again below.

Typical micro-structural features observed for all wires are (1) local variation of contrast (white arrows in Fig.A.3.2) and (2) faceted cavities with characteristic size of the order 10 nm (black arrows in Fig.A.3.2).

To clarify the nature of observed structural features, selected area electron diffraction patterns were collected (Fig.A.3.3). The obtained data confirm the absence of high angle boundaries in the

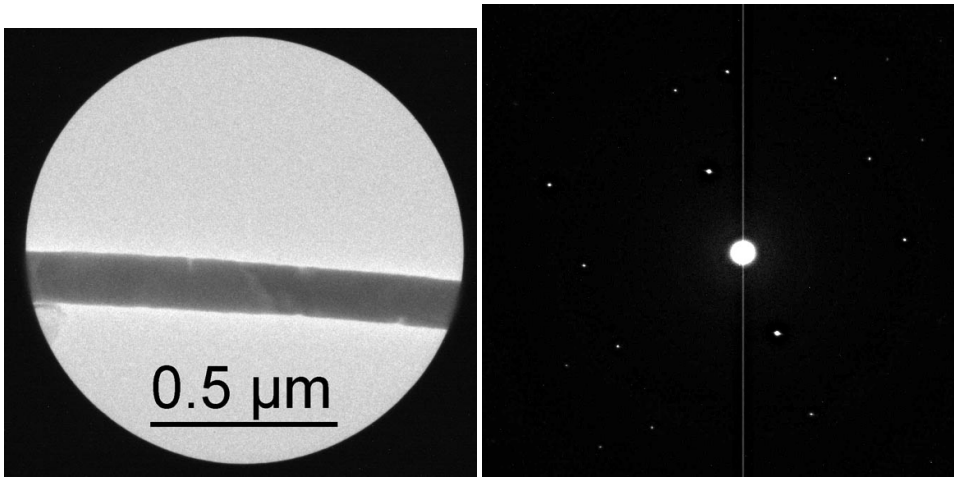

Figure A.3.3: TEM image of the region with several cavities (left) and electron diffraction pattern obtained for this region (right).

vicinity of both contrast variations and of the cavities.

The attempts to confirm this result by direct imaging of atomic planes were strongly complicated by the large thickness of the wires. By the way, no high angle boundaries were found at this stage in TEM images with atomic resolution. Fig.A.3.4 displays such an image of a region without cavities, which demonstrates the high crystal quality of the nanowire core. The external, ca. 10 nm-thick, amorphous layer observed for this particular wire can consist of either Bi oxidation products, or residual polymer originating from the template. According to Ref. [142], the oxide formation at the surface of wires deposited from water-ethylene glycol electrolyte was only possible after heat treatment. However oxide can be formed due to hydrolysis of the Bi(3+) ions in the course of sample washing (in which case no Bi from the wires would be consumed for oxide formation.)

Micro-structural features (black and white arrows on Fig.A.3.2 are typical for Bi wires deposited from various electrolytes and with the use of various templates (polymer track-etched membranes or porous anodic aluminum oxide films). Namely, in Ref.[143] the cavities are even more frequent, and at least some of them are located near twinning planes (i.e. low angle boundaries). Cavities and contrast variation are easily seen also in the images reported in Ref.[144]. In that reference the wires are declared to be single crystalline on the basis of selected area ED experiments along a single wire. For our wires, the selected area electron diffraction also demonstrated that orientation of crystal planes is similar for the fragments on either sides of the cavities. It was possible to determine the exact crystallographic orientation of 10 such nanowires. This orientation was found to be sample dependent, with no preferential axis.

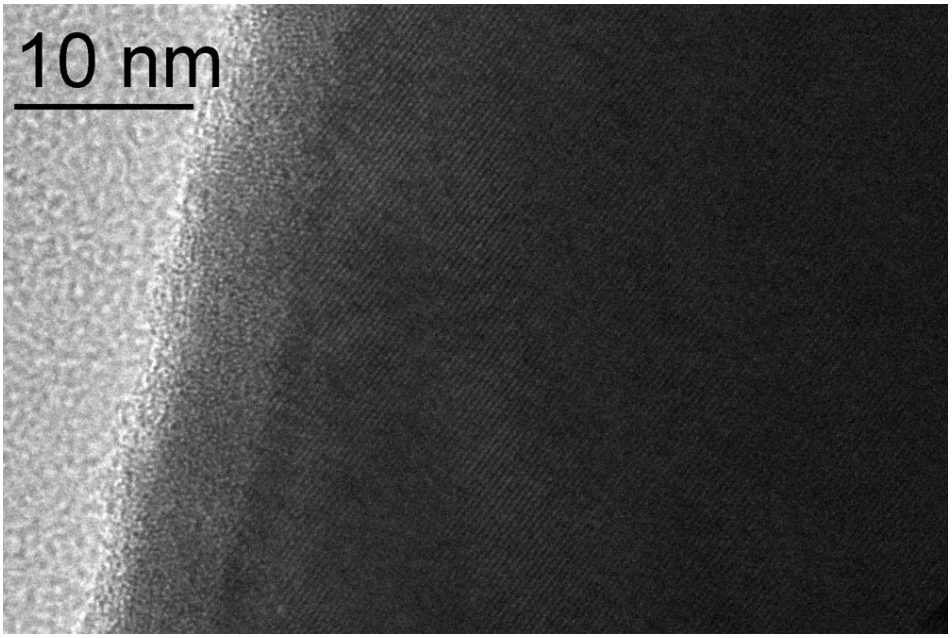

Figure A.3.4: High resolution TEM image of a cavity-free region of Bi nanowire.

Scanning Electron Microscopy of the FIB connected samples

Scanning Electron Microscopy (SEM) of the measured samples (Fig.A.3.5) reveal an irregularly shaped, polymer-like, coating around the nanowires, which we attribute to incompletely dissolved carbonate membrane. We believe that this coating protects the bismuth from fast oxidation. SEM and EDX (Energy Dispersive X-Ray spectroscopy) also confirmed the absence of W contamination of the substrate beyond 300 nm away from the electrodes. Note that other attempts to connect the nanowires with standard lithography techniques after ion (Argon, ion) etching of the contact region failed.

A.4 Superconductivity of the ReW electrodes

ReW is supposed to sustain the superconductivity at high magnetic field. While measuring the sample, we tested the critical current of a ReW wire as a function of magnetic field. The critical current was larger than $3\mu A$ at 55 mK at 7.5T (Fig.A.4.1).

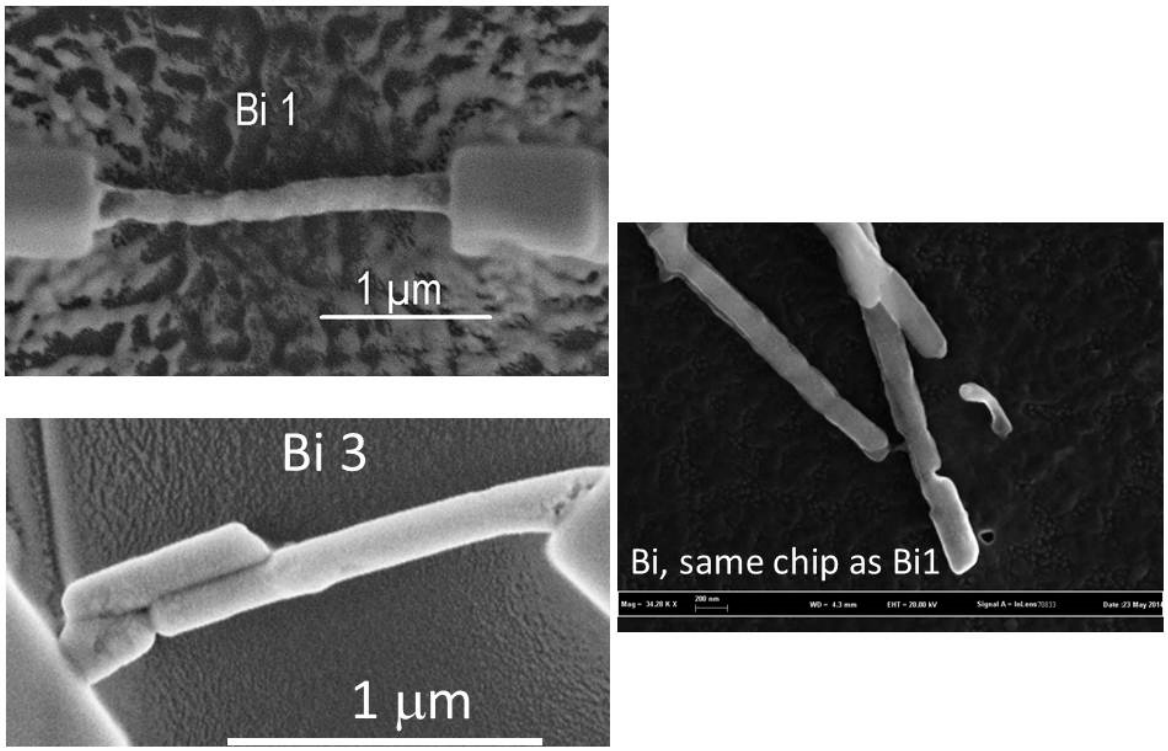

Figure A.3.5: Left: SEM image of two of the measured samples connected for transport measurement, using Focused Ion Beam-induced deposition of tungsten. The small fragment in parallel with the Bi3 wire is not electrically connected to the wire, because of the insulating coating around the wires. Right: SEM image of Bi wires on the same substrate as Bi1, illustrating the irregular-shaped coating that can be attributed to polymer residues from the polycarbonate membrane, and that protects the wires from fast oxidation.

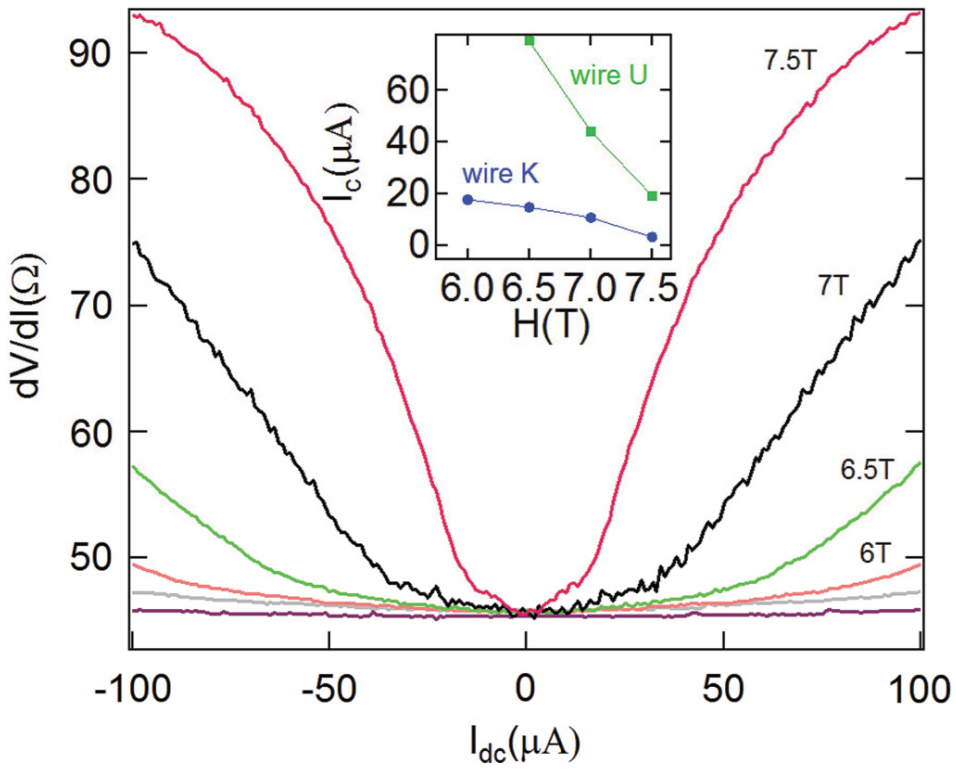

Figure A.4.1: Differential resistance of a ReW wire at different magnetic field, low temperature. (Inset) Critical current of two ReW leads.

B

Supplementary transport measurement

B.1 Highly disordered graphene and indication of a gap opening

We measured the transport properties of the sample G92 presented in Sec. It turns out that the graphene sheets are all highly disordered. We attribute this to the plasma treatment.

Fabrication

Monolayer graphene is exfoliated onto oxygen plasma pretreated SiO_2 substrate. The oxygen plasma is the crucial step in sample preparation. 10 min plasma etching on the surface of SiO_2 substrate. Then standard electron lithograph process is carried on the sample. Ti/Al is deposited as metal contacts by e-beam evaporation. (Ti 6nm and Al 70nm).

Measurement before grafting porphyrin molecules

After lift-off step from hot acetone, the samples are measured under probe station with lock-in at 17Hz. Most of the samples show nice gate dependence by a factor to 5-10 between the resistance of charge neutral point and of doped regime. Several $R(V_G)$ curves are shown below:

(Fig in the small PC)

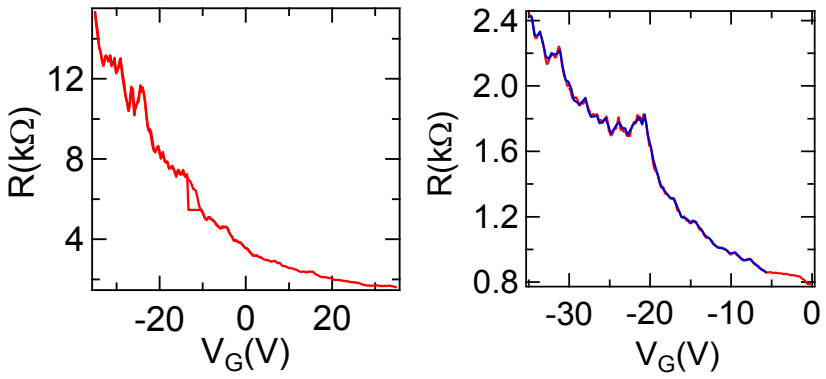

Figure B.1.1: Gate dependence of samples on chip G92. All of them are highly doped and disordered.

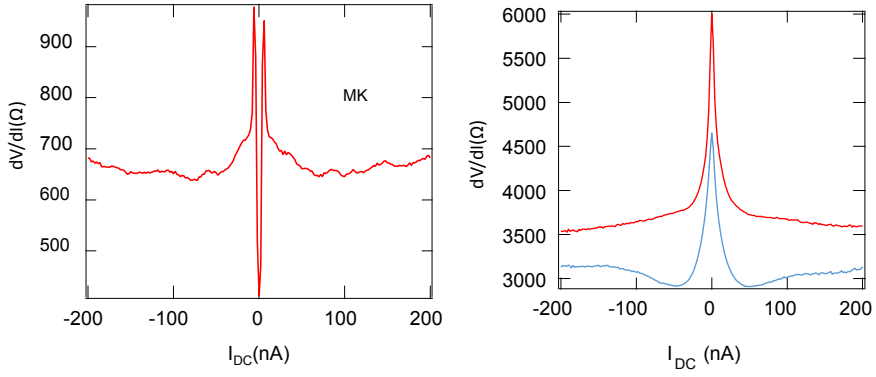

Figure B.1.2: dV/dI curves for different samples before putting porphyrins.

However one night after that (samples are kept in vacuum box during the night), all samples' DP are strongly shifted to negative gate voltage and resistance is increased about 1 order:

Even we increase the gate voltage to -40V, the DP is still missing.

Samples are cooled down to mille kelvin level by wet-H3/H4 mixture dilution fridge. Al electrodes become superconducting at about 1.3K. We found in several samples a dip at the zero bias, which is the indication of superconducting proximity effect.

QHE

We apply perpendicular magnetic field up to 11T and observed interesting magnetoresistance and QHE. Firstly, the samples seems to present a Dirac point around -20V. Because the $\nu = 2$ plateau (identified by the resistance), is presented the right of the DP. Actually, all the plateaus at the elec-

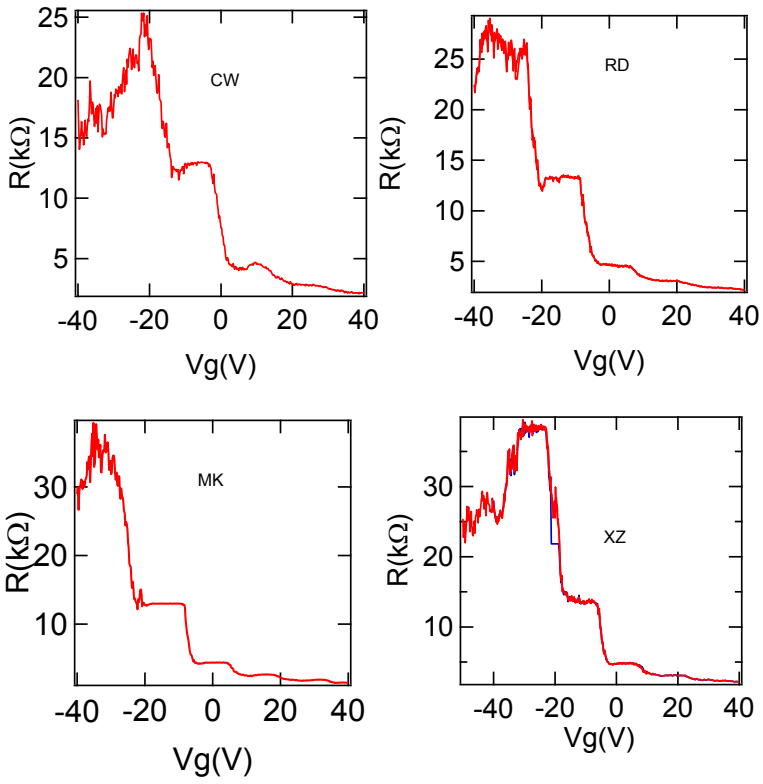

Figure B.1.3: QHE of the 4 samples on chip G92. From the $V_G = 20V$, the

tron doped regime are presented with the right values.

However at another side(hole doped regime) the resistance is very high. As the samples are highly doped, we can barely have second filling factor by sweeping the gate. Some of the samples show a plateau at the position of v=2 (XZ). But the resistance values are not correct. They are much higher than expected value(13kΩ). This may be attributed to a gate dependent additional resistance in graphene which should correspond to the disorders.

References

[1] A. H. Castro Neto, F. Guinea, N. M. R. Peres, K. S. Novoselov, and A. K. Geim. The electronic properties of graphene. *Rev. Mod. Phys.*, 81:109–162, Jan 2009.

[2] A. K. Geim and K. S. Novoselov. The rise of graphene. *Nat Mater*, 6(3):183–191, March 2007.

[3] Z Jiang, Y Zhang, Y-W Tan, HL Stormer, and P Kim. Quantum hall effect in graphene. *Solid state communications*, 143(1):14–19, 2007.

[4] Yuanbo Zhang, Yan-Wen Tan, Horst L Stormer, and Philip Kim. Experimental observation of the quantum hall effect and berry's phase in graphene. *Nature*, 438(7065):201–204, 2005.

[5] Konstantin S Novoselov, Z Jiang, Y Zhang, SV Morozov, HL Stormer, U Zeitler, JC Maan, GS Boebinger, P Kim, and AK Geim. Room-temperature quantum hall effect in graphene. *Science*, 315(5817):1379–1379, 2007.

[6] Yuanbo Zhang, Tan Yan-Wen, L. Stormer, Horst, and Philip Kim. Experimental observation of the quantum hall effect and berry's phase in graphene. *Nature*, 438:201, Nov 2005.

[7] C. W. J. Beenakker. Specular andreev reflection in graphene. *Phys. Rev. Lett.*, 97:067007, Aug 2006.

[8] Katsuyoshi Komatsu, Chuan Li, S. Autier-Laurent, H. Bouchiat, and S. Guéron. Superconducting proximity effect in long superconductor/graphene/superconductor junctions: From specular Andreev reflection at zero field to the quantum Hall regime. *Physical Review B*, 86(11):115412, September 2012.

[9] C. W. J. Beenakker and H. van Houten. Josephson current through a superconducting quantum point contact shorter than the coherence length. *Phys. Rev. Lett.*, 66:3056–3059, Jun 1991.

[10] Hideaki Takayanagi, Tatsushi Akazaki, and Junsaku Nitta. Observation of maximum supercurrent quantization in a superconducting quantum point contact. *Phys. Rev. Lett.*, 75:3533–3536, Nov 1995.

[11] G. E. Blonder, M. Tinkham, and T. M. Klapwijk. Transition from metallic to tunneling regimes in superconducting microconstrictions: Excess current, charge imbalance, and supercurrent conversion. *Phys. Rev. B*, 25:4515–4532, Apr 1982.

[12] M. Ma and A. Yu. Zyuzin. Josephson effect in the quantum hall regime. *EPL (Europhysics Letters)*, 21(9):941, 1993.

[13] Hideaki Takayanagi and Tatsushi Akazaki. Semiconductor-coupled superconducting junctions using nbn electrodes with high hc2 and tc. *Physica B: Condensed Matter*, 249–251(0):462 – 466, 1998.

[14] Hideaki Takayanagi, Tatsushi Akazaki, Minoru Kawamura, Yuichi Harada, and Junsaku Nitta. Superconducting junctions using algaas/gaas heterostructures with high hc2 nbn electrodes. *Physica E: Low-dimensional Systems and Nanostructures*, 12(1–4):922 – 926, 2002. Proceedings of the Fourteenth International Conference on the Ele ctronic Properties of Two-Dimensional Systems.

[15] J. H. LeeEduardo, Kannan Balasubramanian, Ralf T. Weitz, Marko Burghard, and Klaus Kern. Contact and edge effects in graphene devices. *Nat Nano*, 3(8):486–490, August 2008.

[16] Ximeng Guan, Qiushi Ran, Ming Zhang, Zhiping Yu, and H.-S.P. Wong. Modeling of schottky and ohmic contacts between metal and graphene nanoribbons using extended huckel theory (eht)-based negf method. pages 1–4, Dec 2008.

[17] Junsaku Nitta, Tatsushi Akazaki, Hideaki Takayanagi, and Takatomo Enoki. Gate control of spin-orbit interaction in an inverted $in_{0.53}ga_{0.47}as/in_{0.52}al_{0.48}as$ heterostructure. *Phys. Rev. Lett.*, 78:1335–1338, Feb 1997.

[18] Lev P. Gor'kov and Emmanuel I. Rashba. Superconducting 2d system with lifted spin degeneracy: Mixed singlet-triplet state. *Phys. Rev. Lett.*, 87:037004, Jul 2001.

[19] E. V. Bezuglyi, A. S. Rozhavsky, I. D. Vagner, and P. Wyder. Combined effect of zeeman splitting and spin-orbit interaction on the josephson current in a superconductor□two-dimensional electron gas□superconductor structure. *Phys. Rev. B*, 66:052508, Aug 2002.

[20] L. Dell'Anna, A. Zazunov, R. Egger, and T. Martin. Josephson current through a quantum dot with spin-orbit coupling. *Phys. Rev. B*, 75:085305, Feb 2007.

[21] Nikolai M. Chtchelkatchev and Yu. V. Nazarov. Andreev quantum dots for spin manipulation. *Phys. Rev. Lett.*, 90:226806, Jun 2003.

[22] Jay D. Sau, Roman M. Lutchyn, Sumanta Tewari, and S. Das Sarma. Generic new platform for topological quantum computation using semiconductor heterostructures. *Phys. Rev. Lett.*, 104:040502, Jan 2010.

[23] Jason Alicea. Majorana fermions in a tunable semiconductor device. *Phys. Rev. B*, 81:125318, Mar 2010.

[24] V. Mourik, K. Zuo, S. M. Frolov, S. R. Plissard, E. P. A. M. Bakkers, and L. P. Kouwenhoven. Signatures of Majorana Fermions in Hybrid Superconductor-Semiconductor Nanowire Devices. *Science*, 336(6084):1003–1007, May 2012.

[25] B. Andrei Bernevig and Shou-Cheng Zhang. Quantum spin hall effect. *Phys. Rev. Lett.*, 96:106802, Mar 2006.

[26] Yugui Yao, Fei Ye, Xiao-Liang Qi, Shou-Cheng Zhang, and Zhong Fang. Spin-orbit gap of graphene: First-principles calculations. *Phys. Rev. B*, 75:041401, Jan 2007.

[27] Hongki Min, J. E. Hill, N. A. Sinitsyn, B. R. Sahu, Leonard Kleinman, and A. H. MacDonald. Intrinsic and rashba spin-orbit interactions in graphene sheets. *Phys. Rev. B*, 74:165310, Oct 2006.

[28] Jayakumar Balakrishnan, Gavin Kok Wai Koon, Manu Jaiswal, A. H. Castro Neto, and Barbaros Ozyilmaz. Colossal enhancement of spin-orbit coupling in weakly hydrogenated graphene. *Nat Phys*, 9(5):284–287, May 2013.

[29] Sumanta Bhandary, Olle Eriksson, and Biplab Sanyal. Defect controlled magnetism in FeP/graphene/Ni(111). *Scientific reports*, 3:3405, January 2013.

[30] Manuela Garnica, Daniele Stradi, Sara Barja, Fabian Calleja, Cristina Díaz, Manuel Alcamí, Nazario Martín, Amadeo L. Vázquez de Parga, Fernando Martín, and Rodolfo Miranda. Long-range magnetic order in a purely organic 2D layer adsorbed on epitaxial graphene. *Nature Physics*, 9(6):368–374, April 2013.

[31] Andrea Candini, Svetlana Klyatskaya, Mario Ruben, Wolfgang Wernsdorfer, and Marco Affronte. Graphene spintronic devices with molecular nanomagnets. *Nano Letters*, 11(7):2634–2639, 2011. PMID: 21648452.

[32] Tadahiro Komeda, Hironari Isshiki, Jie Liu, Yan-Feng Zhang, Nicolás Lorente, Keiichi Katoh, Brian K Breedlove, and Masahiro Yamashita. Observation and electric current control of a local spin in a single-molecule magnet. *Nature communications*, 2:217, January 2011.

[33] Ph. Hofmann. The surfaces of bismuth: Structural and electronic properties. *Progress in Surface Science*, 81(5):191–245, January 2006.

[34] a. Nikolaeva, D. Gitsu, L. Konopko, M. Graf, and T. Huber. Quantum interference of surface states in bismuth nanowires probed by the Aharonov-Bohm oscillatory behavior of the magnetoresistance. *Physical Review B*, 77(7):075332, February 2008.

[35] Mingliang Tian, Jian Wang, Qi Zhang, Nitesh Kumar, Thomas E. Mallouk, and Moses H. W. Chan. Superconductivity and quantum oscillations in crystalline bi nanowire. *Nano Letters*, 9(9):3196–3202, 2009. PMID: 19736972.

[36] Yu. M. Koroteev, G. Bihlmayer, J. E. Gayone, E. V. Chulkov, S. Blügel, P. M. Echenique, and Ph. Hofmann. Strong spin-orbit splitting on bi surfaces. *Phys. Rev. Lett.*, 93:046403, Jul 2004.

[37] T. Hirahara, K. Miyamoto, I. Matsuda, T. Kadono, A. Kimura, T. Nagao, G. Bihlmayer, E. V. Chulkov, S. Qiao, K. Shimada, H. Namatame, M. Taniguchi, and S. Hasegawa. Direct observation of spin splitting in bismuth surface states. *Phys. Rev. B*, 76:153305, Oct 2007.

[38] Wei Ning, Fengyu Kong, Chuanying Xi, David Graf, Haifeng Du, Yuyan Han, Jiyong Yang, Kun Yang, Mingliang Tian, and Yuheng Zhang. Evidence of topological two-dimensional metallic surface states in thin bismuth nanoribbons. *ACS Nano*, 8(7):7506–7512, 2014.

[39] Shuichi Murakami. Quantum spin hall effect and enhanced magnetic response by spin-orbit coupling. *Phys. Rev. Lett.*, 97:236805, Dec 2006.

[40] HB Heersche and Pablo Jarillo-Herrero. Bipolar supercurrent in graphene. *Nature*, 446(7131):56–59, March 2007.

[41] Dongchan Jeong, Jae-Hyun Choi, Gil-Ho Lee, Sanghyun Jo, Yong-Joo Doh, and Hu-Jong Lee. Observation of supercurrent in pbin-graphene-pbin josephson junction. *Phys. Rev. B*, 83:094503, Mar 2011.

[42] Xu Du, Ivan Skachko, and Eva Y. Andrei. Josephson current and multiple andreev reflections in graphene sns junctions. *Phys. Rev. B*, 77:184507, May 2008.

[43] Chih-Jen Shih, Geraldine L. C. Paulus, Qing Hua Wang, Zhong Jin, Daniel Blankschtein, and Michael S. Strano. Understanding surfactant/graphene interactions using a graphene field effect transistor: Relating molecular structure to hysteresis and carrier mobility. *Langmuir*, 28(22):8579–8586, 2012. PMID: 22587527.

[44] C. Coletti, C. Riedl, D. S. Lee, B. Krauss, L. Patthey, K. von Klitzing, J. H. Smet, and U. Starke. Charge neutrality and band-gap tuning of epitaxial graphene on SiC by molecular doping. *Physical Review B*, 81(23):235401, June 2010.

[45] P. W. Anderson. Localized magnetic states in metals. *Phys. Rev.*, 124:41–53, Oct 1961.

[46] Alexei Fedorov. The all-organic route to doping graphene. *Physics*, 3:46, June 2010.

[47] Rakesh Voggu, Barun Das, Chandra Sekhar Rout, and C N R Rao. Effects of charge transfer interaction of graphene with electron donor and acceptor molecules examined using Raman spectroscopy and cognate techniques. *Journal of Physics: Condensed Matter*, 20(47):472204, November 2008.

[48] sylvie rousset Van Dong Pham, Mouhoub, Ouafi. Electronic Interaction between Nitrogen-Doped Graphene and. *nano*, (9):9403–9409, 2014.

[49] H Vázquez, F Flores, R Oszwaldowski, J Ortega, R Pérez, and a Kahn. Barrier formation at metal–organic interfaces: dipole formation and the charge neutrality level. *Applied Surface Science*, 234(1-4):107–112, July 2004.

[50] Yusuke Tanaka, Kaname Kanai, Yukio Ouchi, and Kazuhiko Seki. Role of interfacial dipole layer for energy-level alignment at organic/metal interfaces. *Organic Electronics*, 10(5):990–993, August 2009.

[51] Hisao Ishii, Kiyoshi Sugiyama, Eisuke Ito, and Kazuhiko Seki. Energy level alignment and interfacial electronic structures at organic/metal and organic/organic interfaces. *Advanced Materials*, 11(8):605–625, 1999.

[52] Mark T Greiner, Michael G Helander, Wing-Man Tang, Zhi-Bin Wang, Jacky Qiu, and Zheng-Hong Lu. Universal energy-level alignment of molecules on metal oxides. *Nature materials*, 11(1):76–81, January 2012.

[53] Gita Sedghi, Víctor M García-Suárez, Louisa J Esdaile, Harry L Anderson, Colin J Lambert, Santiago Martín, Donald Bethell, Simon J Higgins, Martin Elliott, Neil Bennett, J Emyr Macdonald, and Richard J Nichols. Long-range electron tunnelling in oligo-porphyrin molecular wires. *Nature nanotechnology*, 6(8):517–23, August 2011.

[54] J Meyefb, D Schlettwein, and N I Jaeger. Charge transport in thin films of molecular semiconductors as investigated by measurements of thermoelectric power and electrical conductivity. 258:317–324, 1995.

[55] Yoram Selzer, Marco A Cabassi, Theresa S Mayer, David L Allara, V Pennsyl, State Uni, and Uni V Park. Thermally Activated Conduction in Molecular Junctions. pages 4052–4053, 2004.

[56] Bruno Uchoa, Valeri N. Kotov, N. M. R. Peres, and A. H. Castro Neto. Localized magnetic states in graphene. *Phys. Rev. Lett.*, 101:026805, Jul 2008.

[57] R.P. Feynman, R.B. Leighton, and M. Sands. *THE FEYNMAN LECTURES ON PHYSICS, Vol III, Quantum Mechanics*. Addison-Wesley, 1976.

[58] F. Andreev, A. The thermal conductivity of the intermediate state in superconductors. *JETP*, 19:1228, Nov 1964.

[59] P. A. M. Benistant, H. van Kempen, and P. Wyder. Direct observation of andreev reflection. *Phys. Rev. Lett.*, 51:817–820, Aug 1983.

[60] H. A. Blom, A. Kadigrobov, A. M. Zagoskin, R. I. Shekhter, and M. Jonson. Dissipative electron transport through andreev interferometers. *Phys. Rev. B*, 57:9995–10016, Apr 1998.

[61] H. van Houten and C.W.J. Beenakker. Andreev reflection and the josephson effect in a quantum point contact: An analogy with phase-conjugating resonators. *Physica B: Condensed Matter*, 175(1–3):187 – 197, 1991. Analogies in Optics and Micro-Electronics.

[62] F. Andreev, A. Electron spectrum of the intermediate state of superconductors. *JETP*, 22:455, Feb 1966.

[63] J-D. Pillet, C. H. L. Quay, P. Morfin, C. Bena, a. Levy Yeyati, and P. Joyez. Andreev bound states in supercurrent-carrying carbon nanotubes revealed. *Nature Physics*, 6(12):965–969, November 2010.

[64] Akira Furusaki, Hideaki Takayanagi, and Masaru Tsukada. Theory of quantum conduction of supercurrent through a constriction. *Phys. Rev. Lett.*, 67:132–135, Jul 1991.

[65] Philip F. Bagwell. Suppression of the josephson current through a narrow, mesoscopic, semiconductor channel by a single impurity. *Phys. Rev. B*, 46:12573–12586, Nov 1992.

[66] J. C. Cuevas and W. Belzig. Full counting statistics of multiple andreev reflections. *Phys. Rev. Lett.*, 91:187001, Oct 2003.

[67] M. Ferrier, B. Dassonneville, S. Guéron, and H. Bouchiat. Phase-dependent andreev spectrum in a diffusive sns junction: Static and dynamic current response. *Phys. Rev. B*, 88:174505, Nov 2013.

[68] P. Dubos, H. Courtois, B. Pannetier, F. Wilhelm, a. Zaikin, and G. Schön. Josephson critical current in a long mesoscopic S-N-S junction. *Physical Review B*, 63(6):064502, January 2001.

[69] Gilles Montambaux. *Mesoscopic Physics of Electrons and Photons*. Cambridge University Press, 1 edition, 2007.

[70] Bulaevskii L.N., V. Kuzii V., and A. Sobyanin A. Superconducting system with weak coupling to the current in the ground state. *JETP Lett*, 25:290, Apr 1977.

[71] Buzdin A. I., Bulaevskii L. N., and Panyukov S. V. Critical-current oscillations as a function of the exchange field and thickness of the ferromagnetic metal (f) in an s-f-s josephson junction. *JETP Lett*, 35:178, Feb 1977.

[72] Buzdin A. I., Bujicic B., and Kupriyanov M. Yu. Superconductor-ferromagnet structures. *JETP*, 74:124, June 1991.

[73] G Montambaux. interference pattern of a long junction diffusive josephson junction. *cond-mat*, 2007.

[74] Sean Hart, Hechen Ren, Timo Wagner, Philipp Leubner, Mathias Mühlbauer, Christoph Brüne, Hartmut Buhmann, Laurens W Molenkamp, and Amir Yacoby. Induced superconductivity in the quantum spin. *Nature Physics*, pages 1–6, 2014.

[75] Antonio Barone and Gianfranco Paternò. *Physics and applications of the Josephson effect*. Wiley, 1982.

[76] F. Chiodi, M. Ferrier, S. Guéron, J. C. Cuevas, G. Montambaux, F. Fortuna, A. Kasumov, and H. Bouchiat. Geometry-related magnetic interference patterns in long *sns* josephson junctions. *Phys. Rev. B*, 86:064510, Aug 2012.

[77] L. Angers, F. Chiodi, G. Montambaux, M. Ferrier, S. Guéron, H. Bouchiat, and J. C. Cuevas. Proximity dc squids in the long-junction limit. *Phys. Rev. B*, 77:165408, Apr 2008.

[78] F.S. Bergeret and J.C. Cuevas. The vortex state and josephson critical current of a diffusive sns junction. 153(5-6):304–324, 2008.

[79] KSA Novoselov, Andre K Geim, SVb Morozov, Da Jiang, MI Katsnelson IV Grigorieva, SV Dubonos, and AA Firsov. Two-dimensional gas of massless dirac fermions in graphene. *nature*, 438(7065):197–200, 2005.

[80] Andrea F Young and Philip Kim. Quantum interference and klein tunnelling in graphene heterojunctions. *Nature Physics*, 5(3):222–226, 2009.

[81] CWJ Beenakker. Colloquium: Andreev reflection and klein tunneling in graphene. *Reviews of Modern Physics*, 80(4):1337, 2008.

[82] MI Katsnelson, KS Novoselov, and AK Geim. Chiral tunnelling and the klein paradox in graphene. *Nature Physics*, 2(9):620–625, 2006.

[83] N Stander, B Huard, and D Goldhaber-Gordon. Evidence for klein tunneling in graphene p-n junctions. *Physical Review Letters*, 102(2):026807, 2009.

[84] Supriyo Datta. *Electronic Transport in Mesoscopic Systems*. Cambridge University Press, 1995. Cambridge Books Online.

[85] F. D. M. Haldane. Model for a quantum hall effect without landau levels: Condensed-matter realization of the "parity anomaly". *Phys. Rev. Lett.*, 61:2015–2018, Oct 1988.

[86] Yisong Zheng and Tsuneya Ando. Hall conductivity of a two-dimensional graphite system. *Phys. Rev. B*, 65:245420, Jun 2002.

[87] S. Novoselov, K., A. K. Geim, V. Morozov, S., D. Jiang, I. Katsnelson, M., V. Grigorieva, I., V. Dubonos, S., and A. Firsov, A. Two-dimensional gas of massless dirac fermions in graphene. *Nature*, 438:197, Nov 2005.

[88] Ashcroft and Mermin. *Solid state physics*. Saunders, 1976.

[89] Claude Cohen-Tannoudji, Bernard Diu, and Franck Laloë. *Mécanique quantique*. Hermann, 1997.

[90] R. Winkler. *Spin-Orbit coupling effects in Two-dimensional electron and hole systems*. Springer-Verlag, 2003.

[91] F.E. Meijier. Thesis: Rashba spin-orbit interaction in mesoscopic systems.

[92] N. F. Mott. The scattering of fast electrons by atomic nuclei. *Proceedings of the Royal Society of London. Series A*, 124(794):425–442, 1929.

[93] G. Dresselhaus. Spin-orbit coupling effects in zinc blende structures. *Phys. Rev.*, 100:580–586, Oct 1955.

[94] Yu.A Bychkov and E.I. Rashba. Properties of a 2d electron gas with lifted spectral degeneracy. *JETP*, 39:78, Nov 1984.

[95] E. I. Rashba. Properties of semiconductors with an extremum loop. 1. Cyclotron and combinational resonance in a magnetic field perpendicular to the plane of the loop. *Sov. Phys. Solid State*, 2:1224–1238, 1960.

[96] P. Cucka and C. S. Barrett. The crystal structure of Bi and of solid solutions of Pb, Sn, Sb and Te in Bi. *Acta Crystallographica*, 15(9):865–872, Sep 1962.

[97] Yi Liu and Roland E. Allen. Electronic structure of the semimetals bi and sb. *Phys. Rev. B*, 52:1566–1577, Jul 1995.

[98] X. Gonze, J.-P. Michenaud, and J.-P. Vigneron. First-principles study of as, sb, and bi electronic properties. *Phys. Rev. B*, 41:11827–11836, Jun 1990.

[99] Zengwei Zhu, Aurélie Collaudin, Benoît Fauqué, Woun Kang, and Kamran Behnia. Field-induced polarization of Dirac valleys in bismuth. *Nature Physics*, 8(1):89–94, October 2011.

[100] H. Mönig, J. Sun, Yu. M. Koroteev, G. Bihlmayer, J. Wells, E. V. Chulkov, K. Pohl, and Ph. Hofmann. Structure of the (111) surface of bismuth: Leed analysis and first-principles calculations. *Phys. Rev. B*, 72:085410, Aug 2005.

[101] G. Jezequel, Y. Petroff, R. Pinchaux, and Félix Yndurain. Electronic structure of the bi(111) surface. *Phys. Rev. B*, 33:4352–4355, Mar 1986.

[102] G. Jezequel, J. Thomas, and I. Pollini. Experimental band structure of semimetal bismuth. *Phys. Rev. B*, 56:6620–6626, Sep 1997.

[103] Akinori Tanaka, Masayuki Hatano, Kazutoshi Takahashi, Hiroyuki Sasaki, Shoji Suzuki, and Shigeru Sato. Bulk and surface electronic structures of the semimetal bi studied by angle-resolved photoemission spectroscopy. *Phys. Rev. B*, 59:1786–1791, Jan 1999.

[104] J Thomas, G Jezequel, and I Pollini. Photoemission study of the bulk and surface electronic structure of bi(111). *Journal of Physics: Condensed Matter*, 11(48):9571, 1999.

[105] Christian R. Ast and Hartmut Höchst. High-resolution photoemission mapping of the three-dimensional band structure of bi(111). *Phys. Rev. B*, 70:245122, Dec 2004.

[106] Christian R. Ast and Hartmut Höchst. Fermi surface of bi(111) measured by photoemission spectroscopy. *Phys. Rev. Lett.*, 87:177602, Oct 2001.

[107] Yu-Ming Lin, Xiangzhong Sun, and M. S. Dresselhaus1, 2. Theoretical investigation of thermoelectric transport properties of cylindrical bi nanowires. *Phys. Rev. B*, 62:4610–4623, Aug 2000.

[108] Huber T. E., Nikolaeva A., Gitsu D., Konopko L., Foss C. A., and Garf M. J. Confinement effects and surface-induced charge carriers in bi quantum wires. *Appl. Phys. Lett.*, 84:1326, 2004.

[109] Huber T. E., Nikolaeva A., Konopko L., and Graf M. J. Observation of three-dimensional behavior in surface states of bismuth nanowires and the evidence for bulk-bi surface quasiparticles. *Phys. Rev. B*, 79:201304, 2009.

[110] Huber T. E., Adeyeye A., Nikolaeva A., Konopko L., Johnson R. C., and Graf M. J. Surface state band mobility and thermopower in semiconducting bismuth nanowires. *Phys. Rev. B*, 83:235414, 2011.

[111] J. C. Hammer, J. C. Cuevas, F. S. Bergeret, and W. Belzig. Density of states and supercurrent in diffusive SNS junctions: Roles of nonideal interfaces and spin-flip scattering. *Physical Review B*, 76(6):064514, August 2007.

[112] J. Martin, N. Akerman, G. Ulbricht, T. Lohmann, J. H. Smet, K. von Klitzing, and A. Yacoby. Observation of electron–hole puddles in graphene using a scanning single-electron transistor. *Nature Physics*, 4(2):144–148, November 2007.

[113] Michael Stone and Yiruo Lin. Josephson currents in quantum hall devices. *Phys. Rev. B*, 83:224501, Jun 2011.

[114] J. R. Williams, D. A. Abanin, L. DiCarlo, L. S. Levitov, and C. M. Marcus. Quantum hall conductance of two-terminal graphene devices. *Phys. Rev. B*, 80:045408, Jul 2009.

[115] J. R. Williams, L. DiCarlo, and C. M. Marcus. Quantum hall effect in a gate-controlled p-n junction of graphene. *Science*, 317(5838):638–641, 2007.

[116] Y. Takagaki. Transport properties of semiconductor-superconductor junctions in quantizing magnetic fields. *Phys. Rev. B*, 57:4009–4016, Feb 1998.

[117] H. Hoppe, U. Zülicke, and Gerd Schön. Andreev reflection in strong magnetic fields. *Phys. Rev. Lett.*, 84:1804–1807, Feb 2000.

[118] C. W. J. Beenakker. Random-matrix theory of quantum transport. *Rev. Mod. Phys.*, 69:731–808, Jul 1997.

[119] F. Pierre, H. Pothier, P. Joyez, Norman O. Birge, D. Esteve, and M. H. Devoret. Electrodynamic dip in the local density of states of a metallic wire. *Phys. Rev. Lett.*, 86:1590–1593, Feb 2001.

[120] B.L. ALTSHULER and A.G. ARONOV. {CHAPTER} 1 - electron–electron interaction in disordered conductors. In A.L. EFROS and M. POLLAK, editors, *Electron–Electron Interactions in Disordered Systems*, volume 10 of *Modern Problems in Condensed Matter Sciences*, pages 1 – 153. Elsevier, 1985.

[121] U. Sivan and Y. Imry. de haas-van alphen and aharonov-bohm-type persistent current oscillations in singly connected quantum dots. *Phys. Rev. Lett.*, 61:1001–1004, Aug 1988.

[122] Dimitrios Tasis, Nikos Tagmatarchis, Alberto Bianco, and Maurizio Prato. Chemistry of carbon nanotubes. *Chemical Reviews*, 106(3):1105–1136, 2006.

[123] David S. Hecht, Robert J. A. Ramirez, Mikhail Briman, Erika Artukovic, Kelly S. Chichak, J. Fraser Stoddart, and George Grüner. Bioinspired detection of light using a porphyrin-sensitized single-wall nanotube field effect transistor. *Nano Letters*, 6(9):2031–2036, 2006.

[124] M. S. Choi, D. J. Lee, S. J. Lee, D. H. Hwang, J. H. Lee, N. Aoki, Y. Ochiai, H.-J. Kim, D. Whang, S. Kim, and S. W. Hwang. Gate-dependent photoconductivity of single layer graphene grafted with metalloporphyrin molecules. *Applied Physics Letters*, 100(16):–, 2012.

[125] P. Checcoli, G. Conte, S. Salvatori, R. Paolesse, A. Bolognesi, M. Berliocchi, F. Brunetti, A. D'Amico, A. Di Carlo, and P. Lugli. Tetra-phenyl porphyrin based thin film transistors. *Synthetic Metals*, 138(1–2):261 – 266, 2003. Organic Materials for Device Applications. Proceedings of Symposium F, E-MRS Spring Meeting 2002, June 18-21, 2002, Strasbourg, France.

[126] Sumanta Bhandary, Olle Eriksson, and Biplab Sanyal. Defect controlled magnetism in fep/graphene/ni(111). *Scientific reports*, 3(3):3405, December 2013.

[127] Valeri N. Kotov, Bruno Uchoa, Vitor M. Pereira, F. Guinea, and A. H. Castro Neto. Electron-electron interactions in graphene: Current status and perspectives. *Rev. Mod. Phys.*, 84:1067–1125, Jul 2012.

[128] Annica M. Black-Schaffer. Rkky coupling in graphene. *Phys. Rev. B*, 81:205416, May 2010.

[129] Vitor M. Pereira, F. Guinea, J. M. B. Lopes dos Santos, N. M. R. Peres, and A. H. Castro Neto. Disorder induced localized states in graphene. *Phys. Rev. Lett.*, 96:036801, Jan 2006.

[130] IK Drozdov and A Alexandradinata. One-dimensional topological edge states of bismuth bilayers. *arXiv preprint arXiv: ...*, pages 1–28, 2014.

[131] J. W. Wells, J. H. Dil, F. Meier, J. Lobo-Checa, V. N. Petrov, J. Osterwalder, M. M. Ugeda, I. Fernandez-Torrente, J. I. Pascual, E. D. L. Rienks, M. F. Jensen, and Ph. Hofmann. Nondegenerate metallic states on bi(114): A one-dimensional topological metal. *Phys. Rev. Lett.*, 102:096802, Mar 2009.

[132] Andres A. Reynoso, Gonzalo Usaj, C. A. Balseiro, D. Feinberg, and M. Avignon. Spin-orbit-induced chirality of andreev states in josephson junctions. *Phys. Rev. B*, 86:214519, Dec 2012.

[133] Tomohiro Yokoyama, Mikio Eto, and Yuli V. Nazarov. Anomalous josephson effect induced by spin-orbit interaction and zeeman effect in semiconductor nanowires. *Phys. Rev. B*, 89:195407, May 2014.

[134] Buzdin A S. Mironov. unpublished. 2014.

[135] J-P Cleuziou, W Wernsdorfer, V Bouchiat, T Ondarçuhu, and M Monthioux. Carbon nanotube superconducting quantum interference device. *Nature nanotechnology*, 1(1):53–9, October 2006.

[136] A. Buzdin. Direct coupling between magnetism and superconducting current in the josephson ϕ_o junction. *Phys. Rev. Lett.*, 101:107005, Sep 2008.

[137] Victor Barzykin and Lev P. Gor'kov. Inhomogeneous stripe phase revisited for surface superconductivity. *Phys. Rev. Lett.*, 89:227002, Nov 2002.

[138] Y K Kato, R C Myers, A C Gossard, and D D Awschalom. Observation of the Spin Hall. *Science*, 306(December):0–3, 2004.

[139] Jayakumar Balakrishnan, Gavin Kok Wai Koon, Manu Jaiswal, A H Castro Neto, and Barbaros Özyilmaz. Colossal enhancement of spin–orbit coupling in weakly hydrogenated graphene. *Nature Physics*, 9(5):284–287, March 2013.

[140] Nikolaos Tombros, Alina Veligura, Juliane Junesch, J. Jasper van den Berg, Paul J. Zomer, Magdalena Wojtaszek, Ivan J. Vera Marun, Harry T. Jonkman, and Bart J. van Wees. Large yield production of high mobility freely suspended graphene electronic devices on a polydimethylglutarimide based organic polymer. *Journal of Applied Physics*, 109(9):–, 2011.

[141] Raymond P. Briñas, Thomas Troxler, Robin M. Hochstrasser, and Sergei A. Vinogradov. Phosphorescent oxygen sensor with dendritic protection and two-photon absorbing antenna. *Journal of the American Chemical Society*, 127(33):11851–11862, 2005. PMID: 16104764.

[142] C.C. Huang and K.Z. Fung. Effect of the surface configuration on the oxidation of bismuth nanowire. *Materials Research Bulletin*, 41(9):1604 – 1611, 2006.

[143] Mingliang Tian, Jian Wang, Qi Zhang, Nitesh Kumar, Thomas E. Mallouk, and Moses H. W. Chan. Superconductivity and quantum oscillations in crystalline bi nanowire. *Nano Letters*, 9(9):3196–3202, 2009. PMID: 19736972.

[144] Zuxin Ye, Hong Zhang, Haidong Liu, Wenhao Wu, and Zhiping Luo. Evidence for superconductivity in single crystalline Bi nanowires. *Physica B: Condensed Matter*, 403:1529–1530, 2008.

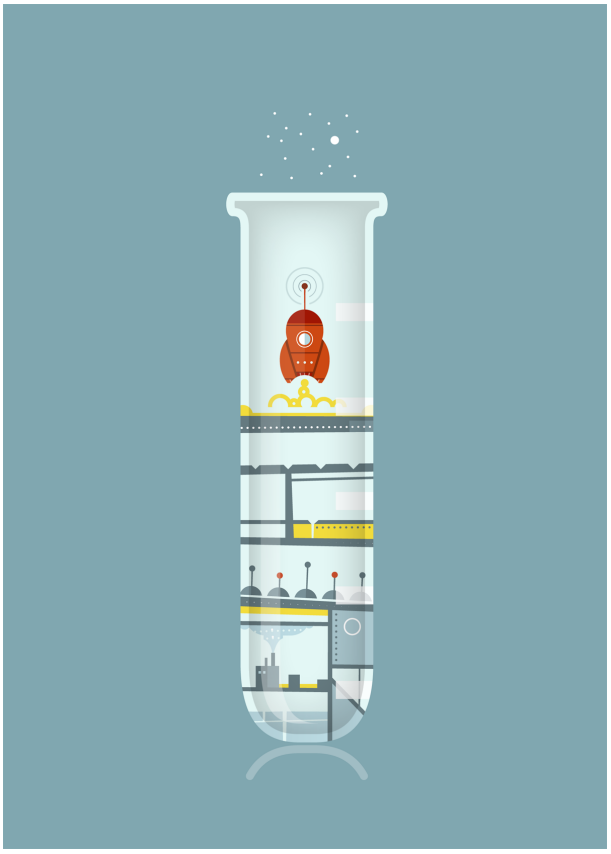

This thesis was typeset using LaTeX, originally developed by Leslie Lamport and based on Donald Knuth's TeX. The body text is set in 11 point Egenolff-Berner Garamond, a revival of Claude Garamont's humanist typeface. The above illustration, "Science Experiment 02", was created by Ben Schlitter and released under CC BY-NC-ND 3.0. A template that can be used to format a PhD thesis with this look and feel has been released under the permissive MIT (XII) license, and can be found online at github.com/suchow/Dissertate or from its author, Jordan Suchow, at suchow@post.harvard.edu.